UNIVERSIDAD AUTONOMA DE MADRID

FACULTAD DE CIENCIAS
DEPARTAMENTO DE FÍSICA APLICADA

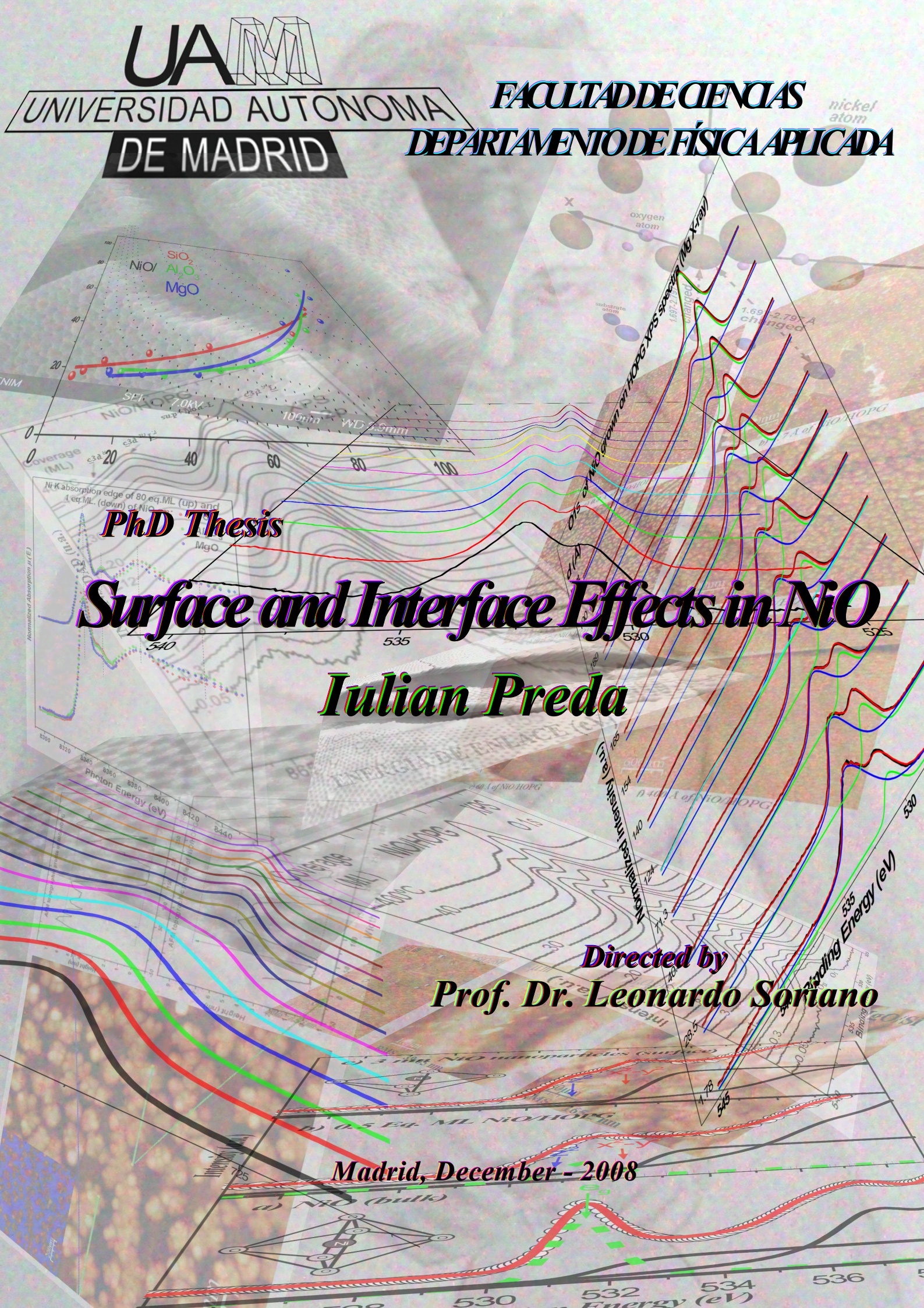

PhD Thesis

Surface and Interface Effects in NiO

Iulian Preda

Directed by

Prof. Dr. Leonardo Soriano

Madrid, December - 2008

UNIVERSIDAD AUTONOMA DE MADRID
FACULTAD DE CIENCIAS
DEPARTAMENTO DE FISICA APLICADA

Tesis doctoral:

"Surface and Interface Effects in NiO"

Memoria presentada por Iulian Preda para optar al titulo de Doctor en Ciencias Físicas.

Fdo. Lic. Iulian Preda

Director:

Prof. Dr.
Leonardo Soriano de Arpe

Madrid, Diciembre - 2008

…mamei, fiicelor ei şi fiului ei dintâi

GRACIAS

Me gustaría agradecer a todos los que, de alguna manera, hayan interaccionado conmigo durante este periodo en el que llevé a cabo este trabajo de investigación. Intentaré nombrarlos, pero…no se si me dará tiempo, tengo que enviar ya esta copia y…jeje…

Prof. Dr. Leonardo Soriano, empiezo con usted, porque… si no le hubieras "hecho caso" a "un rumano"… no se si este trabajo hubiera visto la luz... o si, pero con otro autor.

¡Gracias Lalo!

Y los dos vamos a dar las gracias al **MECT**, *que a través del proyecto* **BFM2003-03277** *y la beca* **BES-2004-6282** *ha ofrecido el suporte material para este estudio.*

Alejandro Gutiérrez, muchísimas gracias para la paciencia con la que me has enseñado utilizar el NEWFITT, tan necesario en este estudio.

José Antonio, debo reconocer que muchos trabajos que hice en el laboratorio no hubieran tardado tanto, si te hubiera escuchado y seguido los provechosos consejos que siempre me has dado. Gracias, para todo.

Quiero agradecer a Javier Luis Méndez, investigador del CSIC - ICMM, cuya experiencia en técnicas AFM ha revelado el verdadero modo en el que el oxido de níquel se sienta sobre el grafito. Y les aseguro que no es fácil. Tampoco se me olvida Lucia Álvarez Gonzáles que me ha iniciado en técnicas AFM. También, quisiera agradecer al señor Pablo Ares de NANOTEC, que completo el estudio AFM con la medida de uno de los estadios del crecimiento.

Recuerdos a Francisco Yubero Valencia, de CSIC- ICM Sevilla, cuya experiencia en el análisis cuantitativa del background de los espectros XPS ha hecho que este no sea simplemente "Shirley substracted".

Muchísimas gracias señor Jesús Chaboy Nalda, ICM Zaragoza, sin su preciosa ayuda, en lo que NEXAFS realmente significa, gran parte del trabajo experimental no hubiera sido aprovechado.

Para el suporte técnico ofrecido en la línea PM4 de BESSY II, me gustaría agradecerle a Antje Vollmer: DANKE!

Y como no voy agradecer a la gente como German R. Castro o Juan Rubio Zuazo, cuyos asiduos trabajos han hecho posibles medidas HAXPES de mis muestras, tan poco frecuentes todavía, hoy en día. ¡Gracias!

Y sin nombrar a nadie en particular, del departamento de Física Aplicada, de la Universidad Autónoma de Madrid, les quiero agradecer a todos los que investigan allá, por acogerme como colega entre ellos.

Thanks a lot Chuck, it was a great experience to work in your team, even if the beam never came, you give me the opportunity to met people like Mark, Marco Brian and Lucasz.

A todo el personal del SEGAINVEX le quiero agradecer por su preciso trabajo.

Nea Mircea, Nea Mihăiță, acum o să înțelegeți de ce nu am avut mai mult timp să "stăm la palavre". Mulțumesc pentru sprijin.

Vintilă, din când în când mi-a venit foarte bine o şedere / ieşire cu tine. Gracias Maria-Jo!

Auraş, nu m-ai fi putut ajuta mai mult!

Mătuşă Stela, unchiu´ Dan, mulțumesc că m-ați lăsat să ştiu că „ sunteți acolo ".

Alina, sărut-mâna pentru tot!

Mama, Lucica, Veronica, Giony that's my PhD thesis.

Raquel, tu turno!

INDEX

EXPERIMENTAL DETAILS

SURFACE EFFECTS in NiO

INTERFACE EFFECTS IN NiO/OXIDES

Chapter I

INTRODUCTION

The first-row transition-metal oxides are among the most interesting series of materials, exhibiting wide variations in physical properties related to electronic structure. The optical and magnetic behavior, in particular, forms the basis of an enormous range of applications. As a result, they have been the subject of extensive experimental and theoretical investigations in the past several years.

In the field of solid state physics, many experimental and theoretical attempts have been made to investigate the interesting physical properties of the 3*d* transition-metal oxides, which are characterized by the partially occupied 3*d*–orbitals. This range of properties also imposes many difficult problems of scientific understanding. Especially, the insulating behavior of these materials has been extensively studied for several decades.

Such as NiO, one of the most favored antiferromagnets, is a prototypic system for strong electronic correlations with high spin AF2 structure at low temperatures and has a simple crystallographic rock salt structure with a lattice constant of 4.194 Å[1] (see figure 1).

Mott and Hubbard have reported that the strong *d–d* Coulomb interaction is essential to explain why some of transition metal compounds play a major role as insulators with

partially filled 3*d* bands, while the others exist as metals[2]. The transport of electrical charge in the solid state is provided by electrons that are subjected to the Coulomb interaction with the ions and the other electrons. The importance of a large Coulomb interaction U_{dd} is implicit in the common Anderson super-exchange theory[3], and is fundamental to the concept of the Mott-Hubbard insulator. When the *d–d* Coulomb interaction is larger than the band width, 3*d*–orbitals are localized and the magnitude of the band gap is determined by the *d–d* Coulomb interaction.

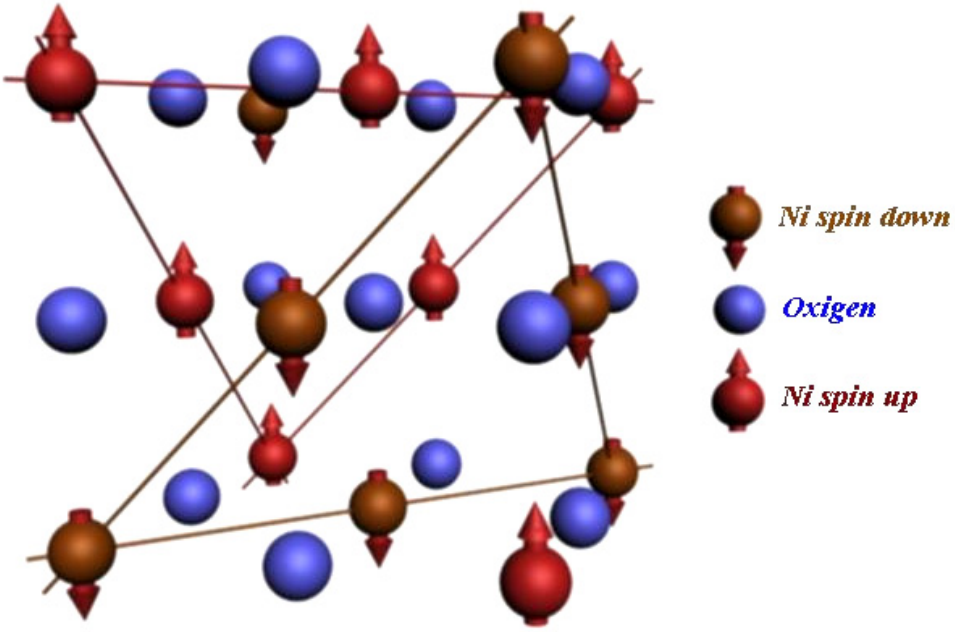

Fig.I.1. NiO Structure showing the antiferromagnetic spin structure.

Later, experimentally the powerful characterizations such as the combination of X-ray photoemission spectroscopy (XPS) and Bremsstrahlung Isochromat Spectroscopy (BIS) measurements of cleaved single crystals of NiO have provided unambiguous evidence[4] that the intrinsic charge transfer gap is 4.3 eV. In addition, the band gap of ~ 4 eV (*p*→*d* character) has been indicated by a range of spectroscopic techniques including optical absorption[5], X-ray absorption spectroscopy (XAS) at the oxygen K-edge[6], and electron energy loss spectroscopy (EELS)[7]. Computationally it has been shown that the band gap of NiO is not determined by *d–d* Coulomb interaction, but by ligand-to-*d* charge transfer energy (Δ) by analyzing the photoemission spectrum with the configuration interaction cluster model approach[8,9]. By using this calculation, one predicts the gap of 5 eV whereas the density functional theory predicts a gap of 0.3 eV[10]. Based on the local-cluster and single-

impurity approach, a classification scheme has been proposed[11], where the TMOs can be classified into two regimes according to the relative magnitude of Δ and U_{dd}. For the Mott-Hubbard regime, $\Delta > U_{dd}$, the band gap is determined by *d–d* transition and its magnitude is given by U_{dd}. For the charge transfer regime, $\Delta < U_{dd}$, the magnitude of a $p \rightarrow d$ band gap is Δ.

Alternatively, several theoretical studies have been carried out, to understand the electronic structure and band gap of NiO. The band structure calculations of TMOs were treated by the local-spin-density approximation (LSDA) as described in reference 10. This model has been successfully applied to describe many details of electronic structure, magnetic coupling, and character of the band gap since a long time. However, the local density approximation (LDA), which is widely used in solid-state physics, fails to describe the band structure of NiO as an insulator and predicts it to be as a metal[12].

Magnetic and optical properties of TMOs are governed by the ground state and low-energy excitation spectrum of the *d* shell of the central TM ion. These spectra are successfully fit to the crystal field theory[13]. Thus, it is the strong Coulomb interaction between the 3*d* electrons that leads to an energy splitting of the d^n and d^{n+1} states. All *d–d* transitions violate the parity selection rule $\Delta l = \pm 1$ (the Laporte forbidden character in centrosymmetric cases). For the earlier work, Newman and Chrenko measured the *d–d* transitions in bulk NiO by using absorption spectroscopy[14].

The calculated *d–d* excitation energies of the bulk and (001) surface of NiO were investigated at first-principles unrestricted Hartree-Fock level of theory by Mackrodt and Noguera[15]. These results allow for comparisons with optical absorption and EELS and with the theoretical works based on first-principles multi-reference[16,17,18] calculations of embedded clusters of the type $(NiO_6)^{10-}$ and $(NiO_5)^{8-}$. From the results of these calculations, which have included electron correlation in different ways, it has been concluded (15,16,17) that the inclusion of electron correlation effects is an essential prerequisite for an accurate description of *d–d* excitations in NiO. These results suggest that for NiO with its highly localized *d*–electrons resulting from strong on-site Coulomb and exchange interaction.

Later on, using cluster calculations, M. A. Veenendaal and G. A. Sawatzky[19], managed to describe, partially, the double peak structure in Ni2p XPS spectra.

Nowadays, it is accepted that NiO is a $3d^8$ charge transfer oxide and the ground state is a mixture of $3d^8$, $3d^9\underline{L}$, and $3d^{10}\underline{L}^2$ configurations[20,21,22]. This gives rise to a complex line shape of the experimental spectra when using spectroscopic techniques, in particular x-ray

photoemission spectroscopy (XPS). The Ni 2*p* photoemission peak line shapes of Ni *2p*3/2 shows a multi-peaked structure which also has been widely discussed in the literature. It has been shown that cluster calculations of the Ni 2*p* photoemission spectrum for a NiO_6 cluster give rise to three different peaks, according to the above description of the electronic structure.

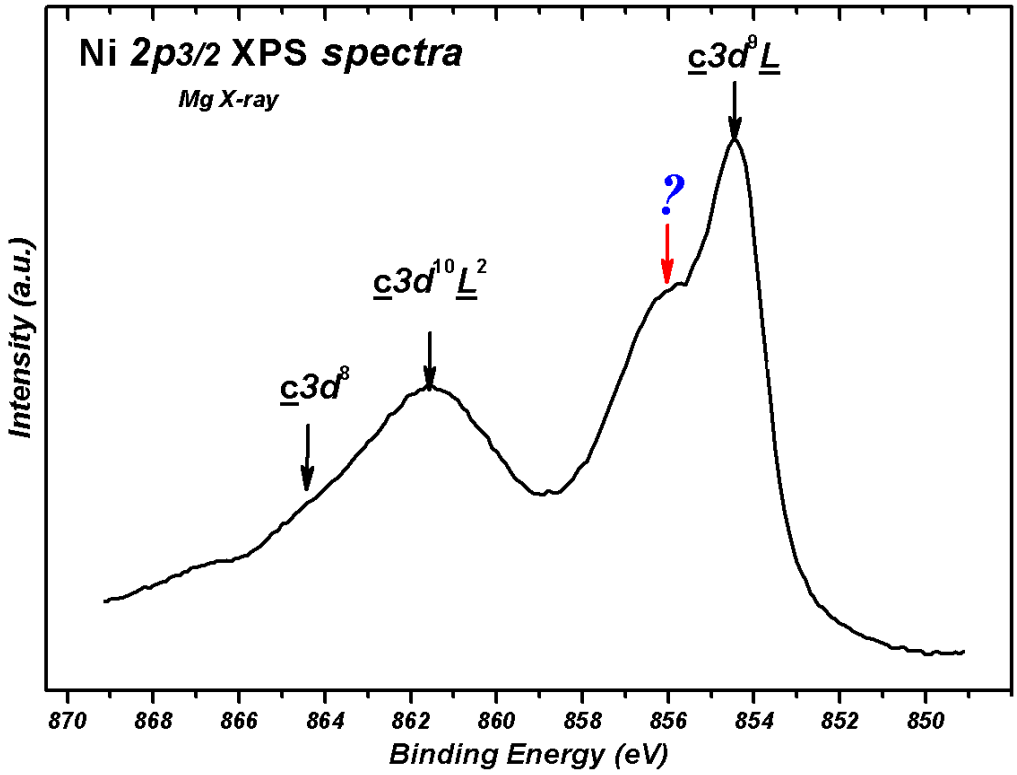

Fig. I.2. Ni 2p3/2 XPS spectra.

However, the very-well-known additional shoulder separated by 1.5 eV at higher binding energies from the main line is absent in those calculations[23]. This satellite appears only when the calculations are extended to a larger Ni_7O_{36} cluster. As a consequence of that, the satellite was called a *non-local screening satellite* and was explained as a screening process due to oxygen atoms belonging to the outer NiO_6 clusters[4].

The so called non-local satellite in the Ni 2*p* XPS spectra has been conventionally assigned to the presence of Ni^{3+} species at the NiO surface[24]. In general, it has been observed that the intensity of this satellite increases with the creation of defects. For instance, Uhlenbrock *et al*[25] concluded that Ar bombardment of a freshly cleaved NiO (100) surface produces the formation of Ni^{3+} species and the simultaneous reduction to Ni^0 when

analyzing the intensity of the satellite with respect to the main line. However, it is well known that Ar bombardment produces oxygen vacancies due to preferential sputtering of oxygen, leading to the reduction of Ni atoms to metallic Ni[26].

Other interesting systems to study the effect of defects in NiO are highly defective 3–5 nm NiO nanoparticles, whose Ni 2*p* XPS spectra show a clear enhancement of the relative intensity of the satellite with respect to the spectrum of a NiO single crystal[27]. This effect was related to the good catalytic properties of the nanoparticles and explained as due to the presence of Ni^{3+} defects. However, in a posterior x-ray absorption spectroscopy (XAS) study of these nanoparticles[28], Ni atoms were unambiguously characterized as high-spin Ni^{2+} species. This conclusion together with the results obtained in previous studies of hole-doped $Li_xNi_{1-x}O$ make[29, 30] doubtful the existence of Ni^{3+} defects at the NiO surface. Other authors found a dependence of the intensity of the satellite on the emission angle of a NiO single crystal[31, 32]. They concluded that the satellite could be associated with the surface Ni atoms but no appropriate theoretical model was proposed to explain the experiment till now.

Other interpretations appearing in the literature assign the satellite[33] to $\underline{c}3d^{10}\underline{L}^2$ states or $\underline{c}3d^9$ multiplets[34]. Therefore, the origin of the satellite at 1.5 eV higher binding energies with respect to the main line in the Ni 2*p* XPS spectra in NiO remains unclear. As mentioned above, the interpretation of the satellite as a non-local process is the most accepted theory at present. This model is supported by experimental results in the systems: $Ni_xMg_{1-x}O$ and[35] one epitaxial NiO monolayer grown on MgO single crystal[36,37]. In these systems, the non-local satellite is absent as corresponds to systems where, in spite of Ni atoms are octahedral surrounded by oxygen atoms, no second neighbouring oxygen atoms exist. The non-local screening model suggests that the satellite structure is intrinsic for bulk NiO. However, when the calculations are restricted to a Ni_6O_{30} cluster, unexpectedly the intensity of the satellite increases. The authors conclude that this could be due to a different coordination of the cluster with the core hole—i.e., fivefold to sixfold[5]. In turn, the model does not explain the absence of the satellite in the Ni 2*p* XPS spectrum of La_2NiO_4 as corresponds to a purely octahedral Ni compound[15].

Our recent results for nanoscopic NiO systems, where the large surface-to-volume ratio permits the detection of surface effects, concern NiO nanoparticles and planar NiO nanoislands grown on highly oriented pyrolitic graphite (HOPG)[38], and in this work we present additional experimental evidence and a theoretical model that show that the origin of

the satellite is not only due to *non-local* effects, but also to surface effects, being its main contribution, so that surface effects are separated from the non-local screening model. These experimental results are theoretically interpreted by cluster model calculations in terms of the reduced symmetry at the surface. The reason for using single NiO_5 and NiO_6 clusters in the calculation is to highlight the surface contribution of the 1.5-eV satellite, even including the non-local screening effect from adjacent clusters.

In order to demonstrate the surface effects in the Ni *2p*3/2 XPS spectra, and also to study the interface effects which occurs in the NiO/oxides, several experimental techniques, as X-ray Photoemission Spectroscopy (XPS), PhotoEmission Spectroscopy (PES), HArd X-ray Photoemission Spectroscopy (HAXPES), X-ray Absorption Spectroscopy (XAS), Atomic Force Microscopy (AFM), Near Edge X-ray Absorption Fine Structure Spectroscopy (NEXAFS), described in the second chapter, were involved.

The third chapter fully describe the sample preparation process and the experimental set up for each particular case of measurements.

Chapter four is dedicated to the study of the NiO growth on HOPG, and the fifth chapter describes the NiO/Oxides interface study.

An application of these results, as preparation of a high surface to volume ratio NiO system, is presented in the sixth chapter.

In the conclusion section the principal characteristics of these studied systems are pointed.

REFERENCE

[1] A. V. Dul'nev, V. N. Efremov, M. A. Obysov, E. Z. Golosman, and V. I. Yakerson, *Russian Journal of Applied Chemistry*, pp. 1491-1499, 77, nº. 9, 2004.

[2] J. Hubbard. *Proc. Roy. Soc. London, Ser. A*, 276:238, 1963.

[3] P. W. Anderson. *Phys. Rev.*, 115:2, 1959.

[4] G. A. Sawatzky and J. W. Allen. *Phys. Rev. Lett.*, 53:2339, 1984.

[5] R. J. Powell and W. E. Spicer. *Phys. Rev. B*, 2:2182, 1970.

[6] P. Kuiper, G. Kruizinga, J. Ghijsen, G. A. Sawatzky, and H. Verweij. *Phys Rev. Lett.*, 62:221, 1989.

[7] S. Hüfner, P. Steiner, F. Reinert, H. Schmitt, and P. Sandl. *Z. Physik. B*, 88:247, 1992.

[8] A. Fujimori and F. Minami. *Phys. Rev. B*, 29:5225, 1984.

[9] A. Fujimori and F. Minami. *Phys. Rev. B*, 30:957, 1984.

[10] K. Terakura, A. R.Williams, T. Oguchi, and J. Kübler. *Phys. Rev. Lett.*, 52:1830, 1984.

[11] I . Pollini, J. Thomas, G. Jezequel, J. C. Lemonnier, and A. Lenselink. *Phys. Rev. B*, 29:4716, 1984.

[12] Z. X. Shen, R. S. List, D. S. Dessau, B. O. Wells, O. Jepsen, A. J. Arko, R. Barttlet, C. K. Shih, F. Parmigiani, J. C. Huang, and P. A. P. Lindberg. *Phys. Rev. B*, 44:3604, 1991.

[13] A. V. Soudackov, A. L. Tchougreeff, and I. A. Misurkin. *Int. J. Quant. Chem.*, 58:161, 1996.

[14] R. Newman and R. M. Chrenko. *Phys. Rev.*, 114:1507, 1959.

[15] W. C. Mackrodt and C. Noguera. *Surf. Sci.*, 457:L386, 2000.

[16] A. Freitag, V. Staemmler, D. Cappus, C. A. Ventrice Jr., K. Al-Shamery, H. Kuhlenbeck, and H.-J. Freund. *Chem. Phys. Lett.*, 210:10, 1993.

[17] C. de Graaf, R. Broer, and W. C. Nieuwpoort. *Chem. Phys.*, 208:35, 1996.

[18] M. Geleijns, C. de Graaf, R. Broer, and W. C. Nieuwpoort. *Surf. Sci.*, 421:106, 1999.

[19] M. A. van Veenendaal, G. A. Sawatzky, *Phys. Rev. Letter*., 70, 2459, 1993.

[20] A. Fujimori, F. Minami, and S. Sugano, Phys. Rev. B, 29 (1984)5225.

[21] G. A. Sawatzky and J. W. Allen, Phys. Rev. Lett., 53 (1984) 2339

[22] S. Hüfner, Solid State Commun., 52 (1984)793.

[23] M. A. van Veenendaal and G. A. Sawatzky, Phys. Rev. Lett. **70**, 2459, 1993.

[24] M. J. Tomellini, J. Electron Spectrosc. Relat. Phenom. **58**, 75,1992

[25] St. Uhlenbrock, Chr. Scharfschwerdt, M. Neumann, G. Illing, and H.-J. Freund, J. Phys.: Condens. Matter **4**, 7973, 1992.

[26] J. M. McKay and V. E. Henrich, Phys. Rev. B **32**, 6764, 1985.

[27] A. R. González-Elipe, J. P. Holgado, R. Alvarez, and G. Munuera, J. Phys. Chem. **96**, 3080, 1992.

[28] L. Soriano, M. Abbate, J. Vogel, J. C. Fuggle, A. Fernández, A. R. González-Elipe, M. Sacchi, and J. M. Sanz, Chem. Phys. Lett. **208**, 460, 1993.

[29] P. Kuiper, G. Kruizinga, J. Ghijsen, G. A. Sawatzky, and H. Verweij, Phys. Rev. Lett. **62**, 221, 1989.

[30] M. Abbate, F. M. F. de Groot, J. C. Fuggle, A. Fujimori, Y.Tokura, Y. Fujishima, O. Strebel, M. Domke, G. Kaindl, J. Van Elp, B. T. Thole, G. A. Sawatzky, M. Sacchi, and N. Tsuda, Phys. Rev. B **44**, 5419, 1991.

[31] F. Parmigiani, in *Cluster Models for Surface and Bulk Phenomena*, edited by G. Pacchioni *et al.* _Plenum Press, New York, 1992, Vol. 1, p. 475.

[32] L. Sangaletti, L. E. Depero, and F. Parmigiani, Solid State Commun. **103**, 421, 1997.

[33] M. Oku, H. Tokuda, and K. Hirokawa, J. Electron Spectrosc. Relat. Phenom. **53**, 201, 1991.

[34] K. S. Kim and R. E. Davis, J. Electron Spectrosc. Relat. Phenom. **1**, 251, 1972.

[35] M. Atanasov and D. Reinen, J. Electron Spectrosc. Relat. Phenom. **86**, 185, 1997.

[36] F. Parmigiani, in *Cluster Models for Surface and Bulk Phenomena*, edited by G. Pacchioni *et al.* Plenum Press, New York, (1992), Vol. 1, p. 475.

[37] D. Alders, F. C. Voogt, T. Hibma, and G. A. Sawatzky, Phys. Rev. B **54**, 7716, 1996.

[38] L. Soriano, A. Gutiérrez, I. Preda, S. Palacín, J. M. Sanz, M. Abbate, J. F. Trigo, A. Vollmer, and P. R. Bressler, Phys. Rev. B **74**, 193402, 2006.

Chapter II

EXPERIMENTAL TECHNIQUES

II.1. X-RAY PHOTOEMISSION SPECTROSCOPY (XPS)

XPS was developed during the 1960's by K. Siegbahn and his research group in Sweden. This work was recognized with a Nobel Prize for Physics in 1981. The photoemission is based on the Einstein's theory of the photoelectric effect of 1905 where quantized photons of an incident electromagnetic radiation field (light) cause the ejection of electrons from a sample surface[1]. The effect was first described by Hertz in 1887.

II.1.1 X-Ray Photoemission Spectroscopy (XPS) Fundamentals

X-Ray Photoemission Spectroscopy (XPS), also known as Electron Spectroscopy for Chemical Analysis (ESCA), is a very surface-sensitive chemical analysis technique used to characterize the surface of solids to a depth of 2-20 atomic layers, (10-100Å depth) depending on the material studied[2]. The technique also has several unique properties including its non-destructive nature, the ability to study plastic and organic surfaces, and the ability to operate at moderate vacuum levels. XPS has been successfully used to study a wide range of materials including polymer surfaces and metal/metal oxide films. While detection limits can approach one atom in 100,000, XPS usually has a detection limit.

II.1.2 Analytical physics of XPS

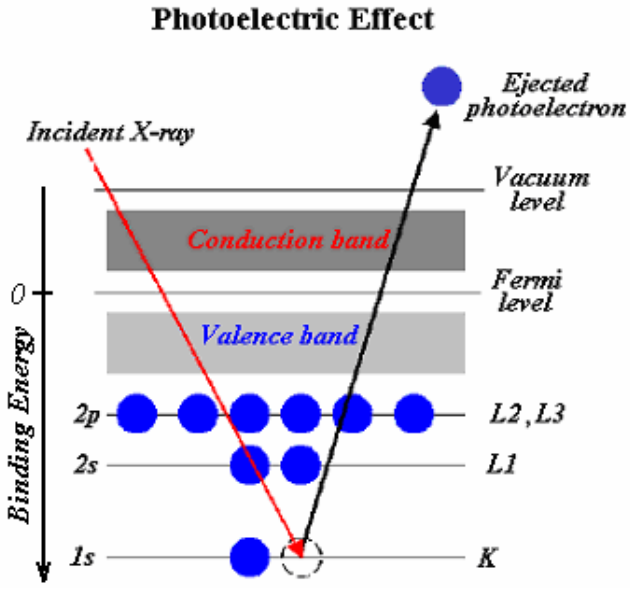

Fig.II.1. Schematic representation of the photoelectric effect.

In XPS, the energy of a photon, as shown in figure II.1, is transferred to the electron in the sample. Electrons released are analyzed for their kinetic energy, which can be used to determine the binding energy level of the electron. The energy of a photon (E) is given by Einstein's equation:

$$E=h\nu$$

Where *h* is the Planck constant (6.626×10^{-34}Js) and ν the frequency (Hz) of the radiation. This energy is known because XPS uses a specific x-ray line for excitation. The energy of the photon must exceed the binding energy of the electron in order to make the electron available for detection. When the photon energy is greater than the binding energy of the electron, the photoelectron is emitted from the sample[3]. This photoionization process / photoelectric effect is summarized in equations below: An atom (A) is hit by a photon ($h\nu$), producing an ionized surface and a free electron.

$$A + h\nu \rightarrow A^{+} + e^{-}$$

The energy of the atom in the sample material plus that of the photon must equal that of the resulting parts:

$$E(A) + h\nu = E(A^{+}) + E(e^{-})$$

Rearranging the equation and renaming $E(e^{-})$ as the kinetic energy (KE) of the photoelectron result:

$$KE = h\nu - (E(A^{+}) - E(A))$$

This equation can be simplified, since we know that the binding energy (BE) of the electron is the difference in energy between the ionized and neutral atoms:

$$KE = h\nu - BE$$

BE is the amount of energy needed to move the electron from the core levels to the vacuum level. The KE of the electron is equal to the energy of the photon minus the energy required to free the electron.

$$BE = h\nu - KE$$

By rearranging the equation, the binding energy of an electron level is found by subtracting the kinetic energy of the collected electrons, as measured, from the known energy of the source x-ray beam. Binding energies for each electron orbital level in an element are unique and useful in identifying the present elements[4].

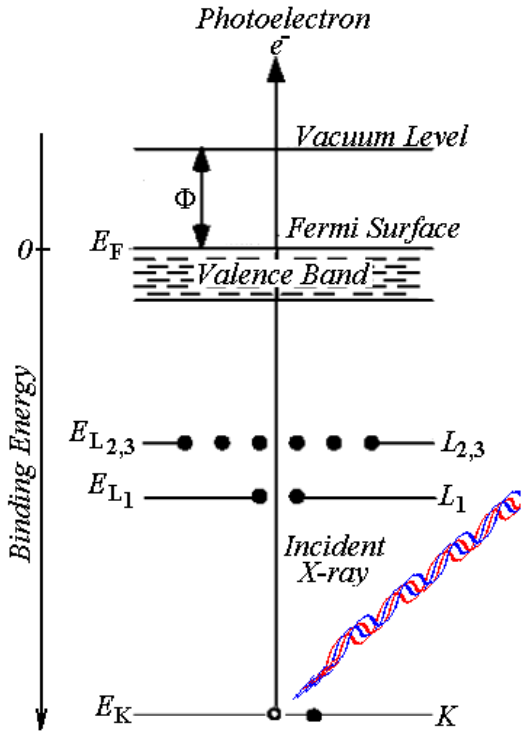

Fig.II.2. Energy diagram with photoelectron being ejected.

The high degree of surface sensitivity that is characteristic of XPS is due to the very short mean free path of electrons in solids. This is the mean distance traveled by an electron before undergoing a significant deflection or collision. This distance is dependent of the energy of the electron and also dependent of the material itself. The photoelectrons which will inelastically collide with the lattice structure of the material will loose insignificant part of their energy, and will give the inelastic peak in the XPS spectra. If the lost energy of the photoelectrons is too high than these photoelectrons will not escape into the vacuum, and will take part in the relaxation processes. Those photoelectrons which will escape into the vacuum with very low kinetic energy will be detected however, if its energy after the collisions still exceeds the binding energy, and like others electrons will account for the background signal in the XPS spectra[3].

However, the binding energies (BE) in solids are usually measured with respect to the Fermi-level of the solid, instead of the vacuum level as was shown above. To correct this discrepancy with the "BE = $h\nu$- KE" equation, a constant is added, accounting for the difference between the Fermi level and vacuum level. This material-dependent constant is

known as the work function (Φ) of the solid. The work function varies with the composition and chemical environment of the material under investigation.

Thus, BE = $h\nu$ - KE - Φ[1].

Figure II.2 shows an energy level diagram with a photoelectron being ejected as in XPS.

The probability of emitting an electron is dependent also on the sensitivity factor which has been determined to consider the effects for each element and each orbital of the elements. These allow for the calculation of accurate surface concentration ratios and quantitative analysis by evaluating the peak intensities[5].

The material sensitivity of XPS is determined by the mean free path in solids, which is in turn determined by the characteristic kinetic energy of the emitted electrons as shown in figure II.3 below. The information depth for a given energy source can be determined from this graph. Knowing that the usual x-ray sources emit photons with 1253.6 eV (Mg K_α) and 1486.6 eV (Al K_α), we can see the information depth between 5-10 monolayers. The mean free path is defined as the average distance traveled by an electron of a given kinetic energy before it loses kinetic energy through inelastic scattering in the material. For this reason only few electrons from further below the surface escape to be detected.

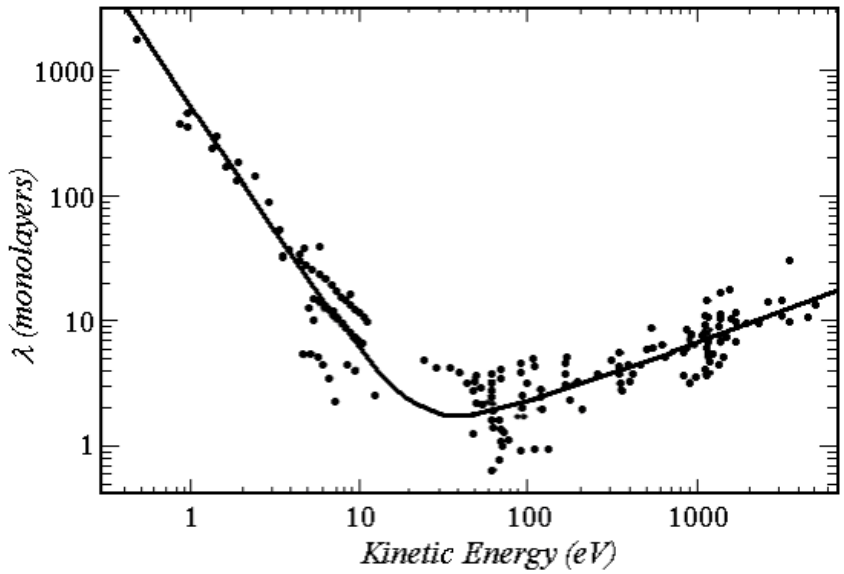

Fig.II.3. Universal Inelastic Mean Free Path curve of the photoelectrons in solids.

So, choosing the photon energy in such way that the kinetic energy of the photoelectons to correspond to the low lambda values, it can be increase the surface sensitivity of the XPS measurements.

There is another way to increase even more the surface sensibility of XPS measurements: increasing the take off angle of the ejected electrons. In well choused geometry of the measurements, as pictured in figure II.4 below, the effective probing depth is near to the material surface.

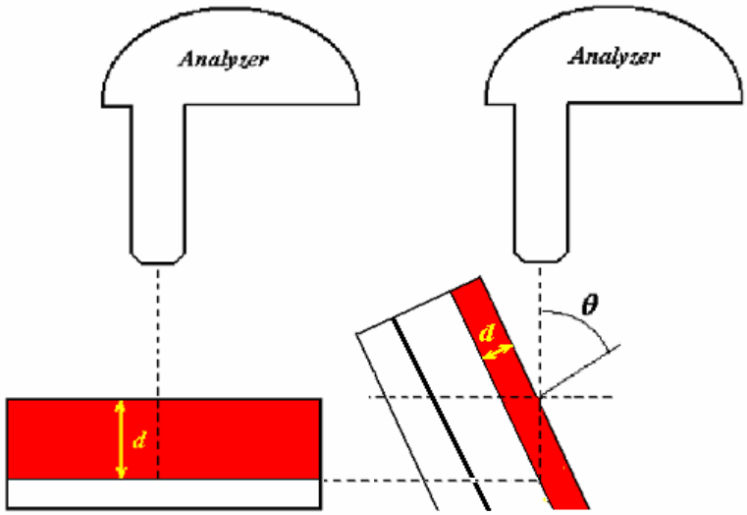

Fig.II.4. Take off angle geometries measurements.

Key Features of XPS:

- XPS probes occupied states;
- XPS technique is highly surface specific due to the short range of the photoelectrons that are excited from the solid;
- The binding energy of the peaks is characteristic of each element. The peak areas can be used (with appropriate sensitivity factors) to determine the composition of the materials surface;
- XPS provide chemical bonding information and oxidation state as well;
- valence band XPS spectra allows the study of the bounding;
- XPS can detect all elements except hydrogen and helium;
- Generally non-destructive analysis

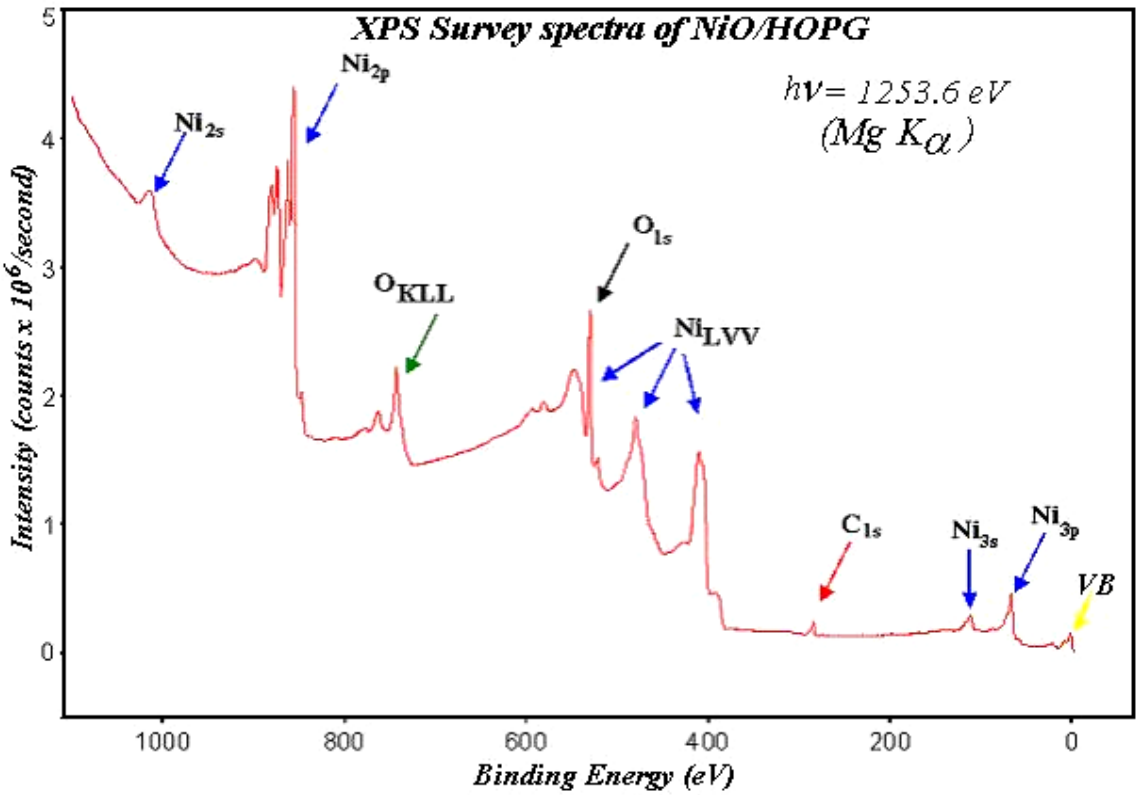

Fig.II.5. Example of XPS survey spectra of NiO on HOPG.

As shown in figure II.5, an XPS spectrum consists of a series of peaks corresponding to the binding energies of the photoelectrons that produce these peaks. The binding energies of photoelectrons in a sample are shown above with higher probability for each electron being represented by a larger peak. The Fermi energy level is shown at the zero binding energy position.

The spectra increase in intensity towards higher binding energies which means low kinetic energies. These intensities are given by the electrons that had energy only to escape the material.

The XPS Survey Spectra (using the magnesium anode x-ray source) provide a snapshot of the elements present in the sample. With core (inner shell) electrons spectra quantitative and chemical analysis can be done. Outer electrons spectra are helpful in chemical bonding analysis.

II.1.3 Energy Calibration

The energy of emitted photoelectrons is not directly obtained. It is necessary to take into account not only the energy balance of electron escape process, but also, the electron analyzer capture of this one. The figure II.6 depicted a sample-analyzer diagram in electric contact (that means equal Fermi level). Looking at the analyzer it can be seen how this measures the kinetic energy of the photoelectrons with respect to its work function Φ_A. For this reason it is necessary to know the value of Φ_A-hν. Following this idea in the calibration process the *4f* level of gold, which is not sensible to the chemical bound, are used.

The measurements of intensities and positions of the peaks in a XPS spectra are sensitive to several factors like chemical composition and atomic concentration of the elements in the sample, charge effects of the surface, inter-atomic and extra-atomic relaxation processes. The simplest model used to explain the binding energy shift in XPS spectra is the *point charge model* which considers the atoms as charged particles with a Δq charge transfer due to the neighboring bounding atoms. In this model the energy shift is given by:

$$\Delta E_b = \frac{k}{r_v}\Delta q - \frac{K \cdot \Phi}{R \cdot \Delta q} - \Delta E_{rel} = \Delta \in -\Delta E_{rel}$$

which contain two contributions: $\Delta \in$ describing the chemical shift due to the initial state of the system, that means charge transfer associated with the chemical bounding and crystal field effects of the network structure, and the second term, ΔE_{rel} which contain all the final state effects, that means the way of relaxation for recovering the fundamental state. There are *intra-atomic* relaxation processes, when the same excited atom is itself responsible with recovering its ground state, and *extra-atomic* relaxation processes when through desexcitation via hybridization the ground state is reached.

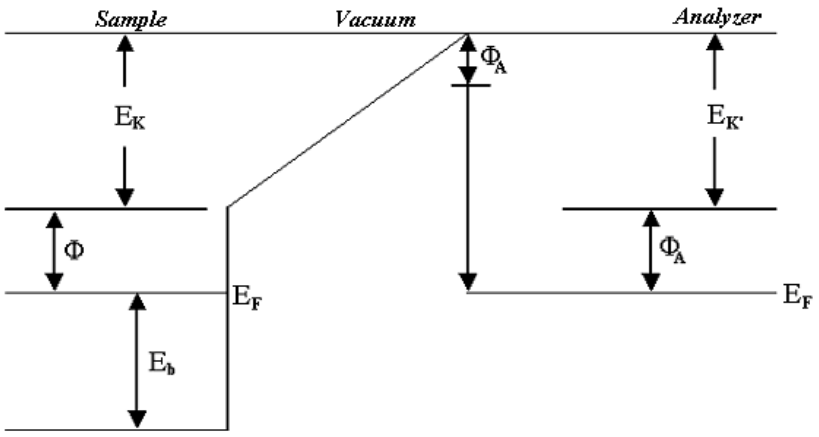

Fig.II.6. Energy diagram in sample-electron analyzer system.

II.1.4 Quantitative Analysis

The intensity of an XPS peak, which means the number of photoelectrons coming from a *j* level of a *Z* atom, counted by the analyzer in a time unity, is given by:

$$I(Z_j) = s \cdot \phi \cdot T(E_j) \cdot R \cdot \sigma \cdot \int_0^\infty N(Z_j, z) P(z, E_j, \theta) dz$$

where

$$P(z, E_j, \theta) = e^{-\frac{z}{\lambda}(E_j)\cos\theta}$$

This expression contain all the effects not only those of the sample nature but also the experimental setup ones.

ϕ, is the incident x-ray flux;*R* is the sample roughness coefficient; *S,* is the sample surface area; $T(E_j)$ is the transmission function of the analyzer; σ, is the cross section photo-ionization process of *j* atomic level; $N(Z_j,z)$ is the z-concentration distribution of the *Z* atoms, corrected with $P(z,E_j,\theta)$ factor and $\lambda(E_j)$ is the inelastic mean free path of the emitted electrons.

II.1.5. System Component Overview

The XPS spectrometer system consists of the following components: an x-ray source, electron energy analyzer, ultra-high vacuum system, and a computer.

X-Ray Source

The x-ray source works by accelerating electrons from a heated filament towards a usually aluminum or magnesium anode. When striking the surface material of the anode, the electrons excite inner shell electrons of the anode atoms. Relaxation of these excited electrons results in the emission of x-ray photons at energies characteristic of the anode material. The characteristic x-ray emission lines result in the emission of photons with a constant, known energy, enabling the photoemission spectroscopy measurement. XPS uses "soft x-rays" of 200-2000 eV radiation to examine core-levels[3]. These x-ray photons are emitted from source and. In a monochromatic system, the characteristic line is selected by the monochromator.

Hemispherical Analyzer (HA)

The electrons are analyzed by the Hemispherical Analyzer (HA) measuring the energy distribution of the electrons. The HA works as shown in figure II.7 below: it consists in two metallic hemispheres, separated by a small distance. Different voltages are applied on each hemisphere creating an electric field between the two hemispheres. One plate has a negative charge and repels the incoming electrons; the second plate has a positive charge and attracts the incoming electrons. Electrons are injected into the gap between the hemispheres. If the electrons are traveling too fast, they will impinge on the outer hemisphere. If they are traveling too slowly, they will be attracted to the inner hemisphere. Hence only electrons in a narrow energy region (called the pass energy, Ep) succeed in getting all the way round the hemispheres to the electron detector. A series of lenses are placed before the HA to focus the electrons by the desired amount[6].

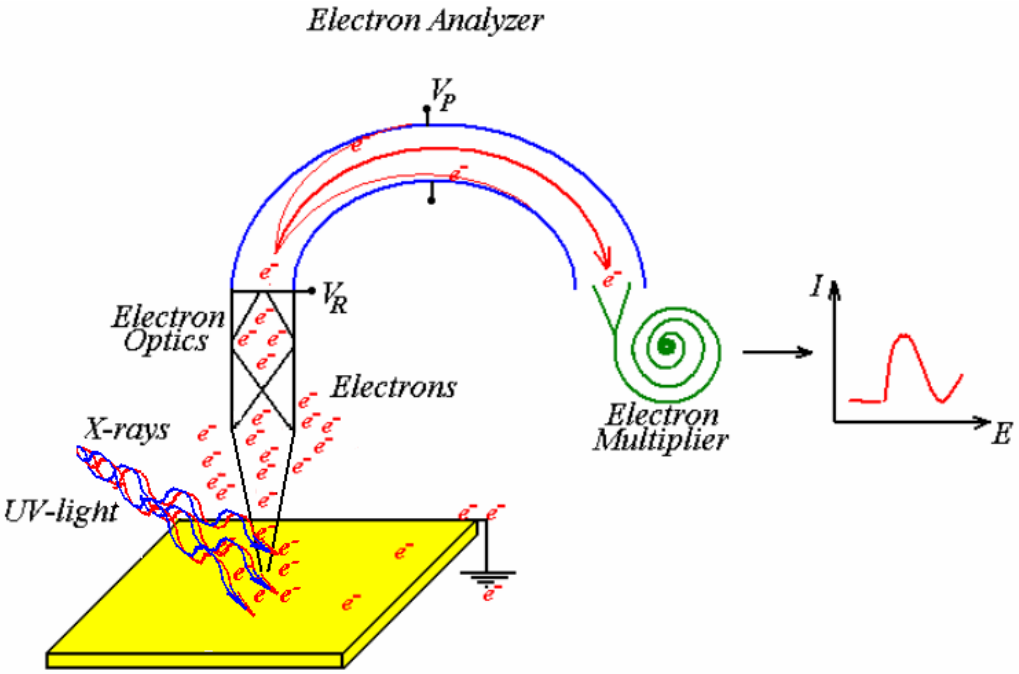

Fig.II.7. Principles of Photoemission Spectroscopy.

Ultra High Vacuum (UHV) System

Why UHV is required for XPS measurements:

- Allows to the electrons to reach the analyzer;
- Prevents the introduction of atmospheric gases onto the sample, as well as removing some that are already present;
- Prevent arcing and ionization of gases which would otherwise be in the chamber during measurements[3].

A UHV environment is considered as one in which pressure is less than $1x10^{-8}$ millibar.

In comparison, normal atmospheric pressure is about 1 bar. This shows that atmospheric gas molecules are about 1 trillion (10^{12}) times less common within the UHV system than in atmosphere. This is important for experimental purposes due to the way that gases and dust can quickly obscure the needed data in even a freshly cleaved sample. Even at relatively low pressures, such as $1x10^{-6}$ mbar, a monolayer of contaminants from residual

gases forms in about 1 second. Maintaining UHV conditions staves low this exposure to a great extent, long enough to complete a measurement.

II.1.6. Quantitative Analysis of Surfaces by Electron Spectroscopy (QUASES)

A new method for non-destructive analysis of the 3 dimensional nano-structure of surfaces by XPS and AES was developed during the past years[7,8,9,10,11,12,13,14,15]. The analysis relies on algorithms that take into account the peak intensity, the peak shape and the background of measured energy spectra. In several recent experimental studies, the method has been demonstrated to give a much more complete and reliable picture of the quantitative composition of the surface region of the solid in comparison to traditional analysis, which relies exclusively on the peak intensity.

II.1.6.1 Concept of the QUASES analysis procedures

Quantitative surface chemical composition analysis by X-ray photoelectron or Auger electron spectroscopy (XPS or AES) relies on several factors[6-8] like for example knowledge of photo-ionization cross sections, inelastic electron mean free paths, and the influence of elastic electron scattering. The most serious problem in quantitative XPS, that gives the largest contribution to errors of analysis, is however assumptions made on the in-depth distribution of atoms. This is so because the measured peak intensity may well vary by orders of magnitude depending on the in-depth profile. As a result, a meaningful interpretation of measured XPS-peak intensities can not be made unless the in-depth distribution of atoms is known. Such information is however usually not at hand in practice, because it is the purpose of the analysis to find the quantitative composition of the surface region of the solid, and if this information were available there would be no point in doing the analysis. To be able to extract quantitative information from measured peak intensity, it is necessary to make an assumption, and for convenience it is usually assumed that the surface region is homogeneous up to a depth of a few nano-meters. This assumption does however make quantification of surface chemical compositions by XPS and AES extremely unreliable as shown below.

In view of the high and rapidly growing technological importance of reliable information on the in-depth composition of the surface region of solids on the nano-meter scale, much effort has in recent years been devoted to the development of new more accurate methods. With this goal in mind, Tougaard et al[3-8] has made systematic studies of electron transport phenomena and on this basis developed a practical technique for determination of the chemical composition of solid surfaces with nano-meter depth resolution. It relies on the phenomenon that the energy loss structure that accompanies an XPS or AES peak carries information on the depth of origin of the detected electrons. The method is non-destructive and therefore allows also studying the change in surface morphology during exposure to various treatments as, e.g., gradual annealing or chemical reaction with an ambient gas. The technique has been applied to study of thin film growth mechanisms and inter-diffusion depth profiles of many systems including also several tests on the validity of the method[14].

The QUASES software package provides a practical tool that makes application of these results possible for routine analysis work.

II.1.6.2 Quantification with Peak Intensities

For a meaningful quantification of measured peak intensities, assumptions on the in-depth distribution of atoms must be made. Usually, the sample composition is taken to be homogeneous up to a depth of a few nano meters[12]. This assumption may result in enormous errors in quantification[12-14]. Thus, solids subjected to surface analysis are hardly ever homogeneous up to a depth of several nano-meters. It is precisely because samples are inhomogeneous on the nano-meter depth scale that analysis is done with XPS or AES rather than with other well-established methods for chemical analysis that are less surface sensitive.

The reason for the dramatic change in peak shape with the surface morphology is that as the electrons move on their way out of the solid, they lose energy. The longer path-length they travel, the larger is the fraction of the electrons that have lost energy. This is illustrated in figure II.9 where the energy spectrum is shown before and after the electrons have passed a thin solid with different thickness. For electrons that pass only a short distance in the solid, the chances that an electron will lose energy is small and the change in energy distribution is small. For electrons that pass a larger distance, larger energy fraction has been lost and the intensity at the peak energy is diminished. These electrons are found at lower energies in the spectrum and the distortion of the energy spectrum is substantial.

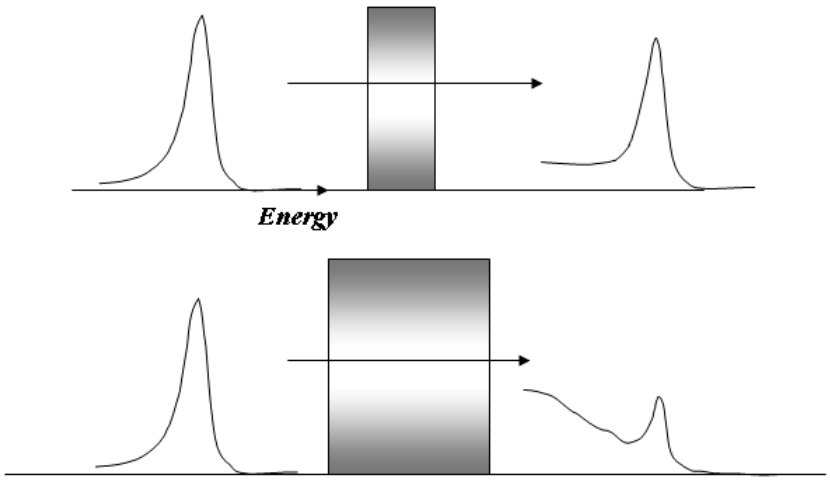

Fig.II.9. Electron energy lose in materials.

The formula mostly applied for quantitative analysis by XPS and AES relies on the assumption that the average concentration in the outermost surface region of the solid is directly proportional to the measured peak intensity. To illustrate the fundamental problem with this procedure we will consider an example of model spectra calculated for different depth distributions of copper in a gold matrix. Thus, figure II.10 shows spectra of the Cu2p peak corresponding to four different surface morphologies. The XPS-peak intensity from all four solids is exactly identical although the surface morphologies are widely different. Quantification based only on the Cu2p peak intensity cannot discriminate between these four structures. Analysis of these spectra under the assumption that the surface concentration is proportional to the peak intensity, would then result in a quantification where the concentration at the surface could be anywhere from 0 % (as in (d)) to 100 % (as in (a)). The total amount of copper material within the surface region could be anywhere from the equivalent of 1.1 Å (as in (a)) or 10 Å as in (c)) or even higher (as in (d)). Quantification based on peak intensities alone is thus subject to extremely large uncertainties and it is hard to keep the imagination of XPS and AES as quantitative techniques.

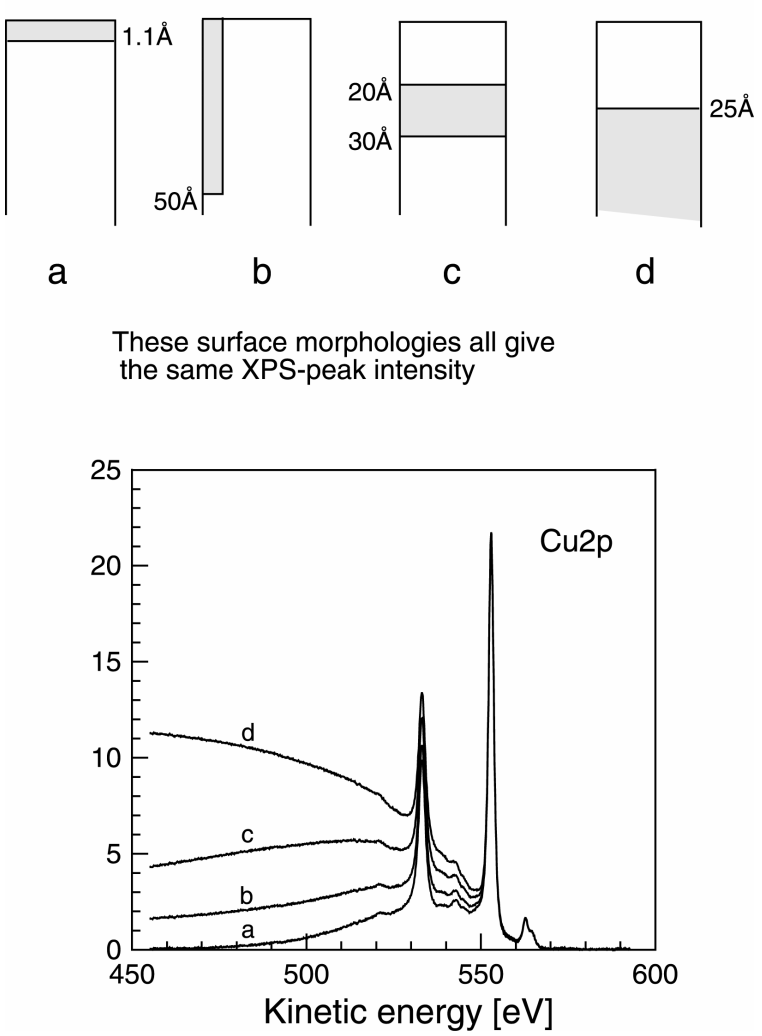

Fig.II.10. Background different shapes as the cooper "seats" on gold.

On closer inspection of the spectra in figure II.10, it is clear that the peak shape in a wider energy range below depend critically on the in-depth distribution of the element. It is thus easy, experimentally, to distinguish between the peak shapes of the four spectra in range of ~ 100 eV. Much more accurate quantification can therefore be accomplished if the dependence of peak shape on surface morphology is taken into account in the analysis. It is a quantitative description of these effects that is the basic principle of surface nano-structure quantification in QUASES.

In figure II.10 *a*, the electrons have traveled only a short distance before they escape through the surface, and consequently, very few have lost energy and the intensity on the low energy side of the peak is small. In figure II.10 *c*, all electrons have traveled ~20-30 Å within the solid before they reach the surface and a larger fraction have lost energy and end

up at lower energies in the spectrum. In figure II.10 *d*, there are additional electrons coming from larger depths, and these electrons will have lost further energy. This is why the intensity ~ 50 – 100 eV below the peak is considerably larger in *d* compared to *c*.

II.1.6.3 Quantification with QUASES

This section briefly summarizes the principles used in QUASES™ to describe the variations in energy distribution of emitted electrons caused by electron transport.

The flux density of photoelectrons excited from a single atom at energy E_0 into the solid angle Ω is denoted $F(E_0,\Omega)$ and the concentration of atoms at depth x is f(x).

Then the measured spectrum of emitted electrons is

$$J(E,\Omega) = \int dE_0\, F(E_0,\Omega) \int f(x)\, G(E_0, x/\cos\theta; E)\; dx$$

where θ is the emission angle with respect to the surface normal. The function G, is the energy distribution of an electron as a function of path length x/cosθ traveled in the solid.

The total energy loss of an electron moving in a solid is determined by the inelastic scattering cross section and the path length traveled. Multiple scattering events are important because in typical cases, the energy spectrum includes electrons that have traveled a distance of several inelastic mean free paths. By K(E,T) is denoted the differential inelastic electron scattering cross section, i.e. K(E,T)dRdT is the probability for one electron of energy E to lose energy in the interval T, T+dT after having traveled a path length dR in the solid. For energy spectra where the total energy loss is small compared with the primary electron energy, K(E,T) ≅ K(T) independent of E. Then the effect of multiple scattering has a rigorous solution, and the spectrum of emitted electrons is

$$J(E,\Omega) = \int dE_0\; F(E_0,\Omega) \int ds\;\; e^{-i\,2\pi s\,(E-E_0)} \int dx\, f(x)\, e^{-x\,\Sigma(s)\,/\cos\theta}$$

with

$$\Sigma(s) = \frac{1}{\lambda_i} - \int_0^{\infty} K(T)\; e^{-isT}\, dT$$

where λ is the inelastic electron mean free path.

Quantification by Background Removal

Formulae to determine the atomic excitation function F(E, Ω) from a measured spectrum were developed for different types of in-depth profiles. It was shown that the integral equation may be solved rigorously for the primary excitation spectrum F(E, Ω)

$$F(E,\Omega) = \frac{1}{P_1}\left[J(E,\Omega) - \int dE' J(E,\Omega) \int ds \exp\left[i2\pi s(E' - E) \right] \left(1 - \frac{P_1}{P(s)}\right) \right] (*)$$

where

$$P(s) = \int dx f(x) \exp\left(-\frac{x}{\cos\theta} \Sigma(s) \right)$$

and

$$P_1 = \int dx\, f(x) \exp\left(-\frac{x}{\lambda_i \cos\theta} \right)$$

Equation (*) may be used to determine either F(E, Ω) if $f(x)$ is known (e.g., for an elemental sample) or it may be used to determine $f(x)$ if F(E, Ω) is known. The exact peak shape in the energy region close to the peak energy up to ~ 10-20 eV below the peak energy is not known since it is largely determined by the chemical bond, lifetime broadening, and intrinsic excitations in the photoemission process which all may depend on the local chemical environment. However, the spectrum F(E, Ω) after background correction must be of zero intensity in an energy region beyond ~ 30eV below the primary peak energy and the spectral intensity must stay at zero intensity for all energies below the peak energy until the energy of another peak in the energy spectrum is reached. This puts a strong constraint on the function F(E,Ω) and this is applied as a criterion to determine $f(x)$ in the sense that $f(x)$ is varied until the constraint is fulfilled.

As another criterion one can use knowledge about F(E,Ω) determined from the analysis of spectra from samples with a well characterized in-depth concentration profile as, e.g., a single element solid. One should be aware of the possible peak shape changes caused by the difference in chemical environment of the atoms in the reference and the sample being investigated. To the extent that these differences can be neglected, the spectrum may be applied as a reference and $f(x)$ is varied until analysis yields a spectrum with the same absolute intensity and peak shape as the reference spectrum. If the peak shape analysis includes peaks from all the elements in a sample then the constraint that the sum of the

concentration of the individual elements at any depth must add up to 100% may also be applied.

II.1.6.4. Inelastic electron scattering cross sections

The cross section K(T) can be described with sufficient accuracy by Universal formulas valid for different classes of materials. Depending on the class of materials, a function with two or either three parameters is needed to describe the cross sections of that class[14]. For most metals, their oxides and alloys, the *Universal cross section*[14]

$$\lambda_i(E)K(E,T)=\frac{B\,T}{\left(C+T^2\right)^2} \quad (**)$$

with C= 1643 eV^2 and B ≅ 3000 eV^2 applies with sufficient accuracy.

For solids with a narrow plasmon structure, the cross-sections can not be well described by a function with two-parameters. For these however it was shown[14] that the main characteristics of the cross section can be described by the *Three-parameter Universal cross section*

$$\lambda(E)K(E,T)=\frac{BT}{\left(C-T^2\right)^2+DT^2} \quad (***)$$

where the three parameters B, C, and D have been determined for each class of materials (e.g. polymers, semiconductors, free-electron-like solids[14])

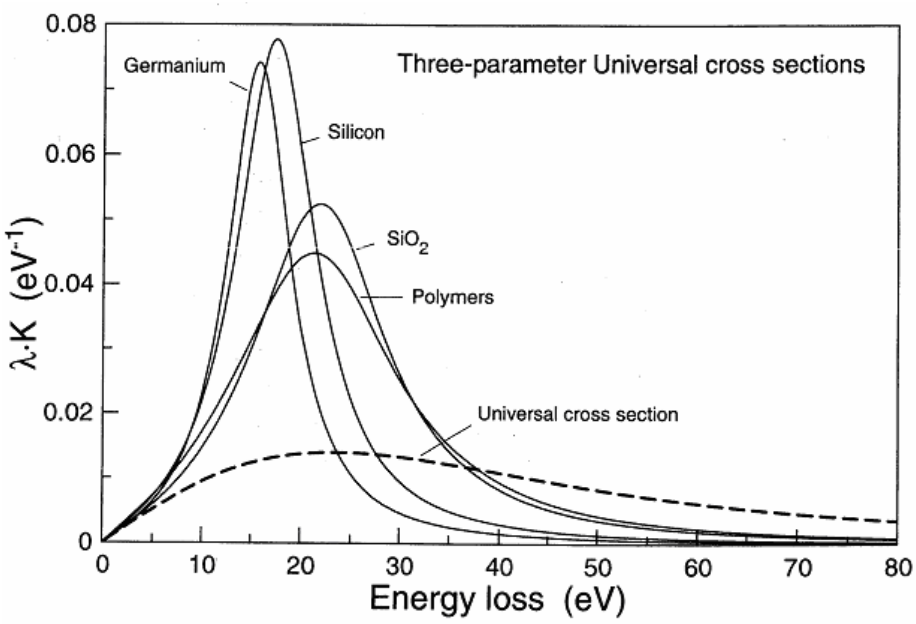

Fig.II.11. Three – parameter Universal cross sections.

Figure II.11 shows cross sections for various types of solids. The parameter values are given in tables below. These cross sections are all included in the QUASES™ software.

Table II.1. Two parameter – Universal Cross Section Parameters (Eq.(**))

Class of materials	**B [eV^2]**	**B^N [eV^2]**	**C [eV^2]**
Metals and their oxides	2866	3286	1643

Table II.2. Three Parameter – Universal Cross Section (Eq.(***))

Class of materials	**B [eV^2]**	**B^N [eV^2]**	**C [eV^2]**	**D [eV^2]**
Polymers	434	396	551	436
Silicon-dioxide	325	299	542	275
Silicon	132	131	325	96
Germanium	73	93	260	62
Aluminum	16.5	21.4	230	4.5

II.1.7. HArd X-Ray PhotoEmission Spectroscopy (HAXPES)

HAXPES is a powerful emerging technique for bulk compositional, chemical and electronic properties determination. It benefits from the exceptionally large escape depth of high kinetic energy photoelectrons enabling the study of bulk and buried interfaces up to several tens of nanometers depth. Lindau et al.[16] made in 1974 the first HAXPES experiment measuring the Au 4f subshell at photon energy of 8 keV. However, no other group followed this pioneering work certainly because of the strong drop of the photoemission cross-section, as shown in figure II.12, at higher photon energies and also to the lack of commercial analyzers available to handle high electron energies.

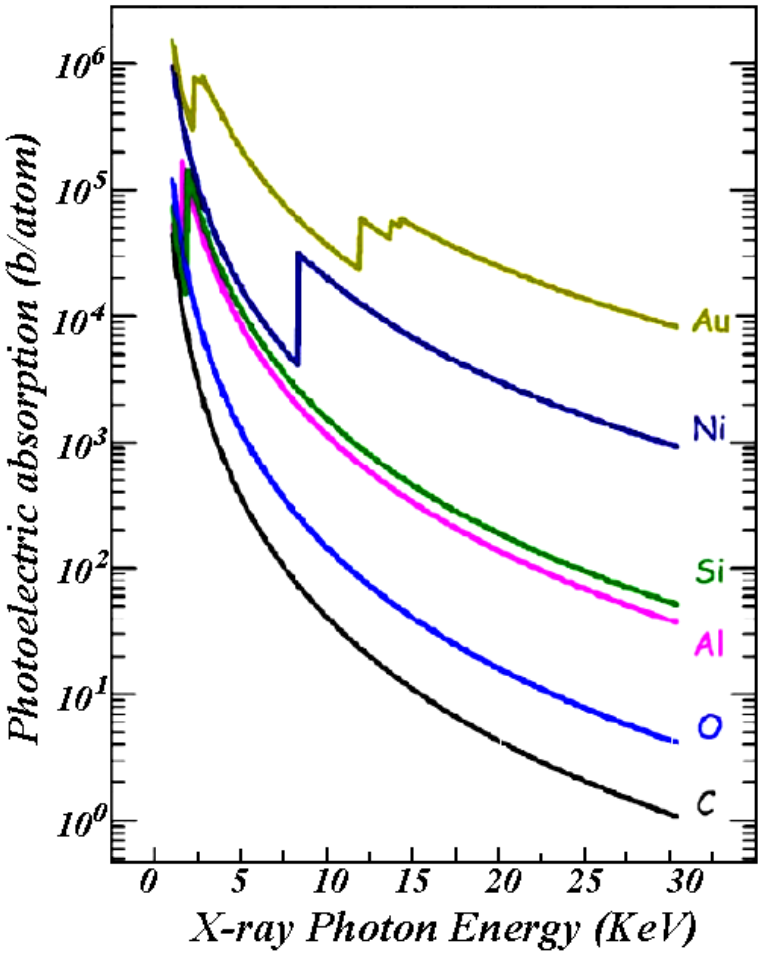

Fig. II.12. Photoionization cross-sections as function of photon energy.

For low-Z elements a drop of up to 4 orders of magnitude is observed when the photon energy is increased from 2 to 15 keV, but in the Ni case, as it can be clearly seen in figure II.12, the photo-ionization cross section decay is not so dramatic.

At the CRG Spanish synchrotron beam-line SpLine installed at the ESRF, Grenoble, France, it was developed a novel[17] cylindrical sector electron analyzer (CSA300HV) which together with the high brilliance of the beam-line fulfills the technical requirements imposed by the HAXPES.

II.2 X-RAY ABSORPTION SPECTROSCOPY

X-ray absorption spectroscopy is an element-specific probe of the local structure (short range) of elements in a sample. Interpretation of XAS spectra commonly uses standards with known structures, but can also be accomplished using theory to derive the structure of a material. In either case, the species of the material is determined based on its unique local structure. An important advantage of this technique is its utility for heterogeneous sample, a wide variety of solid and liquids, including whole soils and liquids, can all be examined directly and non-destructively. Additionally, since the local structure does not depend on long-range crystalline order, the structure of amorphous phases (and that of dissolved species) is easily achieved.

X-ray absorption spectroscopy results form the absorption of a high energy X-ray by an atom in a sample. This absorption occurs at a defined energy corresponding to the binding energy of the electron in the material. The ejected electron interacts with the surrounding atoms to produce the spectrum that is observed. Occasionally, the electron can be excited into vacant bound electronic states (unoccupied orbitals) near the valence band. As a result, distinct absorptions will result at these energies.

Since the electron excited is usually the *1s* or *2p* electrons, these energies are usually quite high (thousands of electron volts), this technique demands high energy (and tunable) X-ray excitation. As a result, it is done at synchrotron radiation facilities. These facilities provide a brilliant source that is required for these experiments to be useful at the concentrations needed.

X-ray absorption spectroscopy is commonly divided into two spectral regions, the first is the X-ray absorption near edge structure (XANES) spectral region. XANES spectra are unique to the oxidation state and speciation of the element of interest, and consequently is often used as a method to determine the oxidation state and coordination environment of materials. XANES spectra are commonly compared to standards to determine which species are present in an unknown sample. Once the species are identified, their relative abundance is quantified using linear-combination fitting (or other curve-fitting algorithms) using XANES standards to reconstruct the experimental data. It is important to note that XANES

is sensitive to bonding environment as well as oxidation state. Consequently, XANES is capable of discriminating species of similar formal oxidation state but different coordination.

The more distant region of the X-ray absorption spectrum is termed the extended X-ray absorption fine structure (EXAFS) region. EXAFS spectra are best described as a series of periodic sine waves that decay in intensity as the incident energy increases from the absorption edge. These sine waves result from the interaction of the elected photoelectron with the surrounding atomic environment. Their amplitude and phase depend on the local structure of excited atom. Since this interaction is well understood, theory is sufficiently advanced that the local structure of the excited atom can be determined by matching a theoretical spectrum to the experimental spectrum. This fitting yields many types of information, including the identity of neighboring atoms, their distance from the excited atom, the number of atoms in the shell, and the degree of disorder in the particular atomic shell (as expressed by the Debye-Waller factor). Linear combination of EXAFS spectra using standards is also commonly used for quantification for samples containing many species since it is quite difficult in practice to separate many species into their component shells.

II.2.1 X-ray Absorption Spectroscopy, edges

NEXAFS:

Acronyms, synonyms

- **X**-ray **A**bsorption **S**pectroscopy
- **X**-ray **A**bsorption **N**ear **E**dge **S**tructure

Measured physical quantities

- X-ray induced dissociation of core electron; core- to valence-level electronic transitions

Information available

- Metal-site oxidation state
- Coordination geometry/number

- Qualitative ligand environment
- Metal-localized charge-density changes from one sample to another

Information NOT available, limitations

- Usually only relative oxidation state is available from comparisons of edges, and then only if the structure of the site in both oxidation states is constant
- If a mixture of sites (of the same metal) is present, deconvolution of spectrum is problematic
- Determination of coordination geometry and number is more difficult with metal sites of low symmetry
- Insensitive to magnetic or isotopic properties of metal sites

Major advantages

- Can obtain (indirect) structural information on amorphous samples (e.g., frozen solutions)
- Technique is element-selective; no interference from other metals

Major disadvantages

- Information obtained is mostly qualitative
- Requires fairly high concentration of metal sites
- Requires synchrotron radiation.

II.2.2. Extended X-ray Absorption Fine Structure

EXAFS:

Acronyms, synonyms

- **X**-ray **A**bsorption **S**pectroscopy
- **E**xtended **X**-ray **A**bsorption **F**ine **S**tructure
- **X**-ray **A**bsorption **F**ine **S**tructure

Measured physical quantities

- Scattering of x-ray induced photoelectron by electron density around neighboring atoms

Information available

- *How many of what type* of atom are at *what distance* from a metalsite
- Coordination number
- Type of coordinating atom
- Metal-ligand distance

Information NOT available, limitations

- Structural information is limited to a radius of ca. 4-5 Å from metal site
- Coordination numbers are usually only accurate to ca. 25%
- Ligand atom type is usually only accurate to Z ± 15% (Z is atomic number)
- If a mixture of sites (of the same metal) is present, deconvolution of spectrum is impossible
- Insensitive to magnetic or isotopic properties of metal sites

Major advantages

- Can obtain direct structural information on amorphous samples (e.g., frozen solutions)
- Technique is element-selective; no interference from other metals
- Metal-ligand distances can be measured very accurately (± 0.02 Å or better)

Major disadvantages

- Requires high concentration of metal sites
- Requires synchrotron radiation
- Coordination numbers and atom-type determinations are relatively accurate
- Often does not give a *unique* determination of ligand environment; depends on simulation and curve-fitting

The absorption edge structure often consists of discrete absorption bands superimposed on the steeply rising continuum absorption edge, see figure II.13. These discrete absorption bands are caused by transitions of core electrons to discrete bound valence levels. The absorption edges that are of most interest are the K-edge (*1s* – *3p*), followed by the three L-edges: L_1-edge (*2s* – *5p*), L_2-edge (*2p*1/2 – *5d*3/2) and L_3-edge (*2p*3/2 – *5d*5/2) [Stöhr]. These edges are element specific and shifts to higher energies when the atomic number increases. Since the core levels depend on the element and its chemical environment, they also show chemical specificity. X-ray absorption spectroscopy is therefore not only an element specific technique, but it is also sensitive to the immediate environment of the absorbing atom.

X-ray energy range of 3 – 30 keV results in accessibility of K-edges from roughly chlorine to silver. The L-edge of elements from molybdenum through the actinides also falls within this energy range. Radiation in the range of 0.1 – 3 keV will make it possible to do XAS studies of the lower atomic number elements such as carbon, nitrogen and oxygen. The availability of third generation synchrotron sources now allows the routine performance of XAS investigations using K absorption edges occurring even above 30 keV. Measurements made at absorption edges in the energy range 40 keV to 90 keV have successfully been accomplished. That means that XAS spectrum at K-edge of lead (88.0 keV) has been measured.

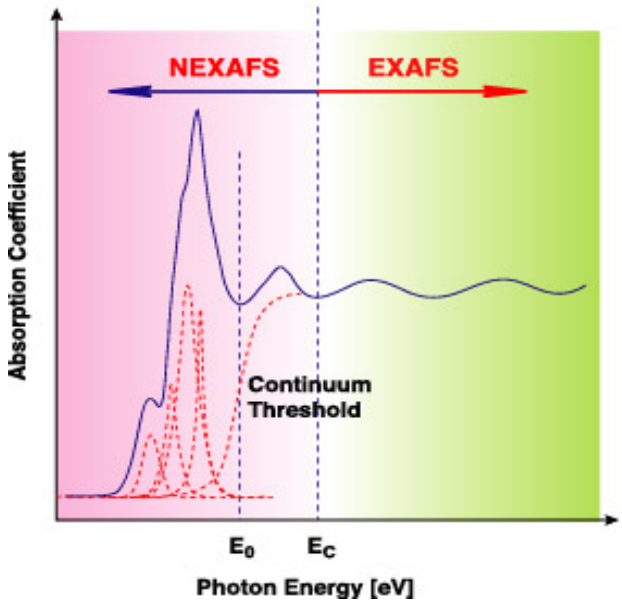

Fig.II.13. The low-energy NEXAFS region with discrete structure from core electron transitions (red dotted lines) superimposed, the NEXAFS region with multiple scattering processes in the continuum (between E_0 and E_c), and the EXAFS region with single scattering processes at higher energies.

There are three types of excited photoelectrons, see figure II.14 The first type has not energy enough to leave the absorbing atom. That electron will do a transition to one of the unoccupied valence states. These transitions will give rise to edge peaks, i.e. peaks before the continuum threshold (ionization threshold) located at the energy value E_0. This energy value E_0 is the threshold energy the photoelectron needs to have if it will escape into the continuum (leave the atom).

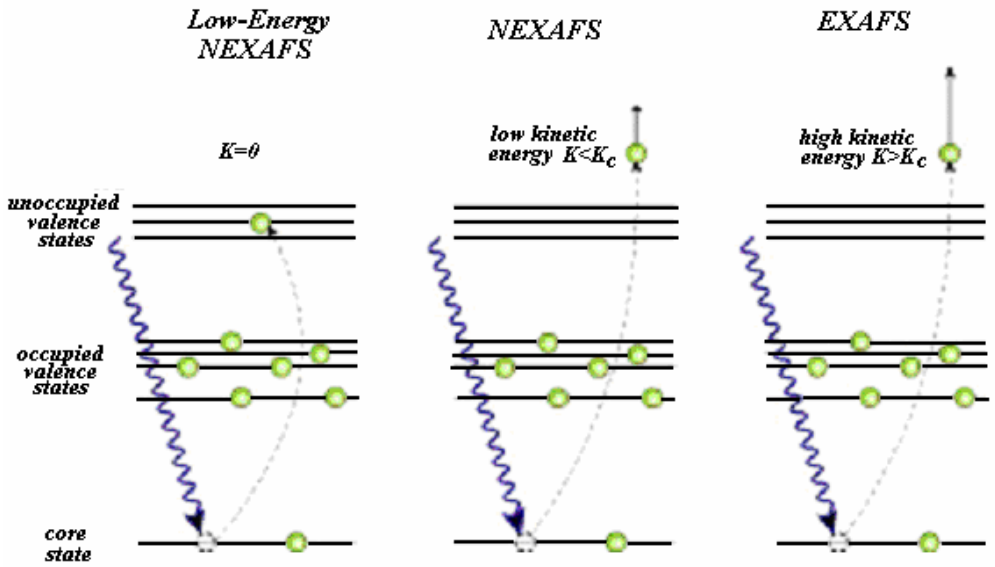

Fig.II.14. Low-energy NEXAFS when k = 0, NEXAFS when 0 < k < k_c = 2/R, (R = distance between the absorbing atom and the closest neighboring atom), and EXAFS when k > k_c.

The second type of excited photoelectron has energy enough to escape into the continuum. But the kinetic energy of the photoelectron is low (10 – 40 eV), and the excited photoelectron is strongly backscattered by the neighboring atoms. Actually, the photoelectron will be part of a multiple scattering process and involve several neighboring atoms, see figure II.14. All of these scattering pathways will contribute to the fine structure near the absorption edge.

When the incoming X-ray has the critical energy value E_c, the wave vector of the photoelectron will have the critical value $k_c = 2/R$. The photoelectron wave will then have a wavelength same as the distance to the closest of the neighboring atoms, see figure II.15. An excited photoelectron, with high kinetic energy, will then be weakly backscattered by only one of the neighbor atoms, and hence a single scattering process will occur.

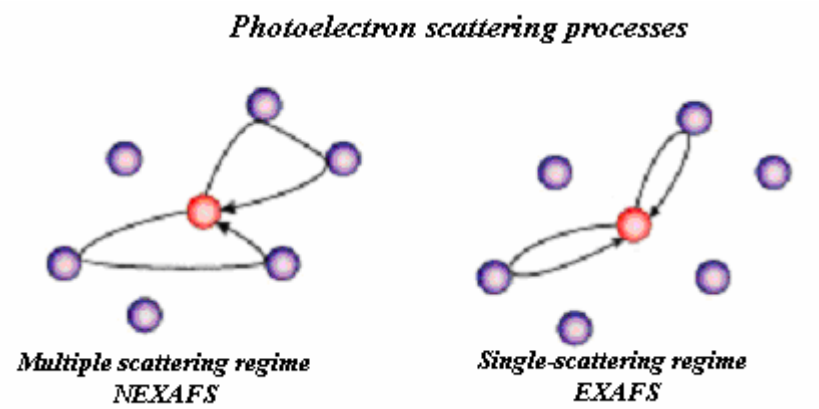

Fig.II.15. A single scattering process will give rise to fine structures ~50 – 1000 eV after the absorption edge (EXAFS), while multiple scattering process will give rise to fine structures ~10 – 50 eV after the edge (NEXAFS).

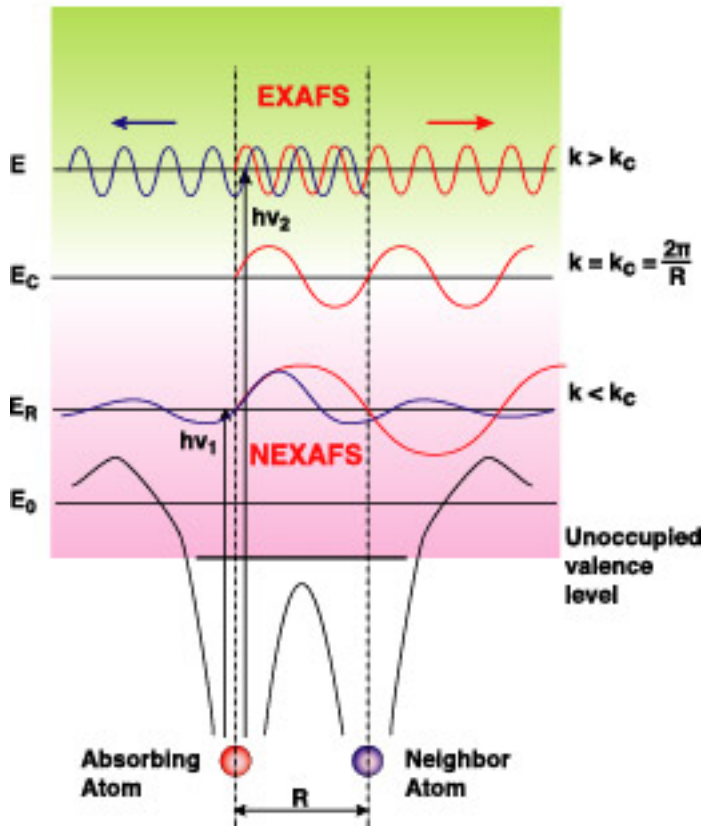

Fig.II.16. The final-state wave function in the core excitation in a diatomic molecule. Excitations at low energies are in the NEXAFS region, and excitations at high energies are in the EXAFS region. When the wave vector for the photoelectron has the critical value $k_c = 2/R$, the NEXAFS merge into EXAFS.

II.2.3. X-ray absorption coefficient vs. photon energy

When a beam of monochromatic X-ray goes through matter, it loses its intensity due to interaction with the atoms in the material. The intensity drops exponentially with distance if the material is homogeneous, and after transmission the intensity is:

$$I = I_0 e^{-\rho\mu d}$$

where I and I_0 are the transmitted and the incident X-ray intensities respectively. ρ is the mass density, μ is the absorption coefficient and d is the thickness of the sample. The absorption co-efficient will decrease smoothly with higher energy, except for certain photon energies, see figure II.17. When the photon energy reaches the critical value for a core electron transition, the absorption coefficient increases abruptly. These abrupt increases in absorption occur whenever the incident photon has just enough energy to promote a core electron to unoccupied valence level or into the continuum (leave the atom). The probability to eject an electron is largest when the photon energy is sufficient for the transition process. After each absorption edge the absorption coefficient will continue to decrease with increasing photon energy.

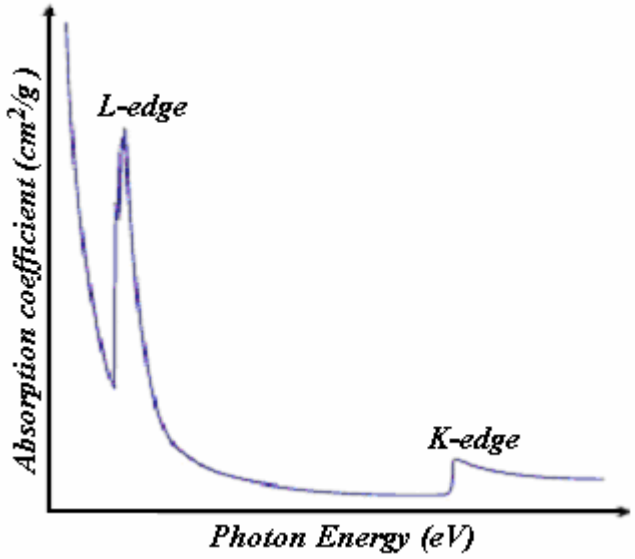

Fig.II.17. The absorption coefficient will decrease smoothly with higher energy, except for special photon energies. When the photon energy reaches the critical value for a core electron transition the absorption coefficient increases abruptly.

The loss in intensity can also be expressed in terms of the photoabsorption cross-section, sabs by the following expression:

$$I = I_0 e^{-n\sigma_{abs}d}$$

where I and I_0 are the transmitted and the incident X-ray intensities, n_a is the atomic density and d is the thickness of the sample. The difference between the two expressions is that a macroscopic description of the photoabsorption process and involve atoms in a particular solid material or molecular form, in the first one, while in the second is a microscopic description of the same process but for single isolated atoms. One benefit in the microscopic description is the possibility to separate the contributions of the various atomic sub-shells.

Photoelectrons as a wave

Electrons can be treated as either a particle or a wave, and to understand the different phenomena-non of XAS the emitted photoelectrons need to be treated as a wave. The wavelength λ and the momentum p of an electron are related by the de Broglie equation:

$$\lambda = h/p$$

where h is Planck's constant. By defining the wave vector k of the electron as:

$$k = 2\pi/\lambda = 2\pi p/h$$

then the kinetic energy of an electron is:

$$E_k = \frac{1}{2}mv^2 = \frac{1}{2}\frac{p^2}{m} = \left(\frac{h}{2\pi}\right)^2 \frac{k^2}{2m}$$

For an emitted photoelectron the kinetic energy is given by:

$$E_k = E - E_0 = h\nu - E_0$$

E is the energy of the incident x-ray, and E_0 is the threshold energy the photoelectron needs to have if it will escape into the continuum. The X-ray energy is quantized with Planck's constant h and the frequency ν.

The last two equations will together give an expression of the wave vector of an emitted photoelectron as a function of the incident photon energy hν:

$$K = \sqrt{\left(\frac{2\pi}{h}\right)^2 2m(h\nu - E_0)}$$

The probability that a core electron will absorb an X-ray photon depends on both the initial and the final states of the atom. If the core electron is excited to the continuum, the initial state corresponds to the ground-state atom and the final state includes both the ionized atom and the photoelectron wave. If the absorbing atom has a neighboring atom, the outgoing photoelectron wave will be backscattered, thereby producing an incoming electron wave. The final state is then the sum of the outgoing and all the incoming waves, one from each neighboring atom. Depending on the wavelength of the photoelectron and the length of the scattering pathway, the scattered wave can interfere constructively or destructively with the photoelectron wave at the absorbing atom, see figure II.18 This interference will affect the absorption cross section, since the cross section is proportional to the matrix element $<\phi_i|$ r $|\phi_f>$, where $<\phi_i|$ and $|\phi_f>$ represent the initial and final states of the system, respectively, and *r* is the distance between the absorbing atom and the neighboring atom. The interference between the outgoing and the incoming waves give rise to a sinusoidal variation of the absorption coefficient μd versus the photon energy E. This effect is known as Extended X-ray Absorption Fine Structure (EXAFS).

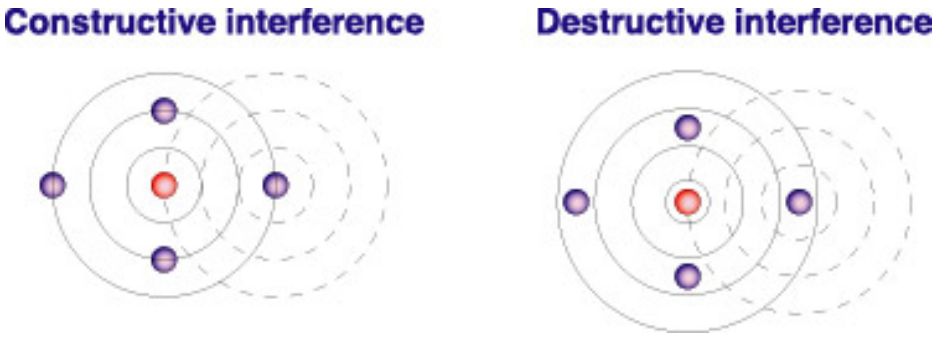

Fig.II.18. The photoelectron wave (solid circles) can be backscattered from the neighboring atoms (dotted circles) and interfere with the photoelectron wave at the absorbing atom. Depending on the wavelength of the photoelectron and the length of the scattering pathway, the scattered wave can interfere constructively or destructively with the photoelectron wave at the absorbing atom.

II.2.4. Computational procedure in NEXAFS

MXAN – software[18]

This procedure is able to simulate the XANES part (from the edge to about 200 eV) of experimental X-ray Absorption data. The method is based on the fitting between the experimental spectrum and theoretical calculations generated by changing the relevant geometrical parameters of the site around the absorbing atom. The x-ray photo-absorption cross section is calculated using the full multiple scattering scheme; different choices of the exchange correlation part of the potential can be utilized.

MXAN uses the MINUIT package of CERN, to search the minimum of the square residue function in the space of the parameters defined as:

$$S^2 = n \frac{\sum_{i=1}^{m} w_i \left[\left(y_i^{th} - y_i^{\exp} \right) \varepsilon_i^{-1} \right]^2}{\sum_{i=1}^{m} w_i}$$

where n is the number of independent parameters, m the number of data points, y_i^{th} and $y_i^{\exp}$ the theoretical and experimental values of absorption, ε_i the individual errors in the experimental data set, and w_i is a statistical weight. For w_i = constant t=1, the square residual function S^2 becomes the statistical χ^2 function. The MXAN procedure[19] needs three input files containing respectively the experimental data to be fitted, the starting atomic coordinates of the cluster (the putative structure), and the commands and options necessary for the chosen minimization strategy[20]. MXAN makes use of the set of programs developed by the Frascati theory group; in particular VGEN, a generator of muffin tin potentials, and the CONTINUUM code for the full multiple scattering cross section calculation[21]. The size of the scattering cluster and the value of the l_{max} in the basis functions expansion can be chosen on the basis of convergence criterion, while the MT radii are chosen on the basis of the Norman criterion.

The exchange correlation part of the potential can be chosen according to the Hedin-Lunqvist (H-L) optical form. Alternatively, either the real part of the H-L potential, or the X-α potential is utilised. In these latter cases, inelastic processes are taken into account by a convolution with a broadening lorentzian function, with a full width given by $\Gamma = \Gamma_c + \Gamma(E)$.

The constant part Γ_c includes the core hole lifetime and the experimental resolution, while the energy dependent term $\Gamma(E)$ represents all the inelastic processes. The $\Gamma(E)$ function is zero below an onset energy E_s, and it begins to increase from a value A_s following the universal functional form of the mean free path in solid. This method introduces three non-structural parameters that are refined on the basis of Montecarlo search at each step of optimisation of the structural parameters. In such a way, together with the MT radii, the MXAN method uses only four non-structural parameters; in facts, coordination numbers and Debye-Waller factors are not treated, whereas the edge jump and the edge position (E_0) are completely unrelated to the fitted structural parameters. As a consequence, the relevant parameters are essentially geometrical. However, careful should be taken to avoid artificial results owing to a bad definition of non-structural parameters. In a final minimization run, they should be fixed.

Program input

The program needs three input files: the *experimental file* (1 line of comment and two columns in free format), the file COMMAND.MIN and the *coordinates file.*

The file command.min contains most of the instructions for the optimizations procedure, including the exact names of the experimental and coordinates files, and the experimental (statistical) error ε, that in this version of the program is assumed constant. If either the file command.min or the coordinates file is absent, the program itself provides samples of these input files to be re-edited and used further. If also the experimental file is absent, the program will produce a theta function in the place of the experimental file, for a pseudo chi-square computation. This last action allows doing simple calculations without fitting. MXAN can read external symmetry file for cubic groups (T_d and O_h), and performs either one shot calculation or fits provided symmetry is not changing.

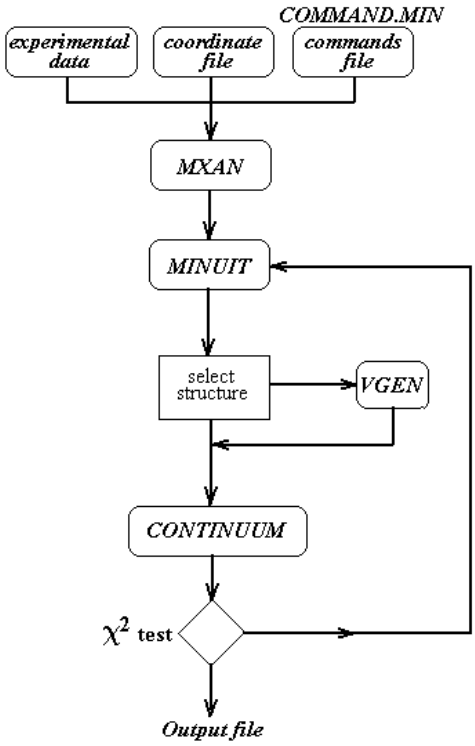

Fig.II.19. Logical scheme of the method.

Minimization strategy

There are essentially two main strategies for doing minimization corresponding to different search mode:

1) Search mode 1SHE or CXYZ. A complete statistical minimization is done in the space of the parameters. The non-structural parameters relating to the Fermi energy and the broadening convolution function are refined by Montecarlo search at each step of the structural optimization. This procedure saves computing time consisting in recalculating the XANES for a search in the complete space of parameters (structural and non-structural, that is still too long in practice) but assumes that the statistical correlation between structural and non-structural parameters is weak.

2) Search mode OPTN. The structure is fixed and a complete statistical minimization is carried out on all the non-structural parameters (i.e. Fermi energy, broadening parameters, and overlap between the muffin-tin radii).

A typical minimization procedure can consist in cycles between these two main strategies.

Coordinates.

A maximum of 90 atoms can be introduced in free format as atomic number *iz,* atomic coordinates *x,y,z,* ligand identity *ilig,* distance *d*. Note that *ilig* is an increasing positive number for each first ligand. Ligands are not necessarily the first neighboring atoms. A maximum value of ilig is eight. Atoms can be linked to move rigidly by the parameters ilig. This means that the linked atoms move all together during the minimization procedure without changing the relative position. Atoms linked to a first ligand have the same value as the first ligand, but with negative sign. The central atom and other atoms not linked to first ligands have ilig = 0**.** Distance ***d*** is a parameter that can be put to zero for commodity, but can be useful to realize the cluster size**.**

Energy independent broadening.

MXAN can convolute each calculated spectrum with a lorentzian function which width can be set by the user. The energy independent broadening value Γ_c accounts for the core-hole width and the experimental resolution. If option Y is used, MXAN will make random trials to get the best value. The spectrum is first cut at the Fermi energy, i.e. the photoabsorption cross section is zero below this value. Then the convolution integral between the spectrum and the lorentzian function is evaluated to get the convoluted spectrum to be compared with the experimental data.

Energy dependent broadening

An energy dependent broadening can simulate the effect of finite electron mean free path due to the inelastic losses of any type suffered by the photoelectron in its way out in the system. We have already given some information in the introduction. If option Y is used, MXAN will add this value to the width of the lorentzian function used in the convolution.

In the chapter V of this work are illustrated the structural changes used in order to simulate the experimental NEXAS spectra.

II.2.5. Low energy absorption spectroscopy (XAS)

The single particle description of X-ray absorption works well for all K edges and a range of dedicated computer codes exist to calculate the X-ray absorption cross-section. Applying one-electron codes (where one-electron applies to a one-electron core excitation, not to the treatment of the valence electrons) to systems such as transition metal oxides one finds excellent agreement for the metal and oxygen K edges, whereas for the other edges, in particular the metal $L_{2,3}$ edges, the agreement is poor. The reason for this discrepancy is not that the density-of-states is calculated wrongly, but other stronger effects are larger than transition band of TM oxides. The deviation from the density-of-states (DOS) is the strong overlap of the core wave function with the valence wave functions. This overlap present also in the ground state, but because all core states are filled, it is not effective and one can approximate the core electrons with their charge. In the final state of an X-ray absorption process one finds a partly filled core state, for example, a $2p^5$ configuration. In case one studies a system with a partly filled *3d*-band, for example, NiO, the final state will have an incompletely filled *3d*-band. For NiO this can be approximated as a $3d^9$ configuration. The *2p*-hole and the *3d*-hole have radial wave functions that overlap significantly. This wave function overlap is an atomic effect that can be very large. It creates final states that are found after the vector coupling of the *2p* and *3d* wave functions. This effect is well known in atomic physics and actually plays a crucial role in the calculation of atomic spectra. Experimentally it was shown that while the direct core hole potential is largely screened, these so-called multiplet effects are hardly screened in the solid state. This implies that the atomic multiplet effects are of the same order of magnitude in atoms and in solids.

II.2.5.1. Unoccupied Density of States Aproach

In case of *s* core holes, multiplet effects are effectively reduced to just the exchange interaction between the spin of the s core hole and the spin of the valence electrons. The *1s* core states have in all cases a very small exchange interaction, implying that multiplet effects will not be visible. This implies that single electron codes will be effective for all *K* edges (note that for systems that are affected by many body effects, single electron codes are not

necessarily correct, but as in X-ray absorption only effects larger than the lifetime broadening, say 0.2 eV or more, are visible, many body effects that cause small energy effects are not visible). The other *s*-holes have larger multiplet effects, implying a splitting of the spectrum. For the core holes given in boldface, this splitting is clearly visible in the actual spectral shapes.

The most common system to observe this is a transition-metal-oxide, were the O *1s* XAS spectra correspond to O $s \rightarrow p$ transitions, according to the dipole selection rule ($\Delta\ell=\pm1$), so in XAS, only unoccupied O states of p-character can be reached. The spectra are thus, directly related to unoccupied O *p* states mixed with metal-*3d* and metal-*4sp* states via hybridization. The near-edge region of the spectra is dominated by hybridization with metal-*3d* states, thus mapping the metallic *3d* density of states as the figure below show.

The shadowed area is assigned to oxygen p character mixed with transition-metal *3d* states. The broader structure is assigned to oxygen p character mixed with metal *4s* and *4p* bands. To be remarked that the intensity of *3d* band relative to the *4s* band across to the transition-metal serie is decreasing, which reflect the number of unoccupied *3d* states for mixing with O *2p* state, which is decreasing.

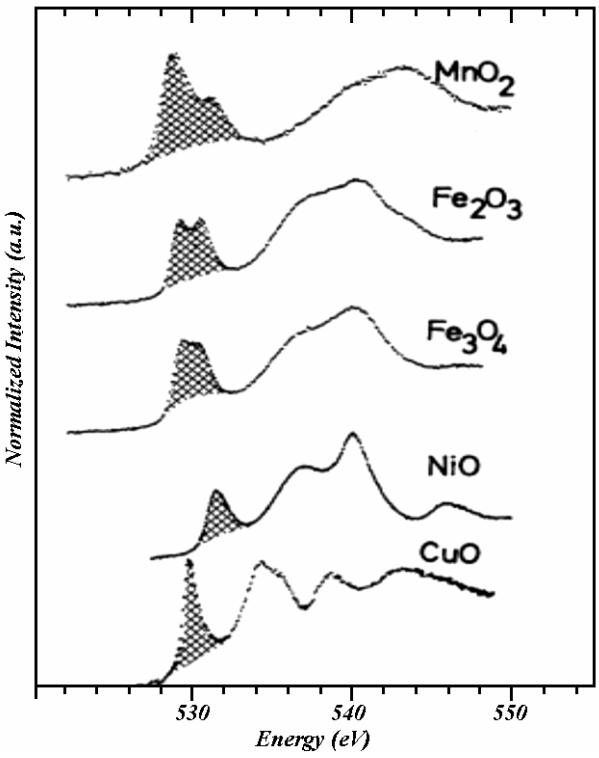

Fig.II.20. O 1s XAS spectra of some transition-metal-oxides[22].

II.2.5.2. Multiplet Theory Approach

For multiplet effects to have a significant effect on the mixing of the L_3 and L_2 edges, the value of the Slater–Condon parameters must be at least of the same order of magnitude as the spin–orbit coupling separating the two edges. If the core spin–orbit coupling is large, there can be an effect from the Slater–Condon parameters. For example, the *2p* and *3p* edges of the *4d* elements have a large spin–orbit splitting and the multiplet effects are not able to mix states of both sub-edges, but multiplet effects still will affect the spectral shapes[23,24]. If a multiplet effect will actually be visible in X-ray absorption further depends on the respective lifetime broadenings. The situation for the *3d* metals is clear: no visible multiplet effects for the *1s* core level (*K* edge) and a significant influence on all other edges. Figure II.20 shows the comparison of all edges for Ni^{2+} with atomic multiplet effects included.

A cubic crystal field of 1.0 eV is included and splits the *3d* states. The top three spectra are, respectively, the *1s*, *2s* and *3s* X-ray absorption spectrum calculated as the transition from $1s^2 3d^8 4p^0$ to $1s^1 3d^8 4p^1$. The lifetime broadening was set to 0.2 eV half-width half-maximum (its actual value is larger for most edges). One observes one peak for the *1s* spectrum and two peaks for the *2s* and *3s* spectra. The reason for the two peaks is the *2s3d* and *3s3d* exchange interactions. The splitting between the parallel and antiparallel states are ±2.5 and ±6.5 eV, respectively. The actual 1s X-ray absorption spectrum of NiO looks different than a single peak, because one observes an edge jump and transitions from the *1s* core state to all empty states of *p*-character. The complete spectral shape of K edge X-ray absorption is therefore better described with a multiple scattering formalism and this single peak reflects just the first white line or leading edge of the K edge spectrum.

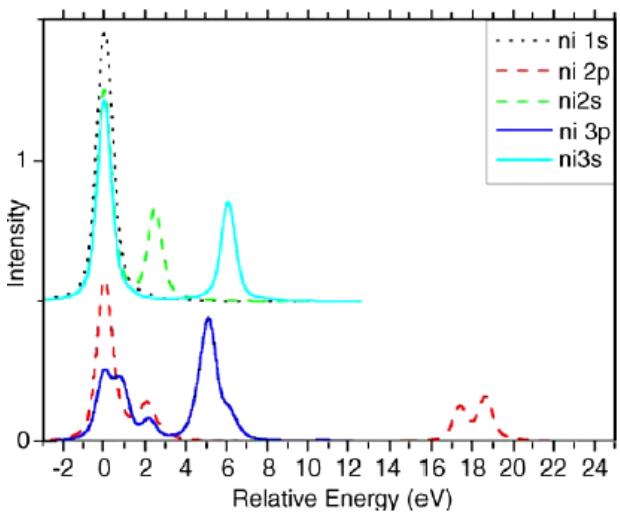

Fig.II.21. The X-ray absorption spectra for Ni^{2+} . The binding energies are 8333, 1008, 870, 110 and 68 eV for 1s, 2s, 2p, 3s and 3p edges, respectively.

The spectra at the bottom of figure II.21 are the *2p* (red dashed) and *3p* (solid) X-ray absorption spectral shapes. These are the well-known *2p* and *3p* spectra of NiO and other divalent nickel compounds. The $2p^5 3d^9$ and $3p^5 3d^9$ final states contain one *p* hole and one *3d* hole that interact very strongly. This gives rise to a multitude of final states. Because the lifetime broadening for *2p* states is relatively low, its spectral shapes can actually be observed in experiment. This gives *2p* X-ray absorption, and to a lesser extends *3p* X-ray absorption, their great potential for the determination of the local electronic structure.

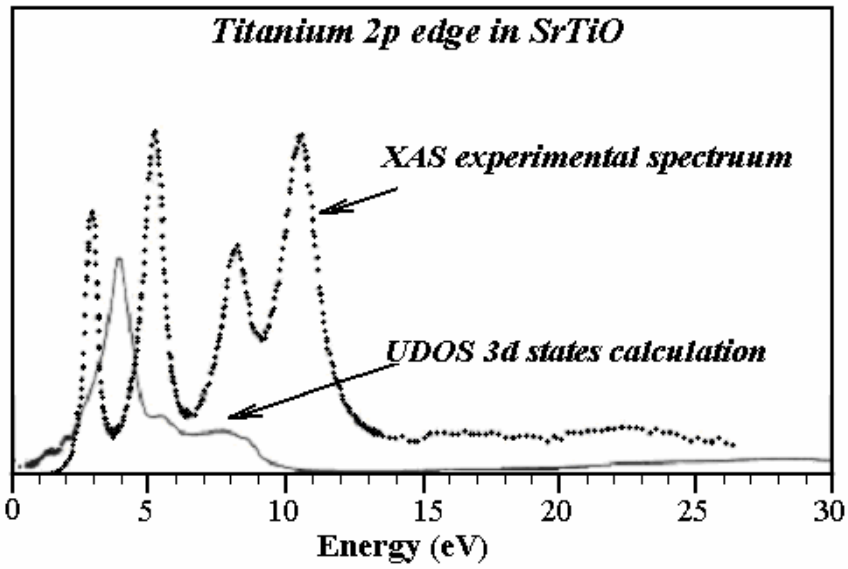

Fig.II.22. Ti 2p absorption spectrum: UDOS calculation (line) and experimental XAS spectrum (dots).

UDOS calculation of the Ti *2p* edge compared with the experimental spectra clearly shows that the calculation model involved was wrong chosen.

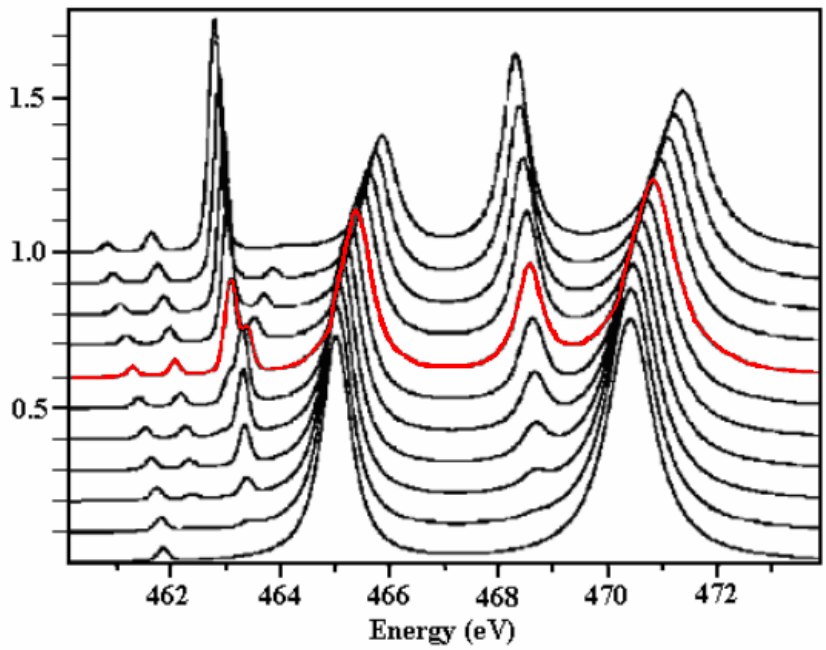

Fig.II.23. Crystal field multiplet calculations for the $3d^0 \rightarrow 2p^5 3d^1$ transition in Ti^{IV}. The bottom spectrum is the atomic multiplet spectrum. Each next spectrum has a value of 10Dq that as increased by 0.3 eV. The top spectrum has a crystal field of 3.0 eV.

Figure II.23 shows the crystal field multiplet calculations for the $3d^0 \rightarrow 2p^5 3d^1$ transition in Ti^{IV}. The first spectra represent the atomic multiplet for Ti 4^+ in spherical symmetry (10Dq=0). After that, this spectra is projected in a crystal field to simulate the solid. The straight of the crystal field (10Dq) is increased in step of 0.3 eV. Sthe right comparation with the experimental XAS spectrum corresponds to a crystal field value 10Dq=1.8 eV (in red). An additional difference in broadening is found between the t_{2g} and the e_g states. This broadening was ascribed to differences in the vibrational effects on the t_{2g}, respectively, the e_g states.

II.3. ATOMIC FORCE MICROSCOPY

The atomic force microscope (AFM) or scanning force microscope (SFM) is a very high-resolution type of scanning probe microscope, with demonstrated resolution of fractions of a nanometer, more than 1000 times better than the optical diffraction limit. The precursor to the AFM, the scanning tunneling microscope, was developed by Gerd Binnig and Heinrich Rohrer in the early 1980s, a development that earned them the Nobel Prize for Physics in 1986, marking the biggining of nanotechnology.

Binnig, Quate and Gerber invented the first AFM in 1986. The AFM is one of the foremost tools for imaging, measuring and manipulating matter at the nanoscale. The term “microscope” in the name is actually a misnomer because it implies looking, while in fact the information is gathered by "feeling" the surface with a mechanical probe. Piezoelectric elements that facilitate tiny but accurate and precise movements on (electronic) command enable the very precise scanning.

Basic principle

The AFM consists of a microscale cantilever with a sharp tip (probe) at its end that is used to scan the specimen surface. The cantilever is typically silicon or silicon nitride with a tip radius of curvature on the order of nanometers[25]. When the tip is brought into proximity of a sample surface, forces between the tip and the sample lead to a deflection of the cantilever according to Hooke's law. Depending on the situation, forces that are measured in AFM include mechanical contact force, Van der Waals forces, capillary forces, chemical bonding, electrostatic forces, magnetic forces (see Magnetic force microscope (MFM)), Casimir forces, solvation forces etc. As well as force, additional quantities may simultaneously be measured through the use of specialised types of probe. Typically, the deflection is measured using a laser spot reflected from the top of the cantilever into an array of photodiodes. Other methods that are used include optical interferometry, capacitive sensing or piezoresistive AFM cantilevers. These cantilevers are fabricated with piezoresistive elements that act as a strain gauge. Using a Wheatstone bridge, strain in the

AFM cantilever due to deflection can be measured, but this method is not as sensitive as laser deflection or interferometry[26,27].

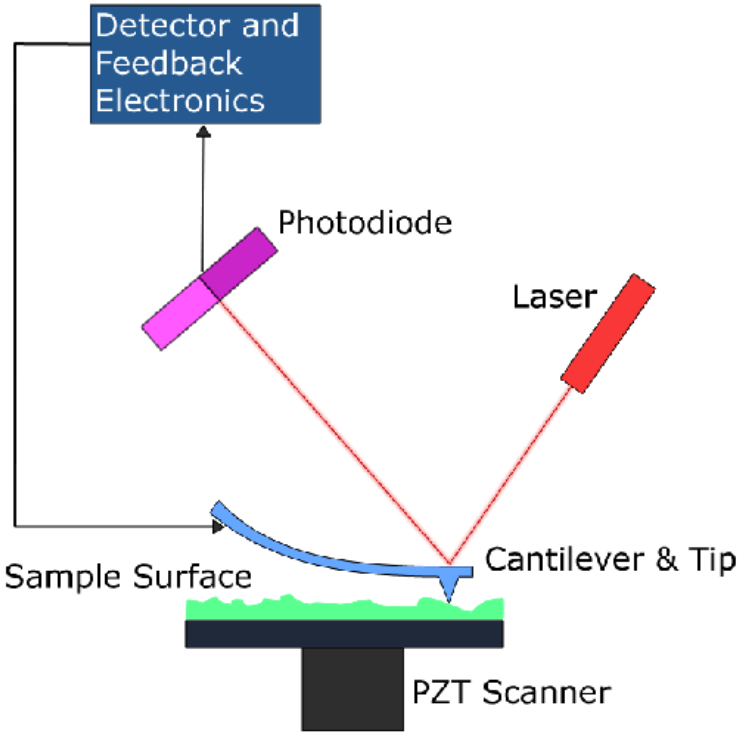

Fig. II.24. Block Diagram of Atomic Force Microscope.

If the tip were scanned at a constant height, there would be a risk that the tip would collide with the surface, causing damage. Hence, in most cases a feedback mechanism is employed to adjust the tip-to-sample distance to maintain a constant force between the tip and the sample. Traditionally, the sample is mounted on a piezoelectric tube, that can move the sample in the *z* direction for maintaining a constant force, and the *x* and *y* directions for scanning the sample. Alternatively a 'tripod' configuration of three piezo crystals may be employed, with each responsible for scanning in the x,y and z directions. This eliminates some of the distortion effects seen with a tube scanner. The resulting map of the area $s = f(x,y)$ represents the topography of the sample.

The AFM can be operated in a number of modes, depending on the application. In general, possible imaging modes are divided into static (also called Contact) modes and a variety of dynamic (or non-contact) modes.

Imaging modes

The primary modes of operation are static (contact) mode and dynamic mode. In the static mode operation, the static tip deflection is used as a feedback signal. Because the measurement of a static signal is prone to noise and drift, low stiffness cantilevers are used to boost the deflection signal. However, close to the surface of the sample, attractive forces can be quite strong, causing the tip to 'snap-in' to the surface. Thus static mode AFM is almost always done in contact where the overall force is repulsive. Consequently, this technique is typically called 'contact mode'. In contact mode, the force between the tip and the surface is kept constant during scanning by maintaining a constant deflection.

In the dynamic mode, the cantilever is externally oscillated at or close to its fundamental resonance frequency or a harmonic. The oscillation amplitude, phase and resonance frequency are modified by tip-sample interaction forces; these changes in oscillation with respect to the external reference oscillation provide information about the sample's characteristics. Schemes for dynamic mode operation include frequency modulation and the more common amplitude modulation. In frequency modulation, changes in the oscillation frequency provide information about tip-sample interactions. Frequency can be measured with very high sensitivity and thus the frequency modulation mode allows for the use of very stiff cantilevers. Stiff cantilevers provide stability very close to the surface and, as a result, this technique was the first AFM technique to provide true atomic resolution in ultra-high vacuum conditions[28].

In amplitude modulation, changes in the oscillation amplitude or phase provide the feedback signal for imaging. In amplitude modulation, changes in the phase of oscillation can be used to discriminate between different types of materials on the surface. Amplitude modulation can be operated either in the non-contact or in the intermittent contact regime. In ambient conditions, most samples develop a liquid meniscus layer. Because of this, keeping the probe tip close enough to the sample for short-range forces to become detectable while preventing the tip from sticking to the surface presents a major hurdle for the non-contact dynamic mode in ambient conditions. Dynamic contact mode (also called intermittent contact or tapping mode) was developed to bypass this problem[29]. In dynamic contact mode, the cantilever is oscillated such that the separation distance between the cantilever tip and the sample surface is modulated.

Amplitude modulation has also been used in the non-contact regime to image with atomic resolution by using very stiff cantilevers and small amplitudes in an ultra-high vacuum environment.

Tapping Mode

In *tapping mode* the cantilever is driven to oscillate up and down at near its resonance frequency by a small piezoelectric element mounted in the AFM tip holder. The amplitude of this oscillation is greater than 10 nm, typically 100 to 200 nm.

Due to the interaction of forces acting on the cantilever when the tip comes close to the surface, Van der Waals force or dipole-dipole interaction, electrostatic forces, etc cause the amplitude of this oscillation to decrease as the tip gets closer to the sample. An electronic servo uses the piezoelectric actuator to control the height of the cantilever above the sample. The servo adjusts the height to maintain a set cantilever oscillation amplitude as the cantilever is scanned over the sample. A *Tapping AFM* image is therefore produced by imaging the force of the oscillating contacts of the tip with the sample surface. This is an improvement on conventional contact AFM, in which the cantilever just drags across the surface at constant force and can result in surface damage.

Tapping mode is gentle enough even for the visualization of supported lipid bilayers or adsorbed single polymer molecules (for instance, 0.4 nm thick chains of synthetic polyelectrolytes) under liquid medium. At the application of proper scanning parameters, the conformation of single molecules remains unchanged for hours[30].

Advantages and disadvantages

The AFM has several advantages over the scanning electron microscope (SEM). Unlike the electron microscope which provides a two-dimensional projection or a two-dimensional image of a sample, the AFM provides a true three-dimensional surface profile. Additionally, samples viewed by AFM do not require any special treatments (such as metal/carbon coatings) that would irreversibly change or damage the sample.

While an electron microscope needs an expensive vacuum environment for proper operation, most AFM modes can work perfectly well in ambient air or even a liquid environment. This makes it possible to study biological macromolecules and even living

organisms. In principle, AFM can provide higher resolution than SEM. It has been shown to give true atomic resolution in ultra-high vacuum (UHV) and, more recently, in liquid environments. High resolution AFM is comparable in resolution to Scanning Tunneling Microscopy and Transmission Electron Microscopy.

A disadvantage of AFM compared with the scanning electron microscope (SEM) is the image size. The SEM can image an area on the order of millimetres by millimetres with a depth of field on the order of millimetres. The AFM can only image a maximum height on the order of micrometres and a maximum scanning area of around 150 by 150 micrometres.

Another inconvenience is that an incorrect choice of tip for the required resolution can lead to image artifacts. Traditionally the AFM could not scan images as fast as an SEM, requiring several minutes for a typical scan, while an SEM is capable of scanning at near real-time (although at relatively low quality) after the chamber is evacuated. The relatively slow rate of scanning during AFM imaging often leads to thermal drift in the image, making the AFM microscope less suited for measuring accurate distances between artifacts on the image. However, several fast-acting designs were suggested to increase microscope scanning productivity[31] including what is being termed videoAFM (reasonable quality images are being obtained with videoAFM at video rate - faster than the average SEM). To eliminate image distortions induced by thermodrift, several methods were also proposed.

AFM images can also be affected by hysteresis of the piezoelectric material and cross-talk between the (x,y,z) axes that may require software enhancement and filtering. Such filtering could "flatten" out real topographical features. However, newer AFM use real-time correction software (for example, feature-oriented scanning, Lapshin, 2004, 2007) or closed-loop scanners which practically eliminate these problems. Some AFM also use separated orthogonal scanners (as opposed to a single tube) which also serve to eliminate cross-talk problems[32].

Due to the nature of AFM probes, they cannot normally measure steep walls or overhangs. Specially made cantilevers can be modulated sideways as well as up and down (as with dynamic contact and non-contact modes) to measure sidewalls, at the cost of more expensive cantilevers and additional artifacts.

REFERENCES

[1]Einstein, A., *On the Electrodynamics of Moving Bodies.* Annalen der Physik, 17(132), 1905.

[2] P. Auger, *Compt. Rend*. 177, 169,1923

[3]Dickson, J., *A Summary of the Technique for Photoemission Spectroscopy (PES) Experimentation*.

[4]Nix, R., *An Introduction to Surface Chemistry,* 1996.

[5]Nelson, A.E., X-Ray Photoelectron Spectroscopy (XPS). 2002.

[6]Grayson, B., *Surface Preparation and Analysis of Silicon Carbide*, University of South Florida: Tampa, 2002

[7]M. P. Seah, in Practical Surface Analysis Vol. 1 Chapt. 5, Eds., D. Briggs and M. P. Seah, Wiley, New York, 1990.

[8]M. P. Seah, Surf. Interface Anal. 2, 222, 1980.

[9]S. Tougaard, Surface and Interface Analysis 11, 453, 1988.

[10]S. Tougaard and H.S. Hansen, Surface Interface Analysis 14, 730, 1989.

[11]S. Tougaard, J. Electron Spectroscopy 52, 243, 1990.

[12]S. Tougaard, J. Vacuum Science and Technology A8, 2197, 1990.

[13]S. Tougaard, J. Vacuum Science and Technology A14, 1415, 1996.

[14] S. Tougaard, Surface and Interface Analysis 26, 249, 1998.

[15] S. Tougaard, Surface and Interface Analysis 25, 137, 1997.

[16] Lindau I, Pianetta P, Doniach S , Spicer W.E, Nature, 250, (1974) 214.

[17] J.Rubio-Zuazo, M.Escher, M.Merkel and G.R.Castro, Journal of Physics: Conference Series 100 (2008) 072032.

[18] Maurizio Benfatto and Stefano Della Longa, 2001.

[19] M. Benfatto, A. Congiu-Castellano, A. Daniele and S. Della Longa J. Sinchrotron Rad, 8: 267-269, 2001.

[20] M. Benfatto and S. Della Longa, J. Sinchrotron Rad., 8: 1087-1094, 2001.

[21] S. Della Longa, A. Arcovito, M. Girasole, J.L. Hazemann, and M. Benfatto, Phys. Rev. Lett. 87, 2001.

[22] F.M.F. de Groot, M. Grioni and J. C. Fuggle, Phys. Rev. B 40, p.5715. 1989.

[23] F.M.F. Degroot, Phys. Rev. B 209, 15, 1995.

[24] Z. Hu, H. Von Lips, M.S. Golden, J. Fink, G. Kaindl, F.M.F. Degroot, S. Ebbinghaus, A. Reller, Phys. Rev. B 61, 5262, 2000.

[25] D. Sarid, Scanning Force Microscopy, Oxford Series in Optical and Imaging Sciences, Oxford University Press, New York, 1991.

[26] R. Dagani, Individual Surface Atoms Identified, Chemical & Engineering News, 5 March, p.13, American Chemical Society, 2007.

[27] R. V. Lapshin, O. V. Obyedkov, Fast-acting piezoactuator and digital feedback loop for scanning tunneling microscopes, Review of Scientific Instruments, vol. 64, no. 10, pp. 2883-2887, 1993.

[28] F. Giessibl, Advances in Atomic Force Microscopy, Reviews of Modern Physics 75 (3), 949-983, 2003.

[29] Q. Zhong, D. Innis, K. Kjoller, V. B. Elings, Surf. Sci. Lett. 290, L688, 1993.

[30] Y. Roiter and S. Minko, AFM Single Molecule Experiments at the Solid-Liquid Interface: In Situ Conformation of Adsorbed Flexible Polyelectrolyte Chains, Journal of the American Chemical Society, vol. 127, iss. 45, pp. 15688-15689, 2005.

[31] R. V. Lapshin, O. V. Obyedkov, Fast-acting piezoactuator and digital feedback loop for scanning tunneling microscopes, Review of Scientific Instruments, vol. 64, no. 10, pp. 2883-2887, 1993.

[32] F. Giessibl, Advances in Atomic Force Microscopy, Reviews of Modern Physics 75 (3), 949-983, 2003.

Chapter III

EXPERIMENTAL DETAILS

III.1. INTRODUCTION

This chapter is entirely dedicated to a detailed description of the experiments setup and measurement equipments and conditions.

In the *sample preparation* section, not only the growth of the NiO on graphite or on the selected oxides, but also, the graphite cleaning method, and more, the oxides obtaining processes, are fully described.

The samples preparation is followed by the description of the experimental equipments used in each corresponding analysis technique. The principal characteristics of the systems and the experimental measuring conditions are given.

III.2. SAMPLE PREPARATION

III.2.1. Strategy of the study

As one of the scopes of this work is to demonstrate the surface effects importance versus bulk effects, in NiO, the samples were prepared in such way that the NiO surface to bulk ratio presents a coherent variation. For this, the NiO samples were prepared by successive depositions, each stage of the growth being measured and analyzed by correspondent techniques (XPS, XAS, AFM, NEXAFS etc.).

A second aim of the work is to study the interface effects in NiO/OXIDES materials. For this, was necessary a maximization of the signal from the interface during the measurements. In order to obtain a maximum utile signal, very low deposition rates were used in the preparation processes of the samples.

Keeping in mind that some of the analysis used techniques are sensible to charge effects, in the study of NiO/OXIDE interfaces, the oxides substrates were prepared as very thin oxide films on conductive supports.

III.2.2. NiO Growth

The NiO was obtained by thermal evaporation of 99.99 % pure metallic nickel provide by *Goodfellows matrials*, in $1 \div 2 \times 10^{-5}$ mbar of molecular oxygen pressure at room temperature. The initial pressure in preparation chamber was in the range of 10^{-9} mbar, so that the oxygen atmosphere was highly contamination free.

In the picture below a schematic view of the Ni evaporator is presented.

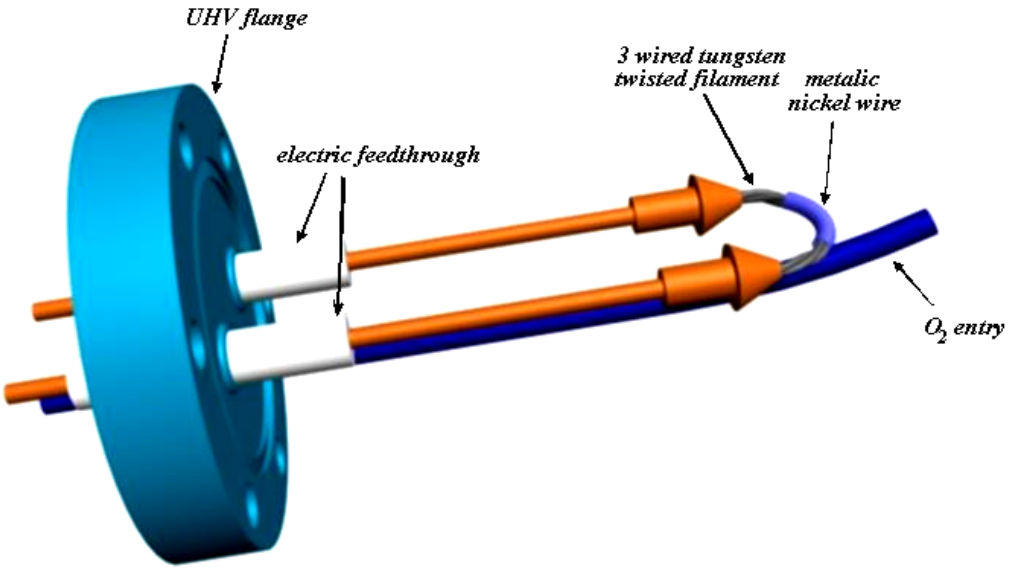

Fig.III. 1. Nickel evaporator system.

As it can be seen in the picture above, the nickel evaporator consists of an ultra high vacuum flange, in which three feedthrough are assembled. Two of them are electrical ones and the third one is a gas entry for locally oxygen insertion, around the substrate. The heating source consists in three twisted tungsten wires filament; each tungsten wire has a 0.25 mm diameter. The twist rate is 4 by each centimeter of the filament length, which makes the entire filament to present an electrical resistance of 0.12 Ω. The nickel evaporator is built covering the middle part of the tungsten filament with 60 turns of a metallic nickel wire with a diameter of 0.25 mm.

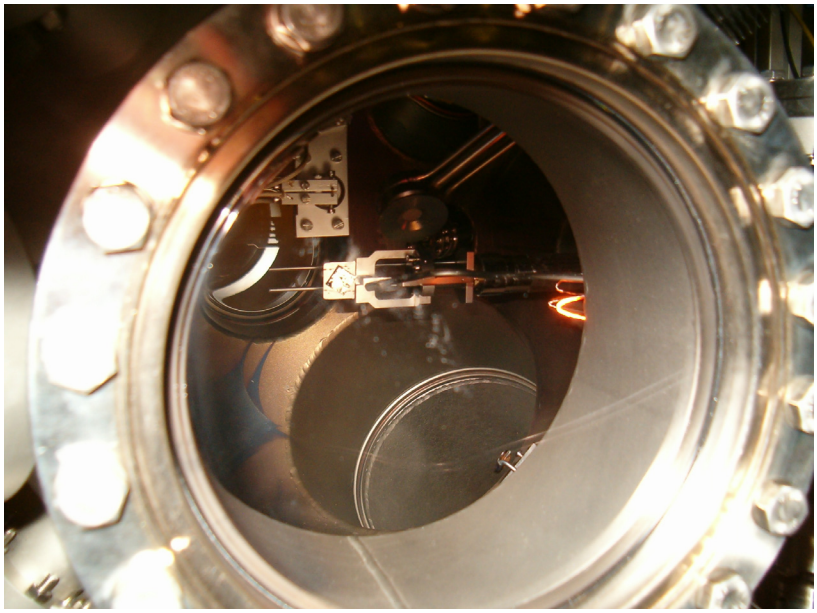

Fig.III.2. Illustration of Ni evaporation in MUSTANG – preparation chamber of PM 4 beam line at BESSY II storage ring.

Taking into account that the distance between the nickel evaporator and substrate, was 10 cm, and varying the filament power between 9.72 VA and 15.8 VA, the deposition rate was evaluated and calibrated using the intensities ratio of the Ni *2p* and C *1s* XPS spectra.

III.2.3. Nanostructured NiO Growth

The nanostructured NiO was prepared by RF magnetron sputtering. A schematic representation of a sputtering process is pictured below in figure III.3.

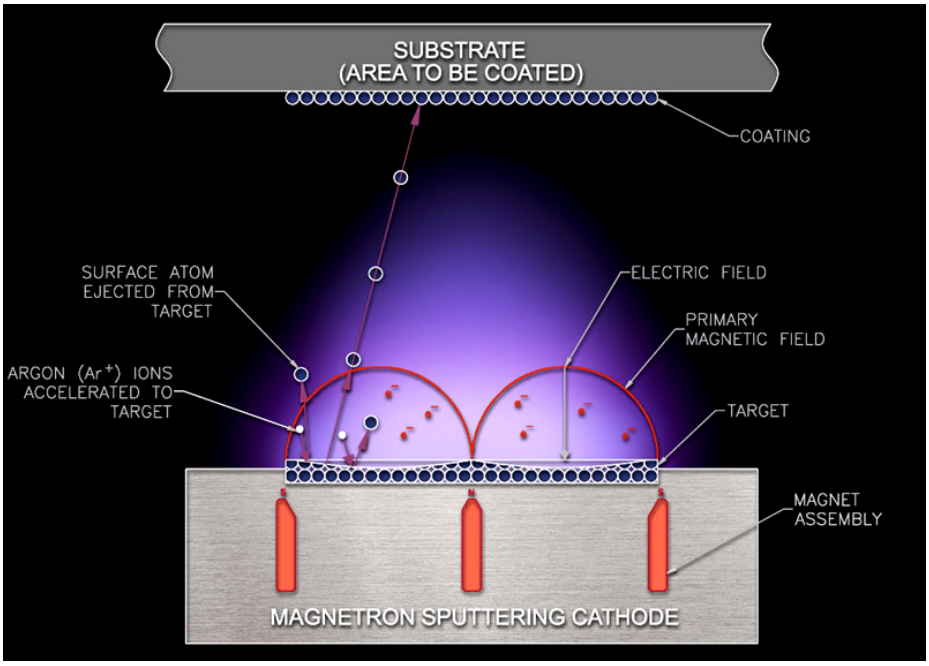

Fig.III.3. Schematic representation of a magnetron sputtering process.

The magnetron sputtering works by applying a high voltage across a low-pressure gas, usually argon at 10^{-2} mbar, to create an argon plasma, which consists of electrons and gas ions in a high-energy state. During sputtering, energized plasma ions strike the target, composed of the desired coating material, and cause atoms from that target to be ejected with enough energy to travel to the substrate.

As special support were used.

The growth parameters are not given since this procedure is still under patent registration.

III.2.4. Graphite cleaning process

In the case of high ordered pyrolytic graphite (HOPG) as substrate, the cleaning process is very well known, and consists in the cleavage of several planes of graphite right before introduction in the vacuum chamber. After a heating treatment, about 60 minutes at 400 °C in 10^{-8} mbar (preparation chamber pressure during heating), an XPS survey scan (figure III. 4) of the graphite presents a spectrum practically identical to those of NIST[1] reference spectra.

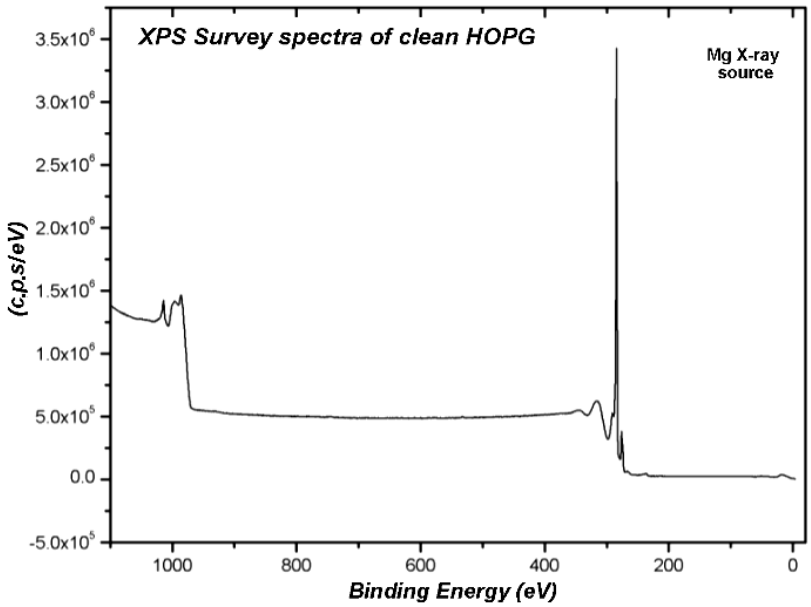

Fig.III.4 Survey XPS spectra of clean HOPG.

AFM images of a clean HOPG are presented in figure III.5 and III.6. In first one a terrace graphite area has been measured in dynamic mode (tapping) using Nanotec's microscope and software[2] and in the second one, the graphite steps are shown in a largest AFM image.

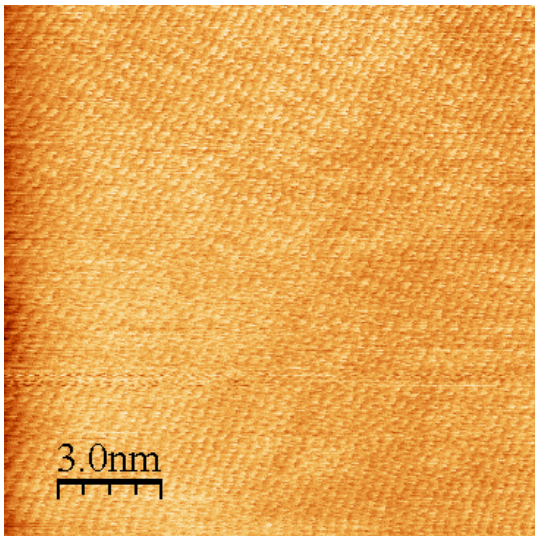

Fig.III.5 AFM HOPG image.

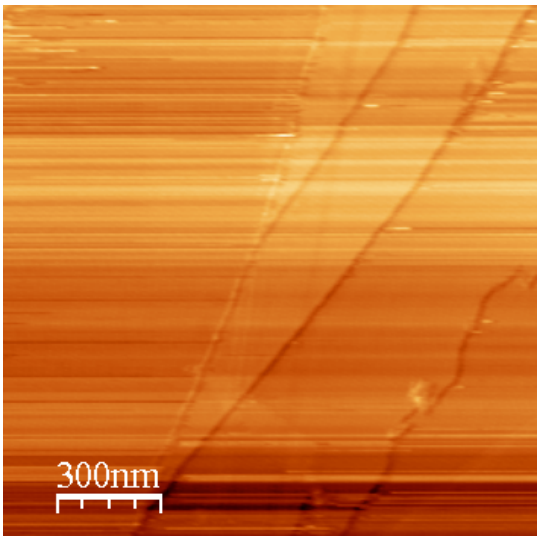

Fig.III.6. Larger area AFM image of HOPG.

The root mean square (RMS) roughness value in first case was 0.187 Å which should reflect the convolution of the graphite symmetry with county level dimension and from the second AFM image the RMS value is 3.157 nm which is principally due to the graphite steps. The graphite steps were found to have heights between 0.6 and 4 nm which means 2 to 12 graphite planes.

III.2.5. Oxide Substrates preparation

The oxide substrates (SiO_2, Al_2O_3, and MgO) have been chosen according to the nature of their chemical bonding, from a more covalent to a more ionic character. Interesting trends in terms of covalency-ionicity of the substrates have already been observed[3,4] in the study of the electronic structure of TiO_2/oxide interfaces with synchrotron radiation spectroscopies.

In the NiO/oxides interface effects studies, thin films substrates of the amorphous or polycrystalline oxides, prepared on conductive materials and following conventional methods, were used.

The ***silica*** substrate consisted of a 200 Å thin film of amorphous SiO_2 grown by dry oxidation of a p-doped Si (111) wafer, provided by *Goodfellows Materials*. The oxidation of silicon in dry O_2 is straight forward, proceeding via the reaction Si + O2 → SiO_2 at 1100 degrees C. The SiO_2 thickness is tilt related with the oxidation time process.

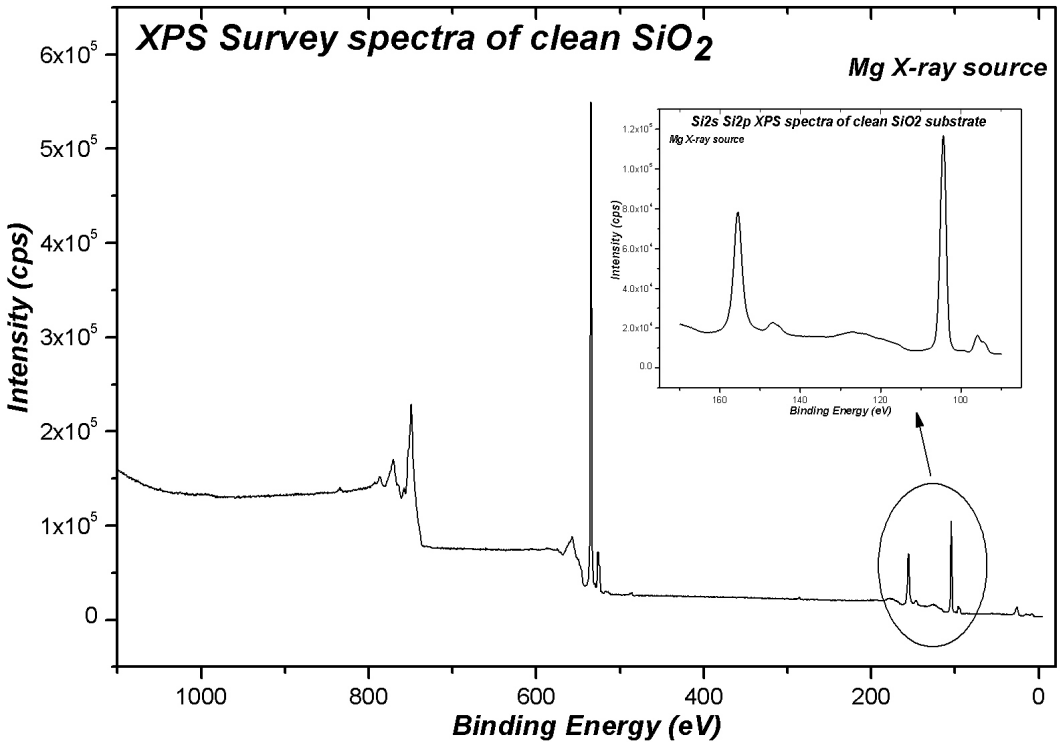

Fig III.7. Survey XPS spectra of SiO_2.

By XPS survey scan of the SiO_2 used as substrate for, no contamination was detected.

The ***alumina*** substrate was an ultra thin film about 25 Å thick grown by thermal oxidation of a pure polycrystalline 99.994% (0.004% Si, 0.001% Fe and 0.001% Cu) Al foil, provided by *Tokyo Aluminum Company,* at 350ºC for 30 min.

The aluminum foil was previously cleaned by Ar ion bombardment, for 60 minutes in $2x10^{-5}$ mbar Ar pressure, with ion beam energy of 1.0 KeV. The discharge voltage was 500 V and the discharge current was 4.5 mA, conditions in which the sample ion current reached approximately 18 μA value.

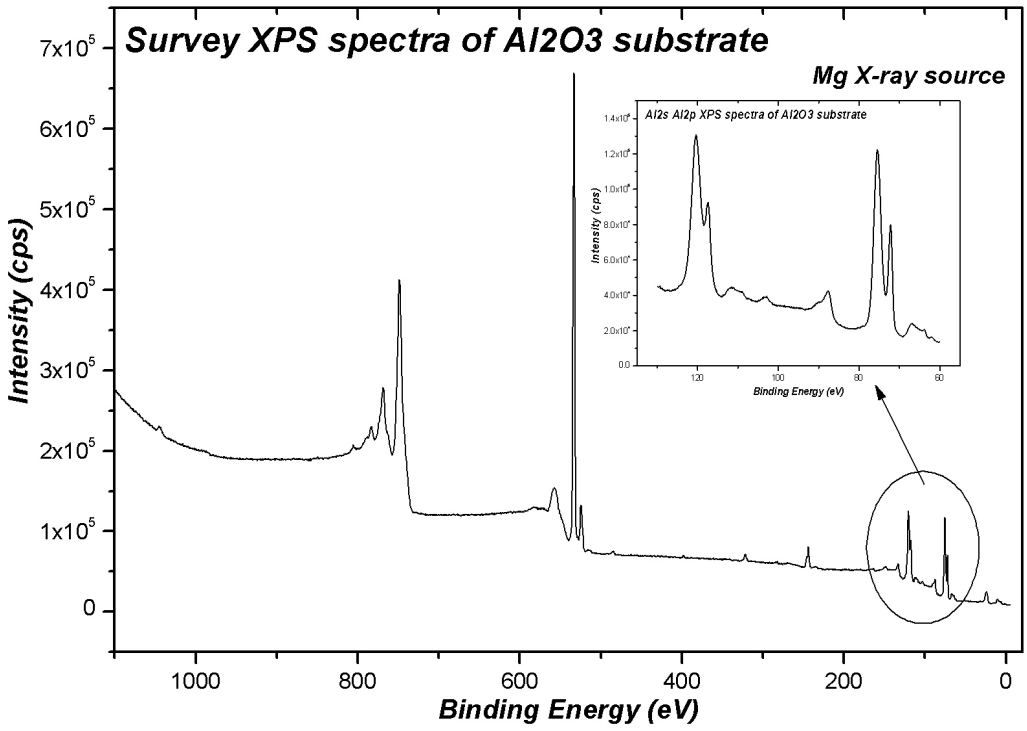

Fig.III.8. Survey XPS spectra of Al_2O_3.

No significant contamination of Al_2O_3 was found by XPS analysis, as shown in the figure III.8.

The ***magnesia*** substrate was obtained by reactive evaporation of 99.99% Mg, provided by *Googfellows Materials*, in $2x10^{-5}$ mbarr oxygen atmosphere, on a p-doped Si (111) wafer. The magnesium was evaporated using a Knudsen cell evaporator for vacuum.

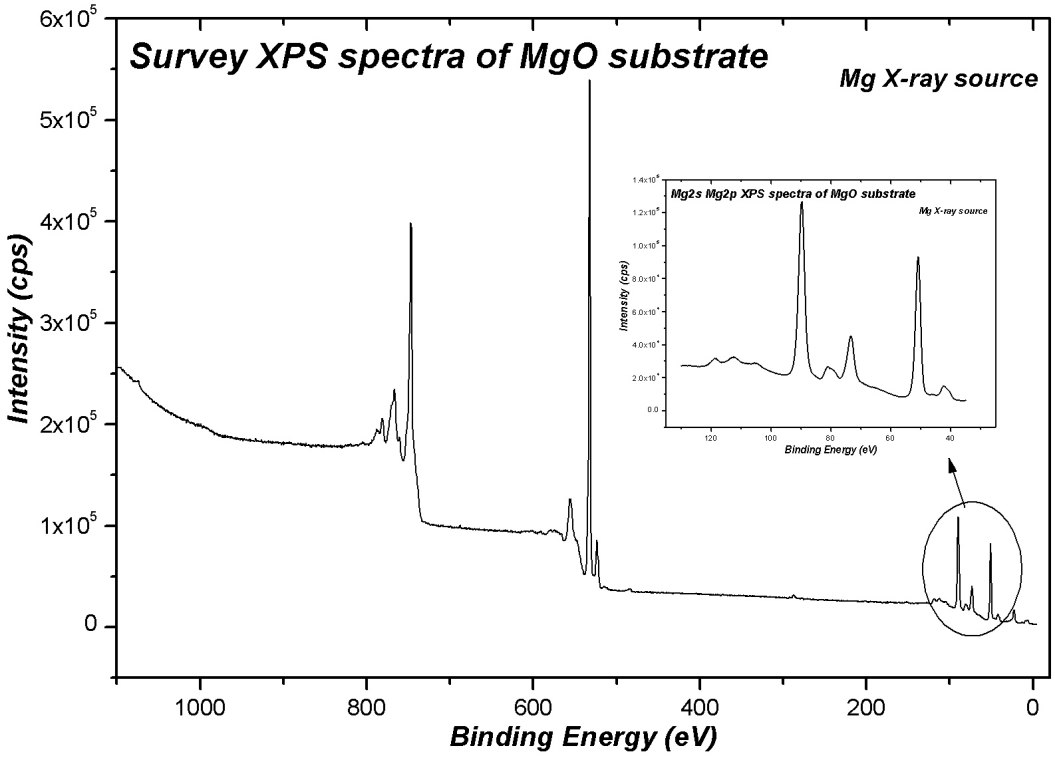

Fig.III.9. Survey XPS spectra of MgO.

The quality of the substrates was previously checked by XPS, and does not present any appreciable contamination.

As it can be observed in the XPS spectra, the SiO_2 and MgO are thick enough to "*hide*" the Si XPS signal, but in the case of Al_2O_3 the oxidized aluminum is not so thick, thus the Al *2s-2p* XPS spectra present also a metallic Al component.

AFM images of these substrates are shown in figure III.10. The silicon oxide shows flat areas with a few contaminants, some of them, prior to the oxide growth: produce a small depression in the oxide around. The roughness is less than half a nanometer as expected from the oxidation of a polished Si single crystal. The Al_2O_3 oxide has an intermediate roughness of 39 nm, which is consistent with the roughness of an oxidized Al polycrystalline sheet. The largest value of the rms roughness corresponds to the MgO substrate (165 nm). The

relatively large roughness for the MgO substrate is produced by the formation of faceted crystallites of about 1 μm size.

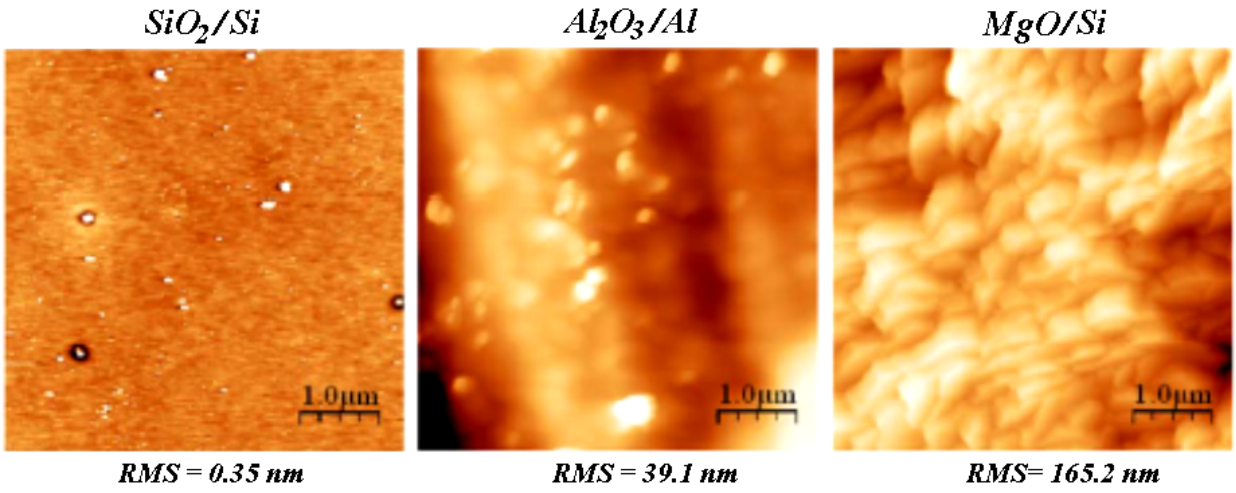

Fig.III.10. AFM topographic images (5x5 μm^2) of the different oxide surfaces, measured in dynamic mode (tapping). RMS (root mean square) roughness values are given for comparison.

III.3. EXPERIMENTAL SYSTEMS FOR MEASUREMENTS

III.3.1. In-house XPS Spectrometer

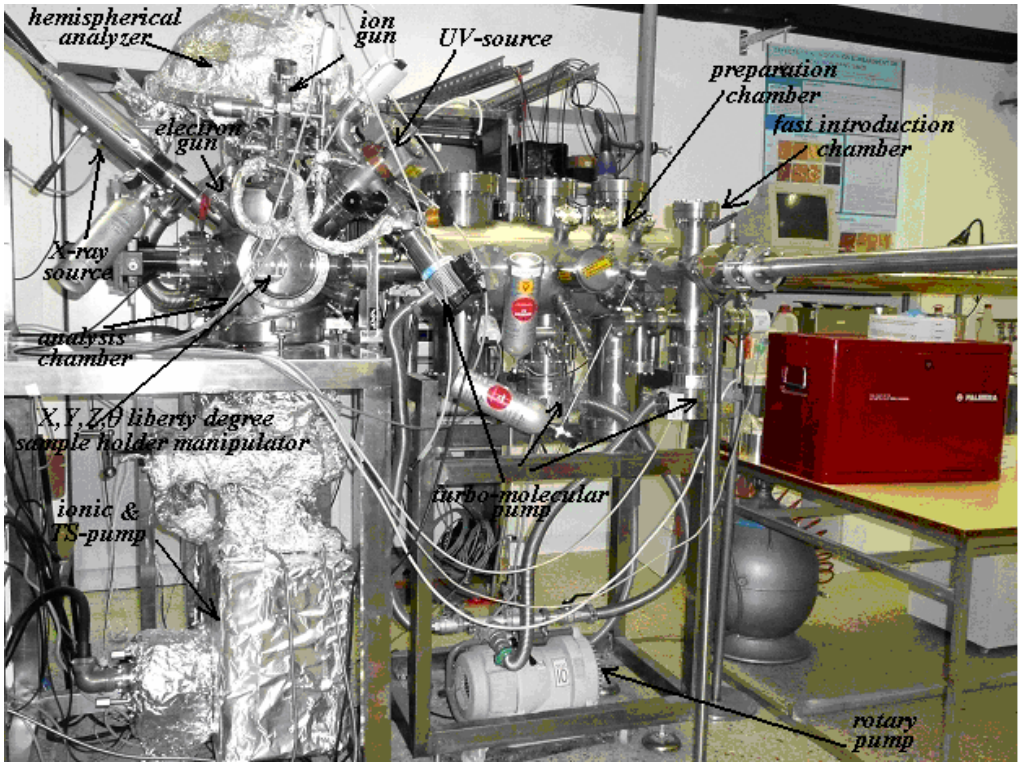

Fig.III.11. CLAM-4 Analysis system from LRN-UAM.

In the picture above, the experimental system used in preparation and analysis sample processes from *Laboratorio de Recubrimientos y Nanoestructuras of University Autónoma de Madrid, Spain,* is illustrated.

III.3.1.1. Transfer system

The system consists of three vacuum chambers: fast introduction, preparation and analysis.

The fast introduction vacuum chamber is a small volume chamber connected to a *Pfeiffer* turbo-molecular pump (70 L/min speed pump), in order to get low pressures of 10^{-7} - 10^{-8} mbar in short time.

An extremity of an outside magnetic manipulating bare is prepared for loading the sample holder in here. When the pressure gets high vacuum values, the UHV valve is opened and the sample can get now into the preparation chamber.

The preparation chamber is pumped down by a *Varian* turbo-molecular pump (speed pump 300L/min), and the usual pressure is in the 10^{-9} mbar range.

Several evaporators, a heating system, an ion gun and several introduction leak valves are mounted on this chamber, allowing cleaning processes, materials evaporation, oxidation and much other sample operations.

III.3.1.2. Measuring system

The analysis chamber is maintained in the 10^{-10} mbar pressures range by a titanium sublimation – ionic combined pump. This chamber is equipped with X-ray and UV-sources, ion and electron guns and an electron analyzer.

The ***X-ray Source*** is a twin (Al/Mg) anode; model XR32E2 provided by *VG Microtech*. This model works at 15 KV providing a power of 300/400 watts. In the standard configuration, the anode is coated on one side with aluminium giving an X-ray line of 1486.6 eV and magnesium at the other side, giving a $K_{\alpha 1,2}$ line of 1253.6 eV. The $K_{\alpha 3,4}$ and K_{β} lines are much less intense than $K_{\alpha 1,2}$ and are almost totally absorbed by an aluminium foil window. A count rate of 900 Kcps with Mg K_{α} radiation for the Ag *3d*5/2 core level peak is obtained.

The ***CLAM4*** MCD analyzer system is provided by *Thermo VG Scientific* and is an 150 mm true hemispherical sector analyzer equipped with four sets of variable slits 0.5 mm, 1 mm, 2 mm and 5 mm. The working distance recommended for this model is 39 mm. The

energy range is 0 to 2500 eV and pass energy range from 0 to 400 eV: 200, 100, 50, 20, 10, 5 and 2 eV, with a retard ratio values: 1, 2, 4, 10, 40 and 100.

All the measurements have been done with a 20 eV pass energy, except the surveys spectra were the pass energy was set at 50 eV. The energy step was 0.1 eV in all the measurements; except the surveys spectra were 0.5 eV energy step was chosen.

III.3.2. PES-XAS measurements at BESSY II

The Berliner Elektronenspeicherring-Gesellschaft für Synchrotronstrahlung (BESSY) operates the only German 3rd generation synchrotron radiation facility.

The storage ring ***BESSY II*** provides ultra-bright photon beams from the long wavelength terahertz region to hard X-rays with complete control of the polarization of the radiation and energy range. Before injection in the main storage-ring, the beam is accelerated over a microtron and a synchrotron to its final energy of 1.7 GeV, with a brilliance of 10^{18} photons/(sec·mm^2·mrad^2 ·0.1% bandwidth) providing photon energies ranging from 10 to 2000 eV from undulators and wigglers[5].

PM 4 is a dipole beam line with a plane grating (PGM) monochromator which provide a photon range energy from 25 to 1800 eV, horizontal polarized radiation, with a flux of $1x10^9 – 1x10^{10}$ photons/(sec·mm^2·mrad^2) with 1.5 mrad horizontal divergence and 1 mrad vertical divergence. The energy resolution can reach a minimum value of 64 eV.

The ***experimental station*** used was MUSTANG, (**M**ulti **U**ser **ST**age for **ANG**ular resolved photoemission), which is a two chamber system with a preparation and an analysis chamber to perform photoemission spectroscopies. The station is equipped with the Phoibos 150 analyser by Specs and the sample transfer system by *Omicron*.

The system is evacuated by a 500 l/s and a 70 l/s water-cooled turbo-molecular pump as pre-vacuum pump. Additionally, the analysis chamber has a 160 l/s ion pump and a titanium sublimation pump with a cryoshroud. The base pressure is better than $2x10^{-10}$ mbar.

Fig. III.12. Illustration of MUSTANG end-station of PM 4 beam-line at BESSY II storage ring.

The maximum achievable temperature in the preparation chamber is 800°C (1073 K). Since the heater is fitted with cooling accessory, the maximum achievable temperature in the analysis chamber is limited to 500°C. To determine the temperature is used a non-magnetic Nicrosil/Nisil (Type N) thermocouple.

The Electron Analyzer

The detector is a 180° hemispherical energy analyzer with a mean radius of 150 mm; nine single channel electron multipliers are arranged 45° geometry to the incident beam. With this it can be performed angular and spatially resolved studies with an energy resolution down to 5 meV, an angular resolution down to ± 0.05° and small spot analysis down to 100 μm resolution.

The ***XAS measurements*** at PM4 were done in total electron yield detection mode at normal and grazing incidences to take advantage of the linear polarization of the synchrotron light in order to enhance transitions towards planes parallel to the surface, it means, towards atoms in the direction to the surface normal (surface enhancement). The estimated overall resolution of the plane grating monochromator (PM4) was better than 100 meV at the O 1s edge (530 eV). The spectra were normalized to the I_o current coming from a fresh gold sample, in order to correct the spectra from the contamination of the optical elements and beam losses.

III.3.3. NEXAFS measurements at ESRF and BESSY II

In 1988, twelve European countries joined forces to create the synchrotron in Grenoble. Since then, seven more countries have joined the group. Together they create the indispensable synergy needed, the ***ESRF*** (**E**uropean **S**ynchrotron **R**adiation **F**acilities), to carry out advanced scientific research.

The main parameters of the electron beam in the storage ring are summarized in the table bellow[6]:

Table III.1. Main parameters of ESRF storage ring.

Energy	6.03 GeV
Maximum Current	200 mA
Horizontal Emittance	4 nm
Vertical Emittance (*minimum achieved)	0.025 (0.010*) nm
Coupling (*minimum achieved)	0.6 (0.25*)%
Revolution frequency	355 kHz
Number of bunches	1 to 992
Time between bunches	2816 to 2.82 ns

The radiation brilliance can reach 3.7×10^{21} photons/(sec·mm^2·mrad^2), providing photon energies ranging from 3 to 74 KeV.

The ***BM25 Sp-line*** was built through a coordinated project with the participation of different groups. The project coordination for the beam-line construction was led by the ICMM-CSIC. The construction project has been regulated, followed, and supported by the Spanish Goverment through its Science and Technology Offices and Ministries OCYT, MCYT and MEC.

For ranging the photon energy up to 15 Kev a ***double crystal monochromator*** is used: DLC pseudo channel-cut type, with two Si(111) crystals in the (-n,+n) configuration moved together by a simple goniometer circle. The sagital dynamical focusing at the different sample positions is achieved by a novel bender that curves a multi-rips thin Si(111) crystal (ESRF-model).

The experimental end station for *in-situ* NEXAFS experiment is illustrated in the picture below. Due to the X-ray windows material the final pressure was $2x10^{-6}$ mbar obtained with a 300 l/min turbo-molecular pump together with a dry scroll primary pump.

Fig. III.13. NEXAFS end station of BM25 SpLine, branch A at ESRF.

For *in-situ* and *ex-situ* fluorescence measurements a single Si(Li) element liquid nitrogen cooled detector was used.

For Ni K absorption edge (8.33333 KeV) the photon energy was varied between 8.2 and 9.0 KeV in constant K step.

In both cases the spectra were normalized to the I_o current measured with an ionization chamber.

The NEXAFS measurements performed at ***KMC-2*** of BESSY II were also done in *ex-situ* conditions. The KMC-2 beam-line has a KMC (Dip-09-1) monochromator, which provide a horizontal polarized radiation with a flux of 10^7 - 10^{10} photons/(sec·mm^2·mrad^2), in

an energy range from 5 to 14 KeV, with a resolution of 5000 eV. Both, the horizontal and vertical divergences, are 0.1 mrad.

III.3.4. HAXPES measurements at ESRF

As stated in chapter II the HAXPES measurements requires two principal conditions: one is a high photon flux, for compensate the low value of the photo-ionization cross section in this energy range and, the second one, is the electron analyzer, which should be able to handle electrons of high kinetic energy. Both of these requirements are complete at BM25 SpLine at ESRF.

The X-ray Source

The set-up is placed on branch B of SpLine at the ESRF. The bending magnet D25 of the ESRF provides the X-rays for the SpLine. Branch B is llocated on the hard edge (-10.5 mrad) of the bending magnet accepting a horizontal angular divergence of 2 mrad. The energy range covered is 5–45 keV. Two Si (111) crystals placed at ~30m from the source serve as a double-crystal monochromator, which gives a wavelength resolution of $\Delta\lambda/\lambda = 1{,}5 \times 10^{-4}$. At the critical energy of 20.6 keV a flux of 10^{13} photons/s can be achieved (see figure III.14), that is well adapted for the HAXPES requirements. The first crystal is water cooled in order to remove the heat load caused by the beam, while the second is kept at room temperature. Horizontal focusing is achieved by the second monochromator crystal through sagittal cylindrical bending. For more details see reference[7].

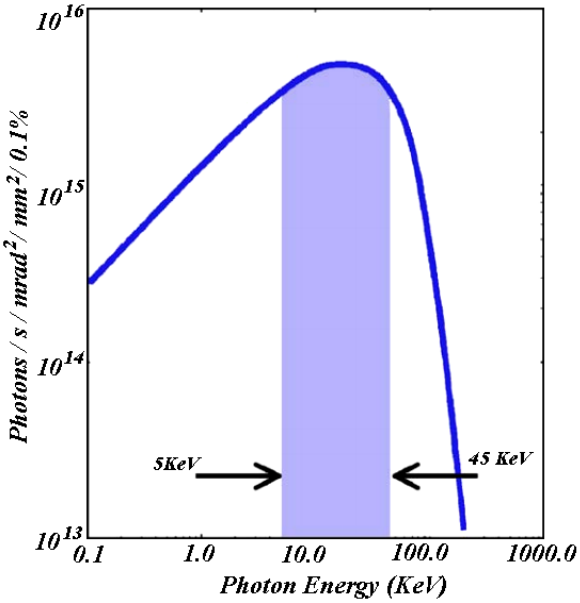

Fig. III.14. Radiation brilliance corresponding to SpLine branch B. In the beamline energy range (shadowed region) the brilliance achieved is larger than 10^{15} Photons/s/mrad^2/mm^2/0.1%bw at 200mA electron current.

The electron analyzer[8]

A schematic layout and a picture of the analyzer CSA300HV are shown in figure III.15. The analyzer is a sector of a cylindrical mirror analyzer with a five-element retarding zoom lens system. The lens is operated at fixed spatial magnification (M=1..60) and varying retardation ratios $R=E_{kin}/E_p=0.01..1500$. The internal and external radii are 32mm and 130mm, and the entrance to exit slit distance is 300 mm. The entrance central angle is 45° and the total deflection angle of 90°. The sample-to-lens distance is 50mm and the lens and analyzer angular acceptances are ±15° and ±5.4°, respectively. Due to the large dispersion values[9] the CSA300HV has a reduce dimension and weight of ~30 kg only. The fully computer-controlled high voltage power supply with a stability <30meV can be operate continuously from few eV to 15 keV without changing the electronics setup.

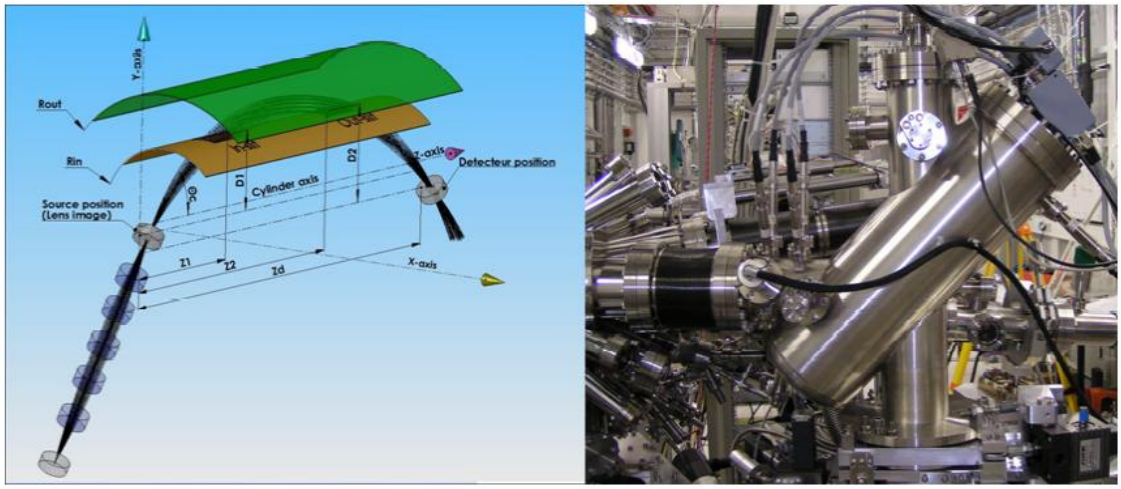

Fig. III.15. Schematic optical layout (left) and a picture (right) of the developed CSA300HV analyzer.

III.3.5. AFM Imaging

The AFM study was performed in atmospheric condition (pressure and temperatures). The selected stages of the NiO/HOPG, NiO/oxides, and the oxides substrates, were analyzed in the CSIC (Consejo Superior de Investigaciones Científicas), ICMM (Instituto de Ciencias de Materiales Madrid), *Grupo de Estructura de Sistemas Nanometricas*, with a ***Nanotec*** microscope and software.

The samples were measured in dynamic mode; *tapping*, with small amplitude, and some images were acquired in *jumping* mode.

The county level used was a PPP-FM type, of 2.8 N/m force and a resonance frequency of 75 KHz.

REFERENCES:

[1] National Institute of Standard Technologies.

[2] I. Horcas, R. Fernández, J.M. Gómez-Rodríguez, J. Colchero, J. Gómez-Herrero, and A.M. Baró, Rev. Sci. Instrum. 78, 013705 (2007).

[3] L. Soriano, G. G. Fuentes, C. Quirós, J. F. Trigo, J. M. Sanz, P. R. Bressler, and A. R. González-Elipe, Langmuir **16**, 7066, 2000.

[4] M. Sánchez-Agudo, L. Soriano, C. Quirós, M. Abbate, L. Roca, J. Avila, and J. M. Sanz, Langmuir **17**, 7339, 2001.

[5] www.bessy.de

[6] www.esrf.eu

[7] J.R. Rubio-Zuazo, G.R. Castro / Nuclear Instruments and Methods in Physics Research A 547 (2005) 64–72.

[8] J.Rubio-Zuazo, M.Escher, M.Merkel and G.R.Castro, Journal of Physics: Conference Series 100 (2008) 072032.

[9] Risley J.S, Rev. Sci. Instrum. 43 (1971) 95; Sar-El H.Z, Rev. Sci. Instrum. 38 (1967) 1210; Sar-El H.Z, Rev. Sci. Instrum. 41 (1970) 561.

Chapter IV

SURFACE EFFECTS IN NiO

IV.1. INTRODUCTION

The aim of this chapter is the study of the electronic structure of the NiO deposits during the growth process of NiO on HOPG, paying special attention to the early stages of growth.

Previous AFM results on NiO/HOPG had identified the early stages of growth as nanometric islands[1]. XPS and XAS measurements on this system showed that the shape of Ni *2p* XPS and O1s XAS spectra of the NiO nanostructures had strong resemblance with similar spectra of 3-5 nm NiO nanoparticles. The interesting properties of such nanoparticles and their anomalous shape of the Ni *2p* and O *1s* XPS spectra gives a strong motivation to study this interesting system.

In this chapter, first of all, the morphological properties of the NiO growth are studied by quantitative analysis of the XPS background (QUASES) and AFM imaging. In the second part, the electronic structure of nickel oxide grown on HOPG is studied by X-ray absorption spectroscopy (XAS). These spectra are interpreted by theoretical calculations. Surface effects are clearly observed by means of O1s XAS for the very early stages of growth.

Then, the surface effects of NiO are studied by XPS and are also supported by theoretical calculation (cluster approach).

In order to corroborate the surface effects observed by XPS, HArd X-ray PhotoEmission Spectroscopy (HAXPES) measurements of the Ni1s and Ni *2p*3/2 core levels of a NiO (100) single crystal have been performed. It is worthy to note that for the first time, these core levels have been measured at high energies. In particular, the Ni1s core level has not been measured using photoemission up to now.

Also the XPS study of the whole NiO/HOPG growth process is presented at the end of this chapter, as a clearly example of the surface effects in NiO.

IV.2. MORPHOLOGICAL STUDY OF THE GROWTH OF NiO ON HOPG

As described in chapter II, the quantitative analysis of surfaces by electron spectroscopy (QUASES) technique, developed by Tougaard *et al*[2], is able to describe the way of growth of a material on a substrate if successive XPS spectra are measured.

By AFM imaging and its analysis tools, the morphology and the way in which the NiO grows on HOPG can be directly inferred.

Using these two analysis techniques in the NiO growth on HOPG, qualitative and quantitative description of the process can be done.

The samples were growth in the preparation chamber of XPS spectrometer. The thickness was firstly estimated from the relative intensity ratio of the Ni *2p* and C *1s* XPS peaks, then, the samples were extracted from vacuum to proceed to the AFM analysis.

IV.2.1. QUANTITATIVE ANALYSIS BY MEANS OF XPS INELASTIC PEAK SHAPE (QUASES)

Two regions of the XPS survey spectra of the NiO growth on HOPG, were used to analyze its way of growth by QUASES: one was the Ni *2p* region and the second was a part of the Ni Auger LVV. The use of these two regions gives consistency to this study.

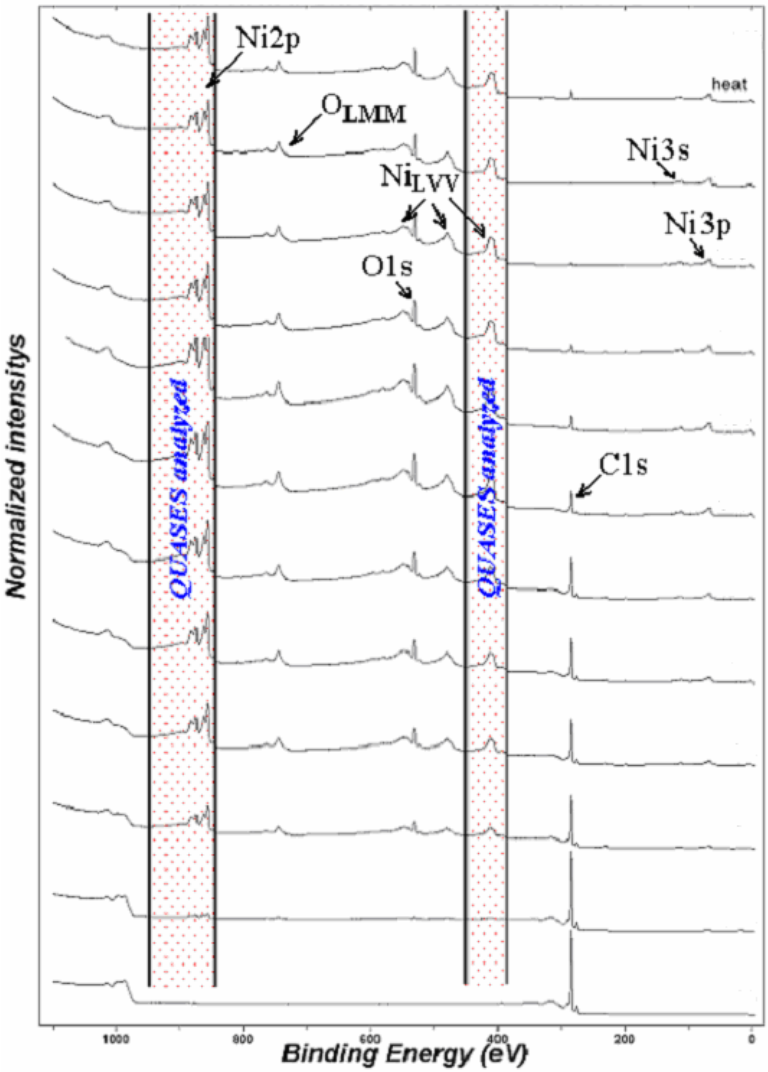

Fig.IV.1. Survey spectra of NiO on HOPG for different stages of growth. Shadowed regions were used in QUASES.

In figure IV.1 the XPS survey spectra of the growth of NiO on HOPG are represented. The XPS peaks and Auger structures are also indicated here.

Table IV.1 contain the values of the main parameters of the growth obtained from QUASES analysis, i.e. islands height, coverage percentage and equivalent thicknesses, for the analyzed regions.

Table IV.1. Summary of the values of the main parameters obtained by QUASES of NiO/HOPG growth:

NiO on **HOPG**						
Evaporation time (min)	Ni LVV Auger analyzed			Ni2p analyzed		
	Island height (Å)	Coverage (%)	Equivalent thickness (Å)	Island height (Å)	Coverage (%)	Equivalent thickness (Å)
10	-	-	-	-	-	-
40	26	7.5	1.95	27	9.6	2.59
120	32	18	5.76	38	20.8	7.9
320	35	32.5	11.3	33	37.2	12.2
640	45	45.6	20.5	45	51.5	23.1
870	57	53.3	30.3	58	58.4	33.8
975	97	75.4	73.1	97	80.9	78.4

Representing these values (figure IV.2), the way in which the NiO "*seats"* on the HOPG, can be described. It can be seen that for the early stages of growth, NiO forms very small islands with heights around 26 Å covering about 8% of the substrate surface. For further depositions, up to 10 Å equivalent thickness, NiO tends to cover more substrate surface. In this range of coverage, up to 40% of the surface, the NiO islands height increases slowly from 26 to 40 Å. Then, further depositions produce a strong increase of the islands height. The full coverage can be approximated by extrapolation of the obtained data, and

should have place for about 50 deposited NiO monolayers. It is worthy to remind here that the QUASES has its limitation in this range of material amount deposited on the substrate.

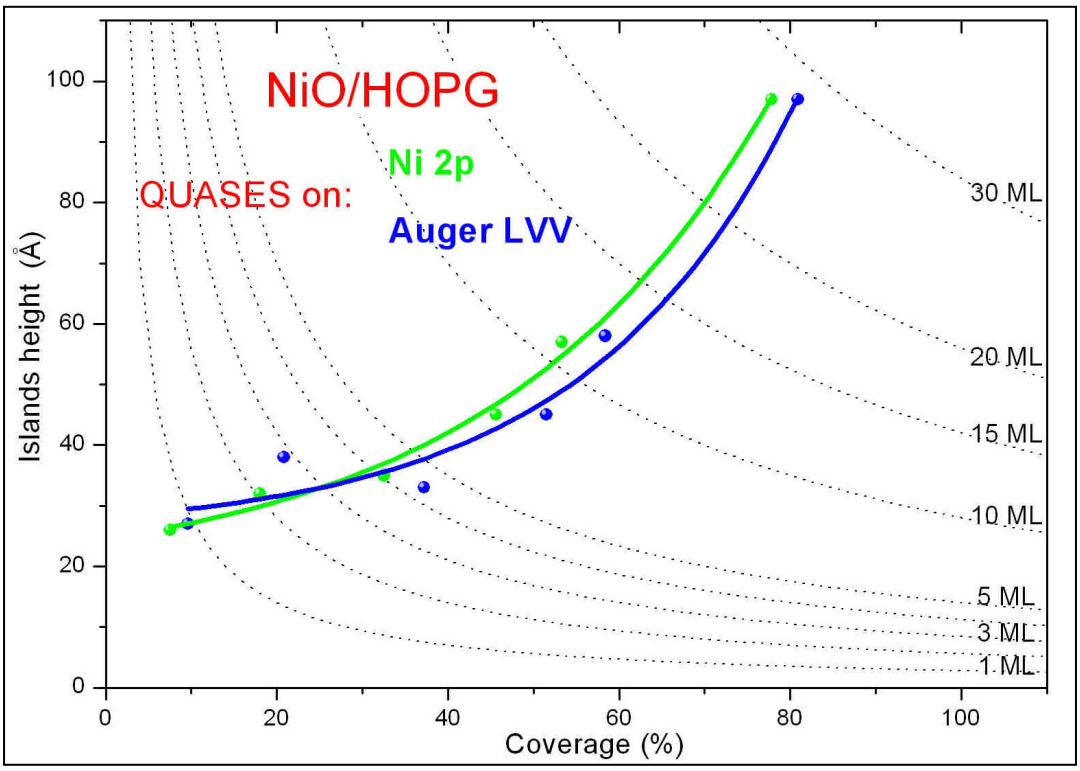

Fig.IV.2. The growth of NiO on HOPG: average particle height versus surface coverage, green and blue line are results given by quantitative analysis by means of XPS inelastic peak shape of Ni2p and Auger LVV respectively, using QUASES software. Dashed lines indicate equivalent amount of NiO deposited material.

In figure IV.2, the average height of the NiO aggregate versus surface coverage, is represented. The good agreement between the values obtained by studying the background of the Ni *2p* XPS spectra (green curve), and that of the Ni LVV Auger structure (blue curve), is evident.

It is difficult to assign the type of way of growth of NiO on HOPG to any of the typical models of growth. According to the results obtained by QUASES, it is clear the formation of small (nanometric in heights) islands. Coalescence is reached for thicknesses range out of the QUASES method limits; therefore, the way of growth is by islands up to 60-80 Å.

IV.2.2. STUDY OF THE GROWTH OF NiO ON HOPG BY AFM

As already explained in chapter II of this work, the atomic force microscope (AFM) is a very high-resolution type of scanning probe microscope, with demonstrated resolution of fractions of a nanometer, which can be easily used on a wide range of materials.

In general, AFM can be used for qualitative and quantitative description of the way of growth. However, in this case, the quantitative analysis is quite limited by of the very low stability of the NiO structures deposited on the HOPG.

As it is explained in chapter II, there are several measuring methods in which an atomic force microscope can be used. The less recommended mode to measure this unstable system is the contact mode. In figure IV. 3 the tip effect of a contact mode imaging of NiO deposited on graphite is shown.

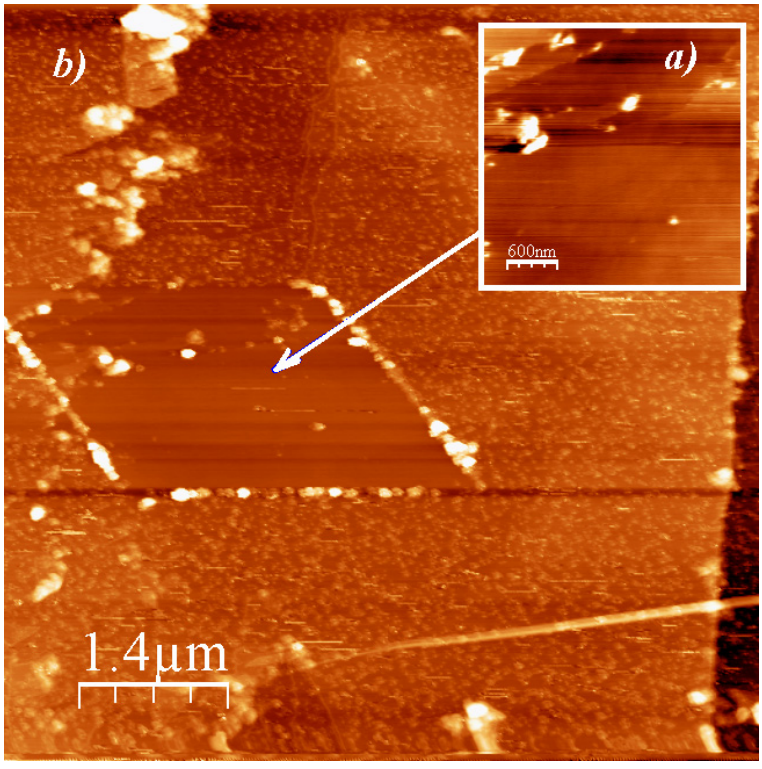

Fig.IV.3. Tip effect of the contact imaging mode of NiO on HOPG: a) 3x3 µm contact mode and b) 7x7 µm non-contact mode AFM image of 0.8 Å NiO/HOPG.

It can be observed in figure IV.3 *b* that the area previously measured in contact mode is NiO free except on the graphite defective areas, where the NiO–HOPG interaction forces

are higher than the NiO–tip adhesion forces. On the borders of the contact mode measured area, the NiO accumulation can be seen. The shape of the 3x3 μm area in the dynamic mode measured 7x7 μm area, is explained in terms of measuring time convolution with the thermal drift.

It is very important to mention here that even in (taping) dynamic mode imaging these effects are still presents, but not as important as in contact mode. For this reason the values given by this analysis, at least the diameters of the NiO structures, are only estimations. It was also found that, with small cantilever amplitudes, more realistic images were obtained in the case of this system.

Starting with very low values for the amount of NiO material deposited on graphite, a detailed morphological AFM study was performed on this system. In figure IV.4 various stages on the NiO growth on HOPG as a function of the deposited material are presented.

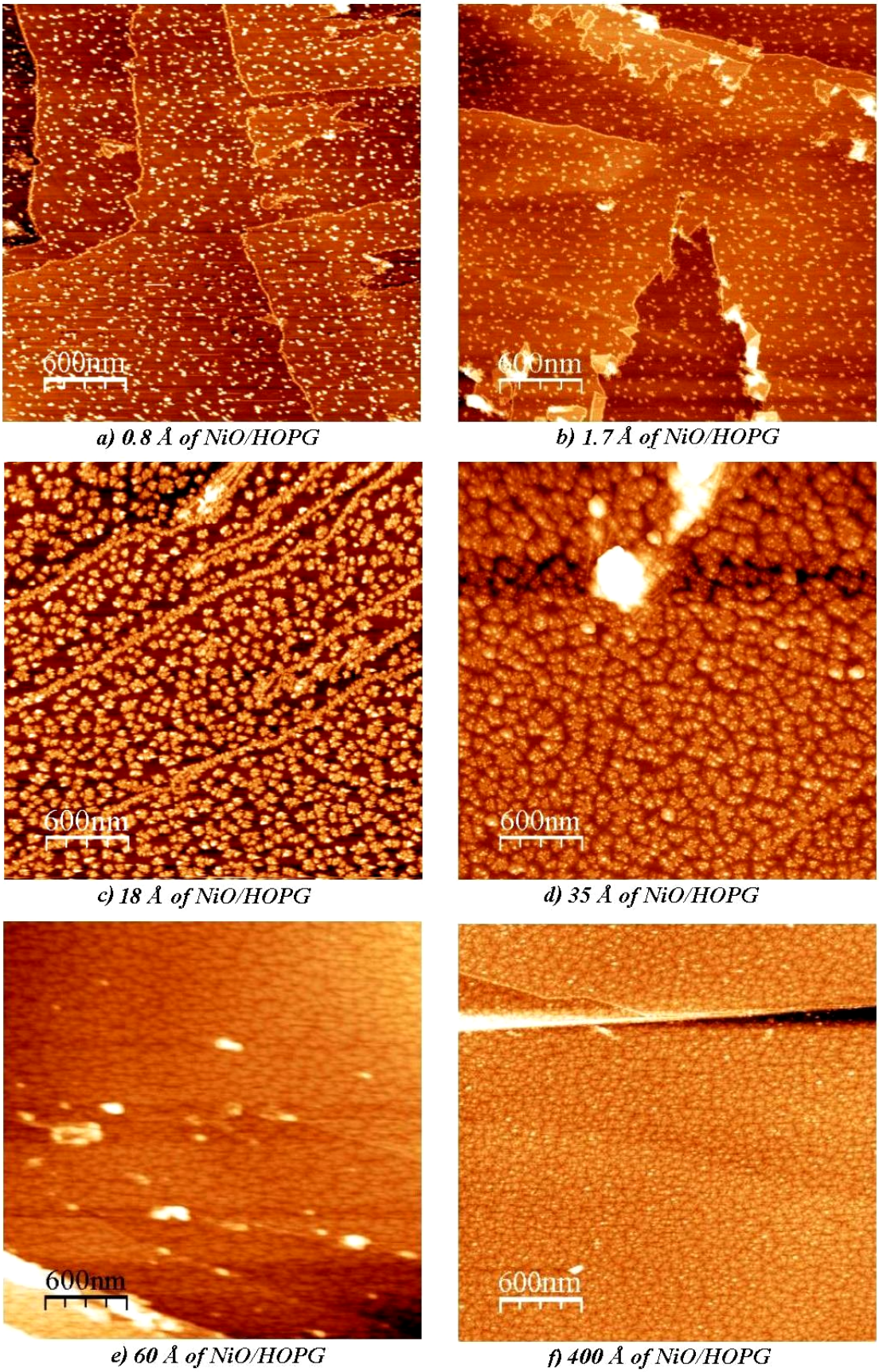

a) 0.8 Å of NiO/HOPG *b) 1.7 Å of NiO/HOPG*

c) 18 Å of NiO/HOPG *d) 35 Å of NiO/HOPG*

e) 60 Å of NiO/HOPG *f) 400 Å of NiO/HOPG*

Fig.IV.4. 3x3 μm AFM images of various stages of the NiO growth on HOPG.

At a first look over the AFM images of the studied stages it can be concluded that NiO starts its growth on HOPG filling the graphite steps and by forming nanometric aggregates on the graphite terraces. Further NiO deposition leads to the accumulations of NiO in the graphite steps and to increase the diameter of the NiO nanoparticles *seated* on the graphite terraces, rather than their heights.

These structures keep rising with the deposited NiO amount, and the coalescence is obtained for about 60 Å equivalent thickness of NiO. From this stage no major difference is observed untill the annealed stage, shown in figure IV.5, where the average particle diameters are higher than those of the non-heated stage.

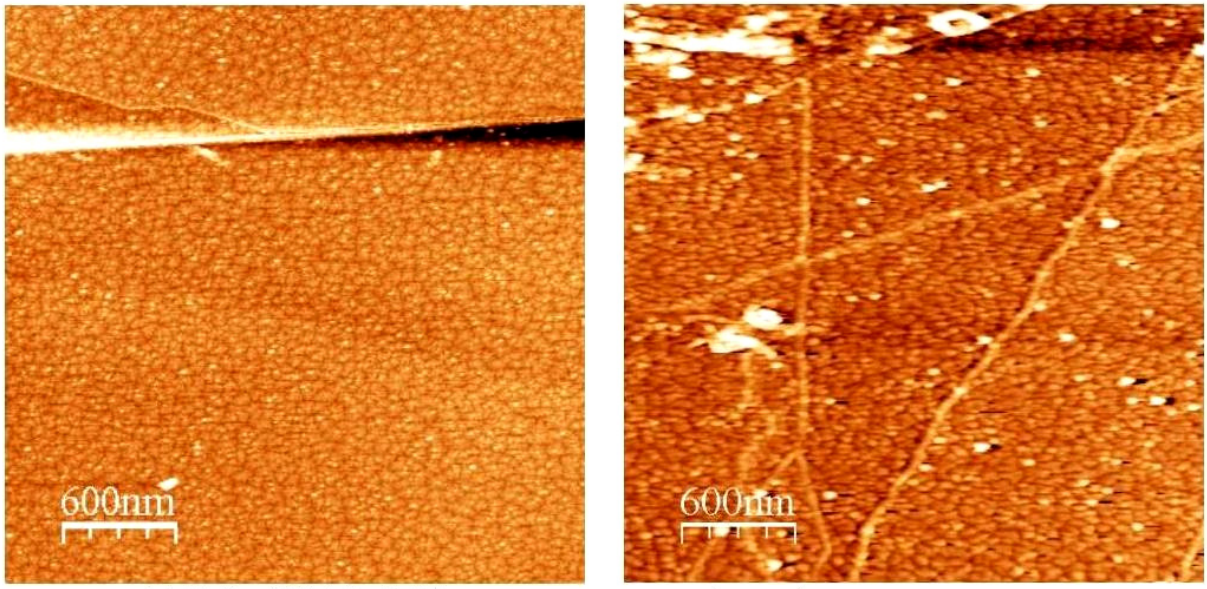

a) 400 Å of NiO/HOPG ***b) 400 Å of annealed NiO/HOPG***

Fig. IV.5. 3x3 μm AFM images of: a) 400 Å of NiO deposited on HOPG and b) annealed 400 Å of NiO deposited on HOPG.

In the following, the AFM images of figure IV.4 and IV.5 will be analyzed and interpreted separately.

Figure IV.4 *a*: shows the AFM image of 0.8 Å equivalent thickness of NiO deposited on HOPG. Here the terraces and the steps of the graphite can be clearly observed.

At a first glance it is seen that NiO is deposited in the graphite steps. A topographic profile analysis was performed in different steps area, as shown in figure IV.6.

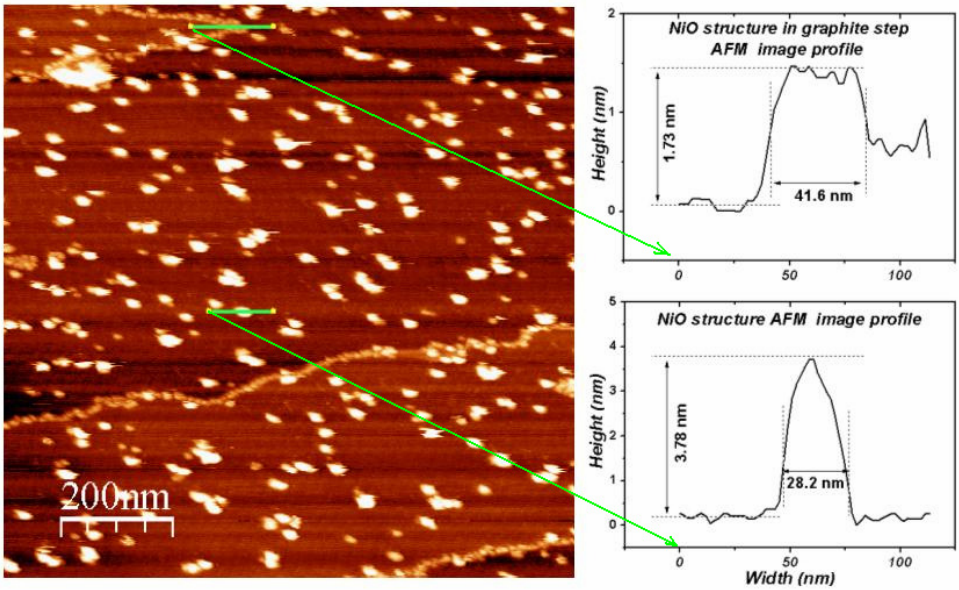

Fig.IV.6. Example of 1x1 μm AFM topographic profile analyze of 0.8 Å equivalent thickness of NiO on HOPG.

The second AFM image profile presented in figure IV.6 is attributed to a moved NiO aggregate. This affirmation is supported by the fact that, in the graphite steps, the NiO aggregates are much smaller than these other aggregates, having the same dimension as the non-moved ones. In figure IV. 7, this trend is demonstrated by an AFM image of the structures formed on the graphite terraces and in its steps, along with the topographic profiles of these structures.

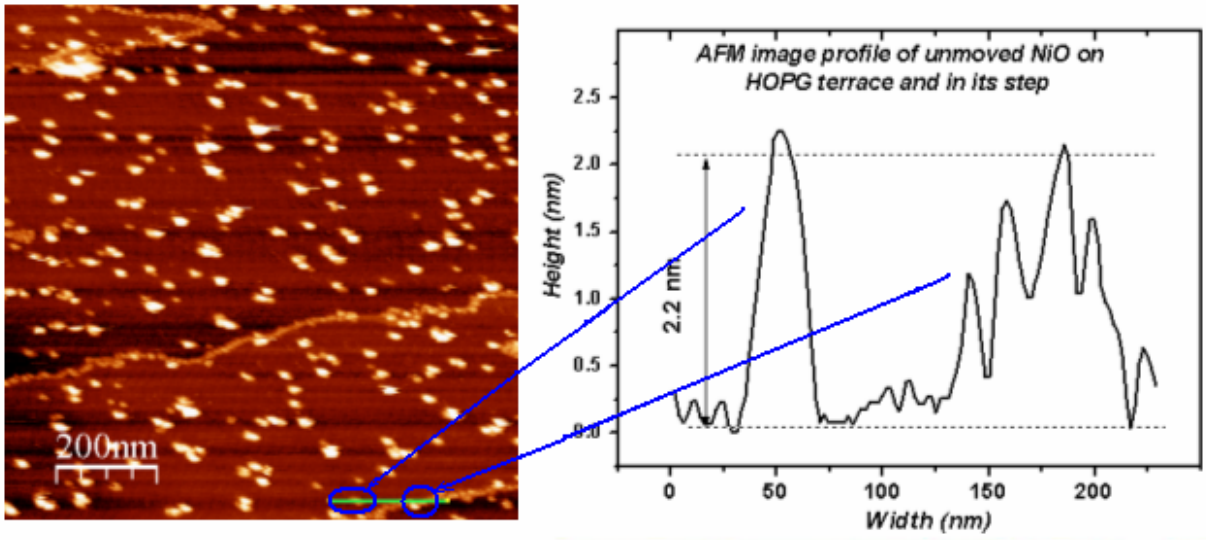

Fig.IV.7. 1x1 μm AFM image of NiO aggregates deposited on the graphite terraces and step, together with its topographic profile.

It can be seen that both, the NiO structure deposited on the graphite terrace and the NiO deposited in the HOPG step are having the same height and, even more, the same diameter range, which make believable the affirmation that there remain, on the terraces, NiO structures unmoved by the microscope's tip during the measurements (in optimal conditions).

Flooding analysis, presented in figure IV. 8 of this stage gives values like 5.11 % of surface covered with NiO structures of 1.4 nm maximum heights, but these values are just estimations, as was already stated before.

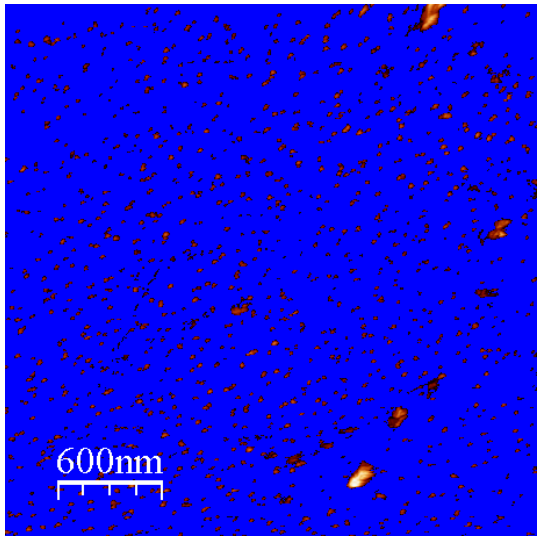

Fig.IV.8. Example of flooding analysis of this stage of the NiO growth on HOPG.

From the analysis of this stage it can be concluded:

- HOPG presents steps with heights between 2 and 10 graphite planes (7-33.5 Å);
- NiO seats along the graphite steps, following their shapes and also on the graphite terraces;
- The RMS of the roughness is practically given by the graphite steps if exists in the measured area, going from 1.53 nm, in a missing step area, up to 3.35 nm;
- The average NiO particle maximum height is 1.4 nm and the average width is 25 nm.

Figure IV.4 ***b*** corresponding to an equivalent thickness of NiO of 1.7 Å, shows that NiO already complete the filling of the graphite steps and also the diameters of the NiO structures formed on terraces starts to increase. The height of NiO aggregates are maintained within the same range.

In figure IV.9 is presented a 1x1 μm AFM image and two topographic profile analysis for different areas: filled step and NiO aggregate on terrace. It seems that the measurements conditions were better, and no NiO aggregates were moved during the measurements.

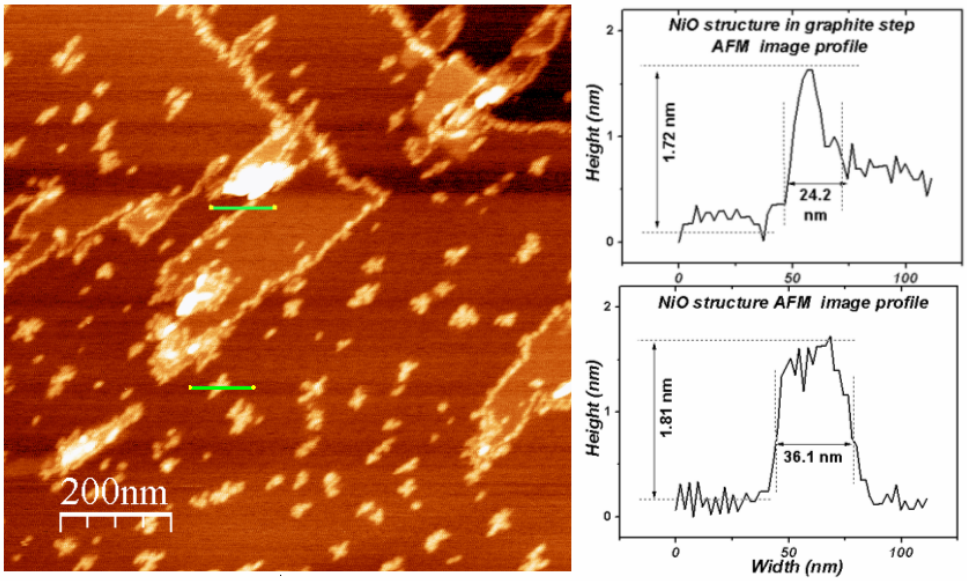

Fig.IV.9. 1x1μm AFM image of 1.7 Å equivalent thickness stage of NiO on graphite and two topographic profiles analyzed areas.

If in the previous, stage the average diameter of the non-moved NiO structure was about 20-25 nm, in this case, the NiO aggregates reach an average diameter of 40 nm. In turn, the heights of the NiO structures looks to maintain the same range values.

The flood analysis gives values of 10.35% area covered by islands with maximum heights of 1.6 nm.

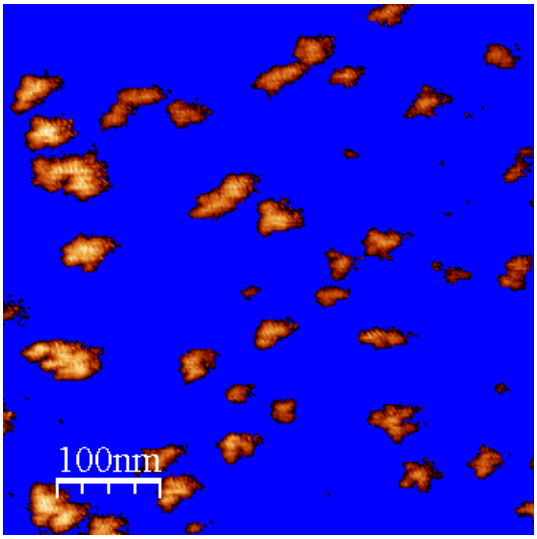

Fig.IV.10. Flood analysis of 1x1 μm AMF image area of 1.7 Å equivalent thickness of NiO/HOPG

Analyzing more regions of this sample, about this stage of growth it can be concluded:

- No graphite step remains unfilled with NiO;
- The height of the NiO structures is maintained in the same ranges, in perfect agreement with the QUASES obtained values;
- The substrate surface covered area is proportional to the amount of NiO deposited on it, as already anticipated by QUASES analysis;
- The average NiO particle height is 1.6 nm and the average width is 40 nm.

Figure IV.4 c corresponds to the 18 Å equivalent thickness of NiO deposited on HOPG. This stage of growth is characterized by the formation of NiO aggregates with maximum height of 55-60 Å and average diameter of 100 nm, which cover up to 55% of the graphite surface, as it can be seen in figure IV.11.

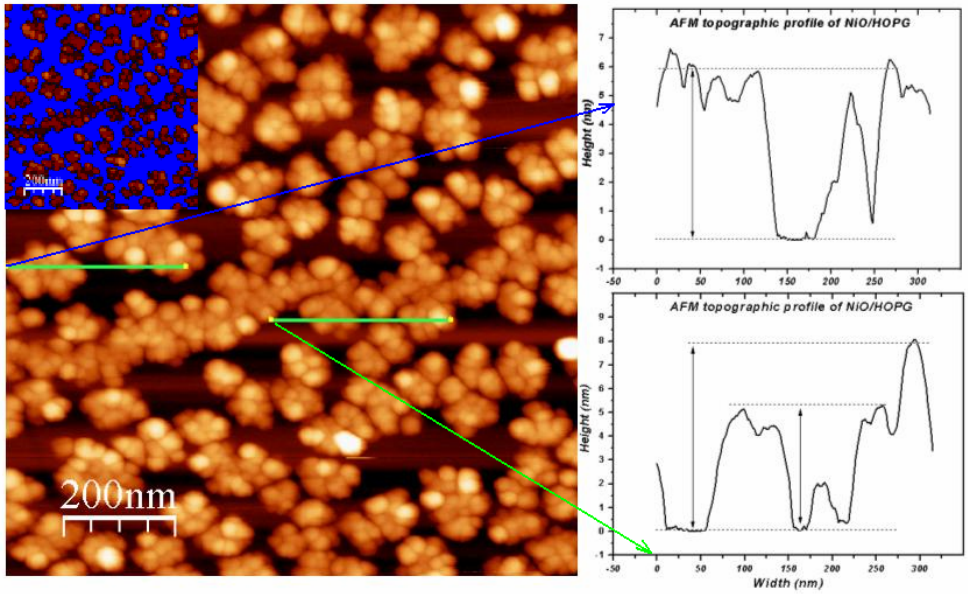

Fig. IV.11. 1x1 μm AFM image and topographic profiles of 18 Å equivalent thickness stage of NiO/HOPG, along with its flooding analysis.

Figure IV.4 d presents an AFM image of a deposition stage of 35 Å equivalent thickness of NiO. The coalescence has not occurred yet but new NiO rearrangement is observed. Each NiO aggregate has a maximum height point, of about 70 Å. In this stage the

graphite surface is about 70 % covered with NiO aggregates of diameter about 80-100 nm, as the topographic profile analysis of AFM images reveals in figure IV. 12.

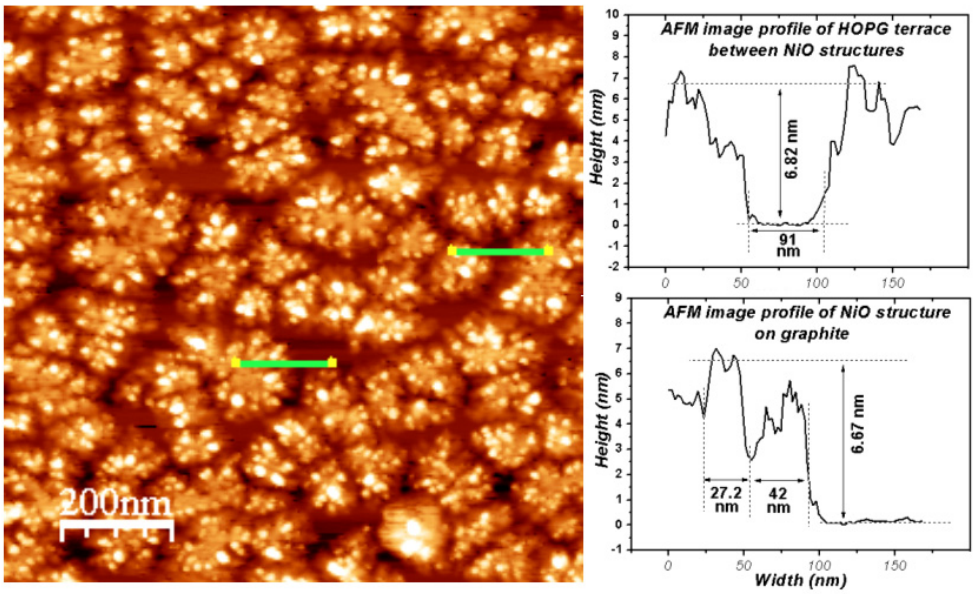

Fig.IV.12. Zoom of 35 Å equivalent thickness stage of growth: AFM image and two topographic profiles of this stage.

In the topographic profile analysis, shown in figure IV.12, the graphite uncovered surface is clearly observed by the topographic analysis. This allows the measurement of the NiO structures heights.

Figure IV.4 e presents an AFM image of 60 Å equivalent thickness of NiO deposited on HOPG. Here the coalescence took place, and no uncovered graphite can be seen. From now is pointless to speak about the NiO structures height but the aggregates diameters evolution still can provide information about the following evolution of the NiO growth.

The average value of the NiO aggregates diameter was found about 95 nm. The height value is varying between 3 and 9 Å, but this should be understood as the height measured between the NiO aggregates borders and its maximum height, not as a height measured respect to the graphite support.

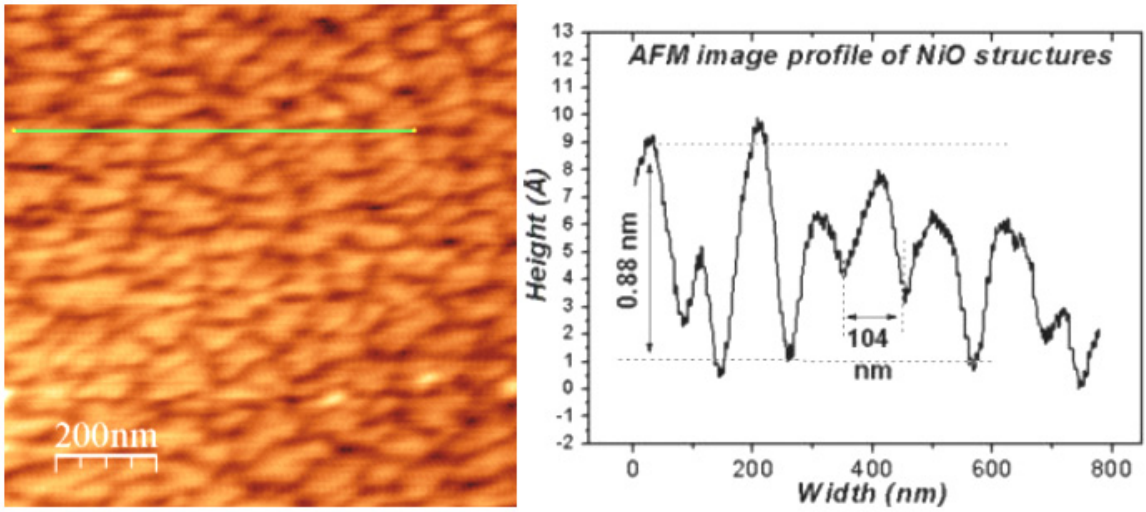

Fig.IV.13 1x1 μm AFM image and topographic profile analysis of 60 Å equivalent thickness of NiO deposited on HOPG

Figure IV.13 support this affirmation with a 1x1 μm AFM image of this stage, along with a topographic profile.

Figure IV.4 f presents the 400 Å equivalent thickness stage of NiO deposition on HOPG. As it was already stated, this stage is characterized by the formation of highest points of NiO on top of the NiO structures. These points reach 30 Å in height, having small diameters in comparison with the NiO base aggregates. If the *old* NiO structures had an average diameter of 100 nm, this new NiO structures reach a 20 nm diameter.

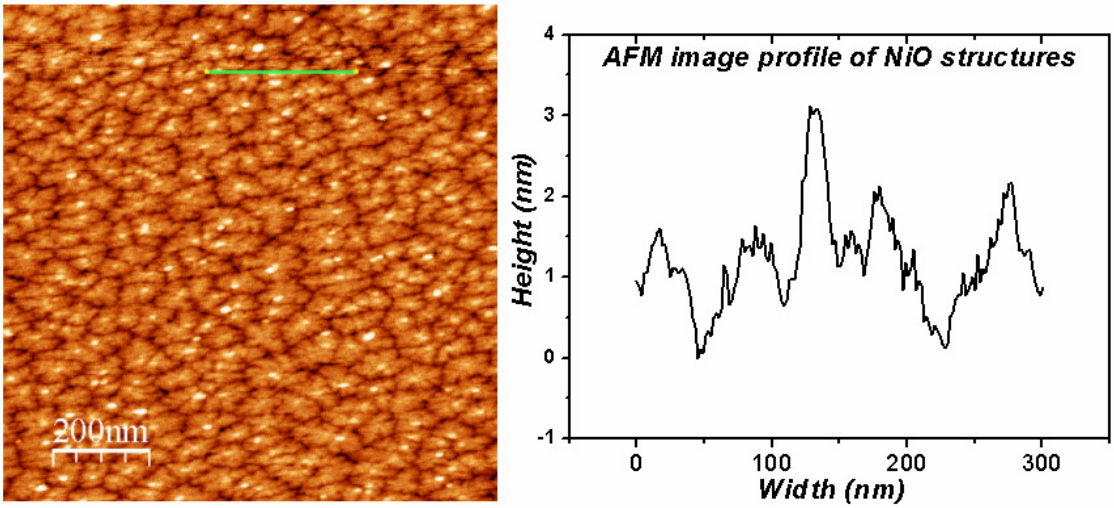

Fig.IV.14. 1x1μm AFM image and topographic profiles of 400 Å equivalent thickness of NiO deposited on HOPG.

Figure IV.5 b correspond to a stage of 400 Å equivalent thickness, presented in figure **IV. 5 a**, but submitted to annealing process at 400 ºC for 60 minutes. It is clear that now it presents a more compact structure, as shown by the topographic profile in figure IV. 15. If the aggregates diameter increases just a few percents, its *height* (between aggregates borders) is now in the 50 Å ranges, that means five times more than in the non-heated stage.

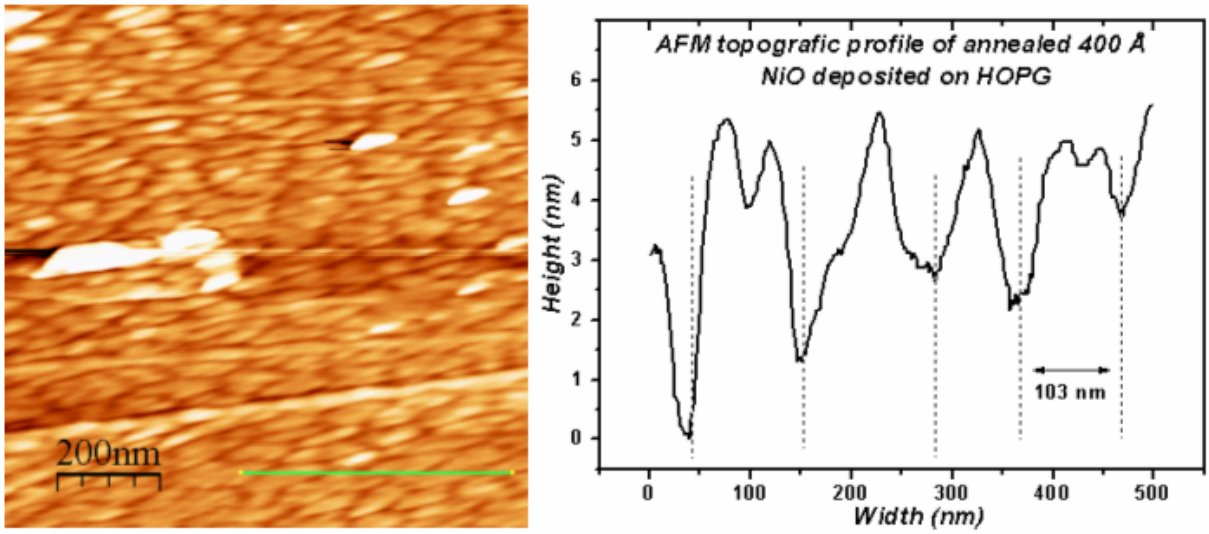

Fig.IV.15. 1x1 μm AFM image and topographic profile of the 400 Å thickness, annealed stage (400 ºC for 60") of NiO on HOPG.

In figure IV.15 is presented a 1x1 μm AFM image and a topographic profile of this stage. It is clear the difference between this annealed stage and the previous one. As we will see below, these structural changes will be reflected in the XPS spectra.

All values obtained by the AFM images analysis are given in the table IV.2, and also represented, along with QUASES result in the figure IV.16 below.

Table IV.2. AFM analysis results:

Equivalent thickness (Å)	Area covered (%)	Height (Å)	NiO Structures diameter (nm)
0.8	5.11	14	25
1.7	10.35	16	40
10	40	35	50-70
18	60	55	100
35.0	70	70	100
60.0	100	-	100
100	100	-	100
400	100	-	100
400 (annealed)	100	-	105

As already stated in the introduction of this part, these values are just estimation, because of the very sensible system analyzed: NiO/HOPG, due to its low stability.

IV.2.3. COMPARISON QUASES–AFM

In this section, the results obtained from the analysis of the AFM images are compared to those obtained from QUASES method. This comparison is shown in figure IV.16. The agreement is excellent.

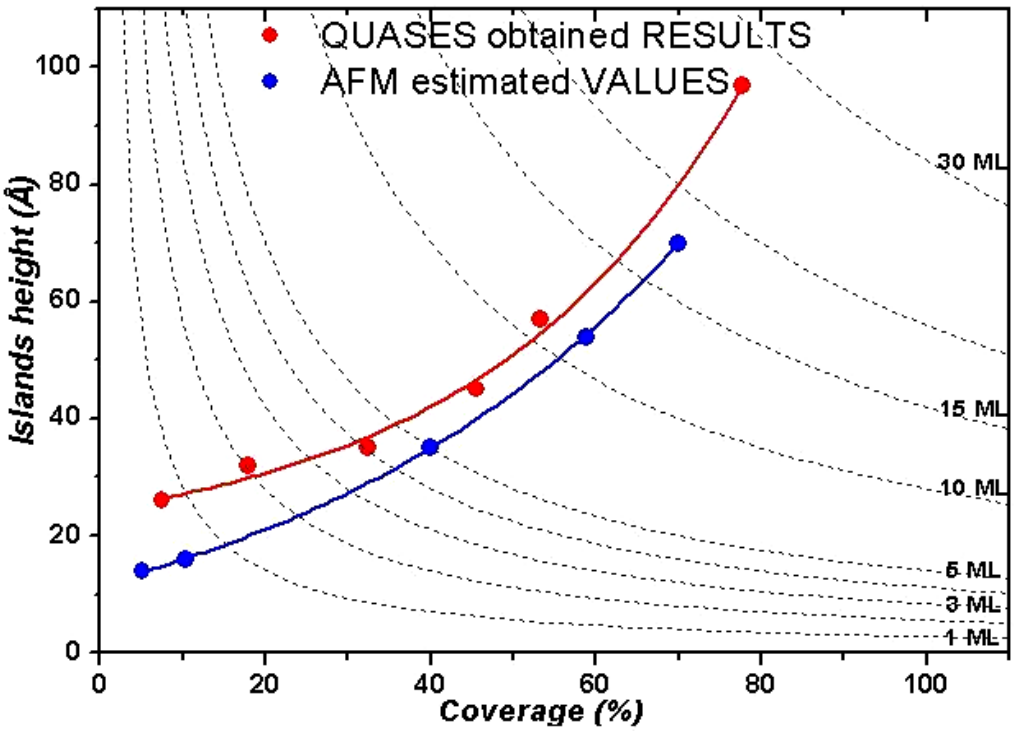

Fig.IV.16. AFM (blue) and QUASES (red) analysis results comparison

As stated at the beginning of this chapter, the results obtained by the AFM imaging analysis are just estimation of the structures heights, diameters and coverage, but, in spite of the difficulty of the AFM imaging due to the very low interaction of NiO with HOPG, the good agreement with the results obtained by QUASES, gives support to such analysis.

IV.3. SURFACE EFFECTS IN NiO

The main purpose of this section is the study of the electronic structure of the early stages of growth of NiO thin film on Highly Oriented Pyrolytic Graphite (HOPG). An important motivation is that the previous AFM and QUASES study on this system has shown that for the early stages of growth, NiO grows by forming nanometric islands (80-110 nm in size and 14-70 Å in height). In the following is presented a combined x-ray photoemission spectroscopy (XPS) and x-ray absorption spectroscopy (XAS) study of the NiO growth on HOPG.

According to the results obtained from AFM and QUASES, the nanostructured NiO formed on HOPG should present a large surface to volume ratio, thus surface effects should be more clearly observed. But, as it will be shown below, surface effects can be observed through the Ni2p XPS spectra, even in a NiO (100) single crystal. Combining XAS, XPS and HAXPES, in this section such surface effects will be studied.

IV.3.1. STUDY OF THE GROWTH OF NiO ON HOPG BY XAS

As mentioned in chapter II X-ray Absorption Spectroscopy (XAS) is a well established technique which, in a first approximation, probes unoccupied electronic states. However, the Ni 2p XAS spectra are dominated by the Ni *2p* spin-orbit splitting, as well as the Ni *2p-3d* Coulomb and exchange interactions. These interactions give rise to strong multiplet effects in the resulting spectra, hiding the information on the density of states[3]. These effects are, in turn, very sensitive to the local symmetry of the initial state, thus being a suitable technique to determine the chemical state of the metal[4].

The XAS measurements were performed at the PM4 beam-line of the BESSY II storage ring (Berlin) as already explained in the third chapter. In this case the coverage has been calculated from the intensities of the XAS spectra following conventional methods, where the thickness, *d*, of the deposited material can be calculated with $I = I_{\infty}(1-e^{-d/\lambda})$, common model in XPS, where λ, the mean free path of the electrons in material, is very well determined. In this work a λ=40 Å, taken from the reference M. Abbate *et al*[5], was used. This method has already successfully used in other XAS works[6]. However assuming a layer by layer way of growth at constant evaporation rate, since the AFM data show that the way of growth of NiO/HOPG is dominated by the formation of nanometric planar islands, the coverage should be understood as an indication of equivalent material to complete such layer.

IV.3.1.1 Ni 2p XAS SPECTRA

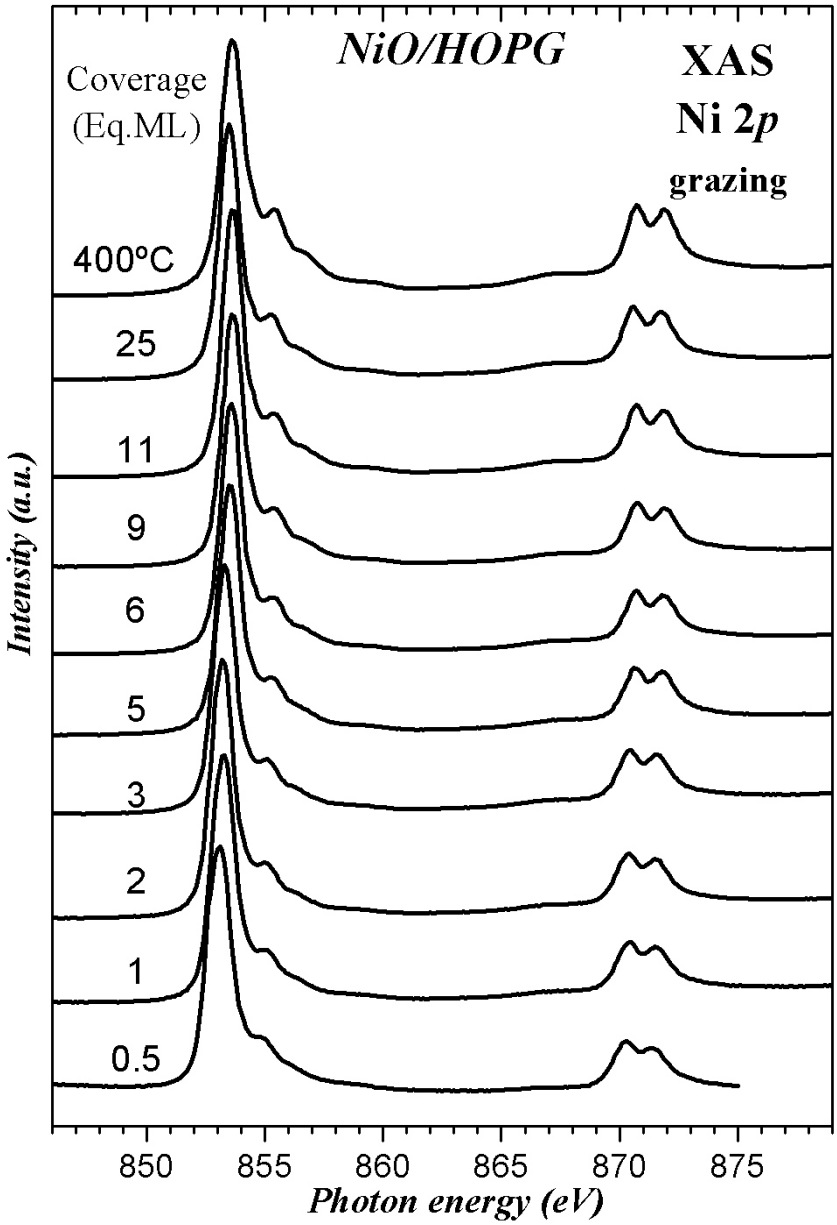

Fig.IV.17. Ni 2p XAS spectra as a function of the NiO coverage.

Figure IV.17 shows the Ni *2p* XAS spectra as a function of the NiO coverage as obtained from the quantitative analysis.

At first sight, all the spectra through the series are similar.

The NiO thin film annealed at 400 ºC matches other published Ni *2p* XAS spectra for bulk NiO[7,8,9]. Also, the spectra for large coverages, prior to annealing, are almost identical. This

is a clear indication that stoichiometric NiO thin film can be grown on the HOPG substrate. However, the most important feature is that the Ni *2p* XAS spectra show the same line-shape during the whole growth process. Even for low coverages, the structures observed in the spectra are the same, although less defined and slightly broader, than those for bulk NiO. These minor discrepancies can be attributed to disorder, and consequently, to a lower value of the crystal field. Although XAS measurements cannot be referred to the Fermi level, this shift is directly related to the increase of the thickness of the NiO isolating thin film. These results seem to indicate that the oxidation state of the Ni atoms remains unchanged and the same as in bulk NiO.

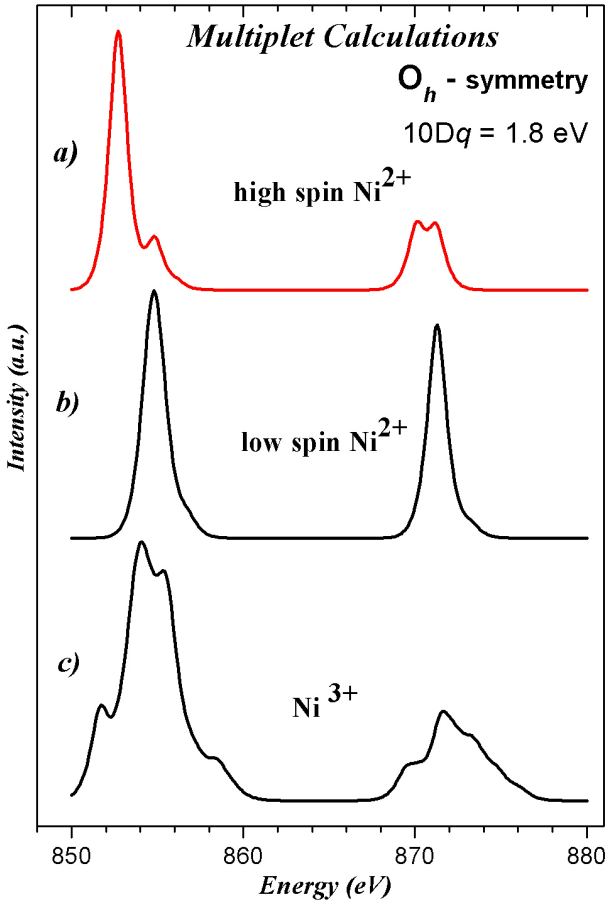

Fig.IV.18 Multiplet calculations for: a) Ni $^{2+}$ with high spin symmetry; b) low spin Ni^{2+}; c) Ni^{3+}.

In order to corroborate the above results, the experimental Ni *2p* XAS spectra were compared with theory. According to de Groot *et al.*[3,4], the spectra can be reproduced by calculating the *2p→3d* multiplet transitions as a first step. In the case of NiO, these transitions have to be projected in an octahedral crystal field of certain strength. A *2p→3d* multiplet calculation was performed for Ni ions in different symmetries: high spin Ni^{2+} (figure IV.18 a),

low spin Ni $^{2+}$ (figure IV.18 b) and Ni^{3+} (figure IV.18 c). The crystal field parameter (10*Dq*) was set to 1.8 eV in all calculations. From the comparison of the calculations with the experimental Ni *2p* spectra it is inferred that, indeed, the Ni atoms involved in the experiment remain in the high spin Ni^{2+} form.

IV.3.1.2 O1s XAS SPECTRA

The near-edge region (in O1s XAS spectra) of the spectra is dominated by hybridization of O *2p* states with metal-3d states, thus mapping the metallic *3d* density of states. It is worthy to recall here that NiO is a $3d^8$ charge transfer oxide with the ground state as a mixture of $3d^8$ + $3d^9\underline{L}$ +$3d^{10}\underline{L}^2$ states[3-5] so that only e_g states remain unoccupied. It will be shown below that surface effects are clearly observed in the O *1s* XAS spectra of the nanostructured NiO system studied here which are completely consistent with the AFM data.

The figure IV.19 shows the O *1s* XAS spectra as a function of the coverage. Once again, the spectrum of the annealed thin film is identical to other spectra published elsewhere for bulk NiO[5,6]. The first peak at 530.5 eV is assigned to the hybridization of O *p* states with Ni *3d* (e_g) states whereas the broad peaks located at 536.0 and 539.0 eV correspond to O *p* states hybridized with Ni *4s* and Ni *4p* respectively. The spectra for high coverages prior to annealing are also similar to that of bulk NiO. This supports again the growth of a stoichiometric NiO thin film on the HOPG substrate.

However, for low coverages (0.5 Eq.ML in figure IV.19) the spectrum differs strongly from the bulk spectrum. The single peak at threshold, assigned to e_g states in bulk NiO, is now split forming a broad band. It is clearly seen that the initial broad band for the very low stages of growth is progressively changing in shape throughout the series to give the final bulk line-shape.

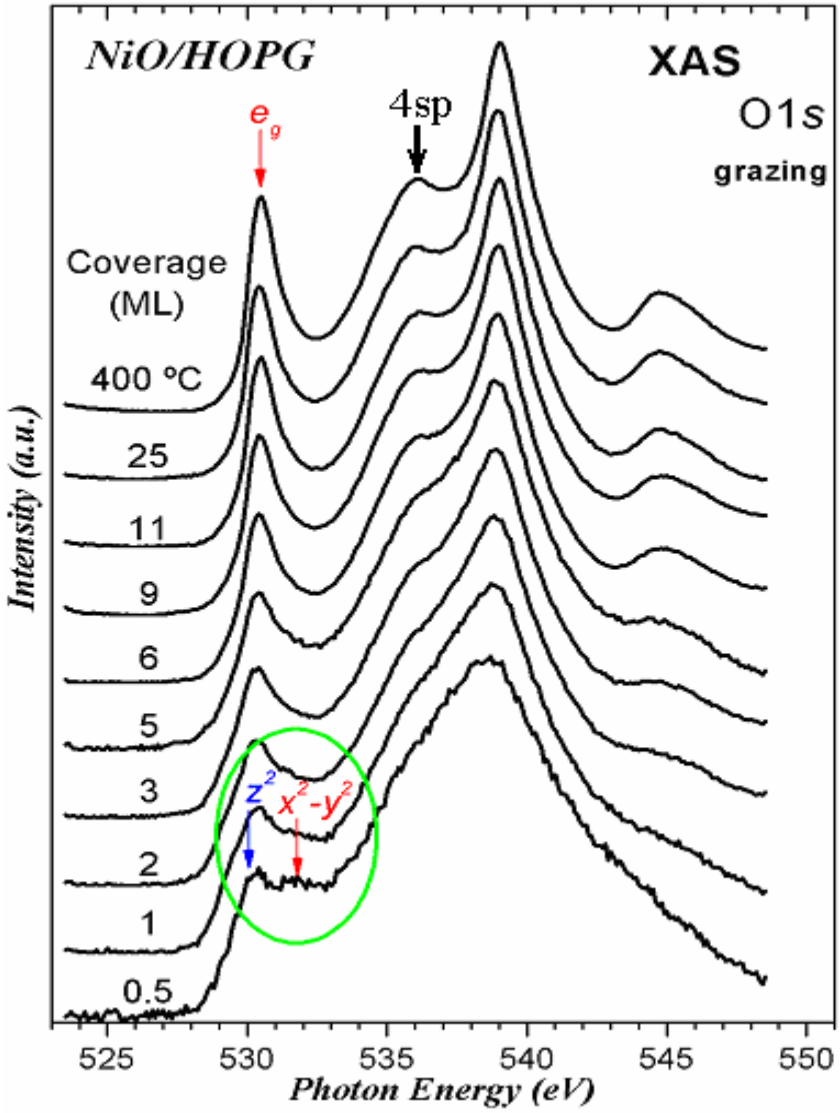

Fig.IV.19. O 1s XAS spectra as a function of the NiO coverage.

To understand this effect the O 1s absorption edge was determined by means of cluster calculations in octahedral (NiO_6) and pyramidal (NiO_5) symmetries. The results of the calculations are presented in figure IV.20 and IV.21. The calculations in octahedral symmetry (green dash line in figure IV.21.a) give a single peak which corresponds to the hybridization with the unoccupied e_g states in bulk NiO, as it is seen by the comparison with the experimental O *1s* XAS spectra of bulk NiO (dots black in figure IV.21.a). In turn, the calculations for pyramidal symmetry (blue and red dot lines in figure IV.21.c) give two peaks separated by 1.5 eV and with relative intensity of 32% and 50% with respect to the intensity of the bulk line.

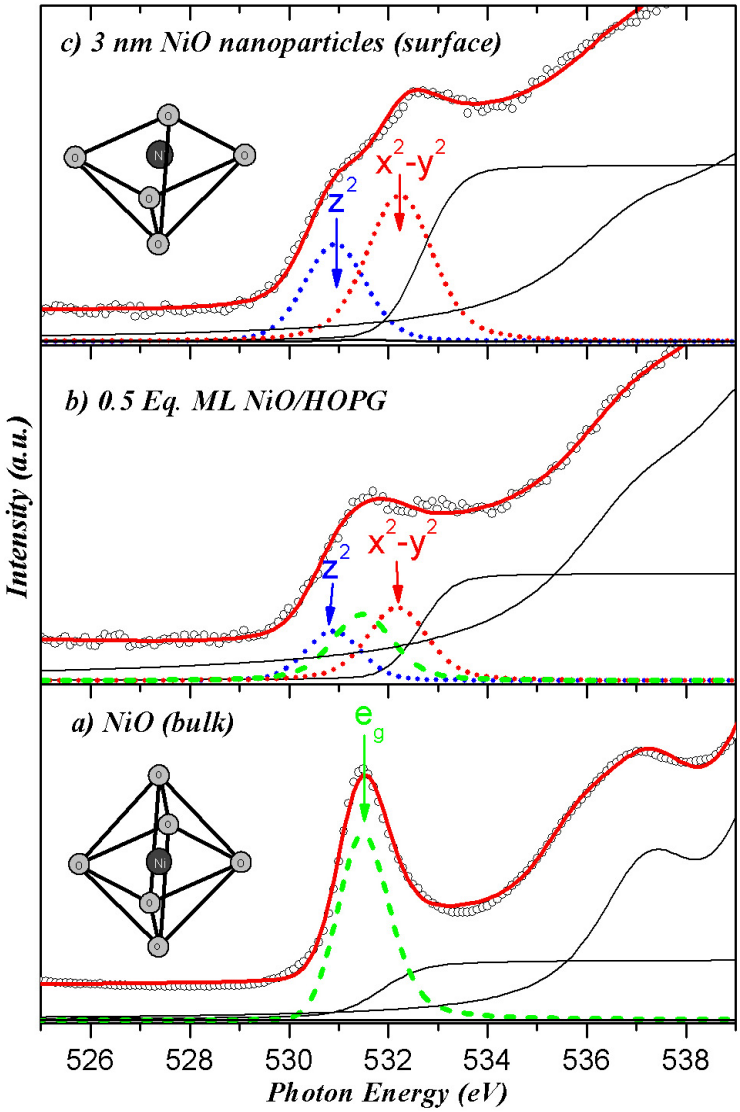

Fig.IV.20. Experimental and calculated near edge region of the O 1s XAS spectra (dots) of: (a) large NiO coverage (bulk); (b) 0.5 ML NiO/HOPG; and (c) 3 nm NiO nanoparticles. Gaussian curves represent the results of the calculations in: octahedral (green dash lines) and pyramidal symmetry (blue and red dot lines). Solid lines represent typical curves used to fit the background.

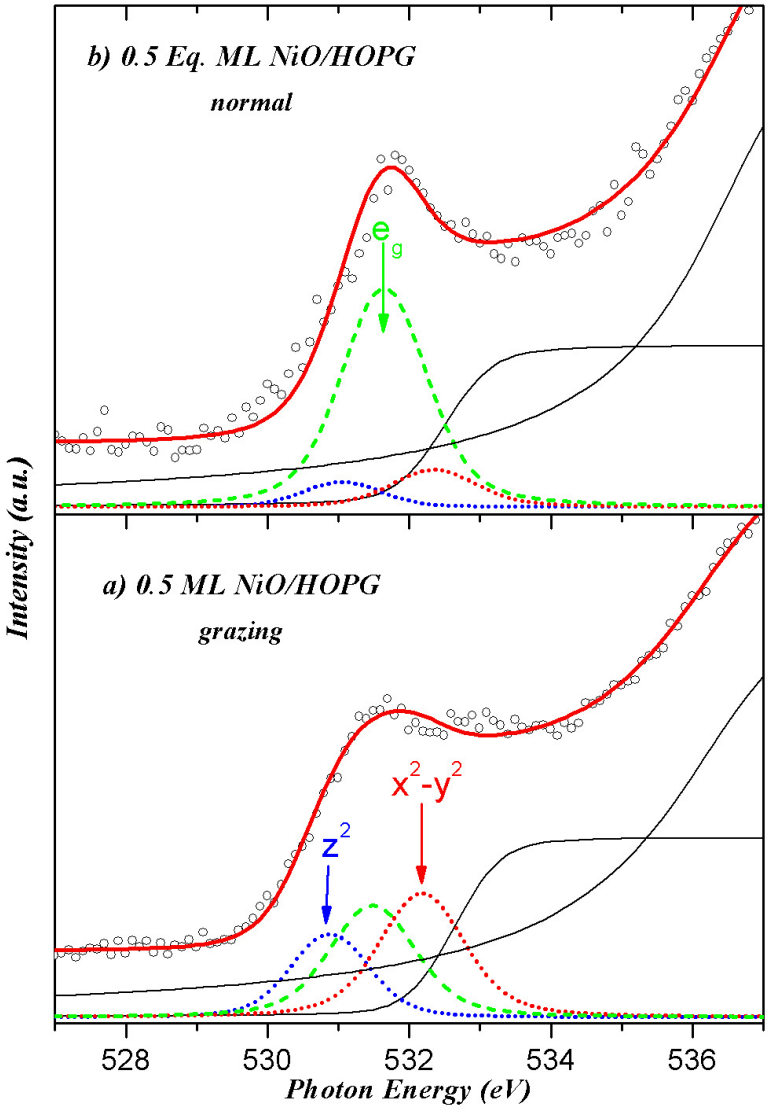

Fig.IV.21. Calculations and experimental data of the near edge region of O 1s XAS spectra of 0.5 ML NiO/HOPG taken at (a) grazing and (b) normal incidence.

These results show that unoccupied e_g states split into z^2 and x^2-y^2 states due to the lack of the apical oxygen at the NiO surface. The calculations in pyramidal symmetry have been compared with the experimental O *1s* XAS spectra of 3nm NiO nanoparticles taken from ref.[10].

This nanometric system shows important surface effects due to the high surface to volume ratio. The calculations perfectly agree with the spectra of the NiO nanoparticles. However, in the case of the spectra of 0.5 Eq.ML of NiO/HOPG, the best fitting has been obtained by introducing a small bulk component in the calculations.

It is important to note here that all the XAS spectra shown here have been taken at grazing incidence to enhance the surface of the planar NiO islands. The quasi-bidimensional

morphology of the NiO islands is reflected in the XAS spectra. The planar islands formed at the early stages of growth present a large surface to volume ratio, allowing the observation of this surface effect. It can be seen that further evaporation produces the increase of the bulk component, indicating an increase of the island thickness. Only when coalescence has been reached (25 ML in figure IV.19), the thin film spectra resemble those of bulk NiO. Another relevant aspect of the results is the presence of a z^2 dangling bond that can be related to the well known catalytic properties of NiO nanoparticles. In this way, the early stages of growth of NiO on HOPG seem to be a suitable system to prepare NiO catalysts.

IV.3.2. SURFACE EFFECTS IN Ni 2p XPS SPECTRA

The complex electronic structure of NiO gives rise to a complex line shape of the experimental spectra when using spectroscopic techniques, in particular x-ray photoemission spectroscopy (XPS). The Ni 2*p* photoemission peak line shape of NiO shows a multipeaked structure which has been widely discussed in the literature. Nowadays, it has been shown that cluster calculations of the Ni 2*p* photoemission spectrum for a NiO_6 cluster give rise to three different peaks, according to the above description of the electronic structure. However, the very-well-known additional shoulder separated by 1.5 eV at higher binding energies from the main line is absent in those calculations[11]. This satellite appears only when the calculations are extended to a larger Ni_7O_{36} cluster. As a consequence of that, the satellite was called as *nonlocal screening satellite* and was explained as a screening process due to oxygen atoms belonging to the outer NiO_6 clusters[11].

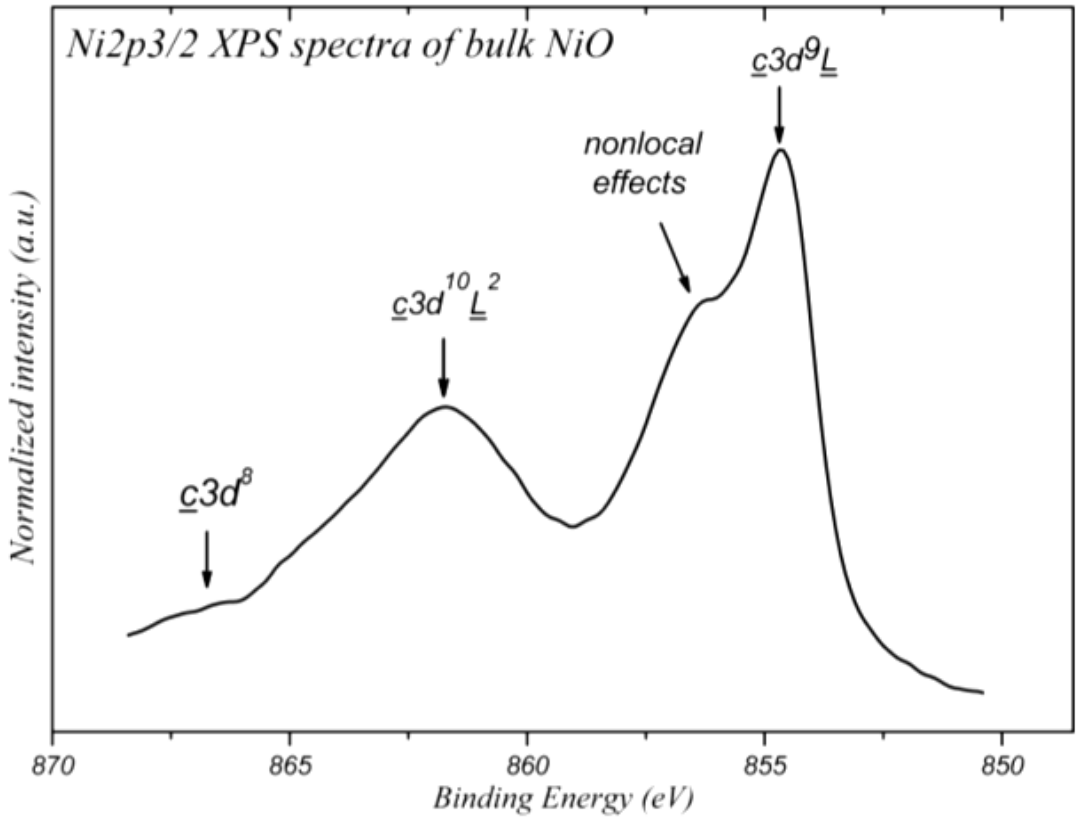

Fig.IV.22. Ni 2p3/2 XPS spectra

The so-called non-local satellite in the Ni 2*p* XPS spectra has been conventionally assigned to the presence of Ni^{3+} species at the NiO surface[12]. In general, it has been observed that the intensity of this satellite increases with the creation of defects. For instance, Uhlenbrock *et al.*[13] concluded that Ar bombardment of a freshly cleaved NiO (100) surface produces the formation of Ni^{3+} species and the simultaneous reduction to Ni^0 when analyzing the intensity of the satellite with respect to the main line. However, it is well known that argon bombardment produces oxygen vacancies due to preferential sputtering of oxygen, leading to the reduction of Ni atoms to metallic Ni[14].

Other authors found a dependence of the intensity of the satellite on the emission angle of a NiO single crystal[15,16]. They concluded that the satellite could be associated with the surface Ni atoms but no appropriate theoretical model was proposed to explain the experiment. Other interpretations appearing in the literature assign the satellite to $\underline{c}3d^{10}\underline{L}^2$ states or $\underline{c}3d^9$ multiplets[17,18]. Therefore, the origin of the satellite at 1.5 eV higher binding energies with respect to the main line in the Ni 2*p* XPS spectra in NiO remains unclear.

As mentioned above, the interpretation of the satellite as a nonlocal process is the most accepted theory at present. This model is supported by experimental results in the systems: $Ni_xMg_{1-x}O$[19] and one epitaxial NiO monolayer grown on MgO single crystal[20]. In these systems, the nonlocal satellite is absent as corresponds to systems where, in spite of Ni atoms are octahedrally surrounded by oxygen atoms, no second neighboring oxygen atoms exist. The non-local screening model suggests that the satellite structure is intrinsic for bulk NiO. However, when the calculations are restricted to a Ni_6O_{30} cluster, unexpectedly the intensity of the satellite increases. The authors conclude that this could be due to a different coordination of the cluster with the core hole i.e., five-fold to six-fold[11]. In turn, the model does not explain the absence of the satellite in the Ni 2*p* XPS spectrum of La_2NiO_4 as corresponds to a purely octahedral Ni compound[16].

It seems reasonable to think that the above splitting of the Ni 3*d* levels at the surface could also be reflected in the Ni 2*p* XPS spectra. To investigate this possibility, two simple experimental XPS measurements of a bulk NiO sample were performed. In XPS there are two main techniques to make the spectrum more sensitive to the surface: by minimizing the inelastic mean free path[21] λ and using grazing takeoff angle measurement geometry. Bellow, the Ni 2*p* XPS spectra of a NiO sample measured at different takeoff emission angles and at different photon energies are presented.

The Ni 2*p*3/2 XPS spectra of the NiO thin film taken with Mg *Kα* radiation at two take-off emission angles (θ) are shown in figure IV.23. The spectrum taken at θ=0° (fig. IV.23 upper) agrees with that of a NiO single crystal[11]. The spectrum taken at θ=80° (fig. IV. 23 bottom) shows a clear enhancement of the intensity of the *shoulder* at 856.0 eV with respect to that measured at θ=0°. Band dispersion and matrix element effects are important for valence levels at low energies, like angle-resolved photoemission spectroscopy (ARPES), but are not expected to significantly influence the core-level spectra at higher energies. Therefore, the results seem to indicate that the satellite contains a considerable surface contribution. Thus, the first experiment is qualitatively consistent with the interpretation made in this part. In figure IV.24, the Ni 2*p*3/2 XPS spectra of the NiO thin film taken at different photon energies are depicted.

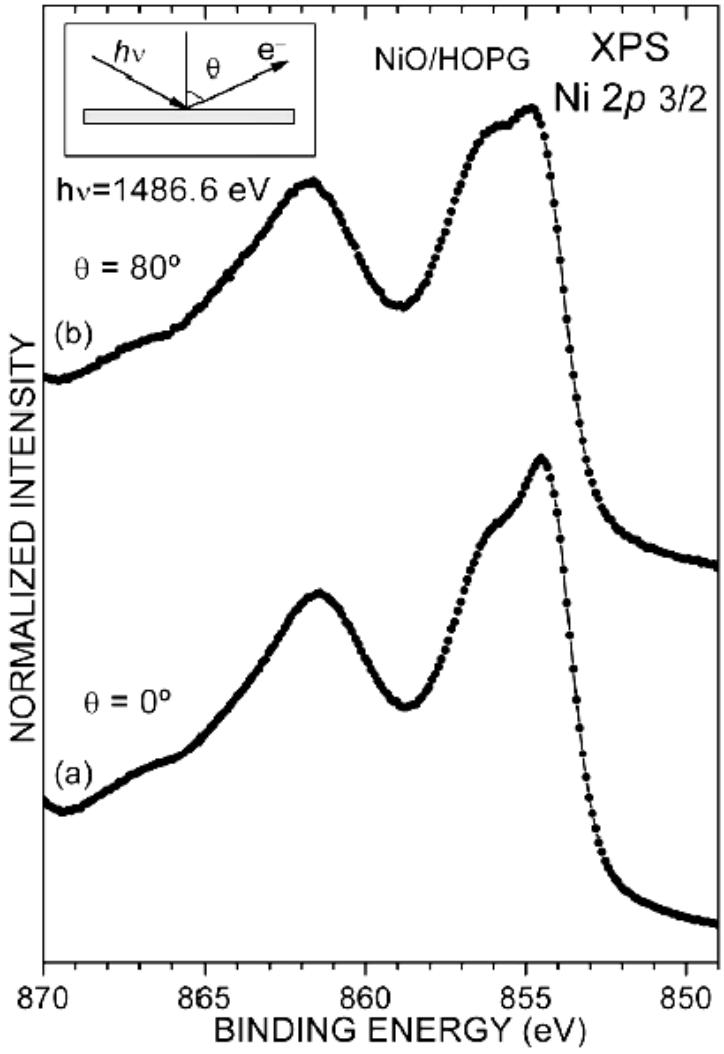

Fig.IV.23. Ni 2p3/2 XPS spectra of the NiO thin film taken with Mg K_α radiation at various emission angles (θ).

The kinetic energy of the photoelectrons in the conventional spectrum taken with Al *K*α radiation (fig. IV.24 upper) is about 630 eV, whereas in the spectrum taken in the synchrotron at 1000 eV photon energy (fig. IV.24 bottom) is about 145 eV, thus giving values for the inelastic mean free path of 12.66 Å and 4.24 Å, respectively. These values have been calculated using the Tanuma, Powell and Penn formula[21]. The spectrum taken with synchrotron light at 1000 eV shows a large increase of the relative satellite intensity.

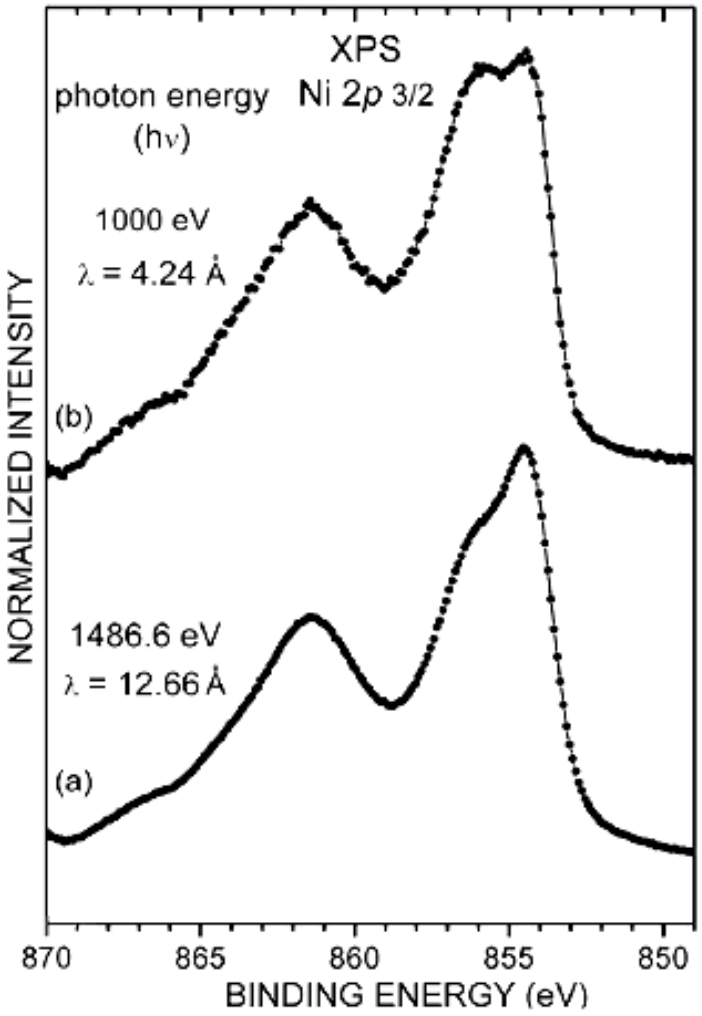

Fig.IV.24. Ni 2p3/2 XPS spectra of the NiO thin film taken at different photon energies

The changes of the cross section with energy affect all the component of the core-level spectra and cannot account for the change of only one component as observed in the experimental data. Also the Mg $K\alpha_{3,4}$ satellites which are not present in the spectrum taken with synchrotron radiation, cannot explain such increase of the shoulder. Therefore, these results are again consistent with the interpretation that the satellite at 856.0 eV has a large

surface contribution. However, detailed XPS quantitative analysis of both peaks indicates that the intensity of the satellite is too high to be explained as only due to the surface contribution. This seems to indicate that other processes, like *non-local screening effects*[11,20] , could also contribute to the satellite intensity and should be not neglected..

In order to give an interpretation to the experimental data, cluster model calculations to theoretically reproduce the Ni 2*p* core-level spectra have been performed. The clusters were NiO_6 in octahedral symmetry (bulk) and NiO_5 in pyramidal symmetry (surface). The ground state was expanded in the $3d^8$, $3d^9\underline{L}$, and $3d^{10}\underline{L}^2$ configurations, where $\underline{L}$ denotes a symmetry adapted O 2*p* hole[22]. The final state was expanded in the $\underline{c}3d^8$, $\underline{c}3d^9\underline{L}$, and $\underline{c}3d^{10}\underline{L}^2$ configurations, where $\underline{c}$ here denotes a hole in Ni 2*p* core level. The Ni 2*p* photoelectron spectra were then calculated using the sudden approximation[20].

The parameters of the model were the charge transfer energy Δ=4.0 eV, the Mott-Hubbard repulsion U=7.5 eV, the core-hole potential Q=9.0 eV, and the *p-d* transfer integral T_σ=2.6 eV[23]. These values give the best agreement with the experiment and are in agreement with previous estimates. The multiplet splitting was given in terms of the Raccah parameters B=0.13 eV and C=0.58 eV, as well as the crystal field parameter $10Dq$=0.10 eV. The transfer of the x^2-y^2 level involved T_σ in both octahedral and pyramidal symmetries. The transfer of the z^2 level involved also T_σ in octahedral symmetry, but only $2/3T_\sigma$ in pyramidal symmetry due to the lack of the apical O[24]. Figure IV. 25 show the result of the calculation in octahedral (a) and pyramidal (c) symmetries, whereas the figure IV.25 (b) shows the calculation of 40 % - 60 % surface – bulk contributions, respectively.

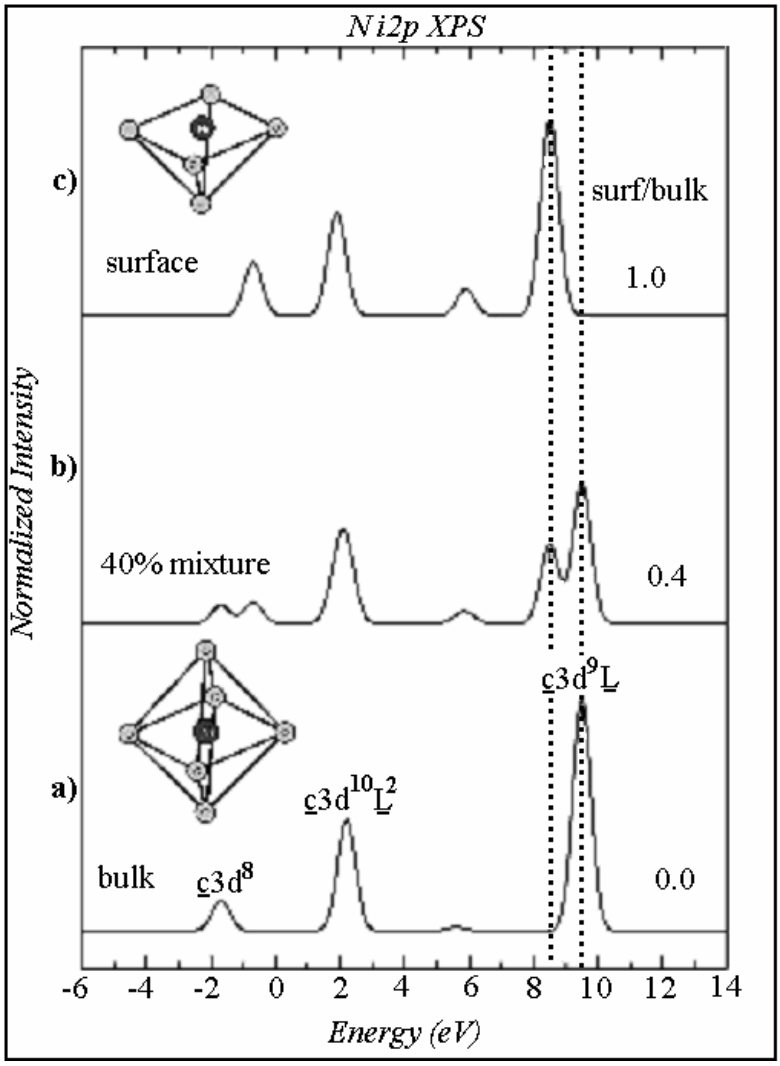

Fig.IV. 25. Results of the cluster calculations performed in (a) octahedral symmetry, (b) a combination of a 60% octahedral and 40% pyramidal symmetries, and (c) pyramidal symmetry

For the bulk NiO_6 cluster, the calculation presents the standard $\underline{c}3d^9\underline{L}$, $\underline{c}3d^{10}\underline{L}^2$, and $\underline{c}3d^8$ peaks. For the surface NiO_5 cluster, the calculations show these peaks but the energy spread is smaller (the additional peak in the spectrum is due to the different hybridization of the x^2-y^2 and z^2 levels). The overall energy separation between the peaks is roughly given by $\Delta E^2=(Q-\Delta)^2+4T_{eff}^2$. The smaller energy spread above is attributed to the reduced T_{eff} in pyramidal symmetry. The $\underline{c}3d^9\underline{L}$ peak at the surface is shifted 1.0 eV toward lower energies with respect to the bulk. These results suggest that the main line of the Ni 2*p* XPS spectra would come from the bulk, whereas the shoulder would contain a considerable surface contribution. In fact, the

mixture of 60% bulk and 40% surface (although nonlocal effects are also expected to contribute to the satellite intensity) components in figure IV. 25 *b* resembles the experimental Ni 2*p* XPS.

Other effects would also place a significant surface contribution at the *non-local* structure. For instance, the changes in the Madelung potential would affect the charge-transfer energy Δ and would also reduce the binding energy of the surface contribution by about 0.5 eV[20]. The differences in the hybridization were the key to interpret the O 1*s* XAS spectra of NiO nanostructures[25]. It is difficult to tell which of these effects dominates in the case of the Ni 2*p* XPS spectrum. Whatever, the theoretical calculations presented in figure IV. 26, of the Ni *2p*3/2 spectra, demonstrate that the non-local screening effects need to be taken into account.

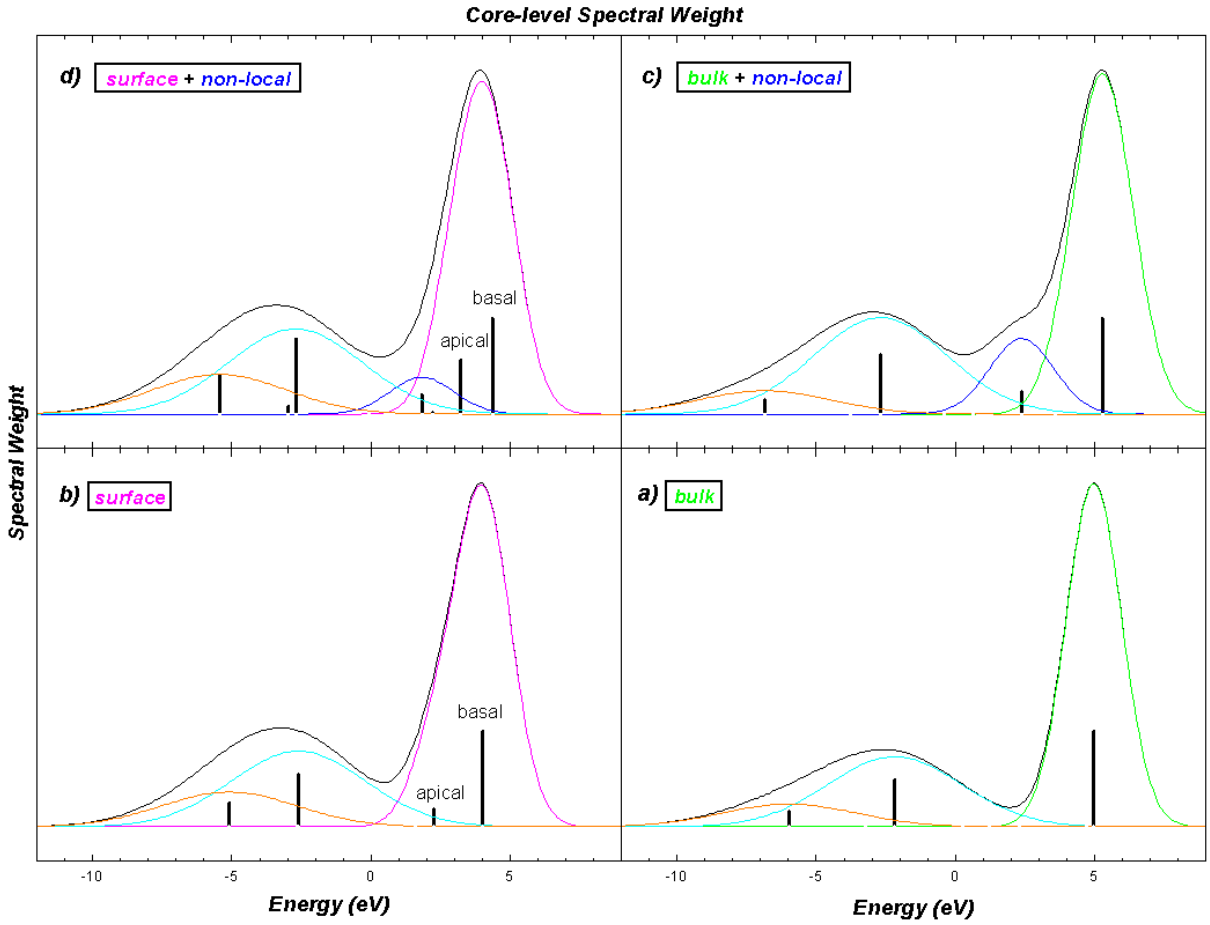

Fig.IV. 26. Theoretical spectra calculation of Ni 2p3/2 photoemission spectra.

In order to support this model in which the spectral weight in the energy region of the shoulder is affected by a combination of both, surface and non local effects, theoretical calculations of the spectral weight of the Ni *2p*3/2 spectrum of NiO has been done, taking into

account these two effects. To this end, octahedral NiO_6 (bulk) and pyramidal NiO_5 (surface) clusters in contact with a non-local bath were considered. The results for these calculations are shown in figure IV. 26.c and IV. 26.d. The results of the same calculations but with the absence of the non-local bath (figure IV 26.a and IV 26.b) are also included for comparison purposes. The results have been broadened to simulate the experimental data.

Describing the results for the calculations without the non-local bath, figure IV. 26.a shows the calculations for an octahedral NiO_6 cluster. In this case the spectrum is formed by three lines corresponding to $\underline{c}\ 3d^9\underline{L}$, $\underline{c}\ 3d^{10}\underline{L}^2$ and $\underline{c}\ 3d^8$ states. These results for octahedral symmetry agree with those previously obtained by van Veenendaal *et al*[26]. and clearly show that the shoulder does not appear in the spectrum. The results shown in figure IV. 26.b correspond to a NiO_5 cluster in pyramidal symmetry. In this case the main line peak ($\underline{c}3d^9\underline{L}$) shifts by 1 eV with respect to the same line in octahedral asymmetry, thus contributing to the spectral weight of the shoulder. A weak additional peak appears also in the spectrum of figure IV 26.b (labelled as apical), due to the different hybridizations of the x^2-y^2 and z^2 levels. Besides, the energy spread is reduced from 11 to 9 eV, as a consequence of the lost of coordination, i.e. the lost of covalence.

To include the non local screening effect, the spectral weight by using an octahedral NiO_6 cluster in contact with a non-local bath has been calculated. This non-local bath has to be considered as a cloud of electrons which allows charge transfer from/to the studied cluster. The results are shown in figure IV. 26.c. In this case, the $\underline{c}3d^9\underline{L}$ peak appears slightly shifted (0.5 eV) towards lower binding energies whereas a new peak appears at 2.9 eV from the main line as consequence of the screening from the non local bath, in the following called as $\underline{c}3d^9\underline{D}$. The other peaks corresponding to $\underline{c}3d^{10}\underline{L}^2$ and $\underline{c}3d^8$ levels slightly change their energy position due to the hybridization with the non-local bath. In fact the states are all mixed so that the assignments correspond to the states with a larger weight at the corresponding energy.

If the spectral weight for a pyramidal NiO_5 cluster in contact with a non-local bath is calculated within the same idea, it is found that the $\underline{c}3d^9\underline{L}$ line is less shifted than in the same calculation without the non-local bath. In turn, the apical line appears at higher binding energies, it means, closer to the main line respect to the calculation without the non-local bath, as shown in figure IV. 26 d. The $\underline{c}3d^9\underline{D}$ appears now shifted towards lower binding energies just 2.6 eV from the main line. The $\underline{c}3d^{10}\underline{L}^2$ and $\underline{c}3d^8$ levels change their energy position, also due to the hybridization with the non-local bath.

The final spectra weight of the Ni *2p* XPS spectrum would consist of a sum of the bulk+non-local and surface+non-local, with their corresponding factors, governed by λ which is determined by the photon energy.

In summary, according to the above calculations of the spectral weight of the main line + shoulder energy region of the Ni *2p* XPS spectra can be envisaged as the contribution from bulk (main line), surface and non-local peak. This allows the fitting of this region of the Ni *2p*3/2 XPS spectra by means of three curves.

Following this idea, in order to describe quantitatively the contributions of surface effects and non-local screening effects in the Ni *2p*3/2 experimental spectra, different fittings were performed. The software used was NEWFITT developed by CERN. The fitting parameters can be found in the appendix section of this work. Figures IV.27 and IV.28 shows the same Ni *2p*3/2 XPS spectra presented in figures IV.23 and IV.24, with the fittings performed in terms of main-line, non-local, surface and satellite peaks.

The best fitting for Ni *2p*3/2 XPS spectra of NiO as bulk material was found for a $I_{main}/I_{nonlocal}$ intensities ratio of 1.40, this value was kept constant for all the fittings from, as also the energy separation of 2.7 eV (main to non-local assigned curves) and the FWHM of the main and non-local assigned peaks.

These values for the fitting of the non-local peak are in agreement with the above calculation, although the calculation I_{Main} / $I_{Surface}$ intensity ratio is lower than that obtained for the best fitting. This minor discrepancy can be explained if one takes into account that the model used in the calculation accounts only for one bath in contact to the main cluster.

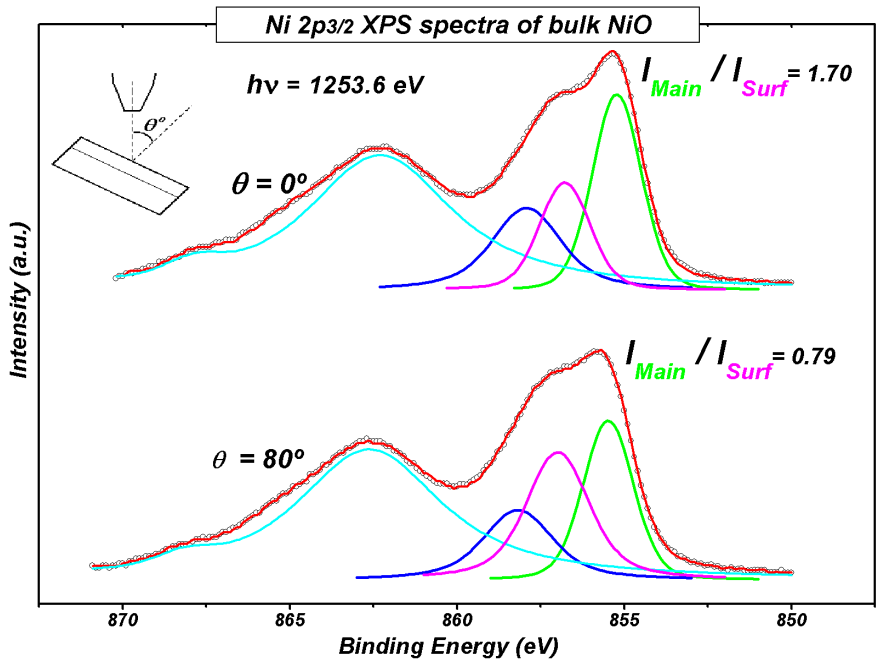

Fig.IV.27. Ni 2p3/2 XPS spectra measured in take-off angle θ=0° (upper) and θ=80 ° (bottom).

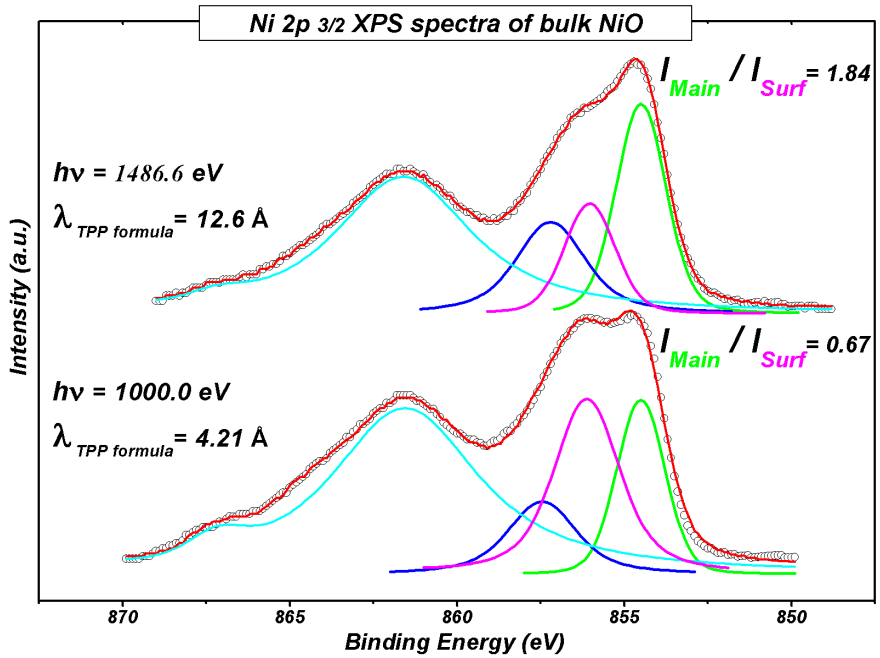

Fig.IV.28. Ni 2p3/2 PES spectra measured with hν=1486.6 eV x-ray energy (upper) and hν=1000 eV X-ray energy (bottom).

Figures IV.27 and IV.28 show the above fittings performed to the experimental spectra presented in figures VI.23 and IV.24, respectively. It is seen the very good agreement of the fittings to the experimental spectra. Even more, in the following, the main to surface intensity

ratio, I_{Main} / $I_{Surface}$, will be used for to estimate the surface importance component in the Ni *2p* XPS spectra.

IV.3.3. STUDY OF THE SURFACE EFFECTS IN NiO BY HAXPES

As already commented in chapter II, this kind of measurements requires very special conditions and equipments. Once the requirements were complete, and a fresh cleaved NiO single crystal was inserted in the UHV analysis chamber, low energy electron diffraction (LEED) images were taken, as shown in picture IV.29.

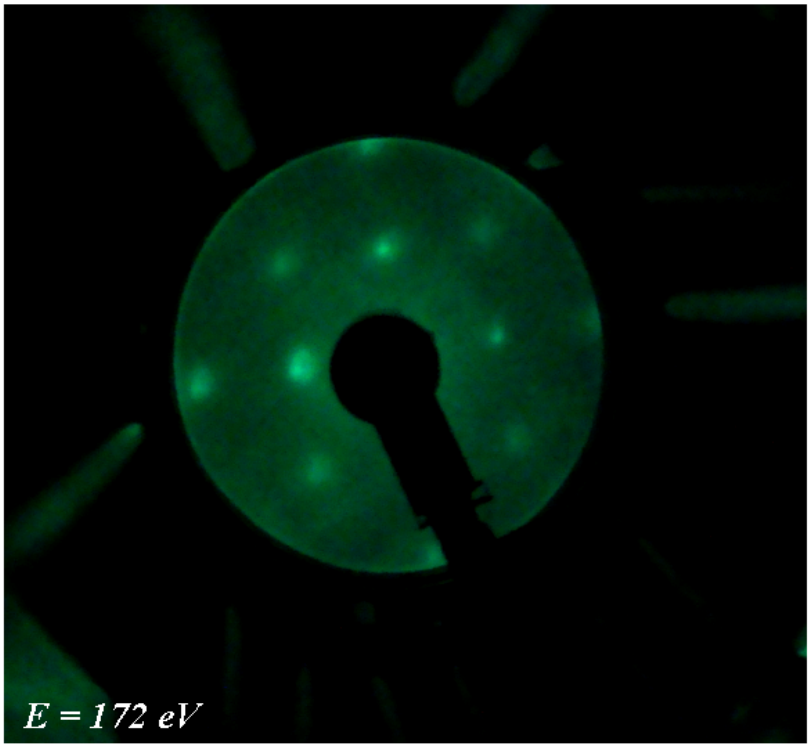

Fig.IV.29. LEED image of a fresh cleaved NiO single crystal. Electron beam energy is 172 eV.

From the picture above, a LEED image taken at 172 eV electron beam energy, it can be clearly seen that the NiO is a single crystal (100), and the surface is quite contamination free.

Both Ni1s and Ni $2p_{3/2}$ of this NiO single crystal sample were measured with two different excitation energies, 9.0 and 12.0 KeV. The normalized measured spectra are presented in figure IV. 30.

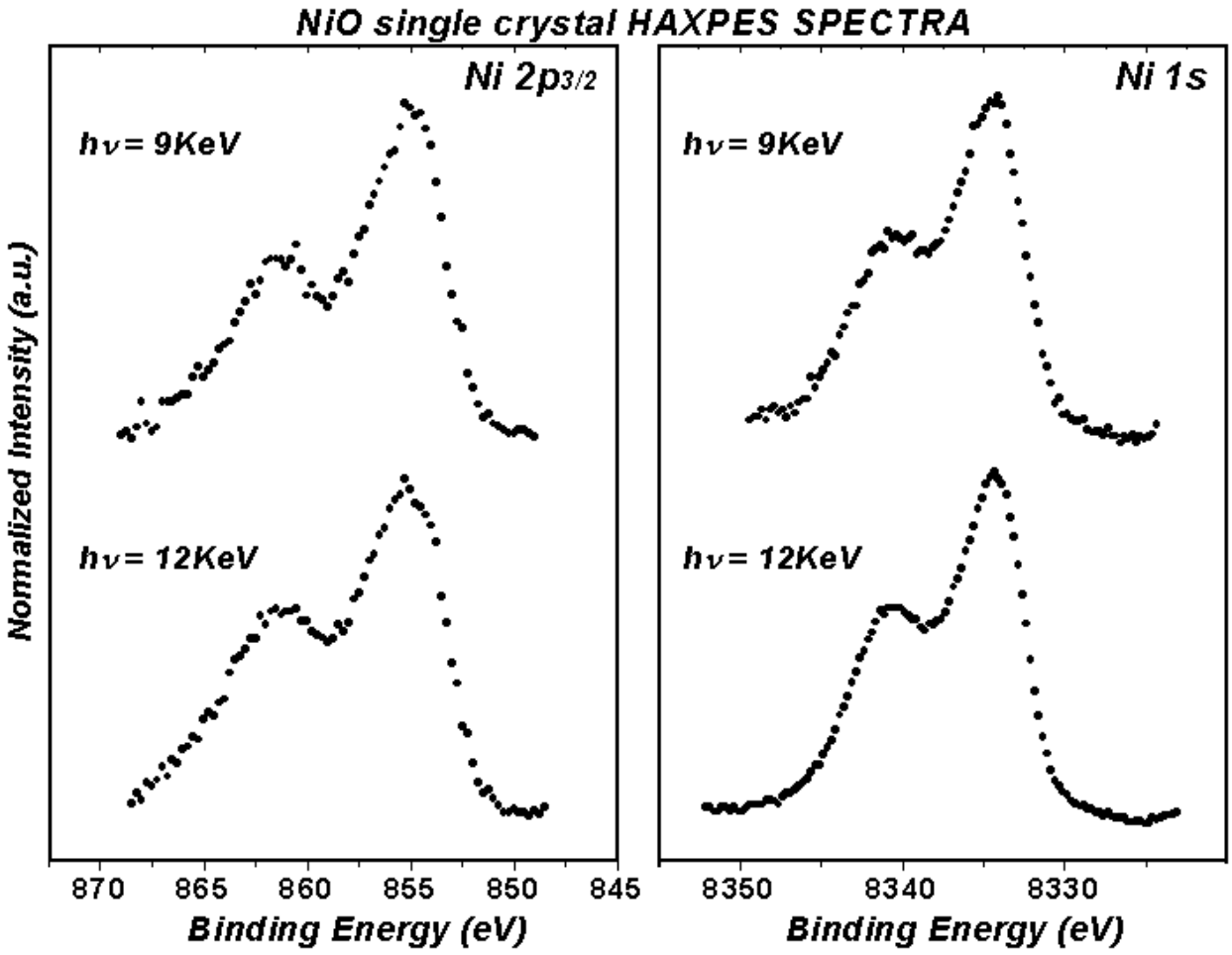

Fig.IV.30. Ni 2p3/2 and Ni1s HAXPES core levels spectra of a NiO (100)

First of all, it is needed to tell that no bibliography was found in the literature about similar measurements of these core levels, so no comparison can be made. Whatever, the Ni *2p*3/2 HAXPES spectra shapes are comparable with the XPS or PES spectra shapes of this core level, with small differences, induced principally, by the different experimental resolution, which makes the peak shapes broader than in the usual excitation energy range in XPS. It is not surprising that the Ni1s HAXPES spectra present the same shape as the Ni *2p*3/2, having in mind that screening effects should be reflected also in the electronic structure of this core level.

According to the results of the previous section, and in order to quantify the surface contribution to these spectra, fittings of the HAXPES spectra, with the same set of parameters as those used for the XPS spectra, have been performed. Only the experimental resolution value, due to the different energy resolution of the monocromator and electron analyzer, has been modified,

accordingly. Whereas this value was 0.67 eV for the XPS spectra and 1.21 eV and 1.32 eV for the HAXPES spectra take it with 9 and 12 KeV of photon energy, respectively[27].

In figure IV.31 the fitted spectra are presented together with the results obtained for the spectra taken with 1000 eV and 1486.6 eV, pointing out the evolution of the surface intensity peak respect to the intensity of the NiO bulk peak, versus the mean free path of the photoelectrons.

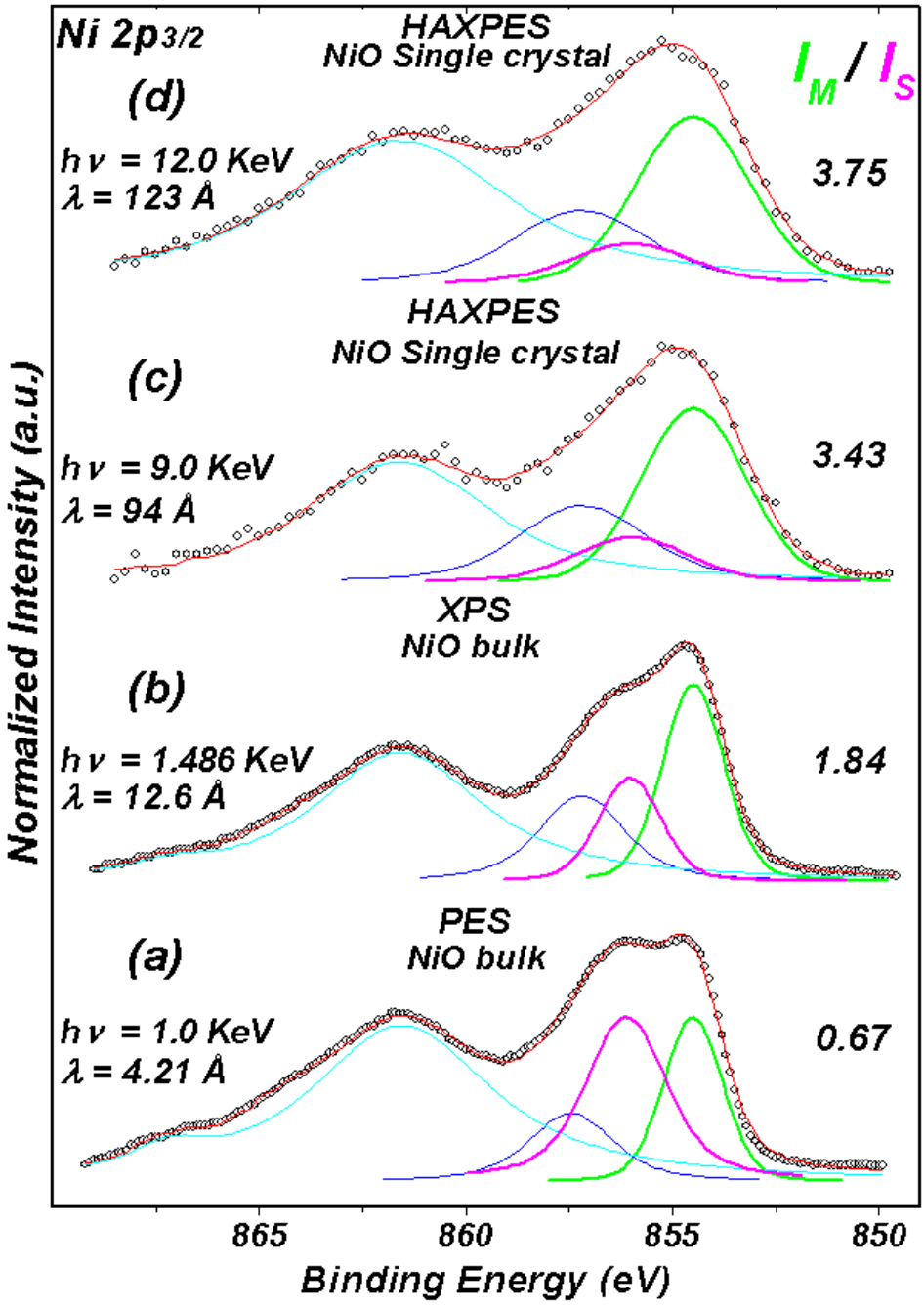

Fig.IV.31. Ni 2p3/2 electronic structure fitted, PES (a), XPS (b) and HAXPES (c and d) spectra, of bulk NiO (a and b) and NiO (100) single crystal (c and d)

It is obvious that the main to surface intensity ratio increase as the mean free path increase, clearly pointed in figure IV.32 below.

Taking into account that the surface will have its contribution in all photoemission spectra the depth of the measured NiO increases, from a measurement to another, due to a higher value of the photoelectrons mean free path, which follows the universal curve dependence of the kinetic energy, as in figure IV.32. where the I_{Main} / $I_{Surface}$ intensity ratio and the IMPF are represented versus the kinetic energy of the photoelectrons.

In the following, a comparison between the Ni *1s* HAXPES and the Ni *2p*3/2 XPS spectra line shapes for a NiO single crystal, is attempted, using their fitted spectra. Also in this fitting process, the experimental resolution for the HAXPES measurement is reflected through a higher Gauss factor, as above indicated.

In figure IV.33 below, the fitting results and the comparison with the Ni *2p*3/2 XPS fitted spectra, are presented.

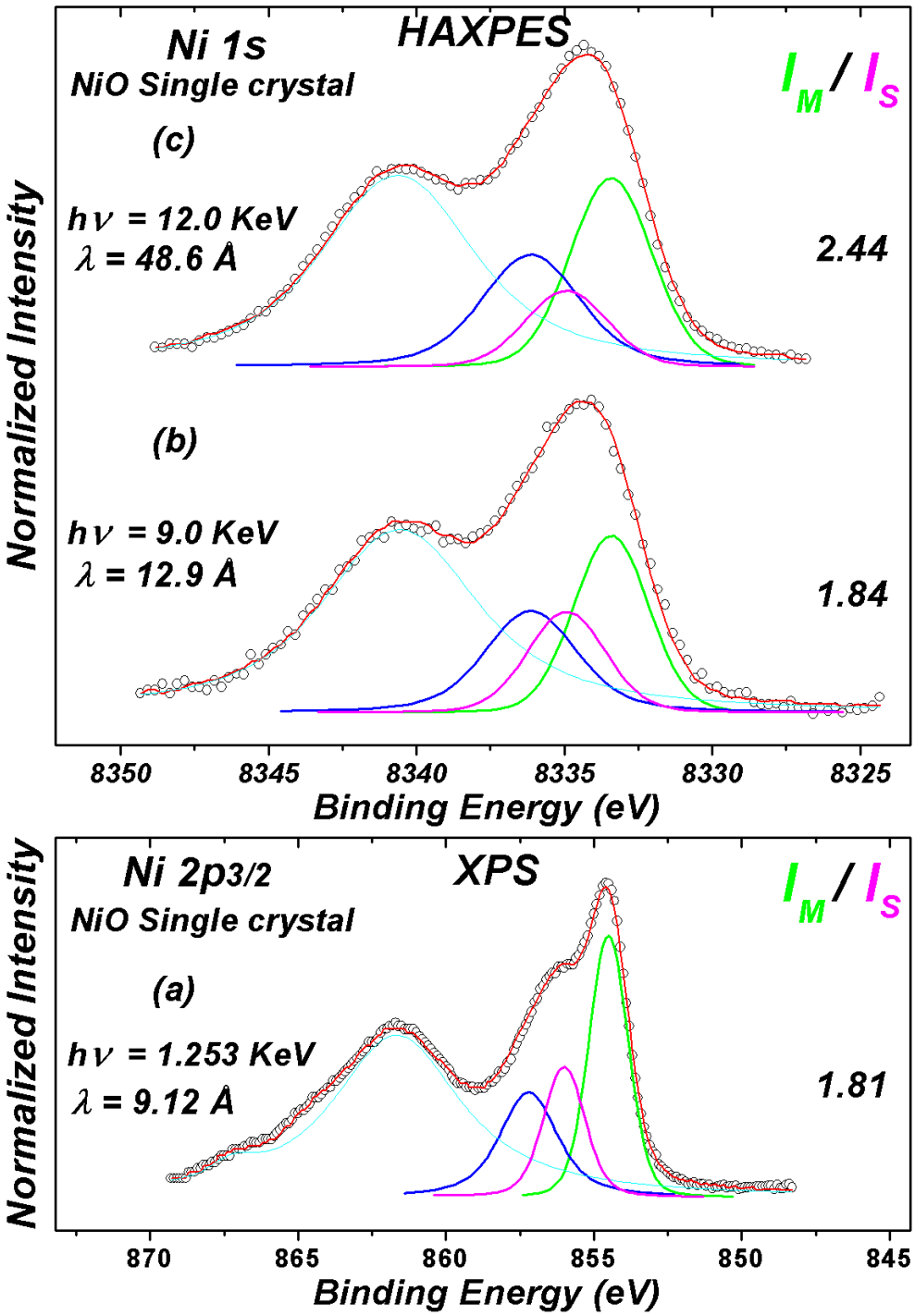

Fig.IV.32. Comparison between Ni 2p3/2 XPS fitted spectra (a) and Ni 1s HAXPES, taken with 9 and 12 KeV, fitted spectra of a NiO (100) single crystal (b and c respectively).

As expected, in this kinetic energy range of the photoelectrons, their mean free path is low again, and less bulk NiO is measured, and as consequence, the surface assigned peak increases its intensity respect to the main-line intensity peak. It is amazing the good agreement between the main to surface intensity ratio values for the Ni *2p*3/2 XPS spectra and the Ni *1s* HAXPES spectra,

given by photoelectrons of a same kinetic energy range, which means the same range of their mean free path.

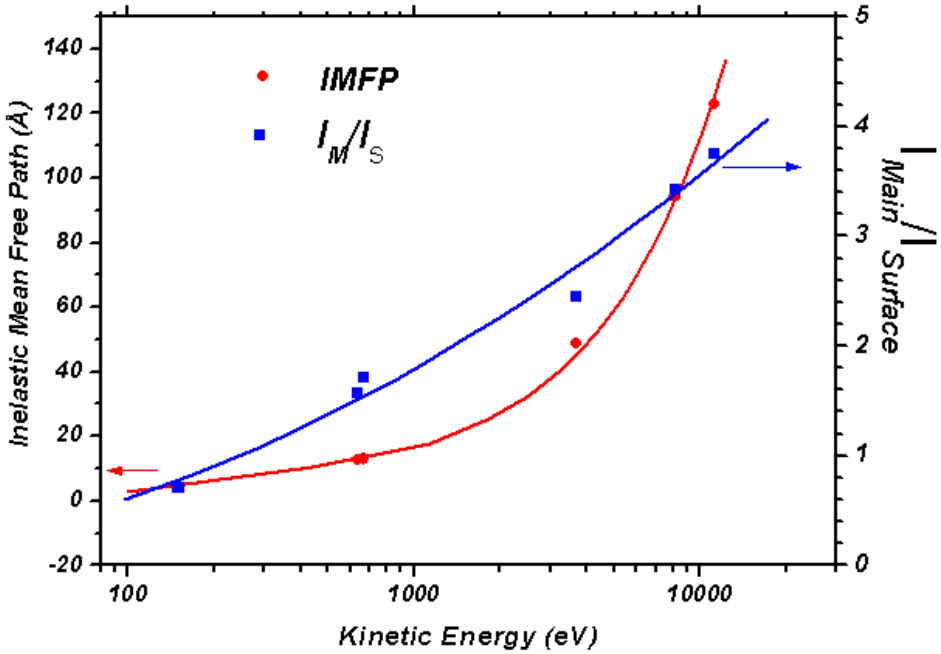

Fig.IV.33. $I_{Main}/I_{Susface}$ intensity ratio and IMFP given by Tanuma-Powell-Penn formula[21] vs. kinetic energy.

Therefore, HAXPES allowed measurements of the same core level with different kinetic energy, showing the goodness of the proposed model. On the other hand, electronic core levels with different binding energies have also shown a very good agreement with the model.

IV.3.4. STUDY OF THE GROWTH OF NiO ON HOPG BY XPS

Once the surface effect has been studied in the photoemission of NiO, here, the study of the growth process of NiO/HOPG is presented as a clear example of this effect. The nanostructured NiO formed during the early stages of the growth, as described in the first section of this chapter, is analyzed by XPS.

IV.3.4.1. The Ni 2p XPS SPECTRA

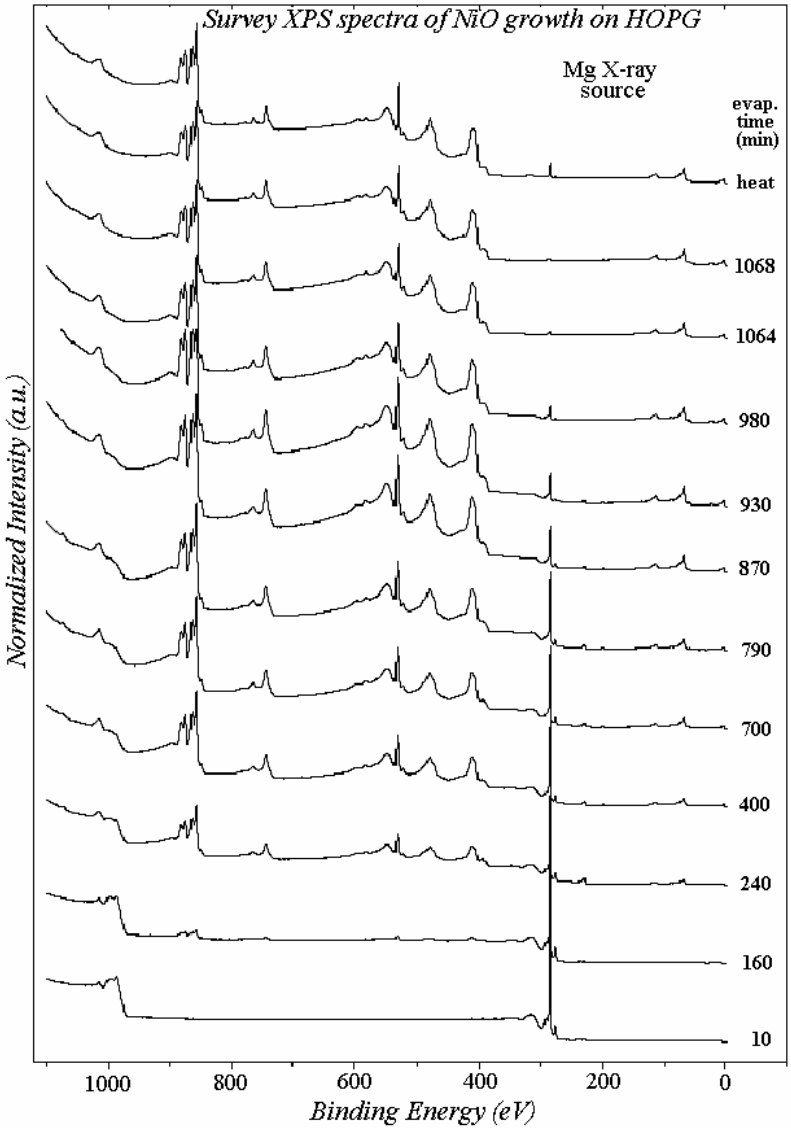

Fig.IV.34. Survey XPS spectra for the NiO/HOPG growth process.

In figure IV.34 the XPS surveys spectra of the whole growth process are presented. It can be observed the successive accumulation of NiO on the HOPG substrate through the increasing intensity of the Ni *2p* XPS spectra. The spectra show the XPS core levels of nickel, oxygen and carbon and also the Auger structures of these elements as expected. Consequently, the intensity of the C *1s* core level is progressively decreasing during the deposition process. In the annealed sample, the C *1s* appears again, probable due to the contamination during the heating process.

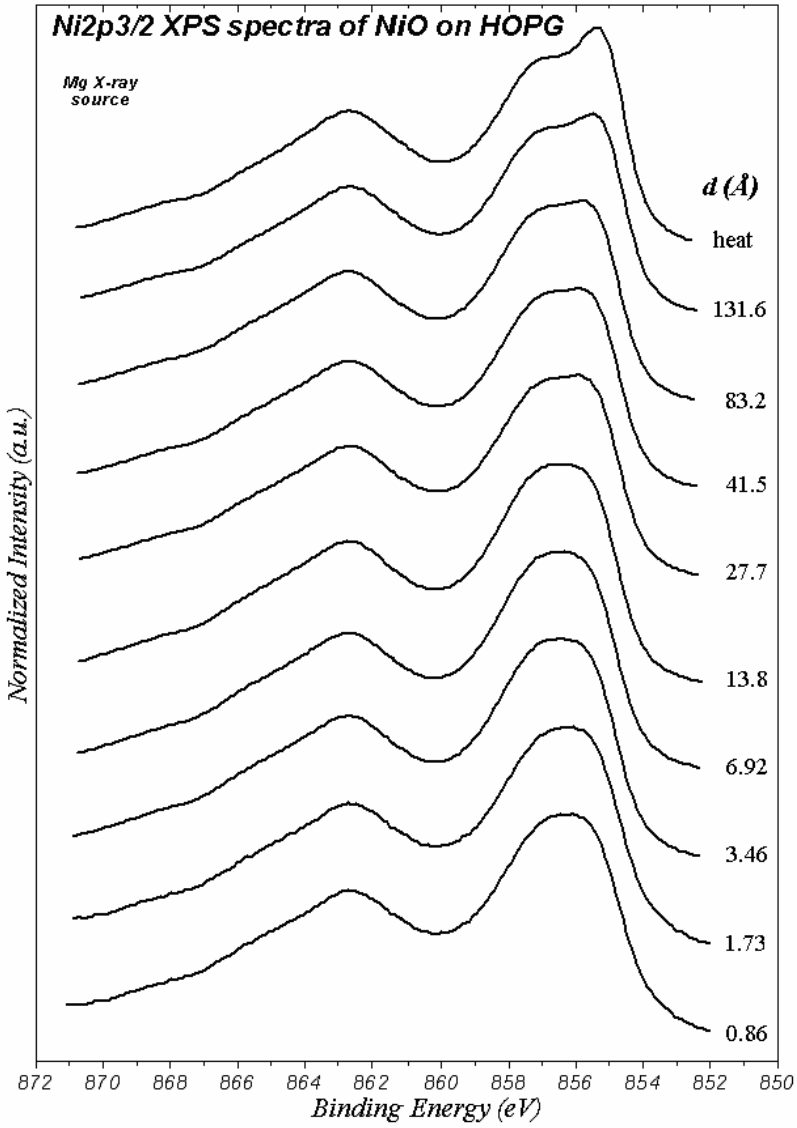

Fig.IV.35. Ni 2p3/2 XPS spectra of the NiO growth on HOPG

Figure IV.35 shows the Ni *2p*3/2 XPS spectra as a function of the equivalent coverage. It can be seen that for large coverages the spectra resemble that of bulk NiO, whereas for low

coverages the spectra present the region of the shoulder with an extra intensity. These results are consistent with the AFM study together with the surface effect model. Only when coalescence is reached, with a compact structure, the spectra agree with that of the bulk NiO. In the previous stages, where NiO is forming nanostructured islands, the effect of the high surface to volume ratio is clearly observed.

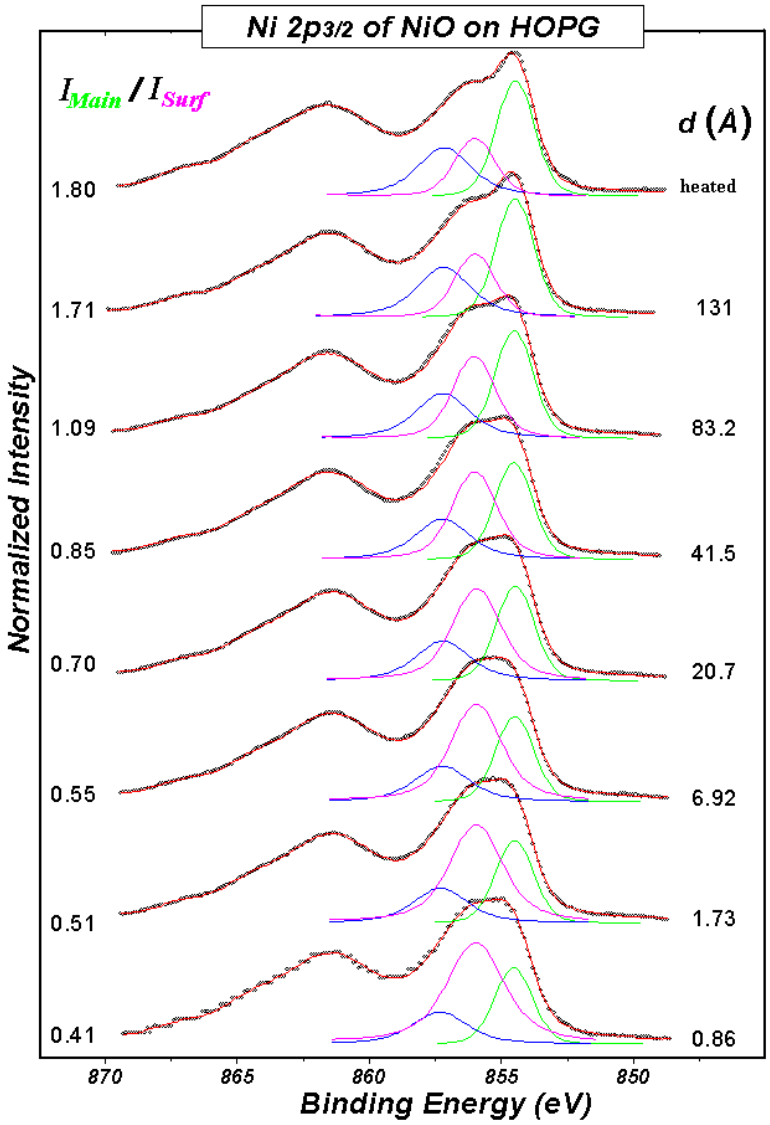

Fig.IV.36. Fittings of Ni 2p3/2 XPS spectra along the deposition process

In order to observe this effect more clearly, the fitting in terms of main-line, non-local, surface and satellite assigned peaks was performed, for the whole XPS spectra of the growth, results presented in figure IV. 36.

It can be seen that in first stage of growth the Ni *2p*3/2 XPS spectra is dominated by surface effects. As the amount of NiO increase, the bulk shape is more important in the spectra. Through the series, the I_{Main} / I_{Surf} intensity ratio increases from 0.38 from the first stage of growth to 1.37 at the end of deposition. Even more, for the heated system this ratio increases to 1.54 what suggest that the heating process the NiO give rise to a reorganization of the NiO on the HOPG substrate and now its surface-to-volume ratio is lower. We should strength again the consistency of these results with the AFM data.

IV.3.4.2. The O 1s XPS SPECTRA

Looking at the O *1s* XPS spectra for the whole growth process, presented in figure IV.37, it can be seen that from the early stages of the growth, two oxygen peaks are clearly visible at 530.0 and 532.5 eV respectively. However, for very large coverage, especially for the heated sample, the peak at 530.0 eV dominates the spectrum. This peak, O_I labelled, was assigned to the O atoms in the bulk NiO lattice.

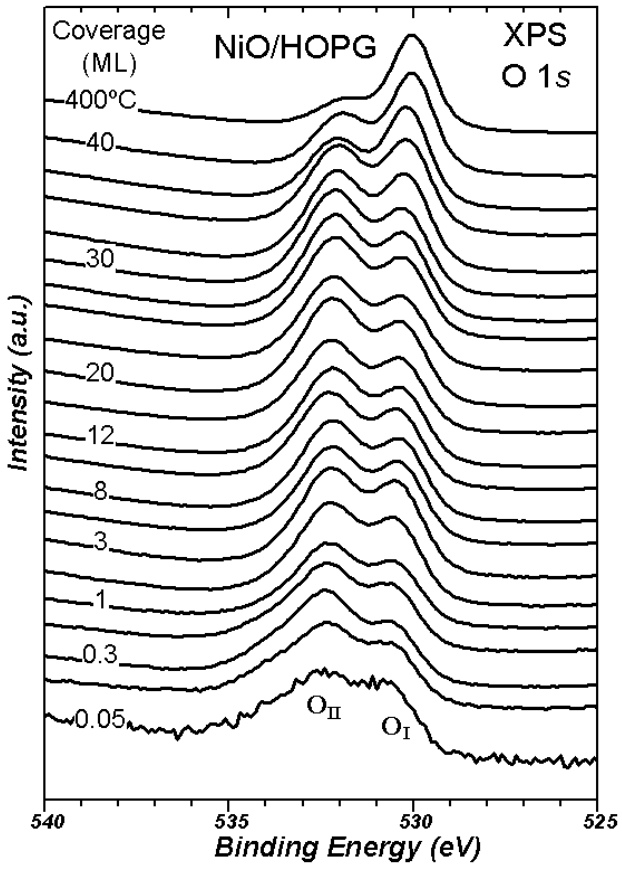

Fig.IV.37. O 1s XPS spectra along the deposition process.

In order to understand the origin of the second peak at 532.5 eV, labelled as O_{II}, the fitting of these spectra was performed, and are presented in figure IV.38.

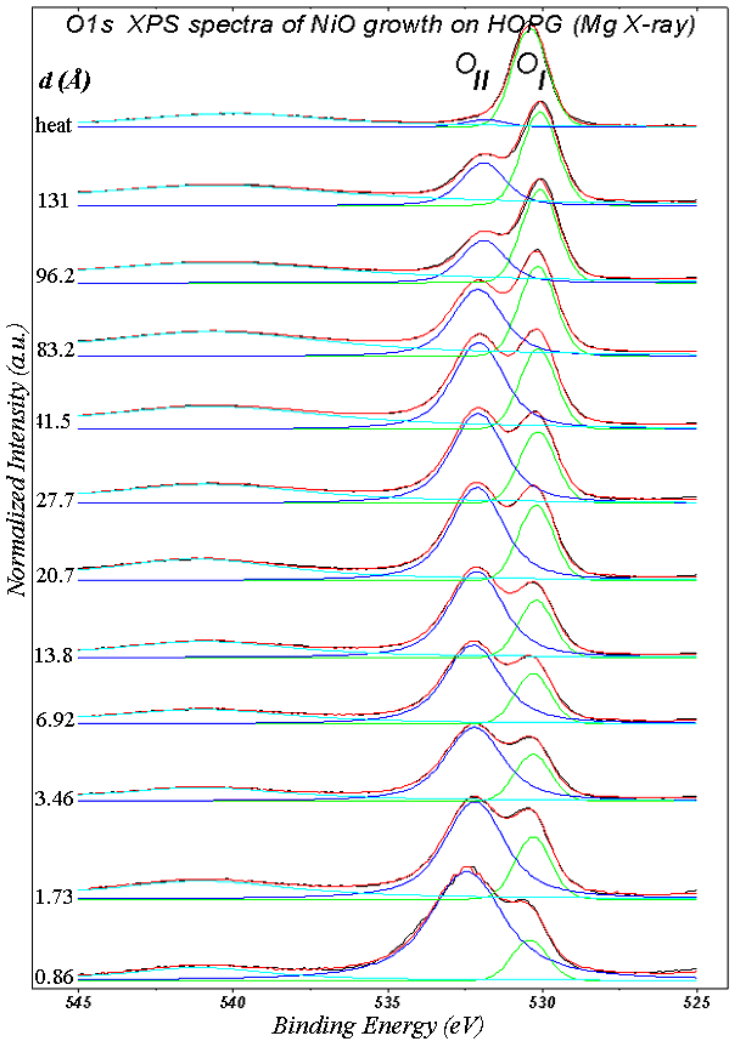

Fig.IV.38 Fittings of O 1s XPS spectra along the growth.

It is worthy to note here that the peak at 532.5 eV is much broader (FWHM of O_{II} = 2.2 eV) than that at 530.0 eV (FWHM of O_I = 1.3 eV). By comparing the evolution through the growth process of both O_I and O_{II} peaks intensities ratio with the evolution of the main-line and surface peaks intensities ratio from the Ni2p XPS spectra, in figure IV.39, the high intensity of the O_{II} peak in the O *1s* spectra seems to be accompanied by the high intensity of the surface peak.

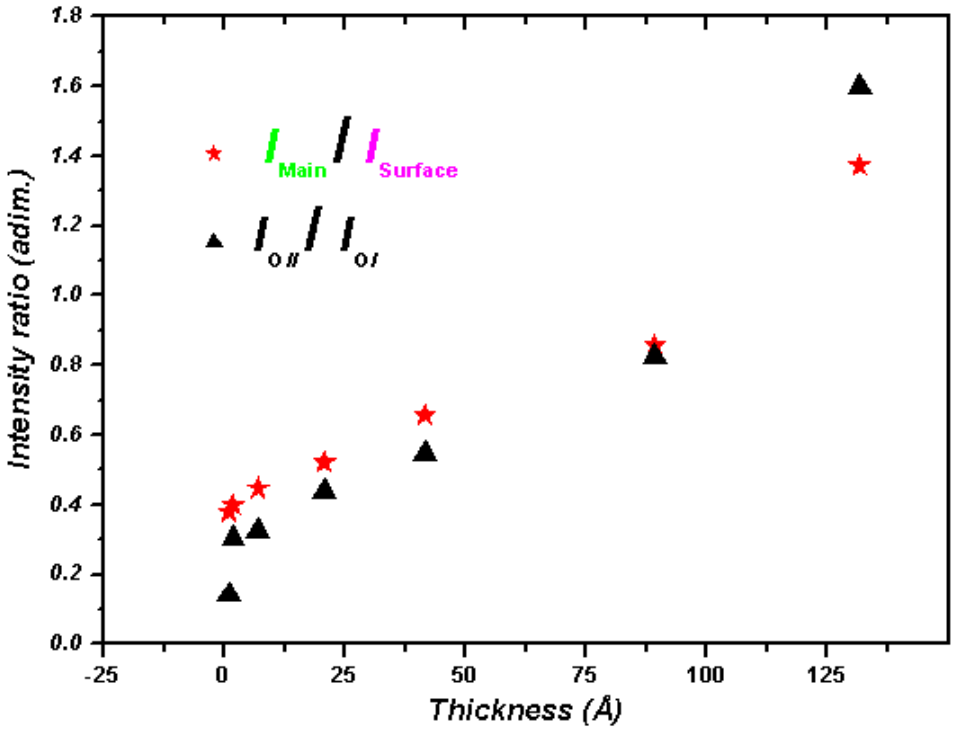

Fig.IV.39. Evolution with thickness of the intensity ratios: main/surface fitting assigned curves of Ni 2p3/2 XPS spectra (red), and O_I/O_{II} fitting assigned curves of O 1s XPS spectra (black).

It is clearly that both ratios have the same behavior which indicates that the presence of the O_{II} peak is strongly related to the shoulder of the Ni2p XPS spectra.

So that, the O_{II} peak will belong to the adsorbed oxygen species in the NiO islands formed until coalescence is reached. This assignment is also supported by the presence of Ni *3d* unsaturated NiO bands, as deduced from O *1s* XAS spectra.

In this picture, the adsorbed oxygen species by these nanostructures seems to be a reasonable model.

CONCLUSIONS

In this chapter, a morphological study of the different stages of growth of NiO on HOPG has been studied by means of quantitative analysis of the XPS background (QUASES method) and AFM. It has been shown that the early stages of growth correspond to the formation of nanometric cuasibidimensional islands of 100 nm in size and 20-70 Å in height. Further evaporation produces coalescence at about a thickness of about 60 equivalent ML. The agreement between the QUASES method and the AFM images gives support to this study.

Surface effects have been observed by the O *1s* XAS spectra for the early stages of growth. Indeed, a splitting of the Ni 3d states from the Ni atoms located at the surface has been observed. These results have been supported by cluster calculations in octahedral and pyramidal symmetries.

Surface enhanced Ni *2p* XPS spectra have demonstrated the significant contribution of the pyramidally coordinated Ni atoms at the NiO surface to the spectra. The known shoulder of the Ni *2p* XPS spectra has been attributed to a combination of surface and non-local peaks. This model allows represent the spectral weight of the shoulder energy region as a contribution of three main curves: bulk, surface and non local. In this picture, new HAXPES spectra of the Ni *2p* and Ni *1s* core levels of NiO have been measured and fitted in the same terms as those obtained by XPS. It has been demonstrated that the bulk/surface contribution ratio follows a similar behavior than that of the inelastic mean free path. This fact strongly supports the proposed model.

Finally, the growth process of NiO on HOPG has been studied by XPS. The Ni *2p* XPS spectra show that for the early stages of growth, where nanostructured NiO is formed according to the AFM images, the intensity of the surface component dominates the spectra, being completely consistent with the surface + non local model. The higher binding energy peak of the O *1s* XPS spectra have been assigned to adsorbed oxygen species in the nanometric NiO islands of the early stages of growth. The intensity of this peak is always related to the surface component of the Ni *2p* XPS spectra.

REFERENCES

[1] C. Morant, L. Soriano, J.F. Trigo and J.M. Sanz, Thin Solid Films, 317, 59 (1998).

[2] S. Tougaard, Surf. Interface Anal. **26**, 249 (1998).

[3] F.M.F. de Groot, J.C. Fuggle, B.T. Thole, G.A. Sawatzky, Phys. Rev. B 41 (1990) 928.

[4] F.M.F. de Groot, J.C. Fuggle, B.T. Thole, G.A. Sawatzky, Phys. Rev. B 42 (1990) 5459.

[5] M. Abbate, F.M.F. de Groot, J.C. Fuggle, A. Fujimori, Y. Tokura, Y. Fujishima, O. Strebel, M. Domke, G. Kaindl, J. van Elp, B.T. Thole, G.A. Sawatzky, M. Sacchi, N. Tsuda, Phys. Rev. B 44 (1991) 5419.

[6] L. Soriano, G. G. Fuentes, C. Quirós, J. F. Trigo, J. M. Sanz, P. R. Bressler, and A. R. González-Elipe, Langmuir 16, 7066 (2000).

[7] S. H¨ufner, Solid State Commun. 52 (1984) 793.

[8] J. Van Elp, B. G. Searl, G. A. Sawatzky, M. Sacchi, Solid State Commun. 80 (1991) 67.

[9] I. Davoli, A. Marcelli, A. Bianconi, M. Tomellini and M. Fanfoni, Phys. Rev. B **33**, (1986) 2979.

[10] L. Soriano, M. Abbate, J.Vogel, J.C. Fuggle, A. Fernández, A.R. González-Elipe, M. Sacchi, J.M. Sanz, Chem. Phys. Lett. 208 (1993) 460.

[11] M. A. van Veenendaal and G. A. Sawatzky, Phys. Rev. Lett. 70, 2459, 1993.

[12] M. J. Tomellini, J. Electron Spectrosc. Relat. Phenom. 58, 75 (1992).

[13] St. Uhlenbrock, Chr. Scharfschwerdt, M. Neumann, G. Illing, and H.-J. Freund, J. Phys.: Condens. Matter 4, 7973 (1992).

[14] J. M. McKay and V. E. Henrich, Phys. Rev. B **32**, 6764 (1985).

[15] F. Parmigiani, in *Cluster Models for Surface and Bulk Phenomena*, edited by G. Pacchioni *et al.* Plenum Press, New York, (1992), Vol. 1, p. 475.

[16] L. Sangaletti, L. E. Depero, and F. Parmigiani, Solid State Commun. 103, 421 (1997).

[17] M. Oku, H. Tokuda, and K. Hirokawa, J. Electron Spectrosc. Relat. Phenom. 53, 201 (1991).

[18] K. S. Kim and R. E. Davis, J. Electron Spectrosc. Relat. Phenom. 1, 251 (1972).

[19] M. Atanasov and D. Reinen, J. Electron Spectrosc. Relat. Phenom. 86, 185 (1997).

[20] D. Alders, F. C. Voogt, T. Hibma, and G. A. Sawatzky, Phys. Rev. B 54, 7716 (1996).

[21] S. Tanuma, C. J. Powell and D. R. Penn, Surf. Interface Anal. 37, 1 (2005).

[22] M. D. Towler, N. M. Harrison, and M. I. McCarthy, Phys. Rev. B 52, 5375 (1995).

[23] G. van der Laan, C. Westra, C. Haas, and G. A. Sawatzky, Phys. Rev. B 23, 4369 (1981).

[24] G. Zampieri, F. Prado, A. Caneiro, J. Briatico, M. T. Causa, M. Tovar, B. Alascio, M. Abbate, and E. Morikawa, Phys. Rev. B 58, 3755, (1998).

[25] L. Soriano, A. Gutiérrez, I. Preda, S. Palacín, and J. M. Sanz, Phys. Rev. B 74, 193402, (2006).

[26] M. A. van Veenendaal, G. A. Sawatzky, *Phys. Rev. Letter*., 70, 2459, 1993.

[27] J.Rubio-Zuazo, M.Escher, M.Merkel and G.R.Castro, Journal of Physics: Conference Series 100 (2008) 072032.

Chapter V

INTERFACE EFFECTS IN NiO/OXIDES

V.1 INTRODUCTION

Oxide thin films have become key materials in many technological applications such as catalysis, magnetic supports, materials with unique mechanical and thermal properties, sensors, etc. In all these applications, the control of the growth of the thin films is of extreme importance. In particular, the knowledge of the mechanisms influencing the growth at the interface could lead to the control of the thin film final properties. Therefore, the study of oxide/oxide interfaces seems to be well justified. In spite of this impact, studies on oxide/oxide interfaces have been scarce in the literature until the appearance of several works on oxide surfaces in the early 1990's[1,2,3,4]. In these works, the authors proposed the growth of thin oxide films on a conductive support in order to avoid charging problems during the characterization of the oxides. Since then, many works on oxide thin films have been done using different characterization techniques, in particular, x-ray and electron spectroscopies[5].

The oxide substrates (SiO_2, Al_2O_3, and MgO) have been chosen according to the nature of their chemical bonding (from a more covalent to a more ionic character). Interesting trends in terms of covalency-ionicity of the substrates have already been observed[6,7] in the study of the electronic structure of TiO_2/oxide interfaces with synchrotron radiation spectroscopies.

In the work presented here, the oxide substrates have been prepared as thin films following different conventional methods on conductive supports. The substrates do not present a long range order being polycrystalline. In spite of that, a lot of important information can be extracted from the Ni 2*p* XPS spectra of these non-ordered systems.

In this chapter, as in the previous one, the analysis starts with the study of the morphology of the NiO deposits on the different oxides by means of the inelastic background analysis following the Tougard method. Unfortunately the combination of this analysis with AFM images has only been possible in the case of the SiO_2 substrate which presents a very low roughness and allows such study. For the Al_2O_3 and MgO substrates, their high roughness did not permit the AFM analysis of the NiO deposits.

Then, a detailed study of the growth of NiO on the selected oxides is presented. As in the case of the growth of NiO on HOPG, surface effects appear for the early stages of growth. The model proposed in the previous chapter for the interpretation of the Ni *2p* photoemission

spectra has also been used in the interpretation of the growth of NiO on these selected substrates. Even more, this model explain the differences in the electronic structure of the NiO/Oxide interface which rise from the covalent to ionic character of the substrates. These interface effects leads to conclusion of the Ni-O-M (M=Si, Al, Mg) cross linking bound formation.

Finally, the potential of NEXAFS has been explored in the analysis of NiO/Oxide interface. The results confirm the conclusions obtained by photoemission study.

The experimental details have been given in the chapter three of this work. Here, some details about the substrates are reminded. The AFM images of these substrates are shown in figure V.1. The silicon oxide shows flat areas with a few contaminants, some of them, prior to the oxide growth: produce a small depression in the oxide around. The roughness is less than half a nanometer as expected from the oxidation of a polished Si single crystal. The Al_2O_3 oxide has an intermediate roughness of 39 nm, which is consistent with the roughness of an oxidized Al polycrystalline sheet. The largest value of the RMS roughness corresponds to the MgO substrate (165 nm). The relatively large roughness for the MgO substrate is produced by the formation of faceted crystallites of about 1 μm size.

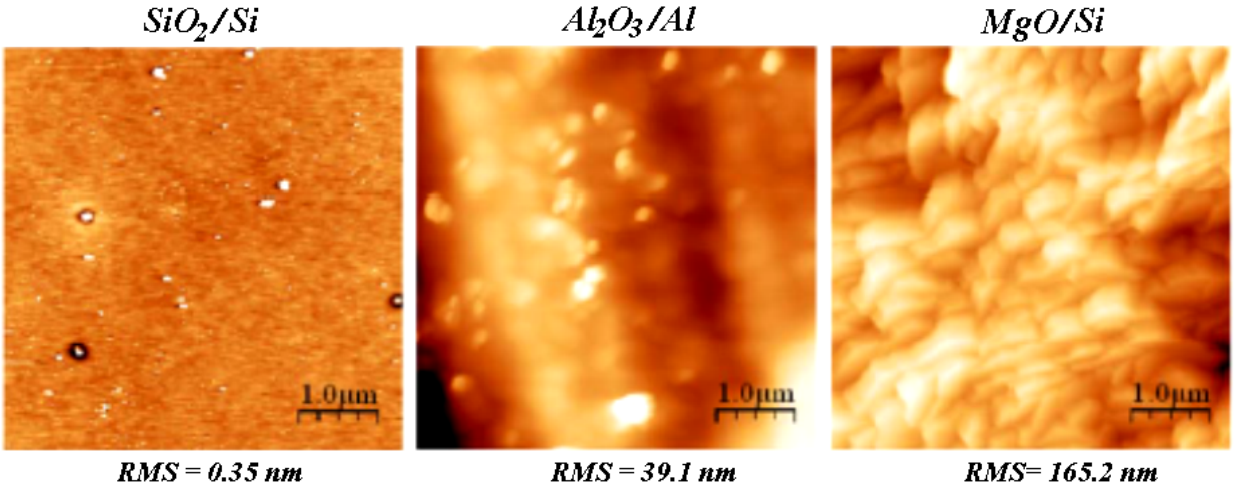

Fig.V.1. AFM topographic images (5x5 μm^2) of the different oxide surfaces, measured in dynamic mode (tapping). RMS (root mean square) roughness values are given for comparison.

V.2. MORPHOLOGICAL STUDY OF THE GROWTH OF NiO ON OXIDES

V.2.1. QUANTITATIVE ANALYSIS BY MEANS OF XPS INELASTIC PEAK SHAPE

As in NiO growth on HOPG case, a detailed XPS study was made in the growth process of NiO deposited on SiO_2, Al_2O_3, and MgO.

In figures V.2, V.3 and V.4 the survey scans for all stages of NiO deposition on each substrate case, SiO_2, Al_2O_3 and MgO, respectively, are presented. The marked regions were used in the quantitative analysis of the way of growth study. The ratios of the intensities of the NiO overlayer (Ni *2p*) and the corresponding main peak of the substrate (Si *2p*, Al *2p* and Mg *2p*) are indicated in the spectra; figure V.2, V.3, V.4 respectively, as a measure of the deposition stage.

It can be seen how the intensity of the Ni *2p* XPS spectra is progressively increasing as the deposition time increases. In turn, the intensity of the substrate selected peak decreases with the deposition time, facts pointed in figure V.5 and V.6, respectively.

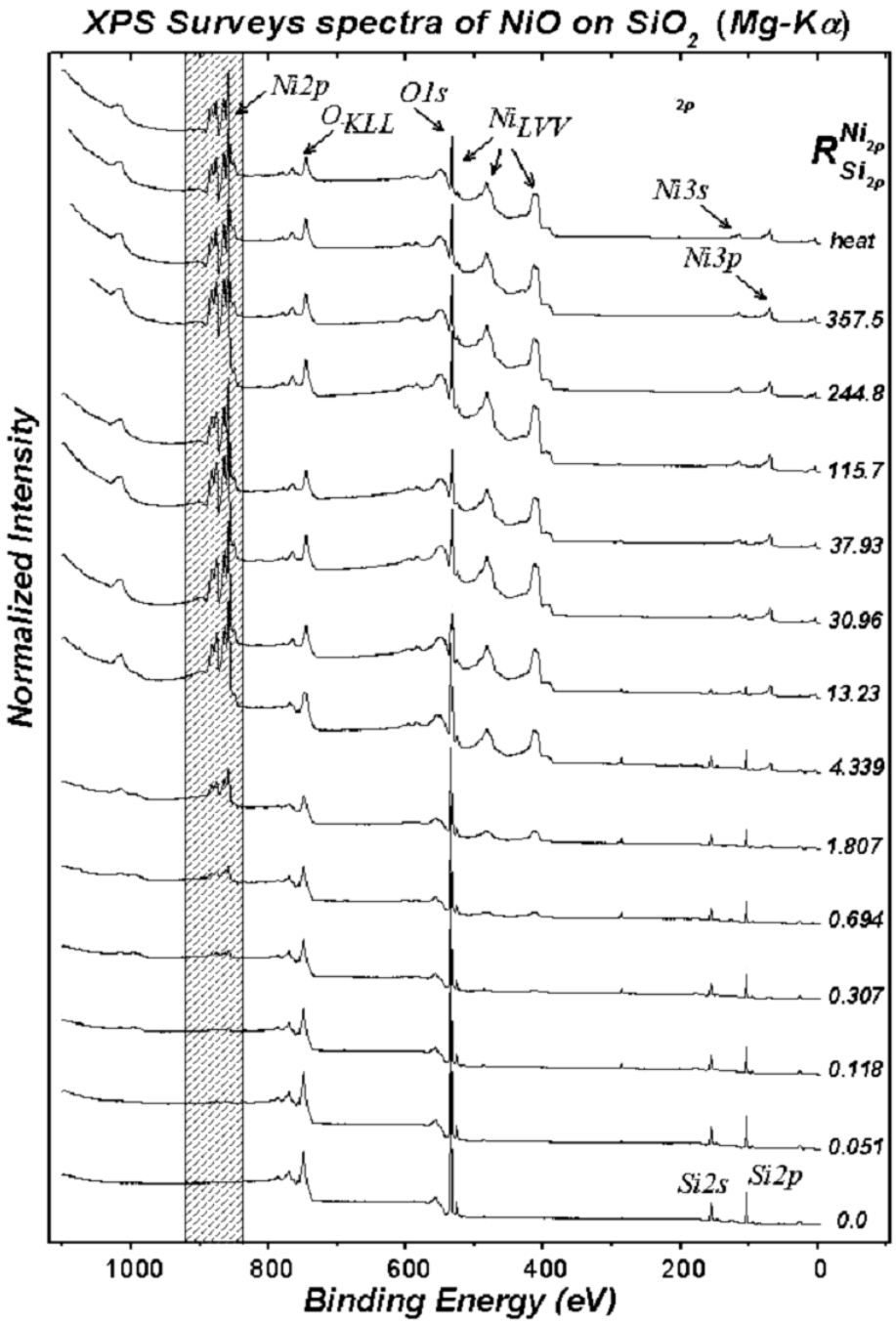

Fig.V.2. XPS surveys spectra of the NiO growth on SiO_2 process.

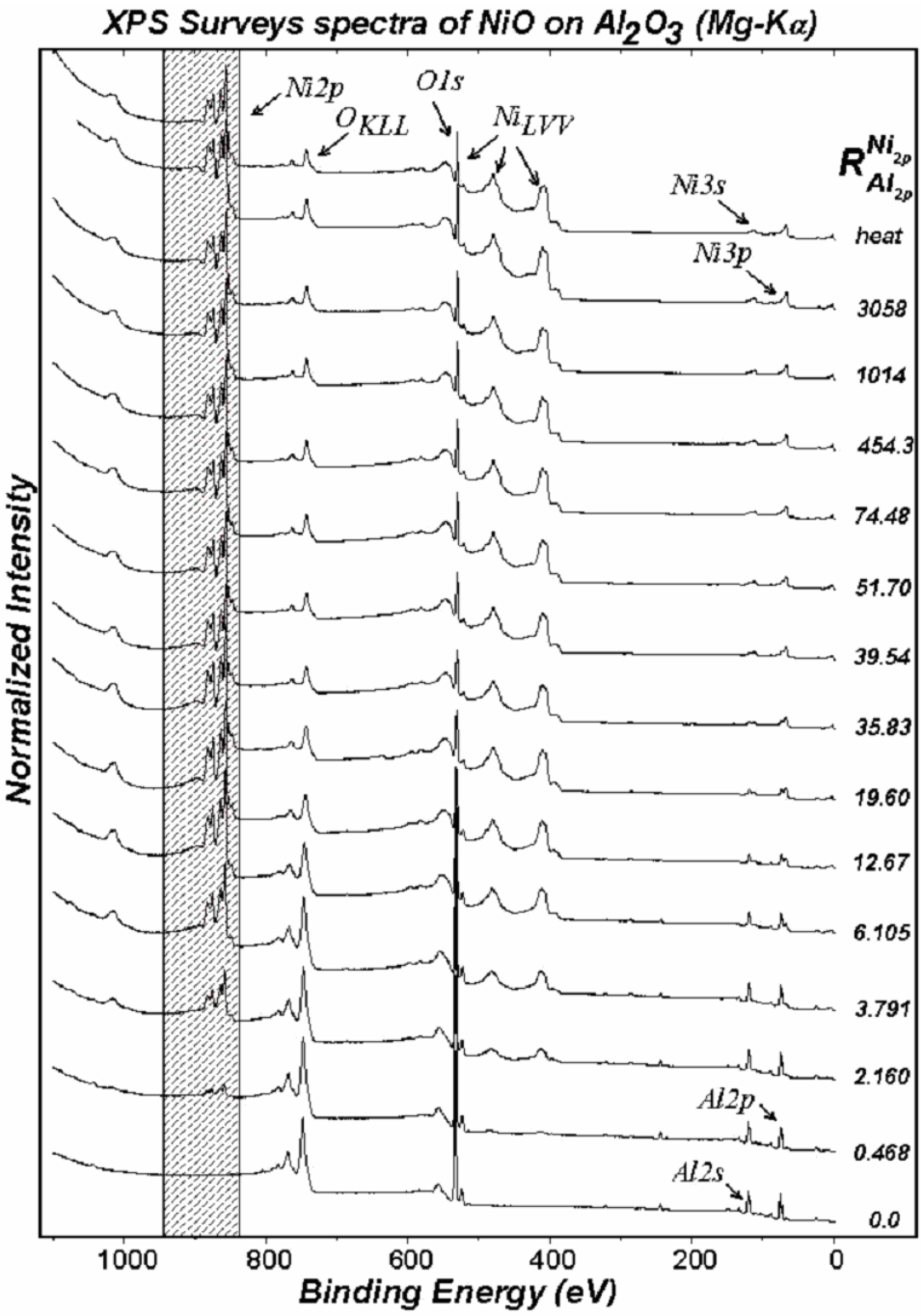

Fig.V.3. XPS surveys spectra of the NiO growth on Al_2O_3 process.

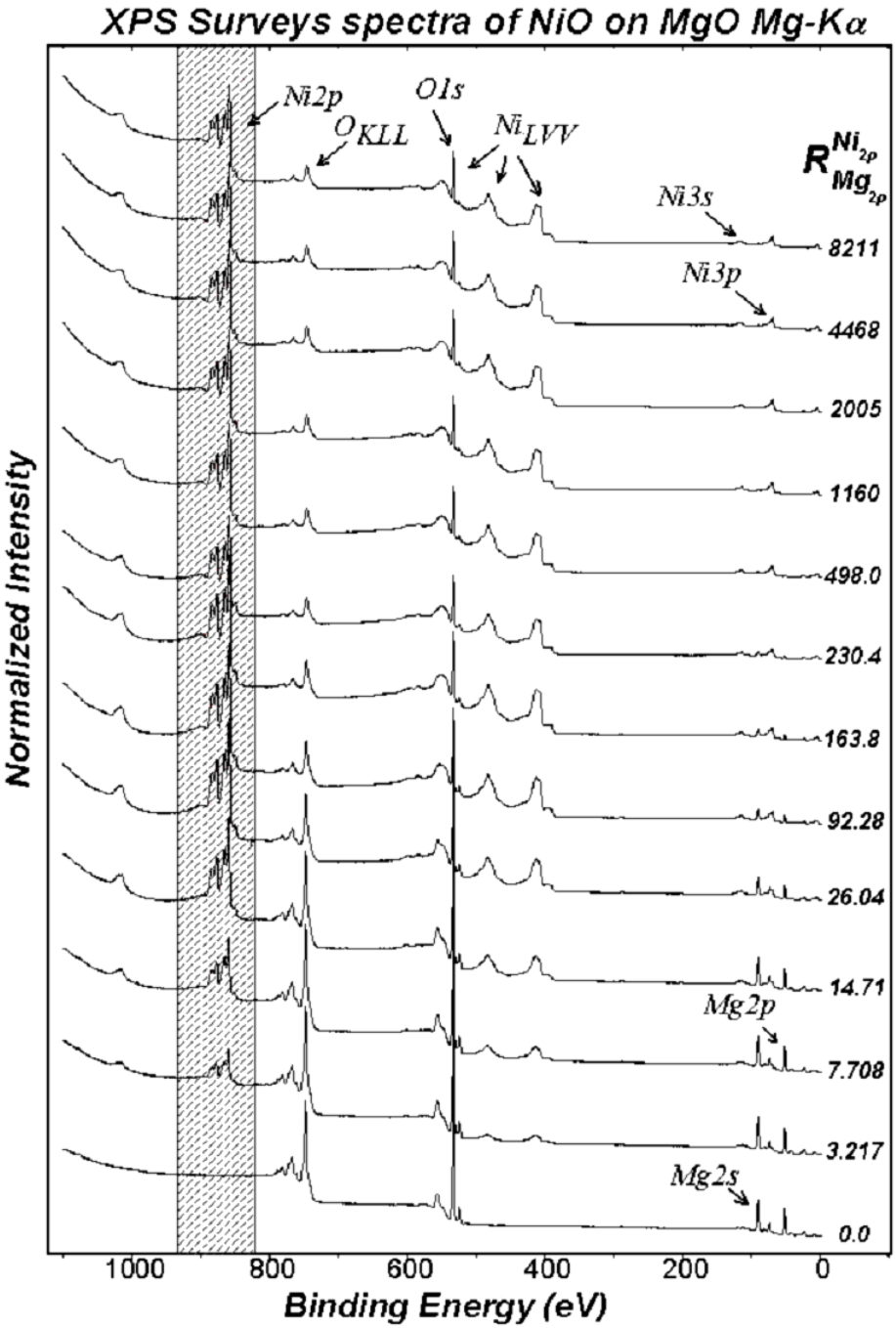

Fig.V.4. XPS surveys spectra of the NiO growth on MgO process.

In figure V.5 the evolution of Ni *2p* XPS intensity versus evaporation time is represented, in order to follow the NiO growth process. It can be seen that the intensity, in each substrate, present a coherent evolution, starting with very low values, for the early stages of growth, and reaching a maximum value around 60 minutes of deposition. After that stage, the detection limits of the experimental technique used (XPS) is reached and no more intense Ni *2p* XPS peak is measured. However, this maximum value in each case is different.

This could be due to the different measurements conditions i.e. sample – analyzer distance (±0.05 mm error), etc.

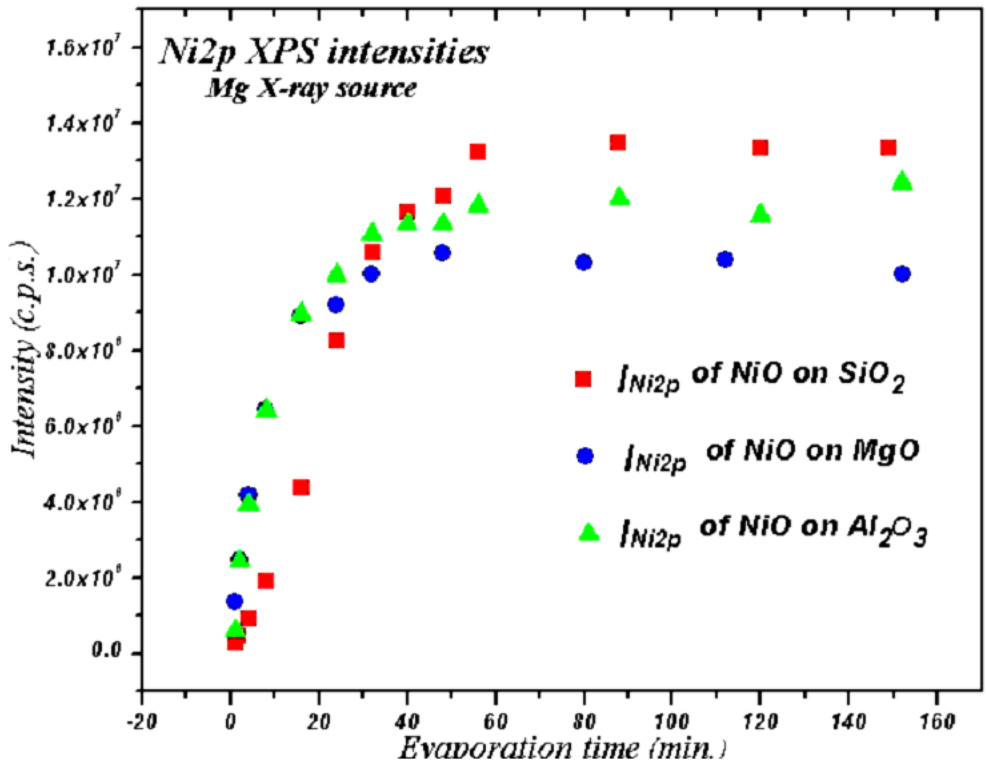

Fig. V.5. Absolute Ni 2p XPS intensities vs. deposition time along the growth processes.

At the same deposition time value (60 minutes), in the figure V.6 it can be seen that the intensity of the substrate XPS peak is reaching a minimum value as expected. In turn, the maximum values of the substrate characteristic peak is different and this is explained in terms of different mean free path of the photoelectrons in each case and also different sensibility factor of the *2p* core level of Si, Mg, and Al.

Figure V.6 shows the behavior of the intensity of the most intense peak of the substrate, Si *2p*, Al *2p* and Mg *2p*, respectively.

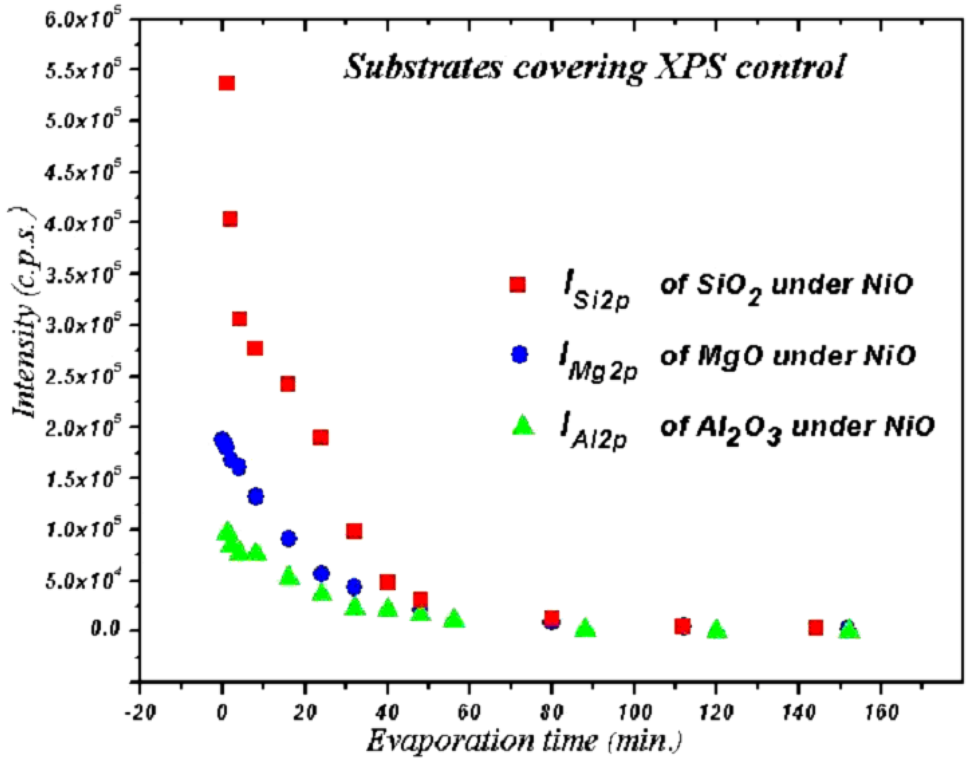

Fig. V.6. Absolute XPS substrate characteristic peak versus deposition time.

V.2.2. QUASES RESULTS FOR GROWTH OF NiO ON OXIDES

As mentioned above, a quantitative analysis of the first stages of NiO growth on SiO_2, Al_2O_3, and MgO by means of XPS inelastic peak shape analysis has been performed. As a first conclusion, the results in figure V.7 reflect that the way of growth of NiO on all the substrates studied here is through the Stransky-Krastanov-like mode, i.e., growth of small islands of a determined height at the early stages of growth. This is in contrast to the layer-by-layer growth found for a MgO(100) single crystal[8]. However, it can be explained as due to the formation of many nucleation centers at the grain boundaries of the polycrystalline material The results suggest that small NiO aggregates (size below 20 Å) are formed; therefore, it seems reasonable that the Ni 2*p* XPS spectra of these nanostructured NiO systems are dominated by the surface component. For further deposition the NiO aggregates slowly increase its average heights but the surface covered is much higher. Once 60-70% of the substrate surface is covered the NiO aggregate's height vs. coverage curve is increasing the slop. The entire substrate is covered in a height's range out of the QUASES limits detection.

The mean island height and the coverage values given by this analysis are presented in the table V.1 a) for NiO/SiO_2, b) for NiO/Al_2O_3 and c) NiO/MgO, and are represented in the figure V.7.

Table V.1.a: QUASES RESULTS of NiO/SiO_2 Ni 2p and Ni Auger LVV

NiO on SiO_2						
Evaporation time (min) [Thickness(Å)]	Ni LVV Auger analyzed			Ni2p analyzed		
	high (Å)	coverage (%)	Equivalent thickness (Å)	high (Å)	coverage (%)	Equivalent thickness (Å)
1 [0.4]	-	-	-	-	-	-
2 [0.7]	-	-	-	17	3.1	0.52
4 [1.4]	-	-	-	19	6.3	1.19
8 [3.02]	24	11.8	2.83	23	12.4	2.8
16 [7.55]	29	24.4	7.0	27	27.4	7.3
24 [17.3]	31	44.7	13.8	32	48.8	15.6
32 [41.7]	40	76	30.4	42	81.7	34.3
40 [69.0]	60	91.7	55.0	60	92.5	55.5

Table V.1.b: QUASES RESULTS of NiO/Al_2O_3 Ni 2p and Ni Auger LVV

NiO on Al_2O_3						
Evaporation time (min) [Thickness(Å)]	Ni LVV Auger analyzed			Ni2p analyzed		
	high (Å)	coverage (%)	Equivalent thickness (Å)	high (Å)	coverage (%)	Equivalent thickness (Å)
1 [0.61]	-	-	-	-	-	-
2 [1.20]	21	15.9	3.33	19	18.8	3.57
4 [2.40]	22	28.5	6.27	19	32.9	6.25
8 [4.80]	22	50.8	11.7	22	51.2	11.2
16 [9.61]	32	67.5	21.6	33	69.5	22.9
24 [14.4]	40	74.7	29.8	38	79	30.0
32 [24.0]	45	89.5	40.1	45	87.7	39.4
40 [33.6]	56	93.2	52.1	55	90.5	49.7
48 [52.8]	64	100	64	66	93.8	61.6
56 [72.1]	71	100	71	71	93.8	66.5
88 [91.3]	120	100	120			

Table V.1.c: QUASES RESULTS of NiO/MgO Ni 2p and Ni Auger LVV

NiO on MgO (Ni Auger analyzed)						
Evaporation time (min)	Ni LVV Auger analyzed			Ni2p analyzed		
	height (Å)	coverage (%)	Equivalent thickness (Å)	height (Å)	coverage (%)	Equivalent thickness (Å)
1	23	10.3	2.36	19	14.9	2. 83
2	27	17.2	4.64	19	25.8	4.90
4	30	31.3	9.39	20	43.9	8.78
8	32	50.0	16.28	26	62.6	16.2
16	40	74.6	29.84	34	85	28.9
24	49	76.9	37.68	48	79.8	38.3
32	62	89.3	55.36	52	96.1	49.9
48	65	97.2	63.18	69	98.8	68.1
80	95	99.2	94.24	95	97.5	92.6

This way of growth is the same for each substrate. For equivalent NiO amount deposited below 1 ML the NiO islands are about 20 Å height.

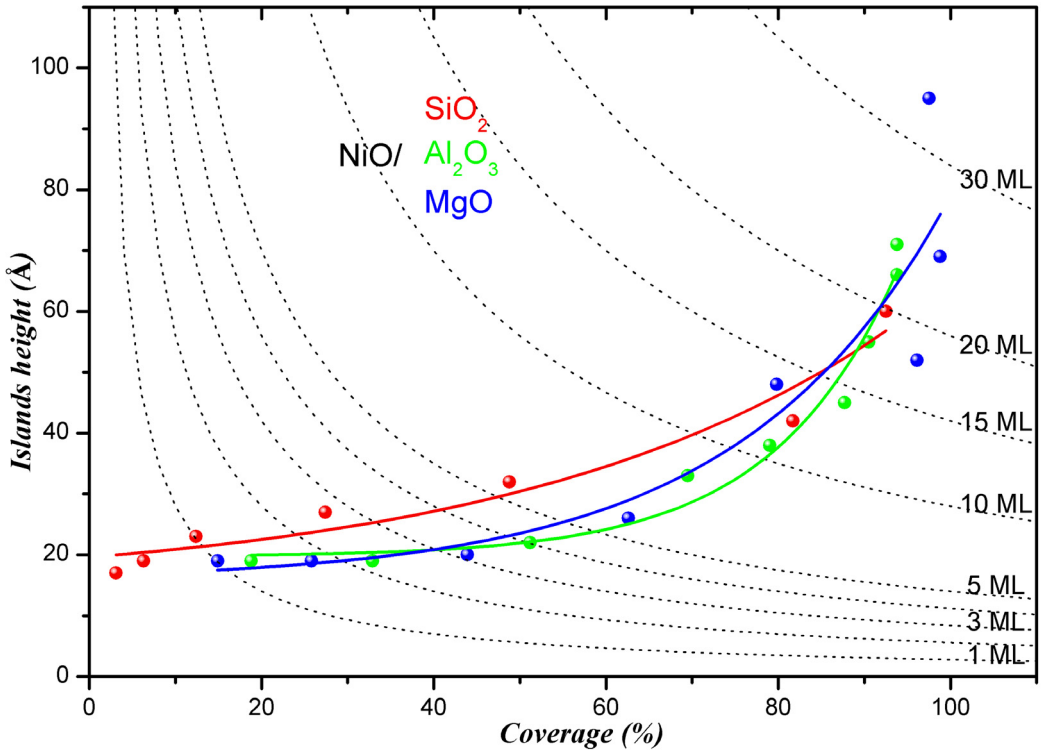

Fig.V.7. Quantitative analysis (average particle height versus surface coverage of the NiO growth on SiO_2 (red), Al_2O_3 (green), and MgO (blue) by means of XPS inelastic peak shape analysis using QUASES software. Doted lines indicate equivalent amount of NiO deposited material.

V.2.3. NiO/SiO_2 AFM STUDY

The Atomic Force Microscopy study of the NiO/SiO_2 growth was performed in order to probe the very early stages of the growth, were QUASES is limited. This system allowed study because of its very low RMS value (0.35 nm). In the case of Al_2O_3 and MgO substrates this study was not possible because of the very high roughness of these systems as shown in figure V.1.

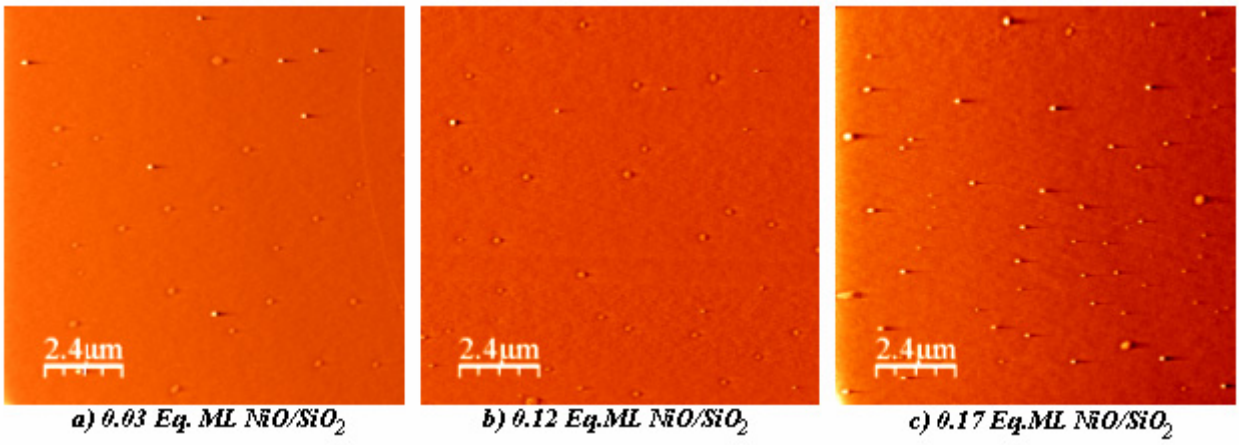

Fig.V.8. AFM images of different growth stages of NiO on SiO_2: a)0.03 eq. monolayer; b) 0.12 eq. monolayer; c) 0.17 eq. monolayer

In the pictures above it can be seen the first three stages of NiO growth on SiO_2 a) 0.03 Eq.ML, b) 0.12 Eq. ML, and c) 0.17 Eq. ML, all out of the limit detection of QUASES. It is reminded here that the samples were measured in atmospheric pressure and for this reason some contamination can be observed on the substrate.

Looking at the AFM images no doubt remains about the growth of NiO is dominated by the formation of small NiO islands. The topographic profile analysis (see all values in the appendix section) of every island for each sample gives the statistic presented in the table V.2.

Table V.2. Statistic results of the NiO growth on SiO_2 AFM topographic profile analysis.

NiO material amount (eq. Ml.)	*Mean number of NiO islands*	*Coverage (%)*	*NiO island mean height (Å)*	*NiO islands mean diameter (nm)*
0.03	*30*	*0.87*	*9*	*230.8*
0.12	*26*	*2.65*	*12.4*	*532.6*
0.17	*65*	*2.94*	*15.2*	*288.2*

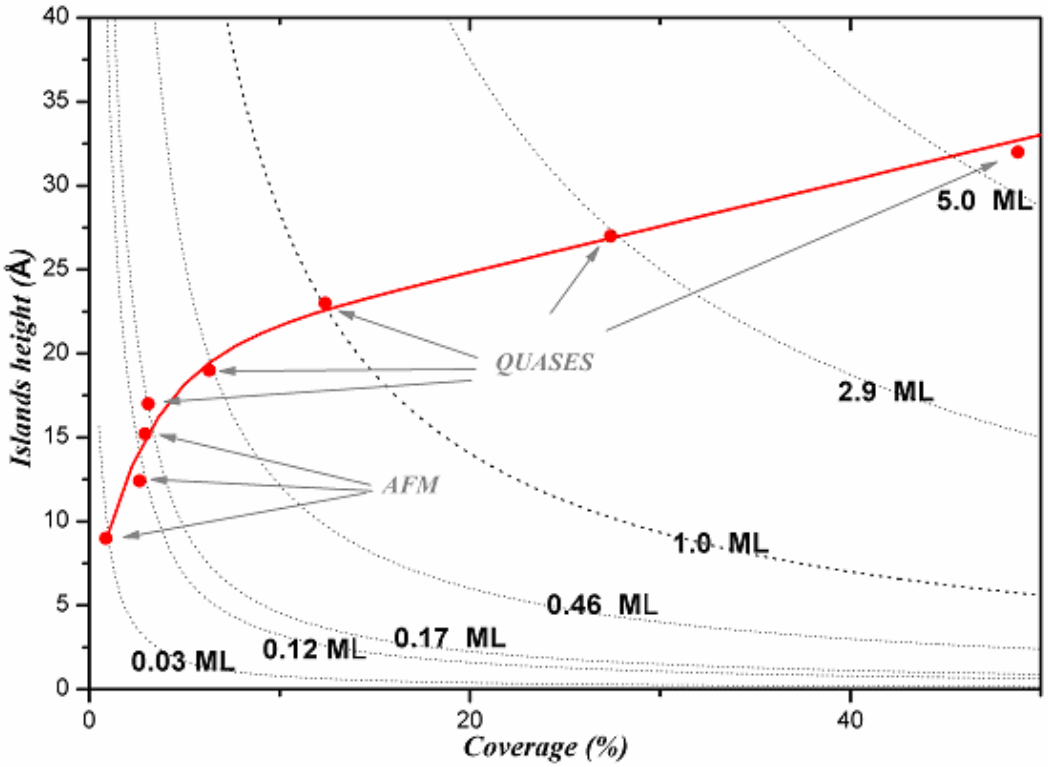

Fig.V.9. Zoom of figure V.7, islands heights versus coverage, for first stages of NiO growth on SiO_2, QUASES – AFM complementary obtained values.

In the figure above, these values together with the QUASES values obtained at its low limit of detection are represented. It can be observed the coherency of the way of growth. So, the full growth process can be now described: the very early stages are dominated by formation of NiO islands with mean heights of 15 Å and mean diameters of 300 nm. Further deposition produces small increase of the islands height, but the covered substrate surface is proportional with the deposited NiO amount. As the coverage reach about 70% of the

substrate surface the islands height vs. covered surface curve, increase its slope. By extrapolation, the full coverage is obtained for islands of about 75-80 Å heights.

V.3. STUDY OF THE GROWTH OF NiO/OXIDES BY XPS

NiO/oxide systems have been extensively studied, but mainly related to the preparation of supported catalysts[9,10,11]. In particular, the growth of thin NiO films on MgO has been studied in more detail[12,13,14,15,16,17]. NiO has been found to grow epitaxially on MgO(100) single crystal[8]. Studies on the electronic structure by XPS during the growth process of NiO on MgO(100) show that for a coverage of 1 ML, the main line of the Ni 2*p* XPS spectra is narrowed and slightly shifted to higher binding energies. In one of the studies, this effect was explained in terms of non-local screening[12], whereas in another work, this peak was assigned to the $\underline{c}3d^9$-3*d* (where 3*d* stands for a hole in the Ni 3*d* orbitals) final state configuration[14]. Structural studies on NiO grown on MgO(001) show that, initially, the overlayer NiO lattice grows coherently until a critical thickness thickness of 60 nm is reached, at which relaxation of the NiO lattice occurs[16]. On the other hand, the work of Warot *et al.*[17] shows that NiO grows forming different nanostructures depending on the MgO surface orientation, giving wires for MgO(110) and tetrahedrons for MgO(111).

The main aim of this part is the understanding the electronic structure of the interfaces formed by the deposition of NiO thin films on selected oxides, (SiO_2, Al_2O_3, and MgO). The experimental technique used in the study is x-ray photoelectron spectroscopy. The results presented in the previous chapter on the electronic structure of nanostructured NiO have shown that the lower symmetry at the NiO surface produces a splitting the unoccupied e_g states, as observed by means of the O 1*s* x-ray absorption (XAS)[18]. Besides, it has also been shown that the contribution to the Ni 2*p* XPS spectrum of the pyramidaly coordinated Ni atoms located at the NiO surface overlaps with the known shoulder at 1.5 eV higher binding energy from the main line in the Ni 2*p* XPS spectra of NiO, thus giving an important surface contribution to the shoulder[19]. In conclusion, the Ni *2p*3/2 photoemission spectra can be envisaged as the sum of four curves, including bulk, surface, non-local and satellite peaks.

These results open up a different scope in the interpretation the Ni 2*p* XPS spectra in nanoscopic systems such as NiO/oxide interfaces. By taking advantage of the above interpretations, it will be shown below that the Ni 2*p* XPS spectra of the NiO/oxide interfaces formed at very low NiO coverage the selected oxide not only contain a strong interface character, but also reflect the influence of the covalent bonding at the interface.

In figure V.10, V.11, and V.12 are presented the Ni *2p*3/2 XPS peak for the spectra for different depositions of NiO on SiO_2, Al_2O_3 and MgO respectively.

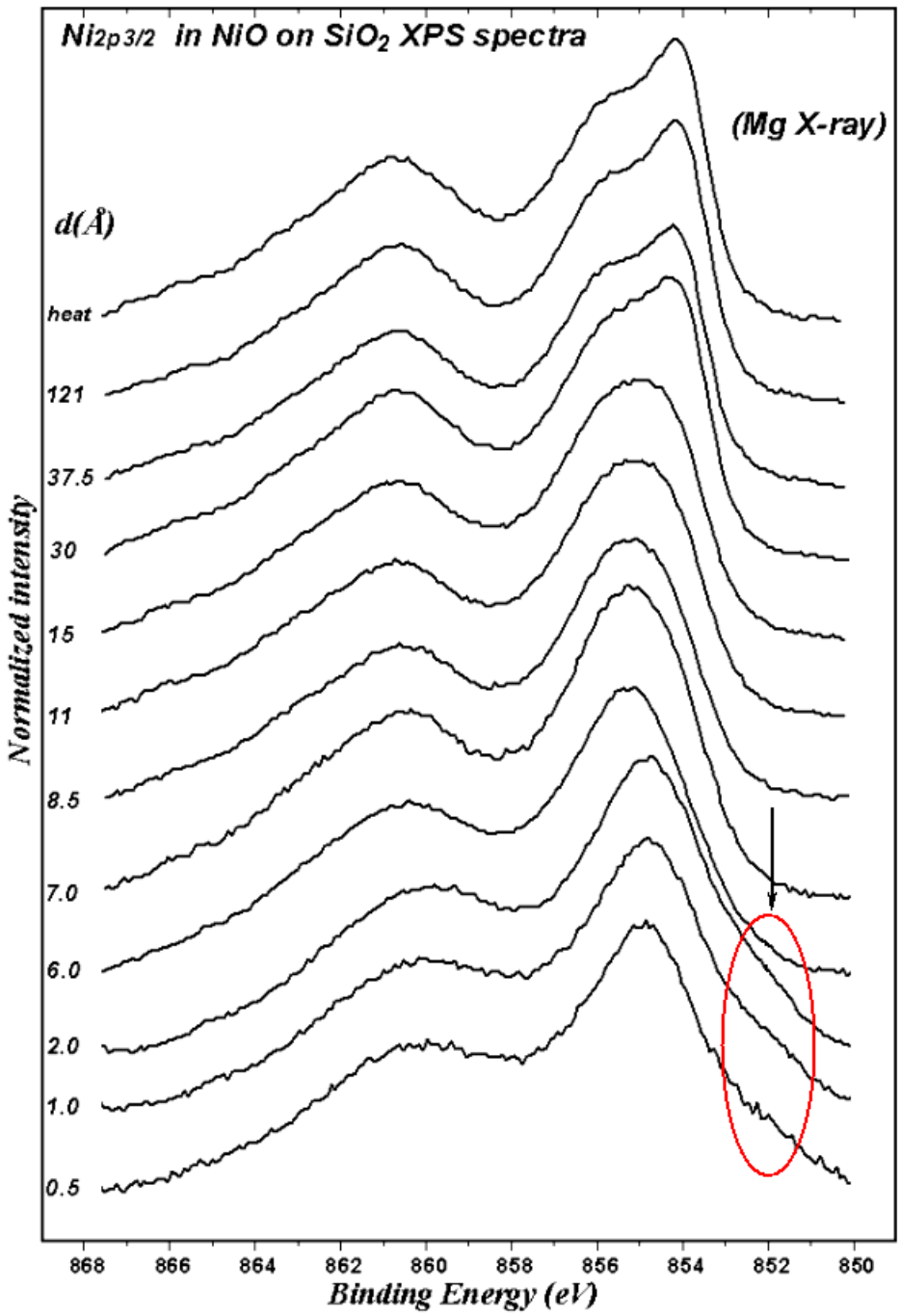

Fig.V.10. Ni 2p3/2 XPS spectra for NiO growth on SiO_2.

For the final stage of the growth of NiO on SiO_2, the Ni *2p*3/2 XPS peak shape, resemble the very well known shape of the bulk NiO. In turn, in the early stages of the growth, the double peak structure at 855 eV is not so well defined. It can also be observed that

for the very early stages of growth, a small amount of nickel remains unoxidized, which gets oxidized once the total equivalent NiO thickness is about 6 Å (app. 2 eq. ML).

In the case of the growth of NiO on Al_2O_3 (figure V.11), also some metallic Ni is observed, but it becomes oxidized when the NiO deposits reach an equivalent thickness of 1.2 Å (app. 0.5 eq. ML).

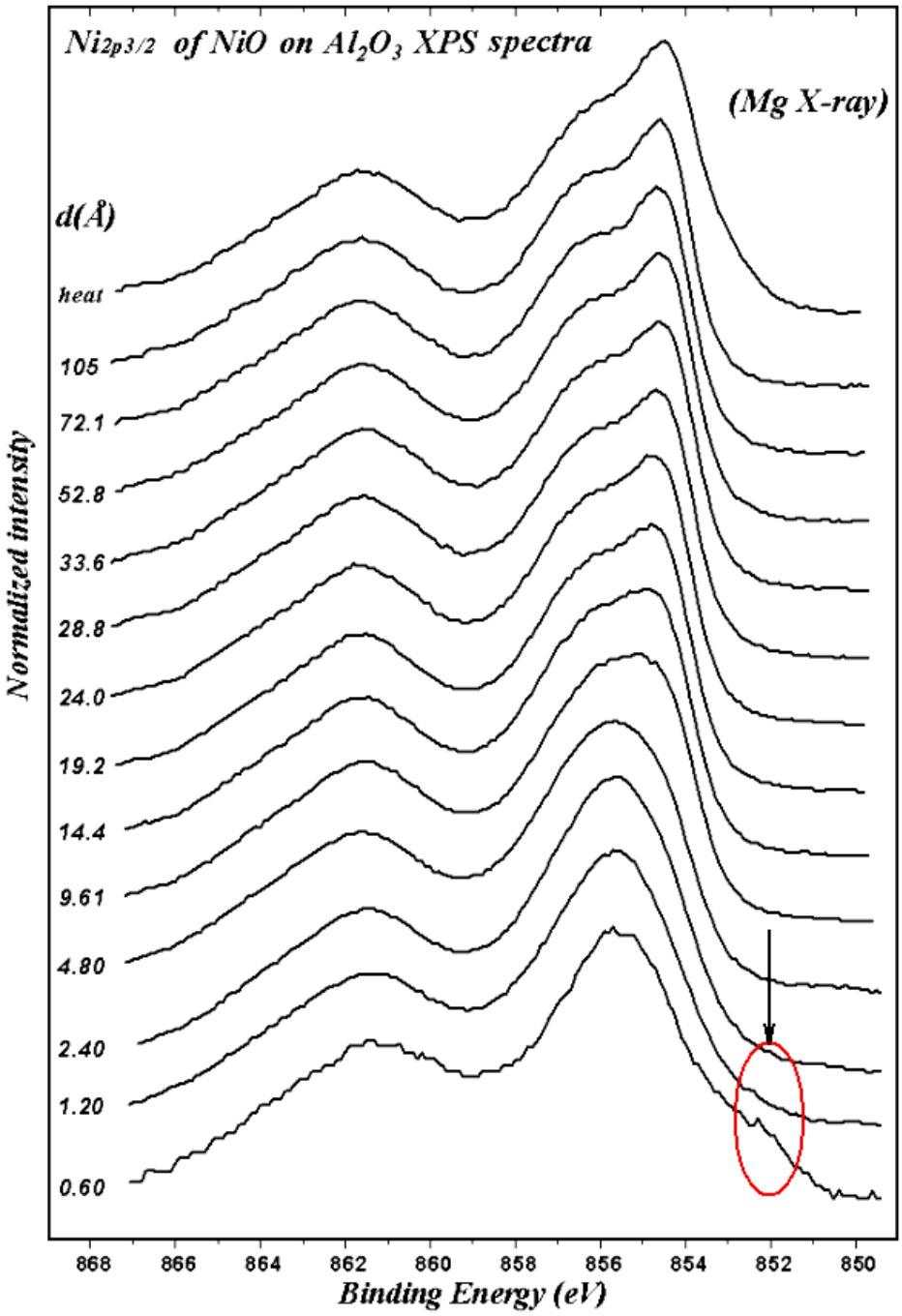

Fig.V.11. Ni 2p3/2 XPS spectra for NiO growth on Al_2O_3.

However, for the growth of NiO on MgO, the spectra shows that NiO becomes completely oxidized at the very early stages of growth, 0.5 Å ~ 0.2 eq. ML. It is worthy to note here that during the growth of NiO on SiO_2 and Al_2O_3, the oxygen pressure had to be increased one order of magnitude, (from $2x10^{-5}$ to $2x10^{-4}$ mbar).

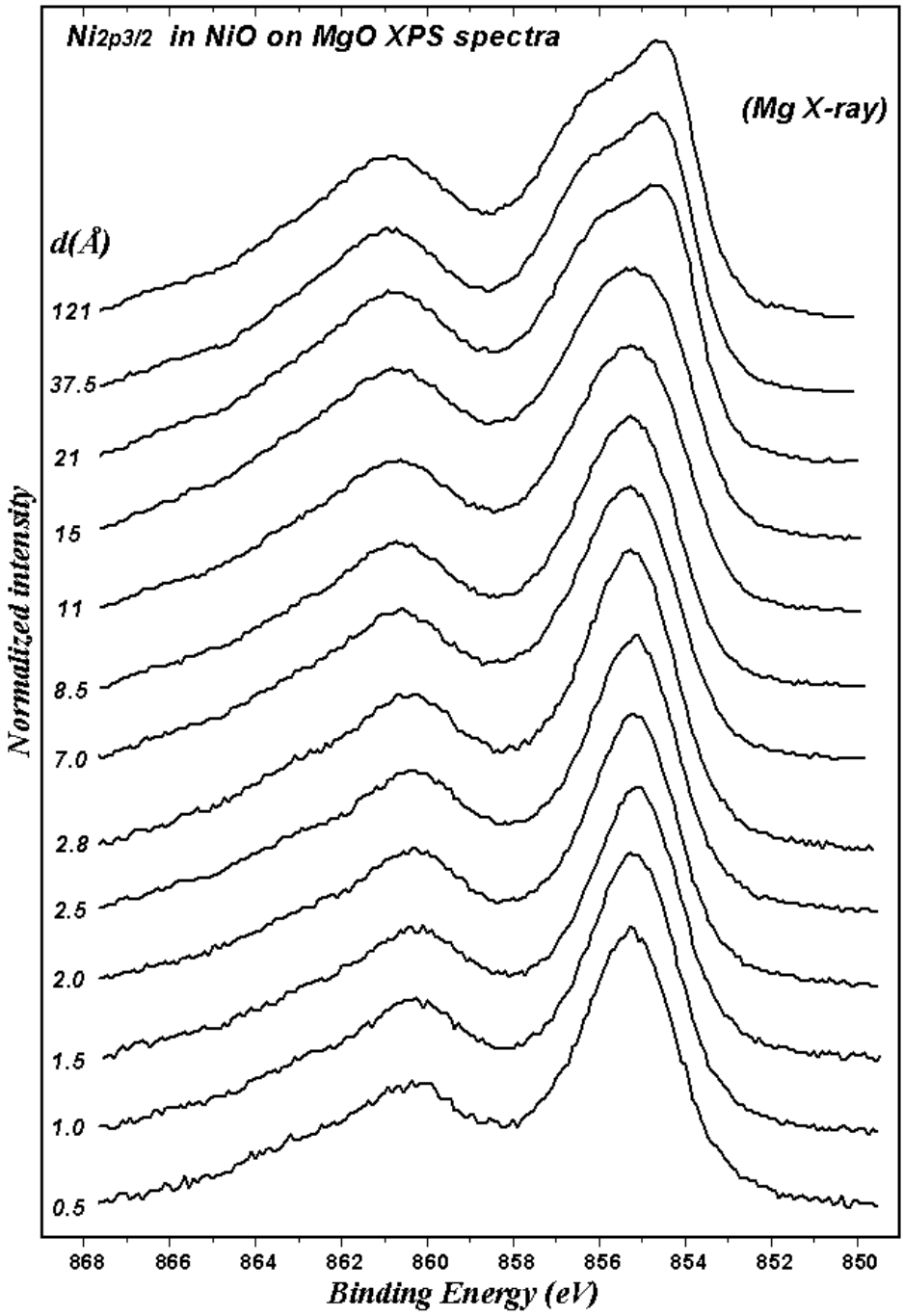

Fig.V.12. Ni 2p3/2 XPS spectra for NiO growth on MgO.

This behavior of the different oxide substrate can be explained in terms of lattice mismatch (see table V.3.).

Table V.3. Lattices parameters:

Oxide	Symmetry	Distance to oxygen (Å)
NiO	Octahedral	2.097
SiO_2	Tetrahedral	1.570-1.601
Al_2O_3	Octahedral	1.85-1.97
MgO	Octahedral	2.10

Indeed, as seen in table V.3, the lattice parameter of NiO is almost identical as that of MgO. Besides, the crystal structure is the same for both oxides (cubic ClNa type), so that is not surprising that NiO grows in an easy way on the MgO substrate. In fact, the epitaxial growth by reactive evaporation of Ni on NO_2 atmosphere, of NiO on a MgO (100) single crystal substrate has already been reported[12].

In order to analyze the spectra shown in figures V.10, V.11 and V.12 in more detail, the fitting of these has been performed according to the model presented in the previous chapter i.e. the Ni *2p*3/2 XPS peak is composed by four components: main line, due to $\underline{c}3d^9\underline{L}$ states coming from NiO_6 clusters, surface peak, due to $\underline{c}3d^9\underline{L}$ states coming from NiO_5 clusters at the surface, non-local screening peak, coming from the second O neighbors and the broad satellite coming from the mixture of $\underline{3d}^{10}\underline{L}^2$ and $3d^8$ direct photoemission states.

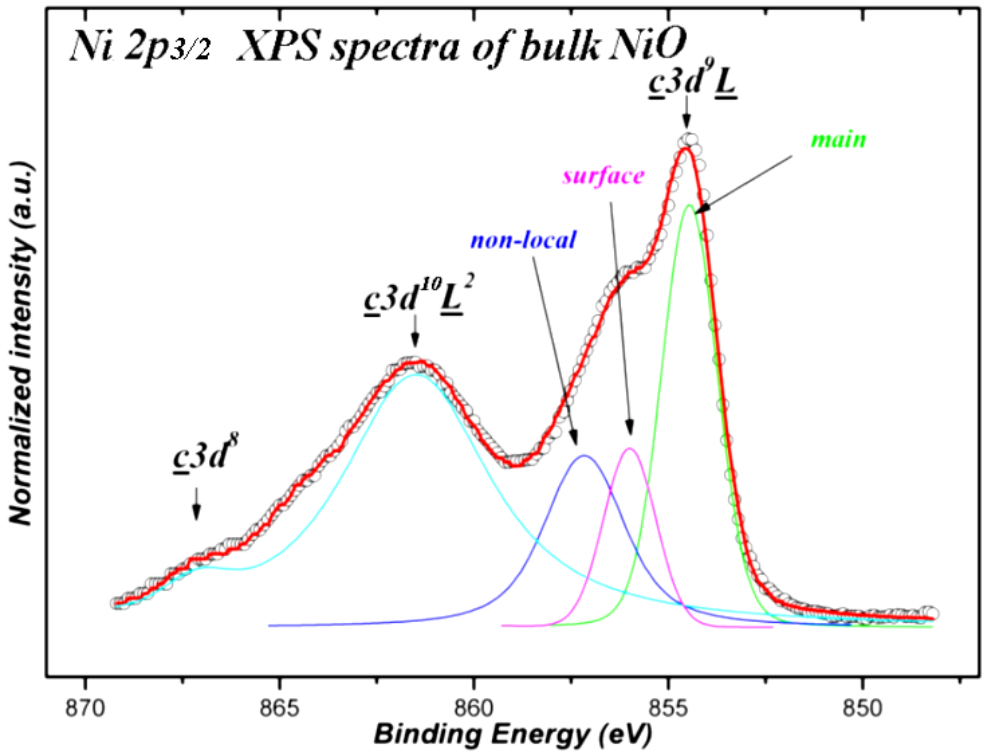

Fig.V.13. The new interpretation of Ni 2p3/2 XPS spectra.

As it will be shown below, the interpretation of the experimental Ni 2*p* XPS spectra of the NiO/oxide interfaces presented here is completely consistent with this model.

V.3.1. THE FINAL AND EARLY STAGES OF GROWTH

The Ni $2p_{3/2}$ XPS spectra for large NiO coverages, approximately 100 equivalent monolayers (Eq.ML), on the corresponding oxide substrates are shown in figure V.14. The bulk NiO reference spectrum has also been included for comparison purposes. In general, all the spectra have the same structures observed in the spectrum of the bulk NiO shown in figure V.13, although this was measured with a better energy resolution.

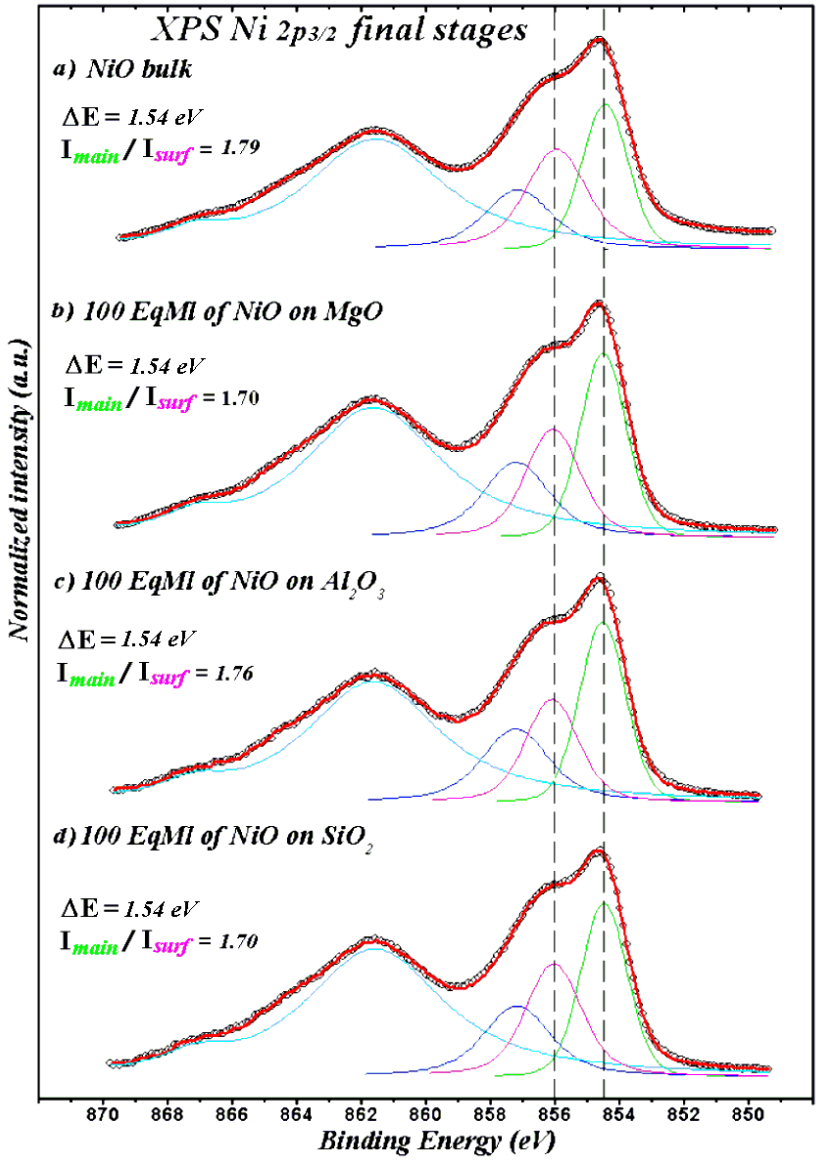

Fig.V.14. (a) Ni $2p_{3/2}$ XPS spectrum of a bulk NiO used as reference.(b-d) Ni $2p_{3/2}$ XPS spectrum of NiO thin films about 100 equivalent monolayer thick, grown on the different oxide substrates.

In order to analyze the peak intensities, all the spectra were fitted using four curves according to the calculations shown in the previous chapter: one for the main line at 854.5 eV, another two for the shoulder: one at 855.9 eV binding energy, for the surface component (pyramidally surrounded Ni), and a second one at 857.1 eV binding energy, assigned to the non-local screening effects. The fourth curve was used to simulate the charge transfer satellite at 861.5 eV.

Should be recalled here that in the entire fitting process the intensity ratio $I_{main} / I_{non\text{-}local} = 1.46$ was maintained constant and also the energy shift $\Delta E_{main\text{-}nonlocal} = 2.7$ eV. According to the calculations shown in figure IV. 26, the $I_{main} / I_{non\text{-}local}$ intensity ratio should be slightly higher. However, the best fittings of the experimental spectra are obtained for the above value. This minor discrepancy between theory and experiment can be neglected, if one looks to the energy separation value, which is in perfect agreement with the calculation value.

Further more, the NiO thin film has a larger effective surface than the NiO single crystal so that, according to the model suggested in the previous chapter and in reference 19, the surface component should be slightly higher. Finally, since all the spectra of the NiO thin films grown on the oxide substrates in figure V.14 are almost identical, we can conclude that a stoichiometric NiO thin film can be grown on any of the selected oxide substrates, and shows the same electronic structure as bulk NiO.

The most important features of the experiment appear for a very low coverage. Figure V.15 shows the Ni $2p_{3/2}$ XPS spectra of the early stages of growth (0.5–0.8 Eq.ML) of NiO on the different oxide substrates. The spectrum of bulk NiO, in figure V.15 a), was also included for comparison. In this case, the spectra of the NiO submonolayer do not match the spectrum of bulk NiO.

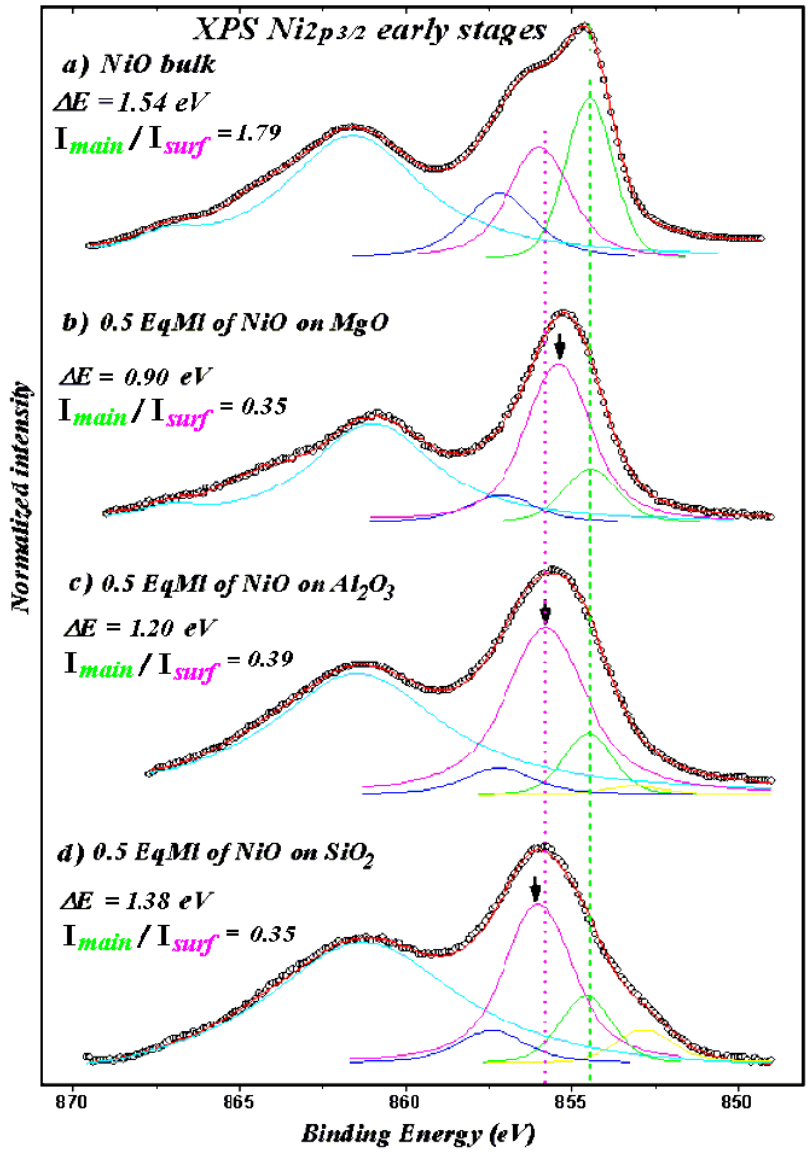

Fig.V.15. (a) Ni 2p3/2 XPS spectrum of bulk NiO, used as reference. (b-d) Ni 2p3/2 XPS spectra of NiO submonolayer (0.5 Eq. ML) grown on the different oxide substrates.

The most interesting feature of the spectra shown in figure V.15 is that the energy shift of the two components, main line and surface line, is not constant throughout the series of spectra. In fact, the highest energy separation is obtained for the SiO_2 substrate (1.38 eV), whereas the lowest (0.90 eV) is found for the MgO substrate, and an intermediate value (1.2 eV) is observed for the Al_2O_3 substrate.

V.3.2 CLUSTER MODEL CALCULATION

To understand this effect, it was performed the same cluster model calculations as those performed in chapter IV, of the Ni 2*p* XPS spectra, but reducing even more the oxygen coordination, going down to zero. Starting from a NiO_6 cluster, the Ni 3*d*-O 2*p* overlap of the apical O atoms were progressively reduced, from $T_{apical}/T_{basal}=1$, corresponding to octahedral symmetry, to 0.66 corresponding to pyramidal symmetry, to 0.33 for square planar symmetry, and more, till this ratio gets zero value. Parameters used in the cluster model calculation are the same as those of the calculations made in chapter IV. And are given in in table V.4.

Table V.4. Cluster model calculation parameters

Main Parameters		***Multiplet Parameters***	
U	***7.5***	***B***	***0.13***
Δ	***4.0***	***C***	***0.58***
pdσ	***1.5***	***10Dq***	***0.1***
Q	***9.0***		

The results of the calculations are shown in figure V.16, where the calculated Ni 2*p* XPS spectra are given as a function of T_{apical}/T_{basal} ratio. As noted above, $T_{apical}/T_{basal}=1$ corresponds to octahedral symmetry, 0.66 to pyramidal symmetry, and 0.33 to square planar symmetry, explanation given already in the previous chapter. So, the overall energy separation between the peaks is roughly given by $\Delta E^2=(Q-\Delta)^2+4T_{eff}^2$. Therefore, the smaller energy spread above is attributed to the reduced T_{eff} in pyramidal symmetry. The results of the calculations show again that the main component of the Ni 2*p* XPS spectra comes from the octahedral coordinated Ni atoms in the bulk, whereas the pyramidal coordinated atoms at the surface contribute at the shoulder energy, shifted around 1.5 eV.

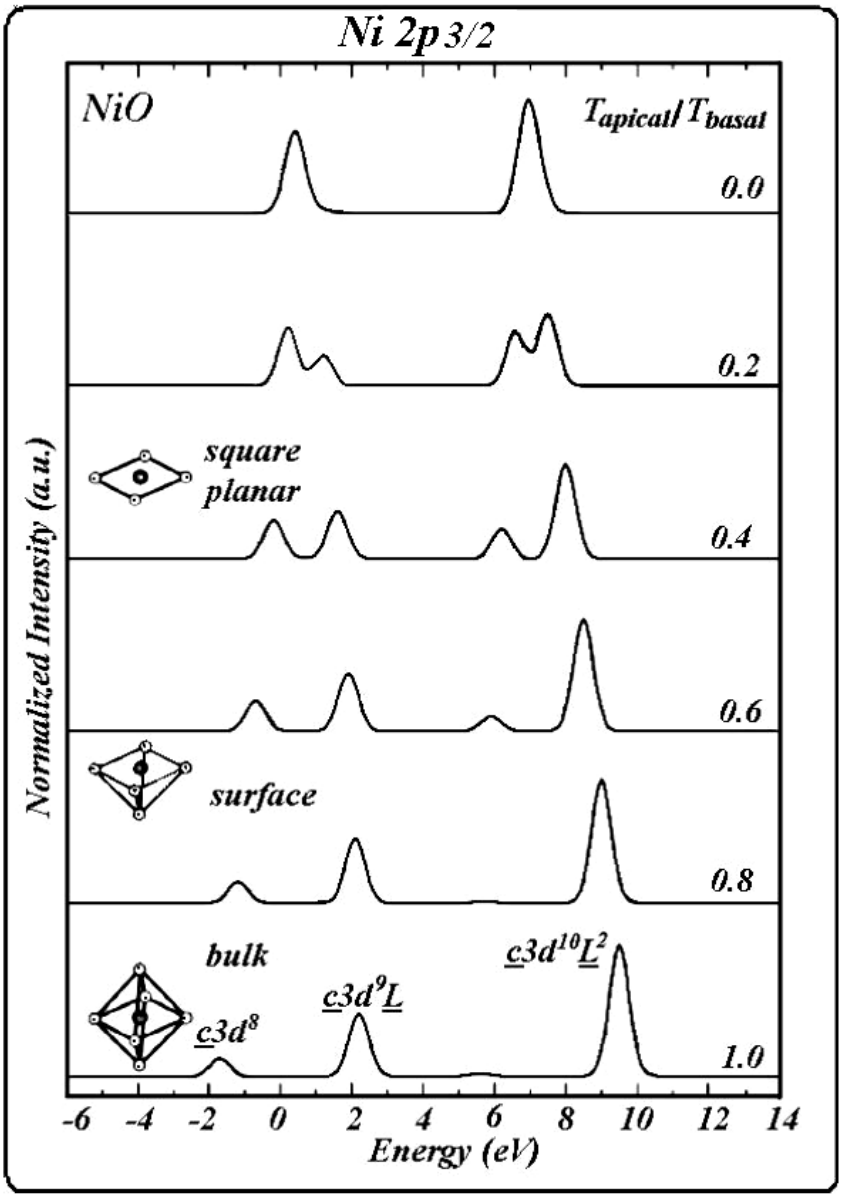

Fig.V.16. Cluster model calculations of the Ni 2p3/2 XPS spectra as a function of the ratio T_{apical}/T_{basal} (1.0 corresponds to octahedral symmetry, 0.66 will corresponds to pyramidal symmetry, and 0.33 to square planar symmetry).

A further symmetry reduction (or a further covalence reduction) would produce an even larger shift. These results also help to explain our experimental results on the NiO overlayers on the different oxides. According to the above calculations, the energy separation of the bulk (main line) and surface peaks decreases with the T_{apical}/T_{basal} ratio. This separation is related to the changes in the covalent interaction at the NiO/oxide interface, being larger for the NiO overlayer on the more covalent SiO_2 substrate and smaller in the more ionic MgO substrate. These results are consistent with the idea of the formation of Ni-O-M cross-linking

bonds (*M*=Si, Al, and Mg) at the interface. In this picture, in the case of the SiO_2 substrate, the Ni 3*d*-O 2*p* overlap in the Ni-O-Si bonds is smaller than in the Ni-O-Al bonds of bulk NiO due to the strong covalent character of the Si-O bonding. On the other hand, the Ni 3*d*-O 2*p* overlap of the Ni-O-Mg bonds is larger than in the Ni-O-Ni bonds due to the more ionic character and consequently less covalent character of the Mg-O bonds.

The above results have been successfully interpreted in terms of the surface and bulk components of the Ni 2*p* XPS spectra according to the model proposed in chapter IV. This is due to the nanostructured character and the high surface to volume ratio of the systems analyzed here. Thus, this model seems to be a suitable tool for the interpretation of the Ni 2*p* XPS spectra in NiO nanostructures. In the following, the influence of other possible effects, such as quantum-size and structural effects, will be explored.

In the study of the similar TiO_2 /SiO_2 system, Lassaleta *et al*[20] found an increase of the band gap for very low coverages. They attributed this shift to a combination of quantum-size and interface (cross-linking bonds) effects, however they pointed out that, in this case, the nature of the substrate is more important than the layer thickness. In our case, the Ni LMV Auger spectra for NiO grown on all substrates do not reveal any apparent energy shift.

On the contrary, they also reflect a peak narrowing as in the case of the Ni 2*p* XPS spectra and are in complete agreement with the spectra reported by Sanz and Tyuliev[14] for the growth of NiO on MgO(100). Therefore, quantum-size effects do not seem to play a significant role in the deposits studied in this work.

The influence of structural effects in the Ni 2*p* XPS spectra should also be evaluated. For instance, Warot *et al*[17] found that the surface morphology of the NiO overlayer depends on the surface orientation in different MgO single-crystal substrates. In our case, the AFM images of the MgO substrate shown in figure V.2 indicate the formation of faceted crystallites of about 1 μm with a random orientation. However, the fact that our spectra on these polycrystalline substrates completely match those obtained on MgO(100) single crystals[12, 21] indicates that surface orientation is not a dominant effect.

Other structural effects such as interface mixing, as well as geometry and lattice mismatch, could also be influencing the spectra. As pointed out by Towler *et al*[20], small changes in the surface geometry can lead to significant effects on the initial states of the ions in oxide materials. Indeed, significant variations of the crystal field of the Ti atoms located at the TiO_2/SiO_2 system have been observed by means of the Ti 2*p* XAS spectra[6]. However, these changes have also been explained in terms of a covalence reduction due to the different

environment of the Ti atoms. The XPS spectra presented here are consistent with an octahedral coordination surrounded by a mixture of Ni and *M* atoms (*M*=Si, Al, and Mg) in the second coordination sphere and are supported by their resemblance with other published spectra. In this picture, the effect of cation intermixing and small lattice parameter variations due to the lattice mismatch would not change these conclusions.

V.3.3. THROUGH THE GROWTH PROCESS

In all the fitted spectra the green curves are assigned to the main line, the blue ones to the non-local peaks and the magenta curves are describing the surface component.

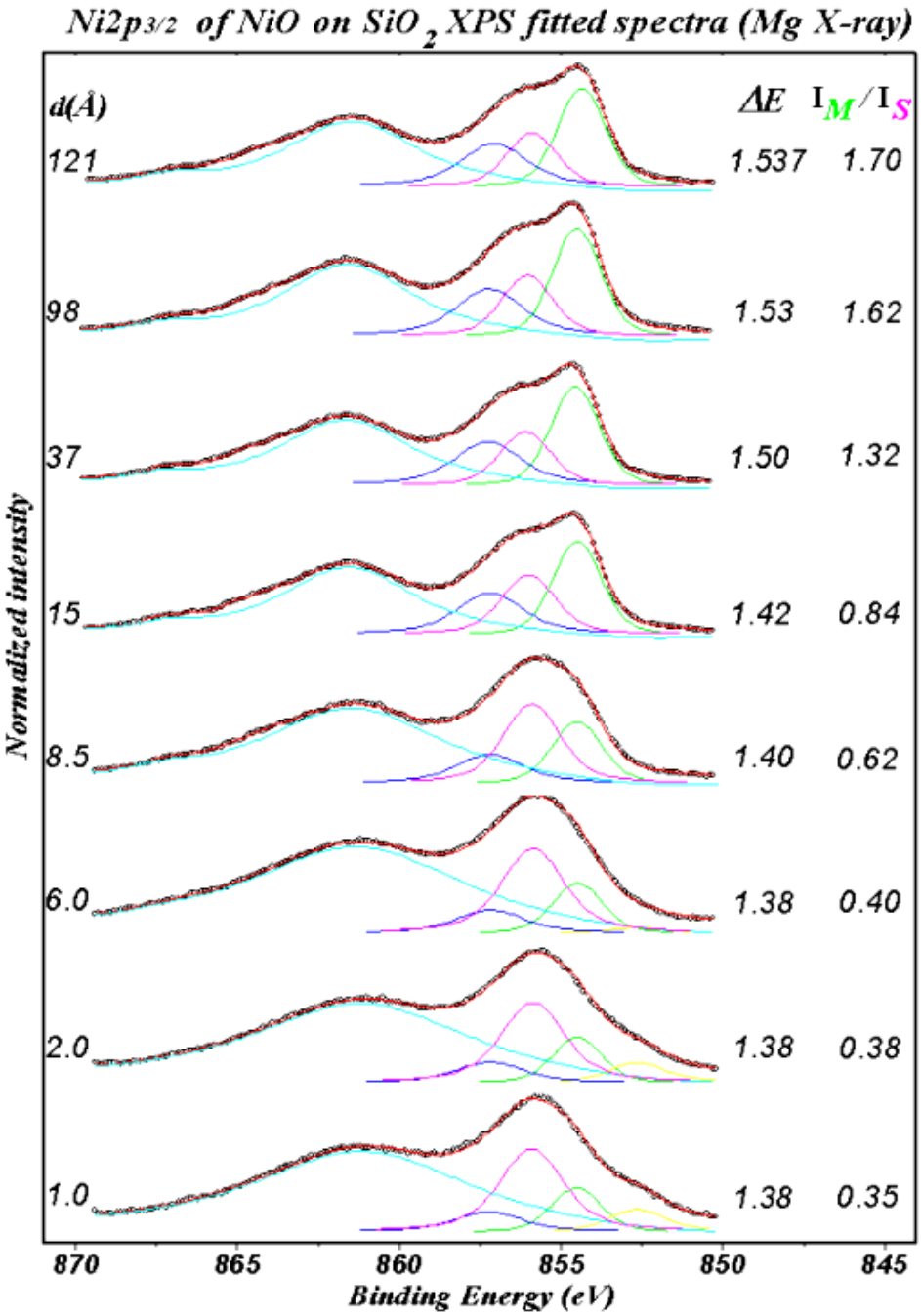

Fig.V.17. Ni 2p3/2 fitted XPS spectra for NiO on SiO_2.

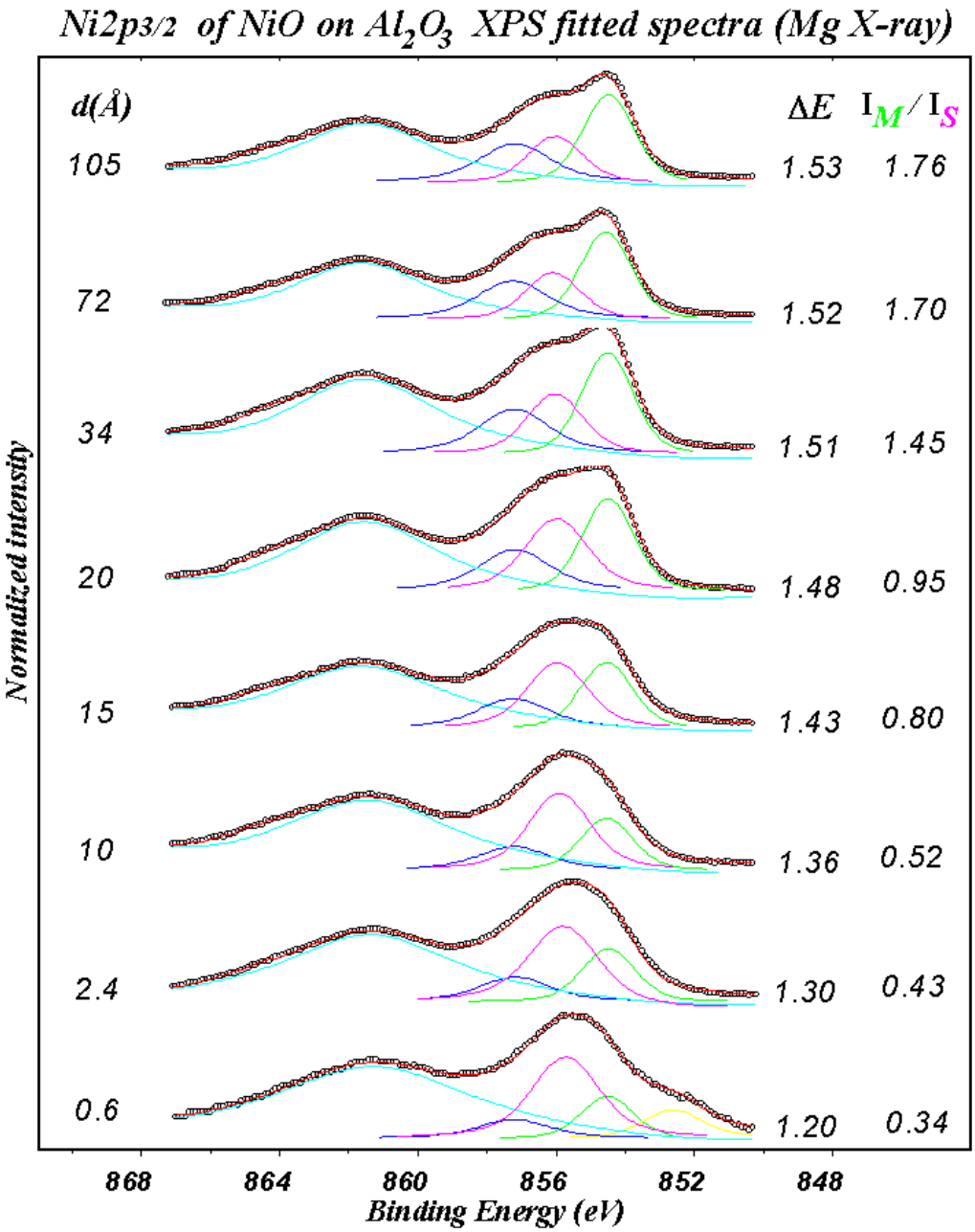

Fig.V.18. Ni 2p3/2 fitted XPS spectra for NiO on Al_2O_3.

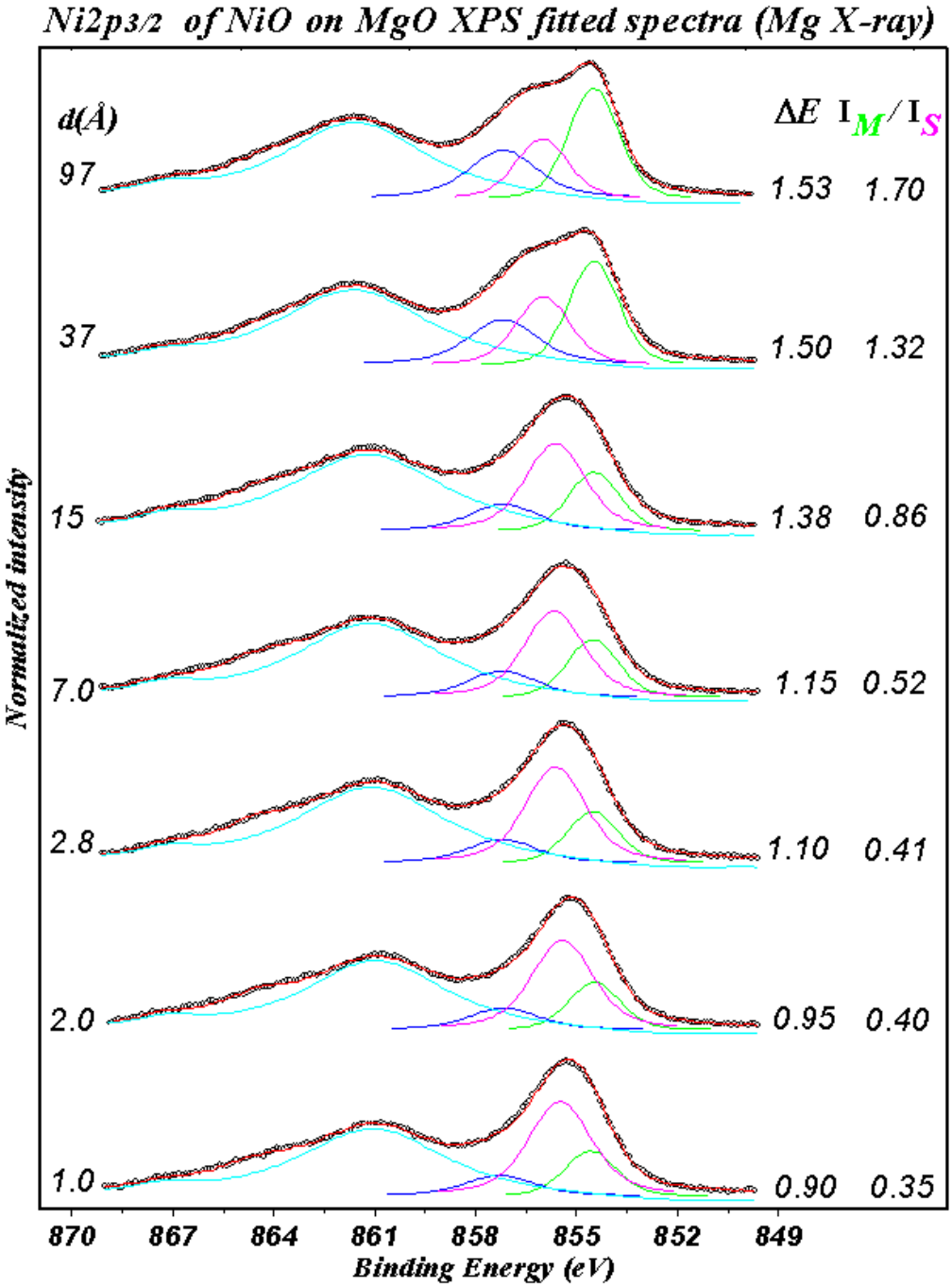

Fig.V.19. Ni 2p3/2 fitted XPS spectra for NiO on MgO.

In the figures above, each stage of growth is described by the equivalent thickness, and by the energy separation and intensity ratio of the main line and surface peaks, values represented also in figure V.20 and V.21 below, for a better understanding.

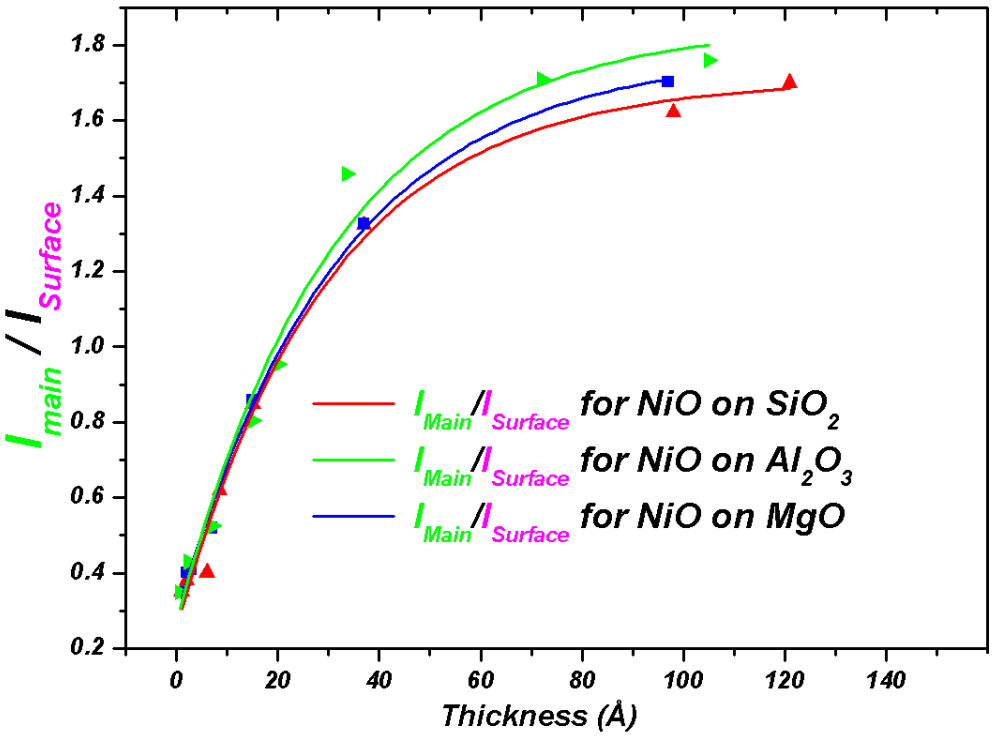

Fig. V.20. Main to Surface intensity ratio evolution during the growth processes for NiO on SiO_2 (red), NiO on MgO (blue) and NiO on Al_2O_3 (green).

The main to surface intensity ratio evolution during the growth process has the same characteristic for all three substrates. It starts with a minimum value, which means that in the early stages the surface component is dominating the XPS spectra. During the growth process this ratio is raising continuously, at the beginning with a higher slope, which change into an asymptotic tendency to a maximum value, around 1.7, the same value as in the growth of NiO on HOPG, which tells that the minimum surface and the maximum bulk XPS signals were reached.

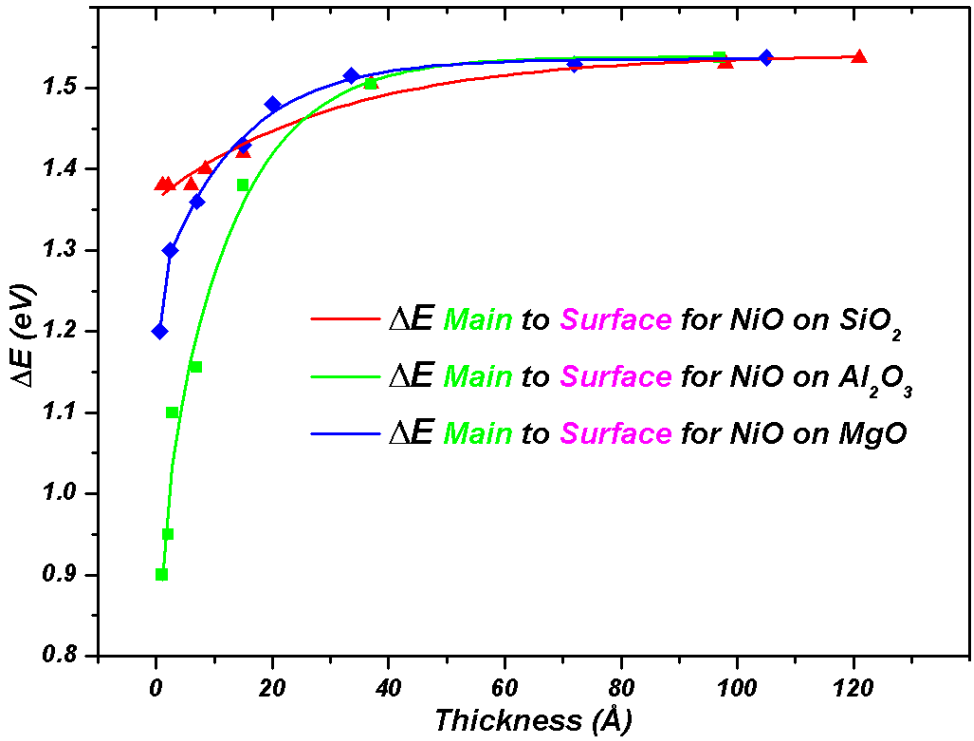

Fig. V.21 Main to Surface energy separation evolution during the growth processes for NiO on SiO_2 (red), NiO on Al_2O_3 (green) and NiO on MgO (blue).

Representing the main to surface energy separation evolution during the growth processes for each substrate, the influence of the substrate is very well pointed out.

In figure V.21, it can be seen that in the early stages this energy separation has different values for different substrate. The lowest energy separation value corresponds to the more ionic substrate (MgO) and the highest corresponds to the more covalent substrate (SiO_2), trends already observed in figure V.15 and predicted by calculations in the above section. For each growth process this energy separation tends to a maximum value about 1.54 eV, which corresponds to a NiO bulk.

V.4. STUDY OF THE GROWTH OF NiO/OXIDES BY NEXAFS

This section presents Near Edge X-ray Absorption Fine Structure (NEXAFS) spectra at the Ni K edge of some stages of the growth of NiO on the selected oxides.

The initial goal of these experiments was the measurement of the EXAFS spectra for different stages of growth in order to obtain the atomic distances at the interface and coordination, to complete the characterization of the NiO growth on oxide substrates. However, the EXAFS obtained spectra did not have enough quality for EXAFS analysis (due to low signal/noise value – mainly determined by the very small amount of deposited material needed for the early stages study). In turn, the Near Edge Absorption Spectra (NEXAFS) were satisfactory to perform structural characterization of the NiO/oxide systems. This has been performed with a powerful NEXAFS analysis tool which is the MXAN software, already presented in the second chapter of this work.

V.4.1. EXPERIMENTAL SPECTRA

The attention was paid for the initial and final stages of growth. Figure V.22 presents the near edge region for these cases, marking the most important differences observed between the initial and final stages of growth.

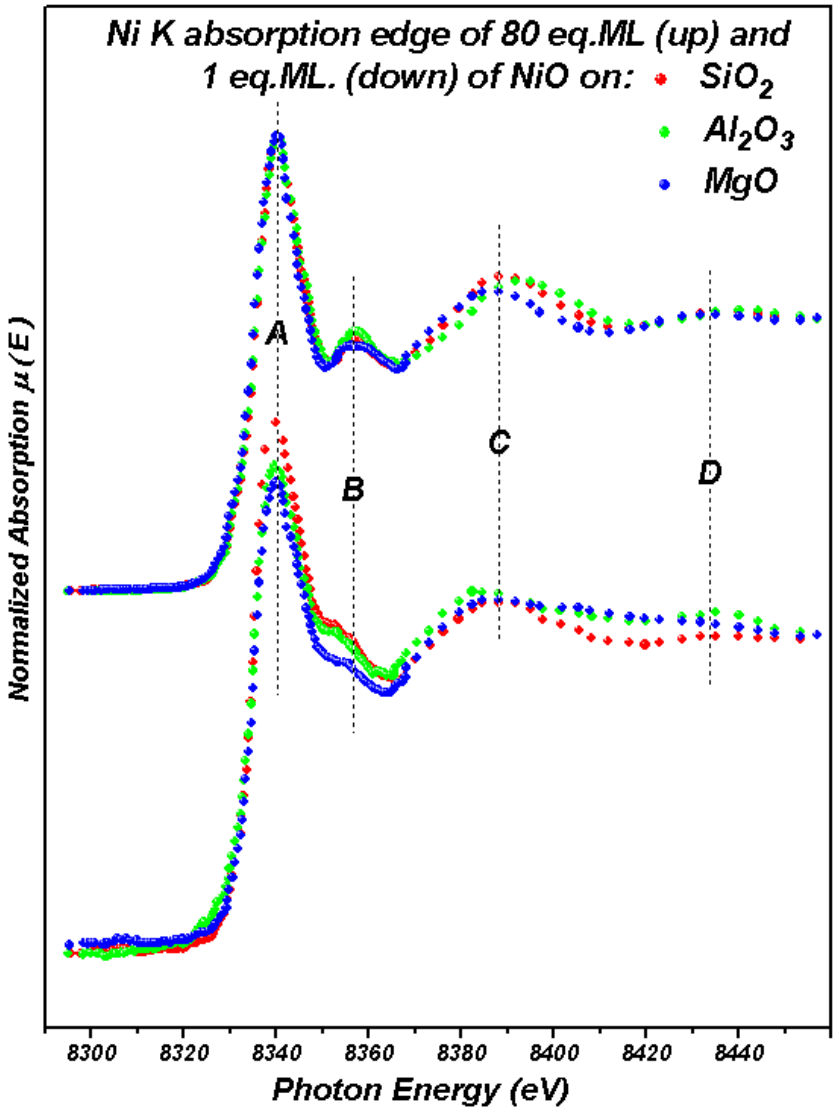

Fig.V.22. Ni K-edge absorption spectra of 80 Eq. Ml. (up) and 1 Eq. Ml. (down) of NiO deposited on SiO_2 (red), Al_2O_3 (green) and MgO (blue).

All three systems exhibit resonant-like structures in the first 20 eV above the K-shell threshold at 8333.33 eV, which are less intense than the resonance structure at higher photon

energy range. It is well known that the resonant–like structures in NEXAFS spectra are highly structure sensitive.

The Ni K edge absorption spectra of 80 Eq. Ml. of NiO deposited on the different oxides presents practically no differences from each other.

However, the spectra for 1 eq. monolayer of NiO/oxide present significant difference with respect to those of 80 monolayer and also between each other. Indeed, the resonance-like structure, at around 20 eV above the absorption edge, labeled as ***B*** in figure V.22, makes the main difference between the absorption spectra of the final deposition stage of NiO (bulk) on oxides, and the early stages of deposition of NiO (nanostructures). Whereas in the NiO bulk absorption spectra, this structure is very well defined, in the nanostructured NiO is not: it doesn't disappear, but its intensity dramatically decreases for very small amount of NiO deposited. This, together with the observation that this resonance-like structure doesn't change with the substrate, suggests that its origin is strongly related with the dimension of the NiO absorbents structures.

Another difference between early and final stages of growth can be found at higher photon energy range, around 60-70 eV above the edge. It seems that for the spectra of NiO deposited on MgO the second resonance-like structure at about 60 eV above the edge is less defined. The absorption edge seems to be more intense for NiO/SiO_2 than for the other two substrates.

V.4.2. EXPLORING CLUSTER SIZE AND EXCHANGE AND CORELATION POTENTIALS

XANES computation requires sophisticated simulation tools[22,]. Most of these *ab initio* codes are built within the one-electron multiple-scattering (MS) framework[23] and by using the so-called *muffin-tin* approximation with the addition of an exchange-correlation potential (ECP). In the case of complex ECP potentials, the imaginary part also accounts for the damping of the excited photoelectron.

At present, the energy dependent Hedin-Lundqvist (HL) complex potential[24,25] is the most widely used in *ab initio* XANES calculations[26]. However, it has been reported that in several cases, the energy dependent Dirac-Hara (DH) exchange potential shows the best agreement to the experimental data[27,28,29,30]. As a result, the choice of the ECP among the usual scattering potential set, ranging from real X_α to complex Hedin-Lundqvist, becomes one

of the most important steps in obtaining a good reproduction of the experimental spectra. The experience accumulated through the calculation of the absorption cross section for different systems suggests that the HL ECP offers good performance in the case of metals, while for ionic and covalent systems, the use of DH seems to be more adequate[36-31].

The computation of the XANES spectra was carried out using the multiple-scattering code CONTINUUM[27-31] based on the one-electron full-multiple-scattering theory[32,32] A complete discussion of the procedure can be found in references 34 and 42.

The Coulomb part of each atomic potential was generated using charge densities from the atomic code of non-local self-consistent Dirac-Fock code[28,33]. Finally, were tested two different choices for the exchange and correlation part of the final state potential: the energy-dependent HL complex potential, and the energy-dependent DH exchange potential. The computed spectra have been compared with the experimental XANES measured spectra.

Using this software procedure[34], which is able to simulate the XANES part (from the edge to about 200 eV) of experimental X-ray Absorption data several conclusions can be made.

In figures V.23 and V.24 are showed two clusters of NiO/oxides used in XANES spectra calculation using MXAN procedure.

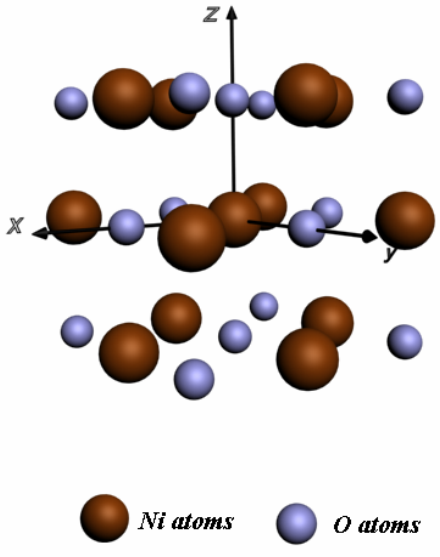

Fig. V.23. 27 atoms cluster

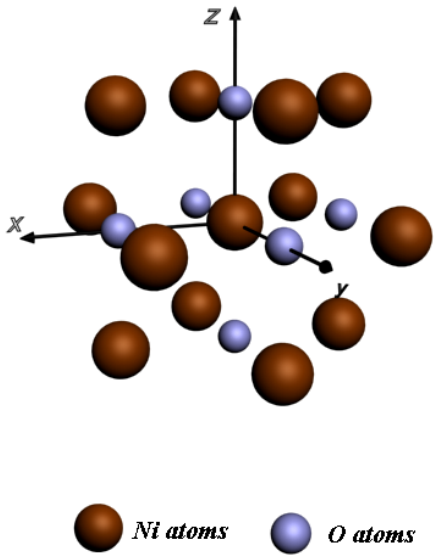

Fig. V.24. 19 atoms cluster

A comparison between the simulated XANES spectra and the experimental spectra, and also the principal characteristics of the NiO/oxide coming out by NEXAFS studies are presented below.

In figure V.25 is represented a comparison between some calculated spectra and the experimental absorption spectra. For starting, it can be seen that the 93 atoms cluster is the one which present, in the simulated spectra, the same number of structures at approximatively the same photon energy as the experimental spectra. Also the 33 atoms cluster calculated spectra shows acceptable concordance with the experimental spectra.

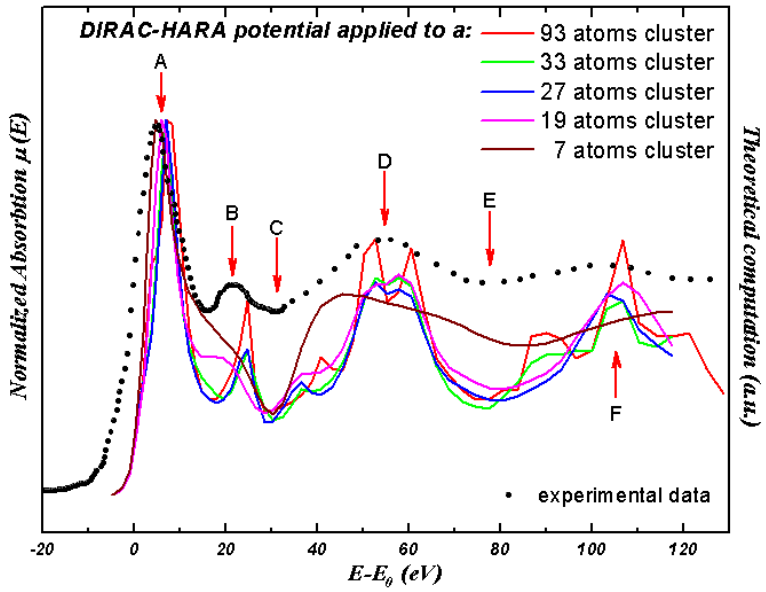

Fig. V.25. Comparison between calculated spectra for 93 (red), 33 (green), 27 (blue), 19 (magenta) and 7 (wine) atoms cluster with the experimental spectra (scatter black) for 80 Ml of NiO deposited on SiO_2.

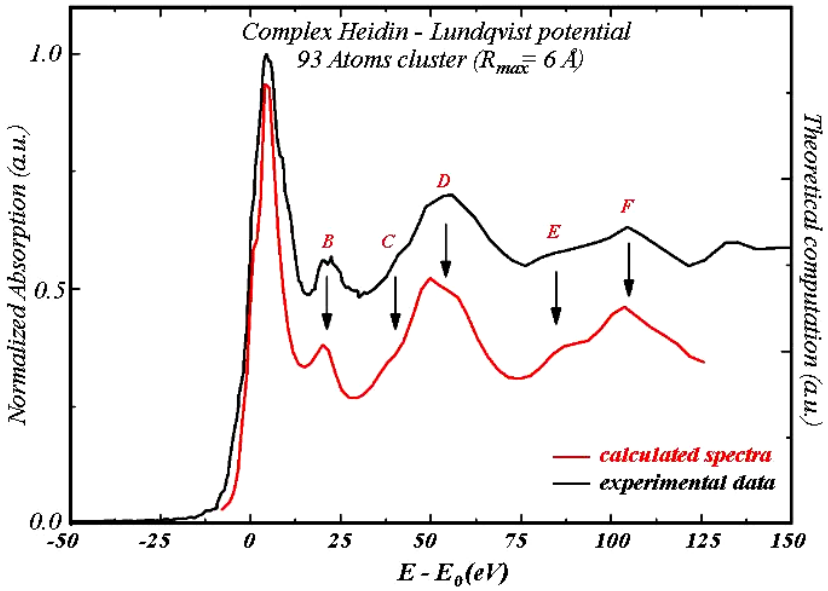

Fig.V.26. The best agreement between the experimental and calculated spectra for 80 Ml of NiO deposited on SiO_2.

From the comparison of the calculated spectra for the 93 and 33 atoms cluster in a complex Heidin-Lundqvist ECP, with the experimental absorption spectra, the best agreement was found for the 93 atoms cluster in a complex H-L potential, as shown in figure V. 26.

For the early stages of growth, according to figure V.25, the simulations indicate that the experimental spectra has to be calculated with smaller cluster. NEXAFS spectra were calculated for 27, 19 and 7 atoms clusters, in both, Dirac-Hara and Heidin-Lundqvist ionization potential, taking in account just the real part or the complex part of the ionization potential. Some of the calculated spectra are presented in figure V.27, in comparison with the experimental spectra of 1 equivalent monolayer of NiO deposited on SiO_2.

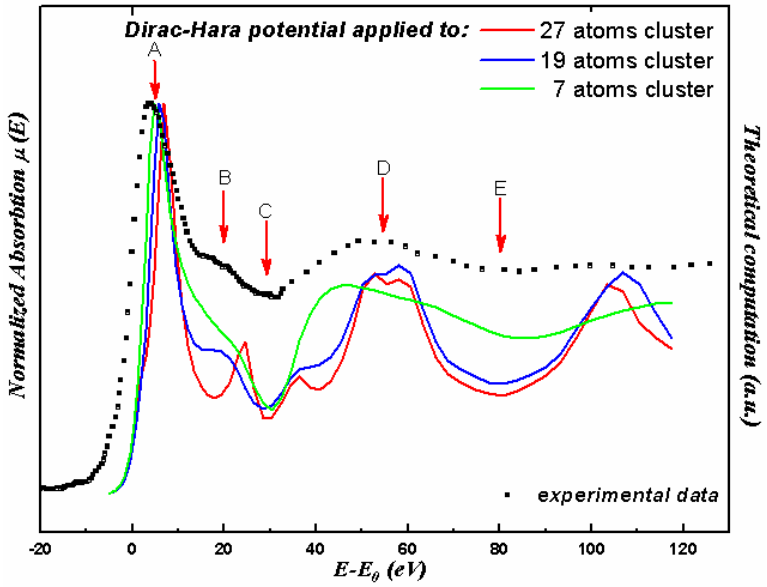

Fig. V.27. Comparison between 27 (red), 19 (blue) and 7 (green) atoms cluster with a Dirac-Hara ionization potential calculation, and experimental spectra of 1 Eq. ML. of NiO/SiO_2.

It can be seen that, even if the absorption structures number and energy position are in good agreement with the experimental spectra, at least for the 19 atoms cluster calculated spectra, the width of the peaks are not reproducing the experimental values. This was solved using for the simulated spectra, the complex form of Dirac-Hara exchange-correlation potential. The simulated absorption spectra in these conditions, for 19 atoms cluster, are compared with the experimental one in figure V.28 below.

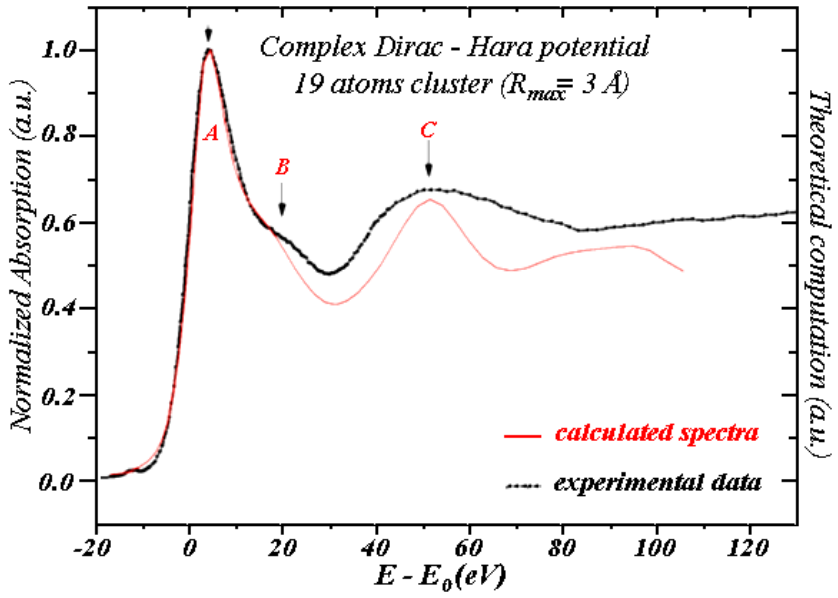

Fig. V.28. The best agreement for the 1 eq. ml of NiO deposited on SiO_2 is obtained for a 19 atoms cluster for a complex Dirac-Hara potential.

As it is shown in figure V.28, the best agreement with the experimental spectra was found for a 19 atoms cluster using the complex Dirac-Hara EC potential.

This first analysis leads to conclude that the spectra corresponding to 80 Ml. of NiO deposited on all substrates are in perfect agreement to that of published[35] bulk NiO and can be calculated by using a 93 atoms cluster using the HL EC potential. On the other hand, the spectra corresponding to 1 Ml of NiO deposited on oxides, needs to be calculated for a 19 atoms cluster using DH EC potential.

V.4.3. EXPLORING INTERFACE EFFECTS

I this section, the influence of the substrates on the NEXAFS spectra are explored. In other words, the interface effects in the absorption spectra of 1 eq. Ml.of NiO/oxides are studied.

To this end, the changes in the simulated spectra induced by structural changes in the 19 atoms cluster of NiO used in the calculation of the absorption spectra are studied. Figure V. 29 depicts structural changes of the used cluster, changes as Ni atom substitutions with substrate atoms.

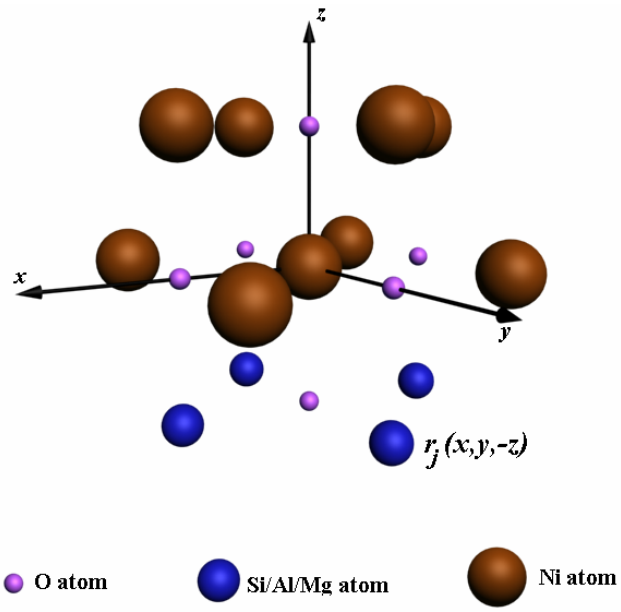

Fig. V.29. Structural changes in 19 atoms cluster: 13 Ni atoms, 6 O atoms and 4 Si, Al and Mg atoms, by case, at $r_j(x, y, -z)$.

Once this analysis has been performed, second atom shell distortion of the 19 atoms cluster will be studied by varying the O-M (M= Si, Al or Mg) distance. Then, the effects of Ni-O distance variation in the simulated spectra will be studied, as first atom shell distortion. As a refinement, both, Ni-O and O-M distances will be varied simultaneously.

According to above description for the analysis, for the first step, figures V.31, V.32 and V.33 show the simulations for each oxide substrate of a 19 atoms cluster, where 0,1,4,8 and 12 Ni atoms have been substituted by M atoms.

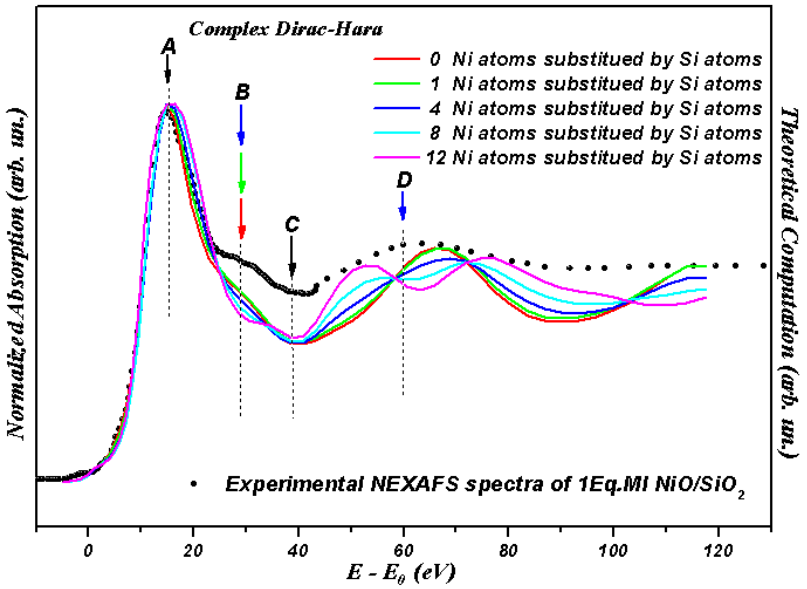

Fig. V.30. Comparison between experimental Ni K absorption edge spectra of 1 Eq. Ml. of NiO/SiO_2 and calculated spectra for different number of Ni atoms replaced with Si atoms.

The colored arrows are pointing the structures of the calculated spectra which approach the experimental ones.

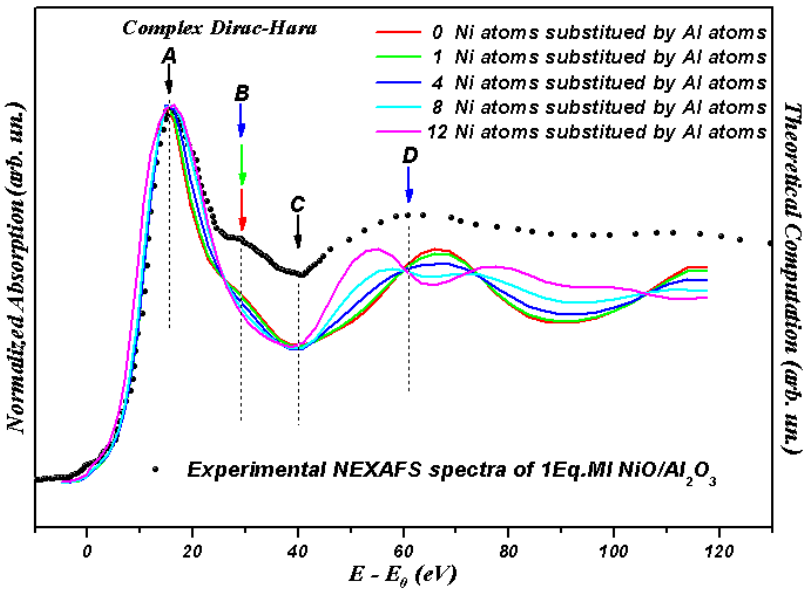

Fig. V.31. Comparison between experimental Ni K absorption edge spectra of 1 Eq. Ml. of NiO/Al_2O_3 and calculated spectra for different number of Ni atoms replaced with Al atoms.

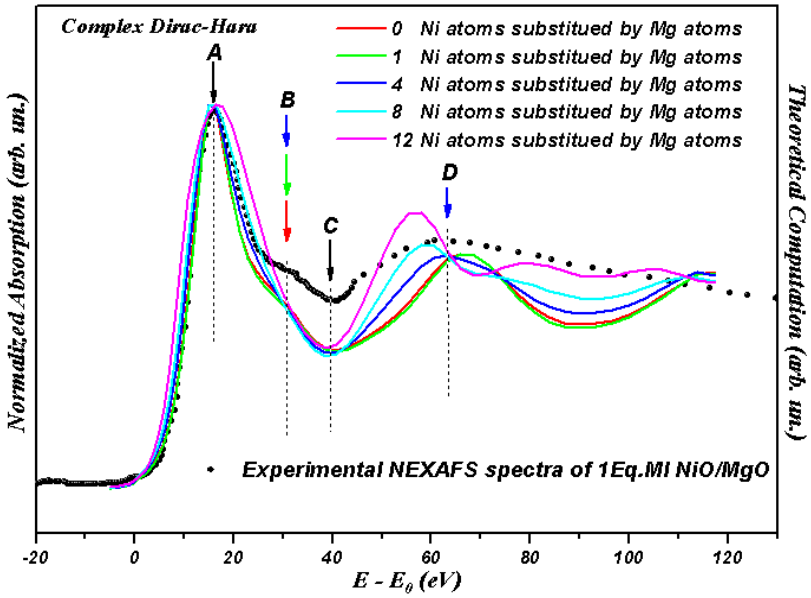

Fig. V.32. Comparison between experimental Ni K absorption edge spectra of 1 Eq. Ml. of NiO/MgO and calculated spectra for different number of Ni atoms replaced with Mg atoms.

It can be seen that the number of Ni atoms replaced by substrate atoms is principally reflected in the resonant-like peak at higher photon energies, above 60 eV from the edge. The first resonance-like structure at 20 eV above the absorption edge is also affected by the number of Ni atoms changed with substrate atoms, but not so severe as the higher photon energy range structures are.

Looking at the energy position and at the widths of the ***A*** to ***D*** labeled structures of the calculated absorption spectra it is obvious that approaching of the experimental spectra is obtained when in the 19 atoms cluster **four** Ni atoms are substituted by substrate atoms for each kind of oxide substrate.

The above results are in perfect agreement with the XPS results that suggest the formation of Ni-O-M cross linking bonds

Following the above described idea of this study, distortion of the second and first atoms shell are induced to the 19 atoms cluster for investigate how the Ni-O-M distances changes as function of the substrate used. Representations of the distortions used are shown in figure V.33 *a* and *b*.

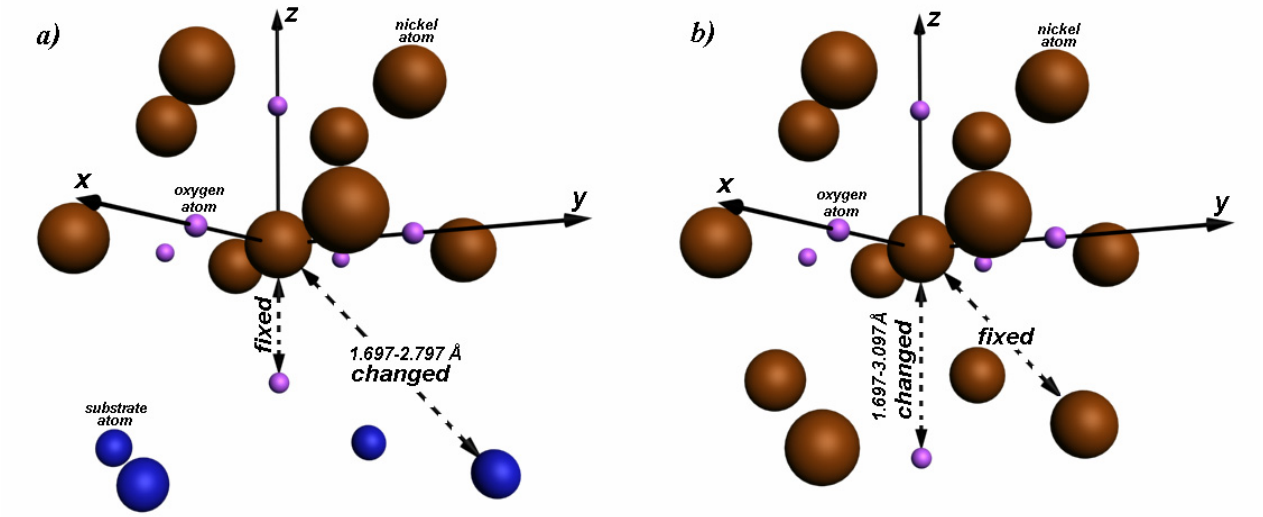

Fig. V.33. Second shell distortion (a), and first shell distortions (b)

Having in mind that the NiO lattice constant is 4.194 Å, then the distortion induced in the cluster by the substrate atoms, were considerate around half of this value. So, in the 19 atoms cluster, the "–z" Ni atoms were replaced with substrate atoms, whose coordinates were changed, in order to simulate the cluster distortion.

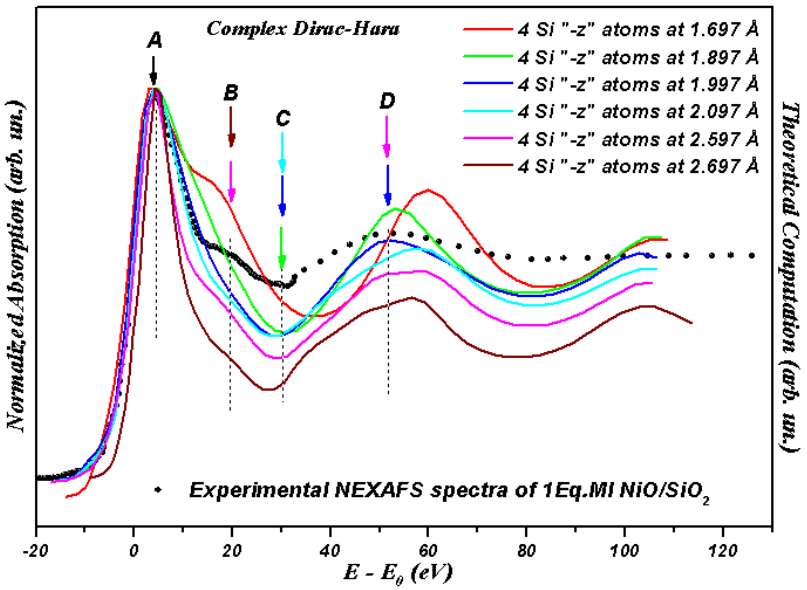

Fig. V.34. Second shell atoms distortion effect in Ni K absorption edge for Ni_{-z} atoms substituted by Si atoms, comparison with experimental K absorption edge for 1 Eq. Ml. of NiO/SiO_2.

For the NiO/SiO_2 case, the better approach to the experimental spectrum is obtained for higher coordinates values of the Si atoms, but not larger that 2.697 Å.

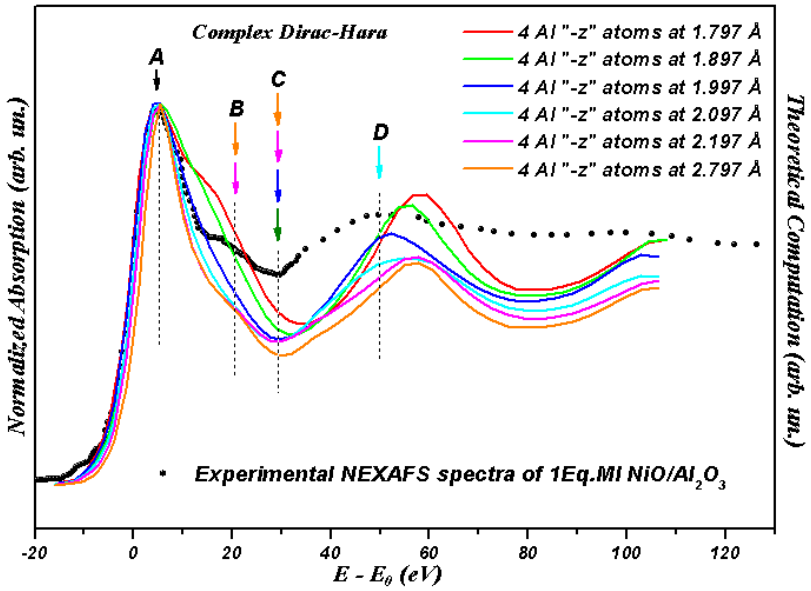

Fig. V.35. Second shell atoms distortion effect in Ni K absorption edge for Ni_{-z} atoms substituted by Al atoms, comparison with experimental K absorption edge for 1 Eq. Ml. of NiO/Al_2O_3.

In the case of NiO/Al_2O_3 good agreement is obtained if the coordinates of the Ni replaced atoms are maintained as in the NiO lattice.

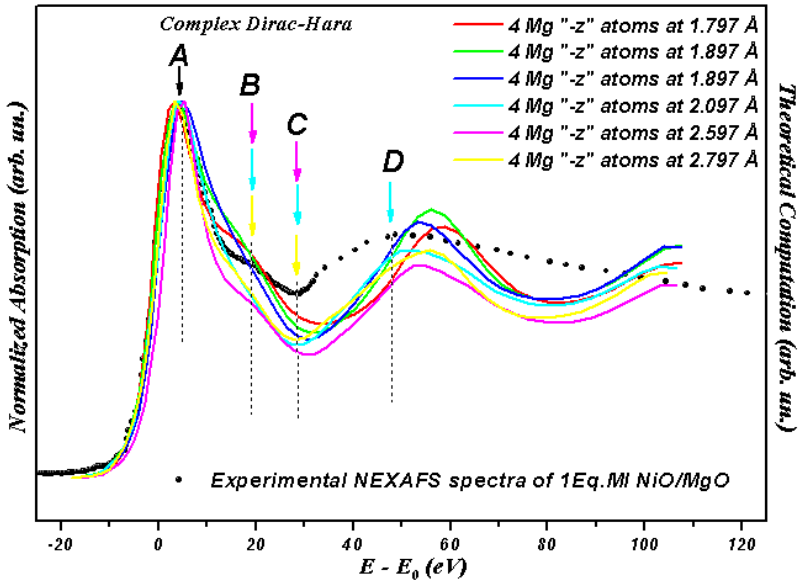

Fig. V.36. Second shell atoms distortion effect in Ni K absorption edge for Ni_{-z} atoms substituted by Mg atoms, comparison with experimental K absorption edge for 1 Eq. Ml. of NiO/MgO.

The NiO/MgO system requires also lowers values for this coordinates, comparable with the half of the NiO lattice constant.

Now, the effects of the variations of the Ni-O distance, as described in figure V. 33 b, are presented. In this case, no substitution of Ni atoms have been included, thus only the effect of the first atoms shell distortion is studied.

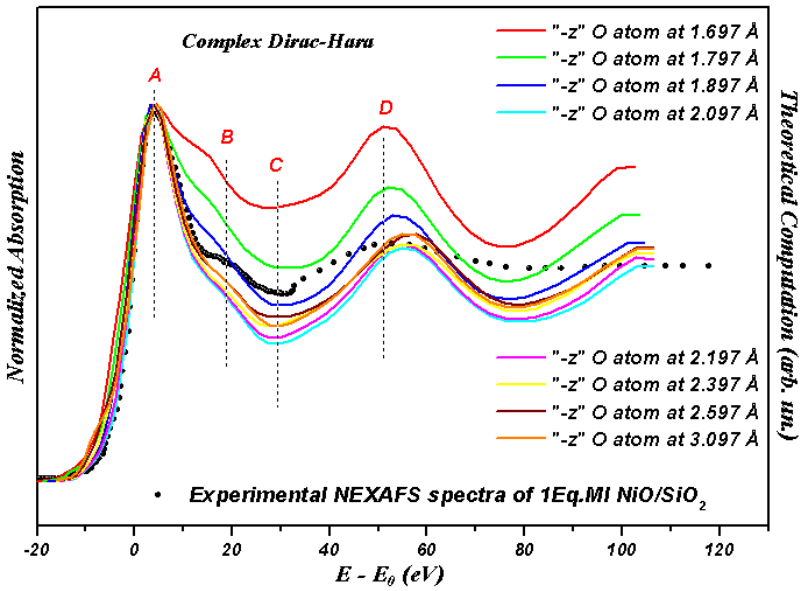

Fig. V.37. Comparison between Ni K absorption edges of 1Eq. Ml. of NiO/SiO_2 (black dots) and several distortion of 19 atoms NiO cluster calculated spectra (lines).

In general, main futures of the calculated spectra don't change by inducing distortion in the first atoms shell. All these simulated spectra present the resonance-like peak at 20 eV above the absorption edge, and at higher energies also the resonant-like structures are present. However, the intensity of the absorption K edge increase for high values of Ni – O_{-z} distance, reaching a maximum value for Ni – O_{-z} distance of 2.097 Å (half of the NiO lattice parameter). This, together with the fact that the experimental absorption spectra presents higher intensity of the absorption edge for 1 equivalent monolayer thickness of NiO deposited on SiO_2 than that deposited on Al_2O_3 or MgO, leads to conclude that the Ni-O_{-z} distance is larger in for NiO/SiO_2 system than in the NiO/Al_2O_3 or NiO/MgO systems. The O_{-z} atom is supposed to participate in the cross linking bounding of Ni with Si, Al and Mg by case.

Finally, trying to simulate the principal difference experimentally found it between the absorption spectra of 1 Eq. ML of NiO deposited on the selected substrates, which is the intensity of the white line, distortions produced by variations of, Ni - O_{-z}, O_{-z} - M distances and also in the substrate lattice parameters, as shown in figure V. 38, are studied.

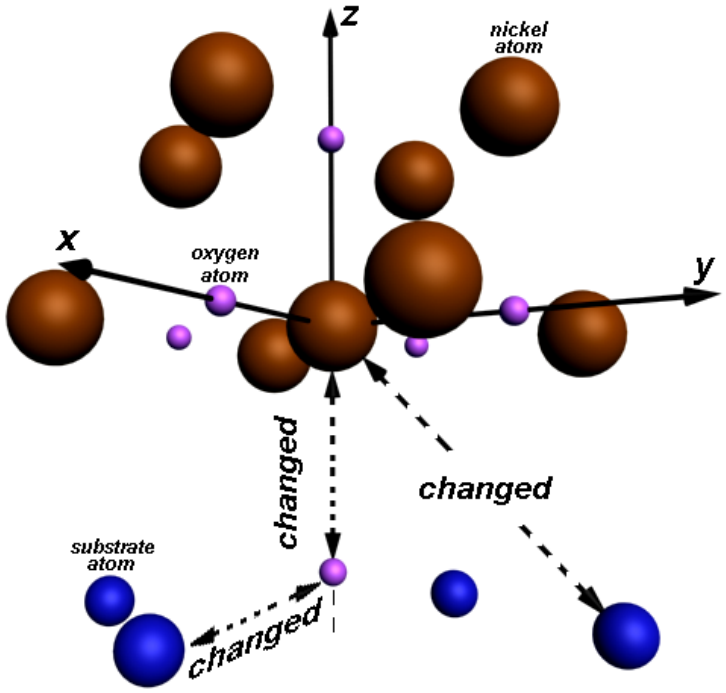

Fig. V.38. Distortion of 19 atoms cluster of NiO/Substrate at interface.

The figures below represent the best comparisons between calculated spectra and the experimental ones for each case.

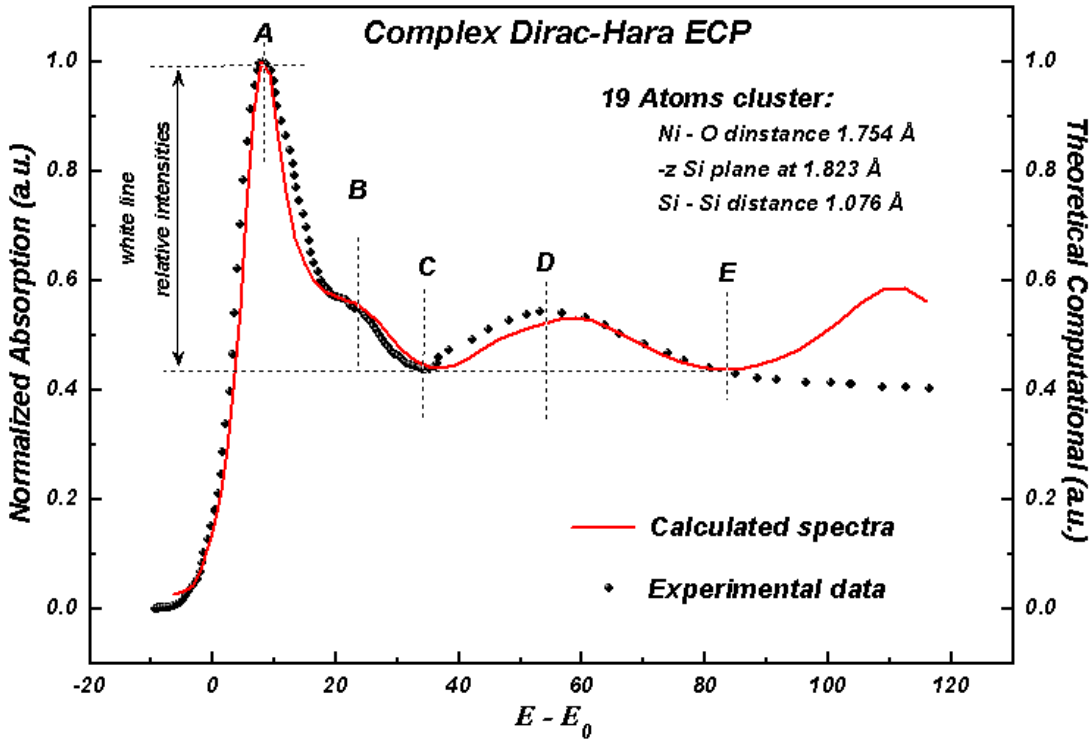

Fig. V.39. Best agreement found for NiO/SiO_2.

The best agreement between the experimental and theoretical spectra was found for a Ni – O_{-z} distance of 1.754 Å, with the "–z" Si atoms plane at 1.823 Å with a semi-lattice parameter of 1.076 Å. It is normal to think that at the NiO/SiO_2 interface, both, NiO and SiO_2 structure will suffer distortions of their structures. In figure V.40 the interface model proposed for the NiO/SiO_2 interface is presented.

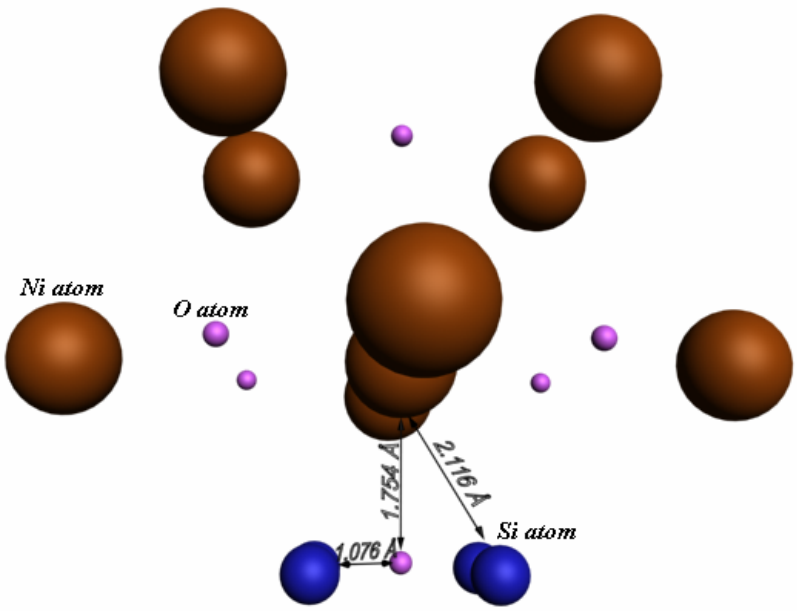

Fig. V.40. NiO/SiO_2 interface model.

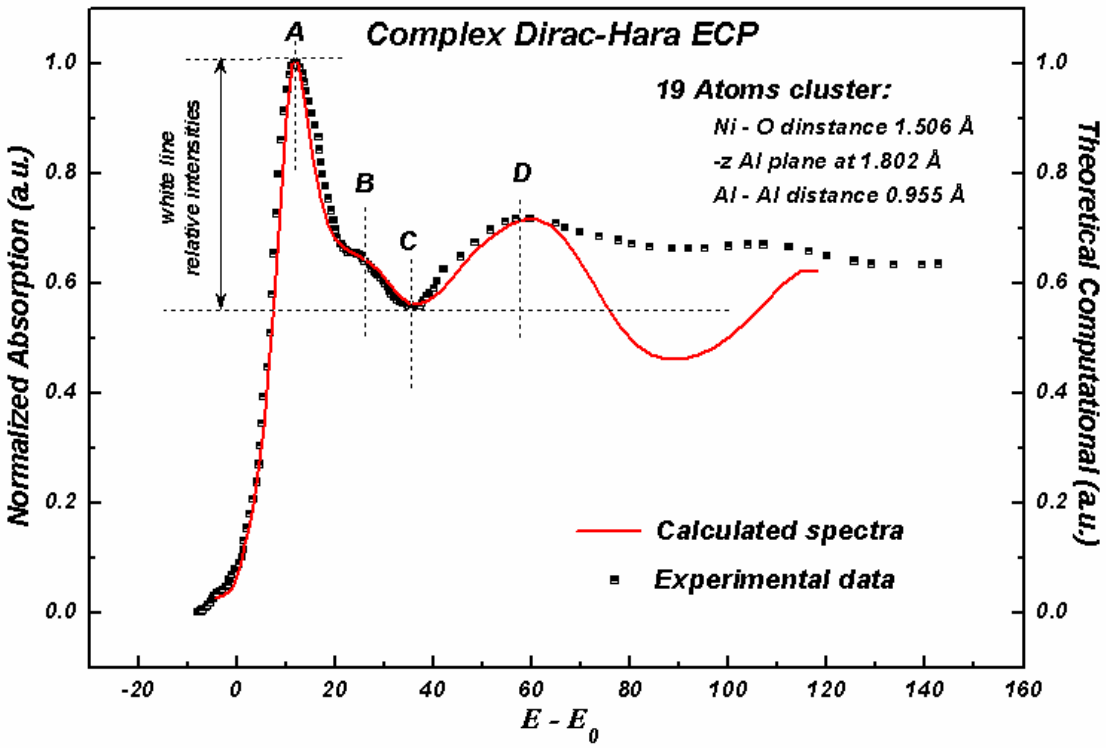

Fig. V.41. Best agreement found for NiO/Al_2O_3.

The best agreement between the experimental and theoretical spectra was found for a Ni – O_{-z} distance of 1.506 Å, with the "–z" Si atoms plane at 1.802 Å with a semi-lattice parameter of 0.955 Å.

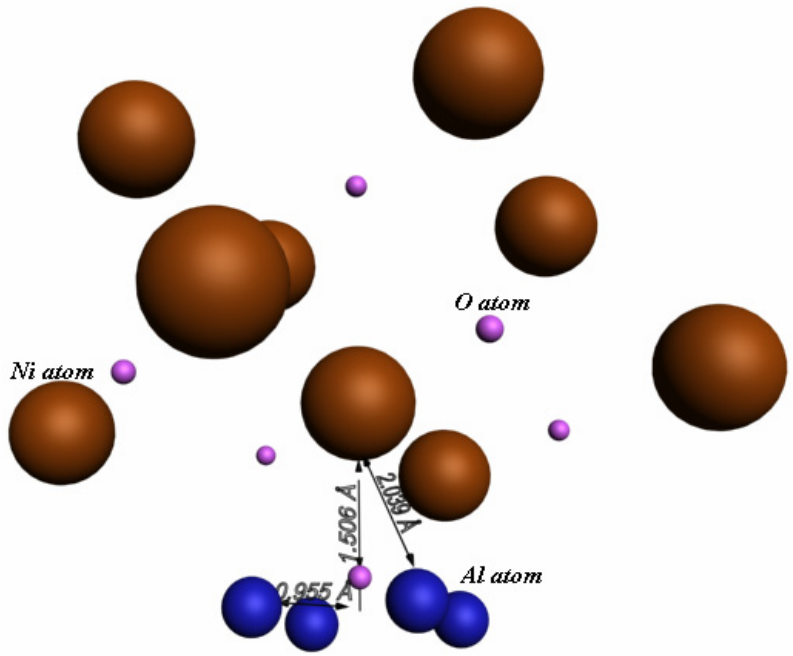

Fig. V.42. NiO/Al_2O_3 interface model.

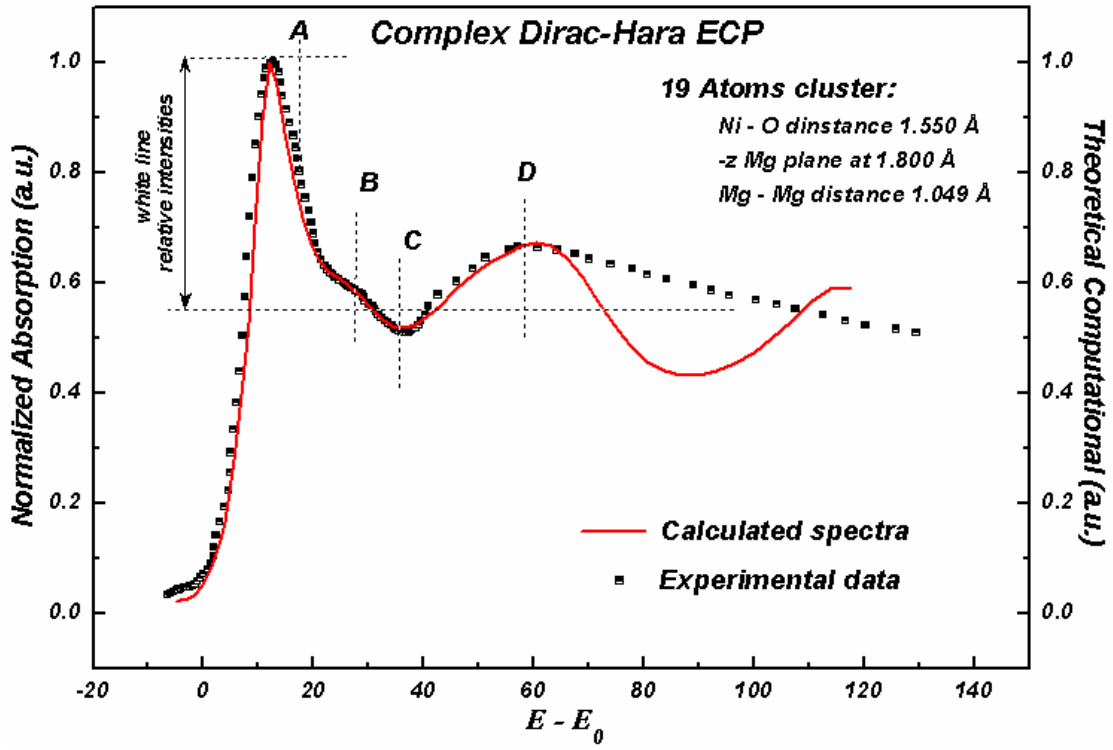

Fig. V.43. Best agreement found for NiO/MgO.

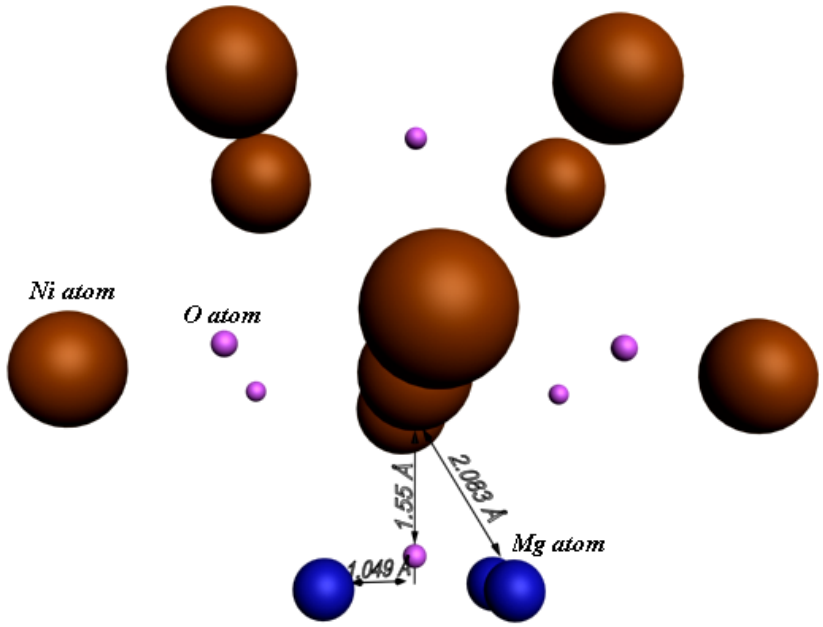

Fig. V.44. NiO/MgO interface model.

For NiO/MgO interface, the best agreement between the experimental and theoretical spectra was found for a Ni – O_{-z} distance of 1.55 Å, with the "–z" Si atoms plane at 1.80 Å with a semi-lattice parameter of 1.049 Å.

The principal conclusion from this study is that cross linking bonds Ni – O – M (M= Al, Si, Mg) are formed at the NiO/OXIDES interfaces, and more, the shared oxygen atom participate more or less in the NiO structure as a function of the covalence character of the substrate, fact predicted by the cluster model calculations and XPS measurements.

CONCLUSIONS

Interface effects have been studied in the early stages of growth of NiO on three selected oxides, namely SiO_2, Al_2O_3 and MgO. As in the previous chapter, the morphology of the growth has been studied by quantitative analysis of the XPS background. AFM study has been only possible on the SiO_2 substrate due to its very low roughness. The formation of nanometric (~2x100 nm) NiO islands at the early stages of growth has been demonstrated.

Once again, the Ni *2p* XPS spectra for the early stages of growth showed that the surface component of the Ni *2p* XPS peak has a high intensity due to the large surface to volume ratio of the nanostructured NiO formed. Even more, the early stages of growth show that the surface peak is affected by the substrate. As obtained by cluster calculations for different covalent reductions, the most covalent substrate (SiO_2) shifts the surface peak towards higher binding energies with respect to the most ionic substrate (MgO). These results are consistent with the formation of cross-linking-bonds at the interface in the form Ni-O-M, where M stands for Si, Al, Mg.

These interface effects have also been studied by NEXAFS. The experimental spectra have been compared to multiple scattering simulations for different clusters and different symmetries. Whereas the early stages of growth (1 ML) have been simulated with a 19 atoms NiO cluster, the final stages (80 ML) agree with the simulations of a 93 atoms cluster. The substitution of 4 Ni atoms of the cluster by M atoms produces an improvement of the simulations. The differences of the NEXAFS spectra for the early stages of growth on the different oxides, mainly in the white line and the resonance structures, are explained by a distortion of the initial cluster induced by the substrate. The most covalent substrate (SiO_2) produce an increase of the Ni-O distance, which is completely consistent with the reduction of the covalence as observed in the XPS spectra.

REFERENCES

[1] G. H. Vurens, M. Salmerón, and G. A. Somorjai, Prog. Surf. Sci. 32, 333, 1990.

[2] V. E. Henrich, Prog. Surf. Sci. 50, 77, 1995.

[3]V. E. Henrich and P. A. Cox, *The Surffce Science of Metal Oxides.* Cambridge University Press, Cambridge, England, 1994, Chap. 7.

[4] R. J. Lad, Surf. Rev. Lett. 2, 109, 1995.

[5] A. R. González-Elipe and F. Yubero, in *Handbook of Surfaces and Interfaces of Materials*, edited by H. S. Nalwa _Academic, San Diego, 2001, Chap. 4.

[6] L. Soriano, G. G. Fuentes, C. Quirós, J. F. Trigo, J. M. Sanz, P. R. Bressler, and A. R. González-Elipe, Langmuir 16, 7066, 2000.

[7] M. Sánchez-Agudo, L. Soriano, C. Quirós, M. Abbate, L. Roca, J. Avila, and J. M. Sanz, Langmuir 17, 7339, 2001.

[8] F. Parmigiani, in *Cluster Models for Surface and Bulk Phenomena*, edited by G. Pacchioni *et al.* Plenum Press, New York, (1992), Vol. 1, p. 475.

[9] A. Corrias, G. Mountjoy, G. Piccaluga, and S. Solinas, J. Phys. Chem. B 103, 10081, 1999.

[10] X. J. Zhang, J. X. Liu, Y. Jing, and Y. C. Xie, Appl. Catal., A 240, 1, 2003.

[11] M. Nurunnabi, B. T. Li, K. Kunimori, K. Suzuki, K. Fujimoto, and K. Tomishige, Catal. Lett. 103, 277, 2005.

[12] D. Alders, F. C. Voogt, T. Hibma, and G. A. Sawatzky, Phys. Rev. B 54, 7716,1996.

[13] S. D. Peacor and T. Hibma, Surf. Sci. 301, 11, 1994.

[14] J. M. Sanz and G. Tyuliev, Surf. Sci. 367, 196, 1996.

[15] J. M. Sanz, L. Soriano, P. Prieto, G. Tyuliev, C. Morant, and E. Elizalde, Thin Solid Films 332, 209, 1998.

[16] M. A. James and T. Hibma, Surf. Sci. 433, 718, 1999.

[17] B. Warot, E. Snoek, J. C. Ousset, M. J. Casanove, S. Dubourg, and J. F. Bobo, Appl. Surf. Sci. 188, 151, 2002.

[18] L. Soriano, A. Gutiérrez, I. Preda, S. Palacín, J. M. Sanz, M. Abbate, J. F. Trigo, A. Vollmer, and P. R. Bressler, Phys. Rev. B 74, 193402, 2006.

[19] L. Soriano, I. Preda, A. Gutiérrez, S. Palacín, M. Abbate, and A. Vollmer, Phys. Rev. B 75, 233417, 2007.

[20] G. Lassaleta, A. Fernández, J. P. Espinós, and A. R. González-Elipe, J. Phys. Chem. 99, 1484, 1995.

[21] M. A. van Veenendaal and G. A. Sawatzky, Phys. Rev. Lett. 70, 2459, 1993.

[22] See, for example, J. Chaboy and S. Quartieri, Phys. Rev. B 52, 6349 (1995), and references therein.

[23] P. A. Lee and J. B. Pendry, Phys. Rev. B 11, 2795 (1975).

[24] L. Hedin and B. I. Lundqvist, J. Phys. C 4, 2064 (1971).

[25] C. R. Natoli, M. Benfatto, S. Della Longa, and K. Hatada, J. Synchrotron Radiat. **10**, 26 (2003).

[26] J. J. Rehr and R. C. Albers, Rev. Mod. Phys. **72**, 621 (2000).

[27] R. Gunnella, M. Benfatto, A. Marcelli, and C. R. Natoli, Solid State Commun. 76, 109 (1990).

[28] S. Díaz-Moreno, A. Muñoz-Páez, and J. Chaboy, J. Phys. Chem. A 104, 1278 (2000).

[29] M. F. Ruiz-Lopez and A. Muñoz-Paez, J. Phys.: Condens. Matter 3, 8981 (1991).

[30] V. Briois, Ph. Sainctavit, and A.-M. Flank, Jpn. J. Appl. Phys., Suppl. 32, 52 (1993).

[31] H. Modrow, S. Bucher, J. J. Rehr, and A. L. Ankudinov, Phys. Rev. B 67, 035123 (2003).

[32] C. R. Natoli, M. Benfatto, C. Brouder, M. F. Ruiz Lopez, and D. L. Foulis, Phys. Rev. B 42, 1944 (1990).

[33] J. P. Desclaux, Comput. Phys. Commun, 9, 31 (1975).

[34] Maurizio Benfatto and Stefano Della Longa, 2001.

[35] A. Corrias, G. Mountjoy, G. Piccaluga, and S. Solinas, *J. Phys. Chem. B*, 1999**,** *103*, (46), pp 10081–10086.

Chapter VI

APPLICATION

INTRODUCTION

In this section a brief XPS study of another nanostructured NiO system whose Ni *2p* XPS spectra agree with the surface + non-local model proposed in this work, is presented.

VI.2. RESULTS

In this case, the NiO systems are nanostructured NiO thin films grown by magnetron sputtering. For these NiO deposits, two different substrates were used. One was a p-doped Si wafer, where some native oxide remains. The other one was a special one, and in the following, it will be called AAM.

Scanning electron microscopy (SEM) images presented below, show the difference between nanostructured NiO growth on AAM and NiO growth on Si, both by magnetron sputtering.

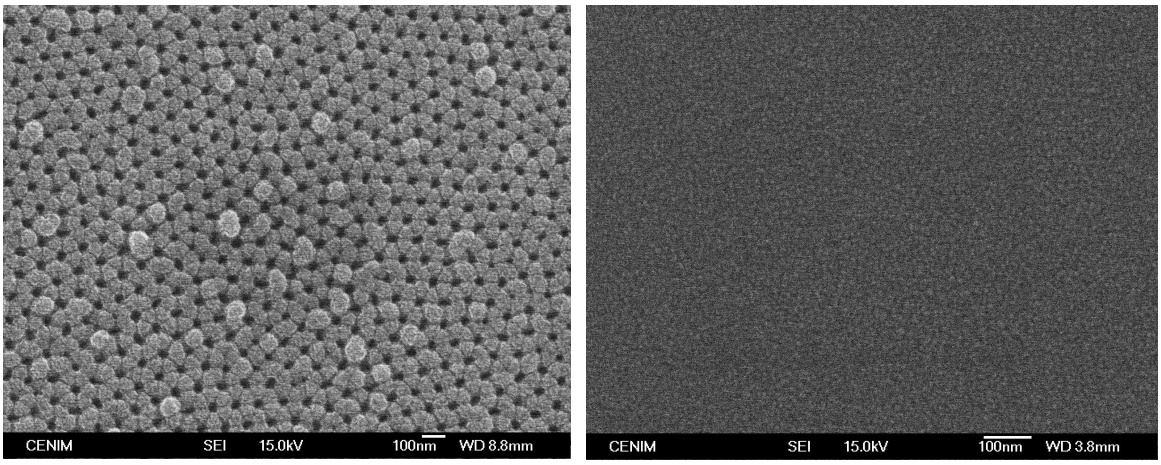

Fig.VI.1. SEM images of NiO/AAM (left) and NiO/ native SiO_2 on p-doped Si wafer (right)

It is obvious that magnetron sputtering method is a suitable technique for nanostructured NiO growth, using the adequate substrate in the mentioned conditions.

XPS measurements of Ni *2p*3/2 in both sample show, once again, that at the surface assigned peak increase its intensity for samples which presents high surface to volume ratio.

Below, two XPS spectra sets of the Ni *2p*3/2 for the same amount of NiO deposited on Al_2O_3 (right 1.b) and SiO_2, (left 2.b) are presented. For comparison purpose, in this representation, Ni *2p*3/2 XPS spectra of NiO single crystal (d) and NiO thick layer deposited

on Al_2O_3 (1.c) and SiO_2 (2.c) were added, as also spectra of Ni *2p*3/2 of early stages of thermal evaporation of NiO/Al_2O_3 (1.a) and NiO/SiO_2 (2.a).

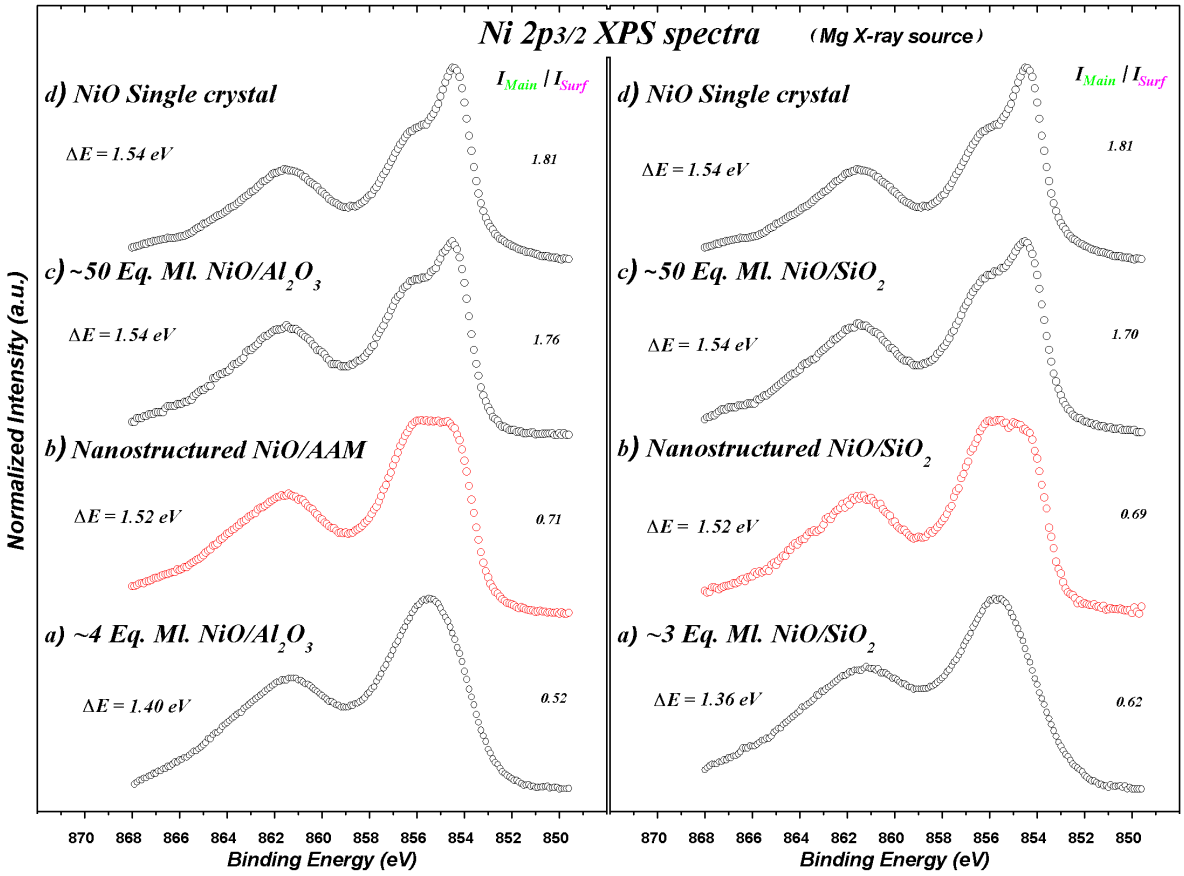

Fig. VI.2. Ni 2p3/2 XPS spectra of NiO single crystal (d), nanostructured NiO/AAM (1.b) and NiO/SiO_2 (2.b), thick layer of NiO/Al_2O_3 (1.d) and NiO/SiO_2 (2.d) and nanoislands of NiO/AL_2O_3 (1.a) and NiO/SiO_2 (2.a)

It can be seen that the spectra of nanostructured NiO present main to surface intensity ratio comparable with those of the NiO nanoislands deposited on both, Al_2O_3 and SiO_2. The energy separation of the *main* and *surface* fitting curves can be due to the oxygen species adsorbed during the sample transfer to analysis chamber in atmosphere.

Figure VI.3 shows the O1s spectra of the nanostructured NiO grown by magnetron sputtering (VI.3 a) together with spectrum of and 40 equivalent monolayer of NiO grown as in chapter V.

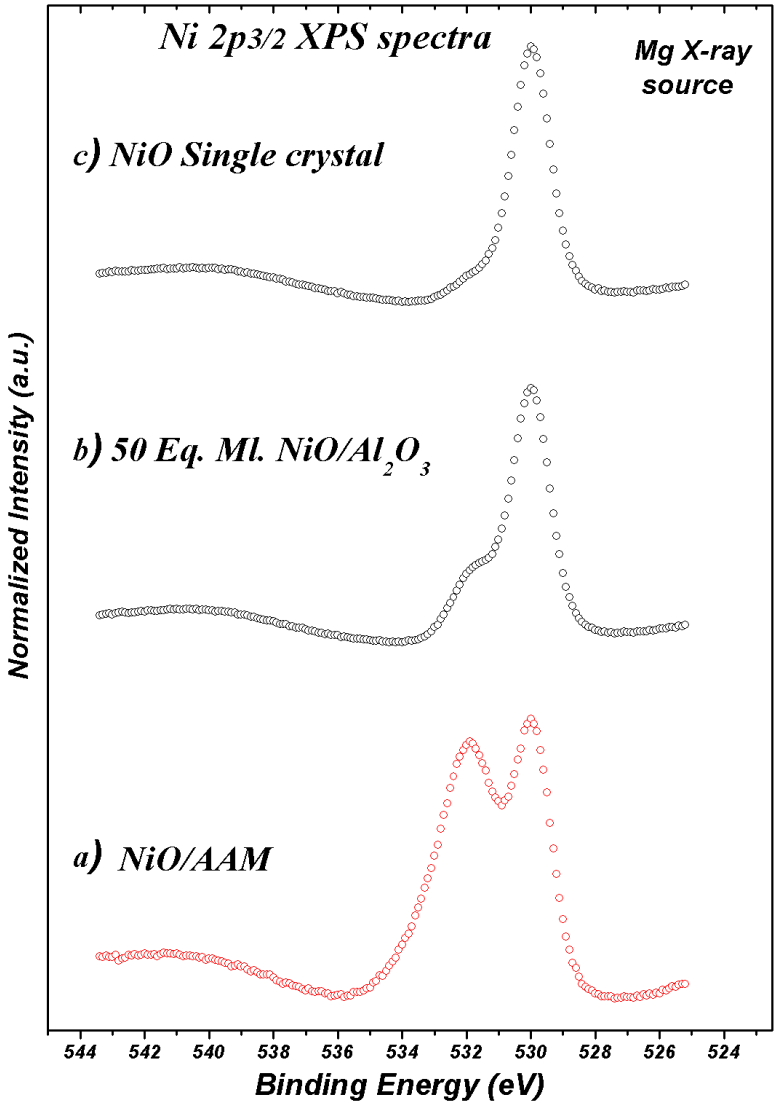

Fig. VI.3. O 1s XPS spectra of NiO/AAM (a), 50 eq. Ml. of NiO/Al_2O_3 (b) and of bulk NiO (c).

It is clear that the spectrum of the porous NiO grown on AAM shows the intensity peak higher than the other spectra. This is not surprising if one takes into account that this peak was assigned as reflecting the oxygen adsorbed species at the nanostructured NiO islands surface. It is reasonable to think that the NiO as membrane is acting as an absorption center for oxygen species when it is exposed to atmosphere. These results confirm the assignment of O_{II} peak in the O *1s* XPS spectra.

CONCLUSIONS

In this work, a morphological study of the different stages of growth of NiO on HOPG has been done by means of quantitative analysis of the XPS background (QUASES method) and AFM. It has been shown that the early stages of growth correspond to the formation of nanometric cuasibidimensional islands of above 100 nm in size and 20-70 Å in height. Further evaporation produces coalescence at about a thickness of about 60 equivalent ML. The agreement between the QUASES method and the AFM images gives support to this study.

Surface effects have been observed by the O *1s* XAS spectra for the early stages of growth. Indeed, a splitting of the Ni 3d states from the Ni atoms located at the surface has been observed. These results have been supported by cluster calculations in octahedral and pyramidal symmetries.

Surface enhanced Ni *2p* XPS spectra have demonstrated the significant contribution of the pyramidally coordinated Ni atoms at the NiO surface to the spectra. The known shoulder of the Ni *2p* XPS spectra has been attributed to a combination of surface and non-local peaks. This model allows to represent the spectral weight of the shoulder energy region as a contribution of three main curves: bulk, surface and non local. In this picture, new HAXPES spectra of the Ni *2p* and Ni *1s* core levels of NiO have been measured and fitted in the same terms as those obtained by XPS. It has been demonstrated that the bulk/surface contribution ratio follows a similar behavior than that of the inelastic mean free path. This fact strongly supports the proposed model.

The growth process of NiO on HOPG has been studied by XPS. The Ni *2p* XPS spectra show that for the early stages of growth, were nanostructured NiO is formed according to the AFM images, the intensity of the surface component dominate the spectra, being completely consistent with the surface + non local model. The higher binding energy peak of the O *1s* XPS spectra have been assigned to adsorbed oxygen species in the nanometric NiO islands of the early stages of growth. The intensity of this peak is always related to the surface component of the Ni *2p* XPS spectra.

Interface effects have been studied in the early stages of growth of NiO on three selected oxides, namely SiO_2, Al_2O_3 and MgO. As in the previous chapter, the morphology of the growth has been studied by quantitative analysis of the XPS background. AFM study has only been possible on the SiO_2 substrate due to its very low roughness. The formation of nanometric (~2x100 nm) NiO islands at the early stages of growth has been demonstrated.

Once again, the Ni *2p* XPS spectra for the early stages of growth showed that the surface component of the Ni *2p* XPS peak has a high intensity due to the large surface to volume ratio of the nanostructured NiO formed. Even more, the early stages of growth show that the surface peak is affected by the substrate. As obtained by cluster calculations for different covalent reductions, the most covalent substrate (SiO_2) shifts the surface peak towards higher binding energies with respect to the most ionic substrate (MgO). These results are consistent with the formation of cross-linking-bonds at the interface in the form Ni-O-M, where M stands for Si, Al, Mg.

These interface effects have also been studied by NEXAFS. The experimental spectra have been compared to multiple scattering simulations for different clusters and different symmetries. Whereas the early stages of growth (1 ML) have been simulated with a 19 atoms NiO cluster, the final stages (80 ML) agree with the simulations of a 93 atoms cluster. The substitution of 4 Ni atoms of the cluster by M atoms produces an improvement of the simulations. The differences of the NEXAFS spectra for the early stages of growth on the different oxides, mainly in the white line and the resonance structures, are explained by a distortion of the initial cluster induced by the substrate. The most covalent substrate (SiO_2) produce an increase of the Ni-O distance, which is completely consistent with the reduction of the covalence as observed in the XPS spectra.

Apart from the particular above conclusions, the main conclusion obtained in this work is that the Ni *2p* XPS spectra can be a powerful tool in the study of nanostructured NiO oxide. In this work, a model describing surface + non local effects has been proposed. This model, supported by theoretical calculations, has been able to explain the Ni *2p* spectra of different nanostructured NiO systems like the early stages of growth of NiO on HOPG, SiO_2, Al_2O_3 and MgO and porous NiO membranes. Other complementary techniques, such as AFM and inelastic background analysis, have allowed the determination of the morphology of the nanostructures. X-ray absorption spectroscopy has been used to corroborate both, surface effects by means of the O 1s XAS spectra and interface effects by means of the Ni *1s* NEXAFS spectra. The use of different techniques and theoretical calculations has given a great support to this study.

APPENDIX

CLUSTER MODEL CALCULATION PARAMETERS

Cluster Model Ni^{2+} - Surf (D4)

Main Parameters

```
u =  7.5;        Repulsion Energy (U)
d =  4.0;        Charge-Transfer (Delta)
p =  1.3;        Transfer Integral (pdsigma)
q =  8.5;        Core-Hole Potential (Q)
```

Multiplet Parameters

```
b  = 0.13;              Racah Parameter (B)
c  = 0.58;              Racah Parameter (C)
a  = u+14*b/9-7*c/9;    Racah Parameter (A)
dq = 0.10;              Crystal-Field Splitting (Dq)
uu = a+4*b+3*c;         Kanamori Parameter (u)
up = a-b+c;             Kanamori Parameter (u´)
jj = 5*b/2+c;           Kanamori Parameter (j)
```

Transfer Integrals

```
ta = sqrt(3)*p/2;       Transfer Integral (apical: 3z^2-r^2)
tb = sqrt(3)*p;         Transfer Integral (basal: x^2-y^2)
```

Ground State: Matrix Elements

```
g1 = 3*uu+25*up-13*jj-12*dq-28*u;
g2 = 4*uu+32*up-16*jj- 6*dq-36*u+d;
g3 = 4*uu+32*up-16*jj- 6*dq-36*u+d;
g4 = 5*uu+40*up-20*jj- 0*dq-45*u+2*d+u;
```

Ground State: Hamilton Matrix

```
gs = [g1   ta   tb   0
      ta   g2   0    tb
      tb   0    g3   ta
      0    tb   ta   g4];
```

Ground State: Values-Vectors

```
[vecg,valg] = eig(gs)
```

Final State: Matrix Elements

```
f1 = g1;
f2 = g2-q;
f3 = g3-q;
f4 = g4-2*q;
```

Final State: Hamilton Matrix

```
fs = [f1   ta   tb   0
      ta   f2   0    tb
      tb   0    f3   ta
      0    tb   ta   f4];
```

Final State: Values-Vectors

```
[vecf,valf]=eig(fs)
```

Energies and Intensities

```
e1 = (valg(3,3)-valf(1,1))
e2 = (valg(3,3)-valf(2,2))
e3 = (valg(3,3)-valf(3,3))
e4 = (valg(3,3)-valf(4,4))
i1 = (vecg(:,3)'*vecf(:,1))^2
i2 = (vecg(:,3)'*vecf(:,2))^2
i3 = (vecg(:,3)'*vecf(:,3))^2
i4 = (vecg(:,3)'*vecf(:,4))^2
```

Cluster Model Ni^{2+} - Bulk (Oh)

Main Parameters

```
u =  7.5;          Repulsion Energy (U)
d =  4.0;          Charge-Transfer (Delta)
p =  1.3;          Transfer Integral (pdsigma)
q =  8.5;          Core-Hole Potential (Q)
```

Multiplet Parameters

```
b  = 0.13;              Racah Parameter (B)
c  = 0.58;              Racah Parameter (C)
a  = u+14*b/9-7*c/9;    Racah Parameter (A)
dq = 0.10;              Crystal-Field Splitting (Dq)
uu = a+4*b+3*c;         Kanamori Parameter (u)
up = a-b+c;             Kanamori Parameter (u´)
jj = 5*b/2+c;           Kanamori Parameter (j)
```

Transfer Integrals

```
ta = sqrt(3)*p;         Transfer Integral (apical: 3z^2-r^2)
tb = sqrt(3)*p;         Transfer Integral (basal: x^2-y^2)
```

Ground State: Matrix Elements

```
g1 = 3*uu+25*up-13*jj-12*dq-28*u;
g2 = 4*uu+32*up-16*jj- 6*dq-36*u+d;
g3 = 4*uu+32*up-16*jj- 6*dq-36*u+d;
g4 = 5*uu+40*up-20*jj- 0*dq-45*u+2*d+u;
```

Ground State: Hamilton Matrix

```
gs = [g1   ta   tb   0
      ta   g2   0    tb
      tb   0    g3   ta
      0    tb   ta   g4];
```

Ground State: Values & Vectors

```
[vecg,valg] = eig(gs)
```

Final State: Matrix Elements

```
f1 = g1;
f2 = g2-q;
f3 = g3-q;
f4 = g4-2*q;
```

Final State: Hamilton Matrix

```
fs = [f1   ta   tb   0
      ta   f2   0    tb
      tb   0    f3   ta
      0    tb   ta   f4];
```

Final State: Values & Vectors

```
[vecf,valf]=eig(fs)
```

Energies and Intensities

```
e1 = (valg(3,3)-valf(1,1))
e2 = (valg(3,3)-valf(2,2))
e3 = (valg(3,3)-valf(3,3))
e4 = (valg(3,3)-valf(4,4))
i1 = (vecg(:,3)'*vecf(:,1))^2
i2 = (vecg(:,3)'*vecf(:,2))^2
i3 = (vecg(:,3)'*vecf(:,3))^2
i4 = (vecg(:,3)'*vecf(:,4))^2
```

QUASES OBTAINED VALUES

NiO/HOPG

NiO on **HOPG**						
Evaporation time (min)	Ni LVV Auger analyzed			Ni *2p* analyzed		
	Island height (Å)	Coverage (%)	Equivalent thickness (Å)	Island height (Å)	Coverage (%)	Equivalent thickness (Å)
10	-	-	-	-	-	-
40	26	7.5	1.95	27	9.6	2.59
120	32	18	5.76	38	20.8	7.9
320	35	32.5	11.3	33	37.2	12.2
640	45	45.6	20.5	45	51.5	23.1
870	57	53.3	30.3	58	58.4	33.8
975	97	75.4	73.1	97	80.9	78.4

NiO/oxides

NiO on SiO_2						
Evaporation time (min)	Ni LVV Auger analyzed			Ni *2p* analyzed		
	height (Å)	coverage (%)	Equivalent thickness (Å)	height (Å)	coverage (%)	Equivalent thickness (Å)
1	-	-	-	-	-	-
2	-	-	-	17	3.1	0.52
4	-	-	-	19	6.3	1.19
8	24	11.8	2.83	23	12.4	2.8
16	29	24.4	7.0	27	27.4	7.3
24	31	44.7	13.8	32	48.8	15.6
32	40	76	30.4	42	81.7	34.3
40	60	91.7	55.0	60	92.5	55.5
NiO on Al_2O_3						
Evaporation time (min)	Ni LVV Auger analyzed			Ni *2p* analyzed		
	height (Å)	coverage (%)	Equivalent thickness (Å)	height (Å)	coverage (%)	Equivalent thickness (Å)
1	-	-	-	-	-	-
2	21	15.9	3.33	19	18.8	3.57
4	22	28.5	6.27	19	32.9	6.25
8	22	50.8	11.7	22	51.2	11.2
16	32	67.5	21.6	33	69.5	22.9
24	40	74.7	29.8	38	79	30.0
32	45	89.5	40.1	45	87.7	39.4
40	56	93.2	52.1	55	90.5	49.7
48	64	100	64	66	93.8	61.6
56	71	100	71	71	93.8	66.5
88	120	100	120			
NiO on MgO						
Evaporation time (min)	Ni LVV Auger analyzed			Ni *2p* analyzed		
	height (Å)	coverage (%)	Equivalent thickness (Å)	height (Å)	coverage (%)	Equivalent thickness (Å)
1	23	10.3	2.36	19	14.9	2. 83
2	27	17.2	4.64	19	25.8	4.90
4	30	31.3	9.39	20	43.9	8.78
8	32	50.0	16.28	26	62.6	16.2
16	40	74.6	29.84	34	85	28.9
24	49	76.9	37.68	48	79.8	38.3
32	62	89.3	55.36	52	96.1	49.9
48	65	97.2	63.18	69	98.8	68.1
80	95	99.2	94.24	95	97.5	92.6

AFM TOPOGRAPHIC PROFILE ANALYSIS VALUES OBTAINED

0.03 Eq. ML of NiO on SiO_2

Nr.	Height (nm)	Width (μm)
1	1.159	0.122
2	0.876	0.127
3	0.682	0.111
4	1.349	0.148
5	0.958	0.122
6	0.434	0.143
7	0.852	0.109
8	0.964	0.106
9	1.4	0.159
10	0.727	0.164
11	0.785	0.143
12	1.241	0.106
13	0.917	0.117
14	0.6	0.084
15	1.328	0.117
16	0.985	0.133
17	0.854	0.101
18	0.916	0.106
19	0.936	0.106
20	0.665	0.117
21	0.747	0.090
22	0.415	0.111
23	0.59	0.095
24	0.798	0.079
25	0.711	0.101
26	1.487	0.164
27	0.573	0.091
28	0.916	0.084
29	0.824	0.084
30	1.331	0.122

0.12 Eq. ML of NiO on SiO_2

Nr.	Height (nm)	Width (μm)
1	0.305	1.493
2	0.164	1.457
3	0.398	2.369
4	0.188	1.153
5	0.164	0.988
6	0.258	1.994
7	0.211	1.386
8	0.188	1.393
9	0.234	2.696
10	0.141	0.976
11	0.164	1.002
12	1.031	0.853
13	0.164	1.027
14	0.164	1.499
15	0.164	1.211
16	0.117	0.774
17	0.211	0.956
18	0.164	1.455
19	0.164	0.948
20	0.211	1.335
21	0.094	0.469
22	0.117	0.569
23	0.188	1.342
24	0.164	1.231
25	0.188	1.345
26	0.07	0.503

0.17 Eq. ML of NiO on SiO_2

Nr.	Height (nm)	Width (μm)
1	0.164	0.74
2	0.140	0.332
3	0.469	2.022
4	0.187	2.443
5	0.210	1.128
6	0.257	1.328
7	0.093	0.873
8	0.281	4.778
9	0.187	1.81
10	0.187	2.851
11	0.164	2.012
12	0.164	2.375
13	0.140	1.664
14	0.070	0.497
15	0.117	0.748
16	0.164	2.242
17	0.140	2.259
18	0.234	0.685
19	0.117	0.738
20	0.093	2.209
21	0.187	0.695
22	0.140	3.063
23	0.140	2.082
24	0.117	1.940
25	0.140	0.640
26	0.117	0.709
27	0.093	0.985
28	0.093	1.631
29	0.117	2.937
30	0.117	2.141
31	0.117	2.881
32	0.140	1.957
33	0.093	0.454
34	0.117	1.788
35	0.140	1.670
36	0.140	1.997
37	0.093	0.690
38	0.093	0.589
39	0.070	0.435
40	0.093	1.020
41	0.117	1.687
42	0.140	1.201
43	0.093	0.869
44	0.117	1.497
45	0.117	1.354

46	0.117	1.234
47	0.070	0.499
48	0.140	1.677
49	0.093	0.754
50	0.093	1.216
51	0.117	1.657
52	0.117	1.391
53	0.304	1.332
54	0.164	2.373
55	0.140	1.058
56	0.140	1.310
57	0.117	1.097
58	0.140	1.431
59	0.281	0.369
60	0.164	2.469
61	0.093	1.264
62	0.117	1.394
63	0.140	2.235
64	0.140	1.862
65	0.164	2.084

Fitting parameters

XPS Ni 2p3/2 of NiO single crystal

1'res ' 0.67000E+00 0.00000E+00
2'intens-1 ' 0.14815E+03 0.71821E+01
3'anch-1 ' 0.16700E+00 0.00000E+00
4'pos-1 ' 0.39916E+03 0.59138E-01
5'fondo-int ' -0.42313E-02 0.25219E-03
6'intens-2 ' 0.70942E+00 0.00000E+00
7'anch-2 ' 0.70000E+00 0.00000E+00
8'pos-2 ' 0.27000E+01 0.00000E+00
9'intens-3 ' 0.24298E+01 0.54317E+00
10'anch-3 ' 0.21092E+01 0.43794E+00
11'pos-3 ' 0.70326E+01 0.21184E+00
12'intens-4 ' 0.81768E-01 0.66565E-01
13'anch-4 ' 0.31571E+00 0.00000E+00
14'pos-4 ' 0.12671E+02 0.00000E+00
15'intens-5 ' 0.25048E+00 0.15012E+00
16'anch-5 ' 0.87175E+00 0.00000E+00
17'pos-5 ' 0.10054E+02 0.00000E+00
18'int-6 ' 0.47769E+00 0.00000E+00
19'anch-6 ' 0.16918E+00 0.12190E+00
20'pos-6 ' 0.15371E+01 0.00000E+00
21'Q-back-c ' 0.90694E+02 0.15820E+01
22'Q-back-A ' 0.35235E-01 0.18930E-02
23'Q-back-x0 ' 0.42083E+03 0.14583E+01
24'intens-1-2' 0.20147E+07 0.14142E+01
25'intens-2-2' 0.22002E+01 0.14142E+01
26'intens-3-2' 0.28619E+01 0.14142E+01
27'intens-4-2' 0.71897E-01 0.14142E+01
28'intens-5-2' 0.64522E-01 0.14142E+01
29'intens-6-2' 0.00000E+00 0.00000E+00
30'fondo-int2' 0.39559E-01 0.00000E+00
31'Q-back-c-2' 0.78458E+06 0.00000E+00
32'Q-back-A-2' 0.86531E+03 0.00000E+00
33'Q-back-x02' 0.42970E+03 0.00000E+00
34'intens-1-3' 0.00000E+00 0.00000E+00
35'intens-2-3' 0.00000E+00 0.00000E+00
36'intens-3-3' 0.00000E+00 0.00000E+00
37'intens-4-3' 0.00000E+00 0.00000E+00
38'intens-5-3' 0.00000E+00 0.00000E+00
39'intens-6-3' 0.00000E+00 0.00000E+00
40'fondo-int3' 0.00000E+00 0.00000E+00
41'Q-back-c-3' 0.00000E+00 0.00000E+00
42'Q-back-A-3' 0.00000E+00 0.00000E+00
43'Q-back-x03' 0.00000E+00 0.00000E+00
44't ' -0.13221E+00 0.14142E+01

XPS Ni 2p3/2 of NiO bulk

1'res ' 0.67000E+00 0.00000E+00
2'intens-1 ' 0.16597E+03 0.60955E+01
3'anch-1 ' 0.16700E+00 0.00000E+00
4'pos-1 ' 0.39902E+03 0.53653E-01
5'fondo-int ' 0.71158E-03 0.43674E-03
6'intens-2 ' 0.70942E+00 0.00000E+00
7'anch-2 ' 0.70000E+00 0.00000E+00
8'pos-2 ' 0.27000E+01 0.00000E+00
9'intens-3 ' 0.26263E+01 0.53217E+00
10'anch-3 ' 0.22298E+01 0.54035E+00
11'pos-3 ' 0.70434E+01 0.16730E+00
12'intens-4 ' 0.78837E-01 0.61695E-01
13'anch-4 ' 0.31571E+00 0.00000E+00
14'pos-4 ' 0.12671E+02 0.00000E+00
15'intens-5 ' 0.20377E+00 0.14778E+00
16'anch-5 ' 0.87175E+00 0.00000E+00
17'pos-5 ' 0.10054E+02 0.00000E+00
18'intens-6 ' 0.58400E+00 0.00000E+00
19'anch-6 ' 0.21792E+00 0.00000E+00
20'pos-6 ' 0.15200E+01 0.00000E+00
21'Q-back-c ' 0.90985E+02 0.22582E+01
22'Q-back-A ' 0.40021E-08 0.25166E-01
23'Q-back-x0 ' 0.42161E+03 0.74294E+02
24'intens-1-2' 0.20149E+07 0.14142E+01
25'intens-2-2' 0.22002E+01 0.14142E+01
26'intens-3-2' 0.28619E+01 0.14142E+01
27'intens-4-2' 0.71897E-01 0.14142E+01
28'intens-5-2' 0.64522E-01 0.14142E+01
29'intens-6-2' 0.00000E+00 0.00000E+00
30'fondo-int2' 0.39559E-01 0.00000E+00
31'Q-back-c-2' 0.78458E+06 0.00000E+00
32'Q-back-A-2' 0.86531E+03 0.00000E+00
33'Q-back-x02' 0.42970E+03 0.00000E+00
34'intens-1-3' 0.00000E+00 0.00000E+00
35'intens-2-3' 0.00000E+00 0.00000E+00
36'intens-3-3' 0.00000E+00 0.00000E+00
37'intens-4-3' 0.00000E+00 0.00000E+00
38'intens-5-3' 0.00000E+00 0.00000E+00
39'intens-6-3' 0.00000E+00 0.00000E+00
40'fondo-int3' 0.00000E+00 0.00000E+00
41'Q-back-c-3' 0.00000E+00 0.00000E+00
42'Q-back-A-3' 0.00000E+00 0.00000E+00
43'Q-back-x03' 0.00000E+00 0.00000E+00
44't ' -0.13221E+00 0.14142E+01

XPS O 1s of NiO/HOPG first stage

1'res	0.57000E+00	0.00000E+00
2'intens-1	0.14992E+05	0.21552E+03
3'anch-1	0.51878E-02	0.71126E-03
4'pos-1	0.72318E+03	0.13606E-02
5'fondo-int	-0.22758E-03	0.12862E-03
6'intens-2	0.38397E+01	0.57887E-01
7'anch-2	0.10804E+01	0.18880E-01
8'pos-2	0.20267E+01	0.11677E-01
9'intens-3	0.95634E+00	0.90240E-01
10'anch-3	0.26210E+01	0.19214E+00
11'pos-3	0.10717E+02	0.13034E+00
12'intens-4	0.00000E+00	0.00000E+00
13'anch-4	0.31571E+00	0.00000E+00
14'pos-4	0.12671E+02	0.00000E+00
15'intens-5	0.00000E+00	0.00000E+00
16'anch-5	0.87175E+00	0.00000E+00
17'pos-5	0.10054E+02	0.00000E+00
18'intens-6	0.00000E+00	0.00000E+00
19'anch-6	0.00000E+00	0.00000E+00
20'pos-6	0.00000E+00	0.00000E+00
21'Q-back-c	0.86171E+05	0.49534E+02
22'Q-back-A	0.15662E+02	0.31410E+00
23'Q-back-x0	0.73000E+03	0.14687E+00
24'intens-1-2'	0.90565E+06	0.00000E+00
25'intens-2-2'	0.29712E+01	0.00000E+00
26'intens-3-2'	0.32489E+01	0.00000E+00
27'intens-4-2'	0.94403E-01	0.00000E+00
28'intens-5-2'	0.27926E+00	0.00000E+00
29'intens-6-2'	0.00000E+00	0.00000E+00
30'fondo-int2'	0.41234E-02	0.00000E+00
31'Q-back-c-2'	0.45540E+06	0.00000E+00
32'Q-back-A-2'	0.95363E-03	0.00000E+00
33'Q-back-x02'	0.48004E+03	0.00000E+00
34'intens-1-3'	0.00000E+00	0.00000E+00
35'intens-2-3'	0.00000E+00	0.00000E+00
36'intens-3-3'	0.00000E+00	0.00000E+00
37'intens-4-3'	0.00000E+00	0.00000E+00
38'intens-5-3'	0.00000E+00	0.00000E+00
39'intens-6-3'	0.00000E+00	0.00000E+00
40'fondo-int3'	0.00000E+00	0.00000E+00
41'Q-back-c-3'	0.00000E+00	0.00000E+00
42'Q-back-A-3'	0.00000E+00	0.00000E+00
43'Q-back-x03'	0.00000E+00	0.00000E+00
44't	0.43305E-01	0.00000E+00

XPS O 1s of NiO/HOPG last stage

1'res	0.57000E+00	0.00000E+00
2'intens-1	0.87260E+06	0.71096E+04
3'anch-1	0.51878E-02	0.71126E-03
4'pos-1	0.72353E+03	0.14713E-03
5'fondo-int	-0.53070E-02	0.58780E-04
6'intens-2	0.46366E+00	0.30505E-02
7'anch-2	0.30709E+00	0.34583E-02
8'pos-2	0.18400E+01	0.12199E-02
9'intens-3	0.17968E+01	0.11571E-01
10'anch-3	0.54083E+01	0.25180E-01
11'pos-3	0.10548E+02	0.12033E-01
12'intens-4	0.00000E+00	0.00000E+00
13'anch-4	0.31571E+00	0.00000E+00
14'pos-4	0.12671E+02	0.00000E+00
15'intens-5	0.00000E+00	0.00000E+00
16'anch-5	0.87175E+00	0.00000E+00
17'pos-5	0.10054E+02	0.00000E+00
18'intens-6	0.00000E+00	0.00000E+00
19'anch-6	0.00000E+00	0.00000E+00
20'pos-6	0.00000E+00	0.00000E+00
21'Q-back-c	0.37504E+06	0.13769E+04
22'Q-back-A	0.38481E+03	0.37579E+01
23'Q-back-x0	0.73696E+03	0.22735E+00
24'intens-1-2'	0.90565E+06	0.00000E+00
25'intens-2-2'	0.29712E+01	0.00000E+00
26'intens-3-2'	0.32489E+01	0.00000E+00
27'intens-4-2'	0.94403E-01	0.00000E+00
28'intens-5-2'	0.27926E+00	0.00000E+00
29'intens-6-2'	0.00000E+00	0.00000E+00
30'fondo-int2'	0.41234E-02	0.00000E+00
31'Q-back-c-2'	0.45540E+06	0.00000E+00
32'Q-back-A-2'	0.95363E-03	0.00000E+00
33'Q-back-x02'	0.48004E+03	0.00000E+00
34'intens-1-3'	0.00000E+00	0.00000E+00
35'intens-2-3'	0.00000E+00	0.00000E+00
36'intens-3-3'	0.00000E+00	0.00000E+00
37'intens-4-3'	0.00000E+00	0.00000E+00
38'intens-5-3'	0.00000E+00	0.00000E+00
39'intens-6-3'	0.00000E+00	0.00000E+00
40'fondo-int3'	0.00000E+00	0.00000E+00
41'Q-back-c-3'	0.00000E+00	0.00000E+00
42'Q-back-A-3'	0.00000E+00	0.00000E+00
43'Q-back-x03'	0.00000E+00	0.00000E+00
44't	0.43305E-01	0.00000E+00

XPS Ni 2p3/2 of NiO final stages of NiO growth on SiO_2

1'res ' 0.67000E+00 0.00000E+00
2'intens-1 ' 0.14619E+03 0.65664E+01
3'anch-1 ' 0.16700E+00 0.10000E+00
4'pos-1 ' 0.39924E+03 0.66079E-01
5'fondo-int ' 0.37369E-02 0.74564E-03
6'intens-2 ' 0.70942E+00 0.00000E+00
7'anch-2 ' 0.70000E+00 0.00000E+00
8'pos-2 ' 0.27000E+01 0.00000E+00
9'intens-3 ' 0.24477E+01 0.65200E+00
10'anch-3 ' 0.21835E+01 0.52254E+00
11'pos-3 ' 0.70966E+01 0.25268E+00
12'intens-4 ' 0.78212E-01 0.83836E-01
13'anch-4 ' 0.31571E+00 0.00000E+00
14'pos-4 ' 0.12671E+02 0.00000E+00
15'intens-5 ' 0.20548E+00 0.18576E+00
16'anch-5 ' 0.87175E+00 0.00000E+00
17'pos-5 ' 0.10054E+02 0.00000E+00
18'intens-6 ' 0.58817E+00 0.10000E+00
19'anch-6 ' 0.25000E+00 0.10000E+00
20'pos-6 ' 0.15371E+01 0.28450E+02
21'Q-back-c ' 0.10132E+03 0.20252E+01
22'Q-back-A ' 0.68322E-03 0.56150E-03
23'Q-back-x0 ' 0.44436E+03 0.96087E+01
24'intens-1-2' 0.20147E+07 0.30601E+06
25'intens-2-2' 0.22002E+01 0.30601E+06
26'intens-3-2' 0.28619E+01 0.30601E+06
27'intens-4-2' 0.71897E-01 0.30601E+06
28'intens-5-2' 0.64522E-01 0.30601E+06
29'intens-6-2' 0.00000E+00 0.00000E+00
30'fondo-int2' 0.39559E-01 0.00000E+00
31'Q-back-c-2' 0.78458E+06 0.00000E+00
32'Q-back-A-2' 0.86531E+03 0.00000E+00
33'Q-back-x02' 0.42970E+03 0.00000E+00
34'intens-1-3' 0.00000E+00 0.00000E+00
35'intens-2-3' 0.00000E+00 0.00000E+00
36'intens-3-3' 0.00000E+00 0.00000E+00
37'intens-4-3' 0.00000E+00 0.00000E+00
38'intens-5-3' 0.00000E+00 0.00000E+00
39'intens-6-3' 0.00000E+00 0.00000E+00
40'fondo-int3' 0.00000E+00 0.00000E+00
41'Q-back-c-3' 0.00000E+00 0.00000E+00
42'Q-back-A-3' 0.00000E+00 0.00000E+00
43'Q-back-x03' 0.00000E+00 0.00000E+00
44't ' -0.13221E+00 0.30601E+06
45'asim ' 0.50000E-01 0.00000E+00
46'pos-asim ' 0.40001E+03 0.00000E+00
47'int-asim ' 0.00000E+00 0.00000E+00
48'anch-asim ' 0.34416E+00 0.00000E+00

XPS Ni 2p3/2 of NiO final stages of NiO growth on Al_2O_3

1'res ' 0.67000E+00 0.00000E+00
2'intens-1 ' 0.16707E+03 0.10103E+02
3'anch-1 ' 0.16700E+00 0.10000E+00
4'pos-1 ' 0.39904E+03 0.80018E-01
5'fondo-int ' 0.22985E-02 0.47286E-02
6'intens-2 ' 0.70942E+00 0.00000E+00
7'anch-2 ' 0.70000E+00 0.00000E+00
8'pos-2 ' 0.27000E+01 0.00000E+00
9'intens-3 ' 0.22988E+01 0.91337E+00
10'anch-3 ' 0.20955E+01 0.54155E+00
11'pos-3 ' 0.70797E+01 0.20134E+00
12'intens-4 ' 0.69131E-01 0.72443E-01
13'anch-4 ' 0.31571E+00 0.00000E+00
14'pos-4 ' 0.12671E+02 0.00000E+00
15'intens-5 ' 0.19091E+00 0.14624E+00
16'anch-5 ' 0.87175E+00 0.00000E+00
17'pos-5 ' 0.10054E+02 0.00000E+00
18'intens-6 ' 0.58451E+00 0.97453E-01
19'anch-6 ' 0.26000E+00 0.10000E+00
20'pos-6 ' 0.15295E+01 0.28450E+02
21'Q-back-c ' 0.10092E+03 0.27547E+02
22'Q-back-A ' -0.73296E-02 0.21352E-01
23'Q-back-x0 ' 0.43794E+03 0.27762E+01
24'intens-1-2' 0.20147E+07 0.14142E+01
25'intens-2-2' 0.22002E+01 0.14142E+01
26'intens-3-2' 0.28619E+01 0.14142E+01
27'intens-4-2' 0.71897E-01 0.14142E+01
28'intens-5-2' 0.64522E-01 0.14142E+01
29'intens-6-2' 0.00000E+00 0.00000E+00
30'fondo-int2' 0.39559E-01 0.00000E+00
31'Q-back-c-2' 0.78458E+06 0.00000E+00
32'Q-back-A-2' 0.86531E+03 0.00000E+00
33'Q-back-x02' 0.42970E+03 0.00000E+00
34'intens-1-3' 0.00000E+00 0.00000E+00
35'intens-2-3' 0.00000E+00 0.00000E+00
36'intens-3-3' 0.00000E+00 0.00000E+00
37'intens-4-3' 0.00000E+00 0.00000E+00
38'intens-5-3' 0.00000E+00 0.00000E+00
39'intens-6-3' 0.00000E+00 0.00000E+00
40'fondo-int3' 0.00000E+00 0.00000E+00
41'Q-back-c-3' 0.00000E+00 0.00000E+00
42'Q-back-A-3' 0.00000E+00 0.00000E+00
43'Q-back-x03' 0.00000E+00 0.00000E+00
44't ' -0.13221E+00 0.14142E+01
45'asim ' 0.50000E-01 0.00000E+00
46'pos-asim ' 0.40001E+03 0.00000E+00
47'int-asim ' 0.00000E+00 0.00000E+00
48'anch-asim ' 0.34416E+00 0.00000E+00

XPS Ni 2p3/2 of NiO final stages of NiO growth on MgO

```
 1'res      ' 0.67000E+00  0.00000E+00
2'intens-1 ' 0.16069E+03  0.25586E+01
3'anch-1   ' 0.16700E+00  0.00000E+00
4'pos-1    ' 0.39641E+03  0.49971E-01
5'fondo-int ' 0.21572E-02  0.15581E-03
6'intens-2 ' 0.70942E+00  0.00000E+00
7'anch-2   ' 0.70000E+00  0.00000E+00
8'pos-2    ' 0.27000E+01  0.00000E+00
9'intens-3 ' 0.26710E+01  0.80844E-01
10'anch-3  ' 0.22914E+01  0.13070E+00
11'pos-3   ' 0.71018E+01  0.12551E+00
12'intens-4 ' 0.81750E-01  0.42261E-01
13'anch-4  ' 0.31571E+00  0.00000E+00
14'pos-4   ' 0.12671E+02  0.00000E+00
15'intens-5 ' 0.19955E+00  0.56719E-01
16'anch-5  ' 0.87175E+00  0.00000E+00
17'pos-5   ' 0.10054E+02  0.00000E+00
18'intens-6 ' 0.58709E+00  0.46876E-01
19'anch-6  ' 0.25000E+00  0.00000E+00
20'pos-6   ' 0.15371E+01  0.00000E+00
21'Q-back-c ' 0.86376E+02  0.78262E+00
22'Q-back-A ' 0.11156E-01  0.84040E-03
23'Q-back-x0 ' 0.42143E+03  0.12050E+01
24'intens-1-2'  0.20147E+07  0.20000E+01
25'intens-2-2'  0.22002E+01  0.14142E+01
26'intens-3-2'  0.28619E+01  0.14142E+01
27'intens-4-2'  0.71897E-01  0.14142E+01
28'intens-5-2'  0.64522E-01  0.14142E+01
29'intens-6-2'  0.00000E+00  0.00000E+00
30'fondo-int2'  0.39559E-01  0.00000E+00
31'Q-back-c-2'  0.78458E+06  0.00000E+00
32'Q-back-A-2'  0.86531E+03  0.00000E+00
33'Q-back-x02'  0.42970E+03  0.00000E+00
34'intens-1-3'  0.00000E+00  0.00000E+00
35'intens-2-3'  0.00000E+00  0.00000E+00
36'intens-3-3'  0.00000E+00  0.00000E+00
37'intens-4-3'  0.00000E+00  0.00000E+00
38'intens-5-3'  0.00000E+00  0.00000E+00
39'intens-6-3'  0.00000E+00  0.00000E+00
40'fondo-int3'  0.00000E+00  0.00000E+00
41'Q-back-c-3'  0.00000E+00  0.00000E+00
42'Q-back-A-3'  0.00000E+00  0.00000E+00
43'Q-back-x03'  0.00000E+00  0.00000E+00
44't        ' -0.13221E+00  0.14142E+01
45'asim     ' 0.50000E-01  0.00000E+00
46'pos-asim ' 0.40001E+03  0.00000E+00
47'int-asim ' 0.00000E+00  0.00000E+00
48'anch-asim ' 0.34416E+00  0.00000E+00
```

XPS Ni 2p3/2 of NiO early stages of NiO growth on SiO_2

```
 1'res      ' 0.67000E+00  0.00000E+00
2'intens-1 ' 0.16323E+03  0.27521E+01
3'anch-1   ' 0.16700E+00  0.00000E+00
4'pos-1    ' 0.39838E+03  0.49909E-01
5'fondo-int ' 0.13907E-02  0.15830E-03
6'intens-2 ' 0.70942E+00  0.00000E+00
7'anch-2   ' 0.70000E+00  0.00000E+00
8'pos-2    ' 0.27000E+01  0.00000E+00
9'intens-3 ' 0.26247E+01  0.83127E-01
10'anch-3  ' 0.22790E+01  0.12933E+00
11'pos-3   ' 0.70681E+01  0.12412E+00
12'intens-4 ' 0.85663E-01  0.41673E-01
13'anch-4  ' 0.31571E+00  0.00000E+00
14'pos-4   ' 0.12671E+02  0.00000E+00
15'intens-5 ' 0.21293E+00  0.56729E-01
16'anch-5  ' 0.87175E+00  0.00000E+00
17'pos-5   ' 0.10054E+02  0.00000E+00
18'intens-6 ' 0.55656E+00  0.46129E-01
19'anch-6  ' 0.20516E+00  0.94764E-01
20'pos-6   ' 0.15371E+01  0.95126E-01
21'Q-back-c ' 0.87121E+02  0.82936E+00
22'Q-back-A ' 0.13563E-01  0.94294E-03
23'Q-back-x0 ' 0.42153E+03  0.10742E+01
24'intens-1-2'  0.20147E+07  0.20000E+01
25'intens-2-2'  0.22002E+01  0.14142E+01
26'intens-3-2'  0.28619E+01  0.14142E+01
27'intens-4-2'  0.71897E-01  0.14142E+01
28'intens-5-2'  0.64522E-01  0.14142E+01
29'intens-6-2'  0.00000E+00  0.00000E+00
30'fondo-int2'  0.39559E-01  0.00000E+00
31'Q-back-c-2'  0.78458E+06  0.00000E+00
32'Q-back-A-2'  0.86531E+03  0.00000E+00
33'Q-back-x02'  0.42970E+03  0.00000E+00
34'intens-1-3'  0.00000E+00  0.00000E+00
35'intens-2-3'  0.00000E+00  0.00000E+00
36'intens-3-3'  0.00000E+00  0.00000E+00
37'intens-4-3'  0.00000E+00  0.00000E+00
38'intens-5-3'  0.00000E+00  0.00000E+00
39'intens-6-3'  0.00000E+00  0.00000E+00
40'fondo-int3'  0.00000E+00  0.00000E+00
41'Q-back-c-3'  0.00000E+00  0.00000E+00
42'Q-back-A-3'  0.00000E+00  0.00000E+00
43'Q-back-x03'  0.00000E+00  0.00000E+00
44't        ' -0.13221E+00  0.14142E+01
45'asim     ' 0.50000E-01  0.00000E+00
46'pos-asim ' 0.40001E+03  0.00000E+00
47'int-asim ' 0.00000E+00  0.00000E+00
48'anch-asim ' 0.34416E+00  0.00000E+00
```

XPS Ni 2p3/2 of NiO early stages of NiO growth on Al_2O_3

1'res	0.67000E+00	0.00000E+00
2'intens-1	0.76158E+02	0.11511E+01
3'anch-1	0.16700E+00	0.00000E+00
4'pos-1	0.39898E+03	0.56289E-01
5'fondo-int	0.89567E-03	0.13786E-03
6'intens-2	0.70942E+00	0.00000E+00
7'anch-2	0.70000E+00	0.00000E+00
8'pos-2	0.27000E+01	0.00000E+00
9'intens-3	0.93089E+01	0.21264E+00
10'anch-3	0.34155E+01	0.13321E+00
11'pos-3	0.67654E+01	0.12911E+00
12'intens-4	0.00000E+00	0.00000E+00
13'anch-4	0.31571E+00	0.00000E+00
14'pos-4	0.12671E+02	0.00000E+00
15'intens-5	0.00000E+00	0.00000E+00
16'anch-5	0.87175E+00	0.00000E+00
17'pos-5	0.10054E+02	0.00000E+00
18'int-6	0.28627E+01	0.63371E+00
19'anch-6	0.61000E+00	0.00000E+00
20'pos-6	0.12000E+01	0.00000E+00
21'Q-back-c	0.98187E+02	0.81206E+00
22'Q-back-A	-0.24479E-02	0.13317E-03
23'Q-back-x0	0.47424E+03	0.21382E+01
24'intens-1-2'	0.20147E+07	0.28284E+01
25'intens-2-2'	0.22002E+01	0.14142E+01
26'intens-3-2'	0.28619E+01	0.14142E+01
27'intens-4-2'	0.71897E-01	0.14142E+01
28'intens-5-2'	0.64522E-01	0.00000E+00
29'intens-6-2'	0.00000E+00	0.00000E+00
30'fondo-int2'	0.39559E-01	0.00000E+00
31'Q-back-c-2'	0.78458E+06	0.00000E+00
32'Q-back-A-2'	0.86531E+03	0.00000E+00
33'Q-back-x02'	0.42970E+03	0.00000E+00
34'intens-1-3'	0.00000E+00	0.00000E+00
35'intens-2-3'	0.00000E+00	0.00000E+00
36'intens-3-3'	0.00000E+00	0.00000E+00
37'intens-4-3'	0.00000E+00	0.00000E+00
38'intens-5-3'	0.00000E+00	0.00000E+00
39'intens-6-3'	0.00000E+00	0.00000E+00
40'fondo-int3'	0.00000E+00	0.00000E+00
41'Q-back-c-3'	0.00000E+00	0.00000E+00
42'Q-back-A-3'	0.00000E+00	0.00000E+00
43'Q-back-x03'	0.00000E+00	0.00000E+00
44't	-0.13221E+00	0.14142E+01
45'asim	0.50000E-01	0.00000E+00
46'pos-asim	0.40083E+03	0.22271E+00
47'int-asim	0.00000E+00	0.10293E+02
48'anch-asim	0.34416E+00	0.00000E+00

XPS Ni 2p3/2 of NiO early stages of NiO growth on MgO

1'res	0.67000E+00	0.00000E+00
2'intens-1	0.69178E+02	0.15076E+01
3'anch-1	0.16700E+00	0.22134E+00
4'pos-1	0.39841E+03	0.54496E-01
5'fondo-int	-0.77308E-03	0.17810E-03
6'intens-2	0.70942E+00	0.00000E+00
7'anch-2	0.70000E+00	0.00000E+00
8'pos-2	0.27000E+01	0.00000E+00
9'intens-3	0.55815E+01	0.22192E+00
10'anch-3	0.23368E+01	0.14556E+00
11'pos-3	0.64736E+01	0.13843E+00
12'intens-4	0.16448E+00	0.10042E+00
13'anch-4	0.31571E+00	0.00000E+00
14'pos-4	0.12671E+02	0.00000E+00
15'intens-5	0.63587E+00	0.14001E+00
16'anch-5	0.87175E+00	0.00000E+00
17'pos-5	0.10054E+02	0.00000E+00
18'intens-6	0.28612E+01	0.14003E+00
19'anch-6	0.55000E+00	0.14413E+00
20'pos-6	0.90000E+00	0.13107E+00
21'Q-back-c	0.81201E+02	0.81923E+00
22'Q-back-A	0.18680E-01	0.59966E-03
23'Q-back-x0	0.42969E+03	0.60947E+00
24'intens-1-2'	0.20147E+07	0.20000E+01
25'intens-2-2'	0.22002E+01	0.14142E+01
26'intens-3-2'	0.28619E+01	0.14142E+01
27'intens-4-2'	0.71897E-01	0.14142E+01
28'intens-5-2'	0.64522E-01	0.14142E+01
29'intens-6-2'	0.00000E+00	0.00000E+00
30'fondo-int2'	0.39559E-01	0.00000E+00
31'Q-back-c-2'	0.78458E+06	0.00000E+00
32'Q-back-A-2'	0.86531E+03	0.00000E+00
33'Q-back-x02'	0.42970E+03	0.00000E+00
34'intens-1-3'	0.00000E+00	0.00000E+00
35'intens-2-3'	0.00000E+00	0.00000E+00
36'intens-3-3'	0.00000E+00	0.00000E+00
37'intens-4-3'	0.00000E+00	0.00000E+00
38'intens-5-3'	0.00000E+00	0.00000E+00
39'intens-6-3'	0.00000E+00	0.00000E+00
40'fondo-int3'	0.00000E+00	0.00000E+00
41'Q-back-c-3'	0.00000E+00	0.00000E+00
42'Q-back-A-3'	0.00000E+00	0.00000E+00
43'Q-back-x03'	0.00000E+00	0.00000E+00
44't	-0.13221E+00	0.14142E+01
45'asim	0.50000E-01	0.00000E+00
46'pos-asim	0.40001E+03	0.00000E+00
47'int-asim	0.00000E+00	0.00000E+00
48'anch-asim	0.34416E+00	0.00000E+00

HAXPES Ni 2p3/2 of NiO single crystal (9 KeV)

1'res ' 0.12107E+01 0.00000E+00
2'intens-1 ' 0.19433E+03 0.49944E+02
3'anch-1 ' 0.16700E+00 0.00000E+00
4'pos-1 ' 0.39912E+03 0.96042E-01
5'fondo-int ' 0.98112E-02 0.20915E-02
6'intens-2 ' 0.70942E+00 0.00000E+00
7'anch-2 ' 0.70000E+00 0.00000E+00
8'pos-2 ' 0.27000E+01 0.00000E+00
9'intens-3 ' 0.18054E+01 0.48864E+00
10'anch-3 ' 0.18002E+01 0.40164E+00
11'pos-3 ' 0.71417E+01 0.17724E+00
12'intens-4 ' 0.00000E+00 0.00000E+00
13'anch-4 ' 0.31571E+00 0.00000E+00
14'pos-4 ' 0.12671E+02 0.00000E+00
15'intens-5 ' 0.00000E+00 0.00000E+00
16'anch-5 ' 0.87175E+00 0.00000E+00
17'pos-5 ' 0.10054E+02 0.00000E+00
18'intens-6 ' 0.33872E+00 0.27371E+00
19'surf ' 0.33000E+00 0.00000E+00
20'pos-6 ' 0.15049E+01 0.00000E+00
21'Q-back-c ' 0.92395E+02 0.29181E+01
22'Q-back-A ' 0.21759E-02 0.64040E-02
23'Q-back-x0 ' 0.42112E+03 0.79116E+02
24'intens-1-2' 0.20148E+07 0.14142E+01
25'intens-2-2' 0.22002E+01 0.14142E+01
26'intens-3-2' 0.28619E+01 0.14142E+01
27'intens-4-2' 0.71897E-01 0.14142E+01
28'intens-5-2' 0.64522E-01 0.14142E+01
29'intens-6-2' 0.00000E+00 0.00000E+00
30'fondo-int2' 0.39559E-01 0.00000E+00
31'Q-back-c-2' 0.78458E+06 0.00000E+00
32'Q-back-A-2' 0.86531E+03 0.00000E+00
33'Q-back-x02' 0.42970E+03 0.00000E+00
34'intens-1-3' 0.00000E+00 0.00000E+00
35'intens-2-3' 0.00000E+00 0.00000E+00
36'intens-3-3' 0.00000E+00 0.00000E+00
37'intens-4-3' 0.00000E+00 0.00000E+00
38'intens-5-3' 0.00000E+00 0.00000E+00
39'intens-6-3' 0.00000E+00 0.00000E+00
40'fondo-int3' 0.00000E+00 0.00000E+00
41'Q-back-c-3' 0.00000E+00 0.00000E+00
42'Q-back-A-3' 0.00000E+00 0.00000E+00
43'Q-back-x03' 0.00000E+00 0.00000E+00
44't ' -0.13221E+00 0.14142E+01

HAXPES Ni 2p3/2 of NiO single crystal (12 KeV)

1'res ' 0.13241E+01 0.99256E-01
2'intens-1 ' 0.21478E+03 0.51053E+01
3'anch-1 ' 0.16700E+00 0.00000E+00
4'pos-1 ' 0.39909E+03 0.67115E-01
5'fondo-int ' 0.11250E-02 0.50061E-03
6'intens-2 ' 0.70942E+00 0.00000E+00
7'anch-2 ' 0.70000E+00 0.00000E+00
8'pos-2 ' 0.27000E+01 0.00000E+00
9'intens-3 ' 0.26776E+01 0.11030E+00
10'anch-3 ' 0.24477E+01 0.51308E+00
11'pos-3 ' 0.71318E+01 0.14710E+00
12'intens-4 ' 0.00000E+00 0.00000E+00
13'anch-4 ' 0.31571E+00 0.00000E+00
14'pos-4 ' 0.12671E+02 0.00000E+00
15'intens-5 ' 0.00000E+00 0.00000E+00
16'anch-5 ' 0.87175E+00 0.00000E+00
17'pos-5 ' 0.10054E+02 0.00000E+00
18'intens-6 ' 0.31800E+00 0.00000E+00
19'surf ' 0.33000E+00 0.00000E+00
20'pos-6 ' 0.15049E+01 0.00000E+00
21'Q-back-c ' 0.88767E+02 0.12883E+01
22'Q-back-A ' 0.33189E-05 0.75752E-01
23'Q-back-x0 ' 0.42000E+03 0.78783E+02
24'intens-1-2' 0.20148E+07 0.20000E+01
25'intens-2-2' 0.22002E+01 0.14142E+01
26'intens-3-2' 0.28619E+01 0.14142E+01
27'intens-4-2' 0.71897E-01 0.14142E+01
28'intens-5-2' 0.64522E-01 0.14142E+01
29'intens-6-2' 0.00000E+00 0.00000E+00
30'fondo-int2' 0.39559E-01 0.00000E+00
31'Q-back-c-2' 0.78458E+06 0.00000E+00
32'Q-back-A-2' 0.86531E+03 0.00000E+00
33'Q-back-x02' 0.42970E+03 0.00000E+00
34'intens-1-3' 0.00000E+00 0.00000E+00
35'intens-2-3' 0.00000E+00 0.00000E+00
36'intens-3-3' 0.00000E+00 0.00000E+00
37'intens-4-3' 0.00000E+00 0.00000E+00
38'intens-5-3' 0.00000E+00 0.00000E+00
39'intens-6-3' 0.00000E+00 0.00000E+00
40'fondo-int3' 0.00000E+00 0.00000E+00
41'Q-back-c-3' 0.00000E+00 0.00000E+00
42'Q-back-A-3' 0.00000E+00 0.00000E+00
43'Q-back-x03' 0.00000E+00 0.00000E+00
44't ' -0.13221E+00 0.14142E+01

HAXPES Ni 1s of NiO single crystal (9 KeV)

1'res	' 0.12107E+01	0.00000E+00
2'intens-1	' 0.19970E+03	0.62392E+01
3'anch-1	' 0.16700E+00	0.00000E+00
4'pos-1	' 0.39976E+03	0.24965E-01
5'fondo-int	' -0.41154E-02	0.48919E-03
6'intens-2	' 0.70942E+00	0.00000E+00
7'anch-2	' 0.70000E+00	0.00000E+00
8'pos-2	' 0.27000E+01	0.00000E+00
9'intens-3	' 0.25907E+01	0.14201E+00
10'anch-3	' 0.25000E+01	0.63738E+00
11'pos-3	' 0.71343E+01	0.21699E+00
12'intens-4	' 0.00000E+00	0.00000E+00
13'anch-4	' 0.31571E+00	0.00000E+00
14'pos-4	' 0.12671E+02	0.00000E+00
15'intens-5	' 0.00000E+00	0.00000E+00
16'anch-5	' 0.87175E+00	0.00000E+00
17'pos-5	' 0.10054E+02	0.00000E+00
18'i-surf	' 0.54250E+00	0.00000E+00
19'a-surf	' 0.22000E+00	0.00000E+00
20'pos-6	' 0.15049E+01	0.00000E+00
21'Q-back-c	' 0.31436E+00	0.11461E+01
22'Q-back-A	' 0.84859E-02	0.88984E-04
23'Q-back-x0	' 0.51000E+03	0.00000E+00
24'intens-1-2'	0.20148E+07	0.82982E+00
25'intens-2-2'	0.22002E+01	0.14142E+01
26'intens-3-2'	0.28619E+01	0.14142E+01
27'intens-4-2'	0.71897E-01	0.14142E+01
28'intens-5-2'	0.64522E-01	0.14142E+01
29'intens-6-2'	0.00000E+00	0.00000E+00
30'fondo-int2'	0.39559E-01	0.00000E+00
31'Q-back-c-2'	0.78458E+06	0.00000E+00
32'Q-back-A-2'	0.86531E+03	0.00000E+00
33'Q-back-x02'	0.42970E+03	0.00000E+00
34'intens-1-3'	0.00000E+00	0.00000E+00
35'intens-2-3'	0.00000E+00	0.00000E+00
36'intens-3-3'	0.00000E+00	0.00000E+00
37'intens-4-3'	0.00000E+00	0.00000E+00
38'intens-5-3'	0.00000E+00	0.00000E+00
39'intens-6-3'	0.00000E+00	0.00000E+00
40'fondo-int3'	0.00000E+00	0.00000E+00
41'Q-back-c-3'	0.00000E+00	0.00000E+00
42'Q-back-A-3'	0.00000E+00	0.00000E+00
43'Q-back-x03'	0.00000E+00	0.00000E+00
44't	' -0.13221E+00	0.14142E+01

HAXPES Ni 1s of NiO single crystal (12 KeV)

1'res	' 0.13241E+01	0.00000E+00
2'intens-1	' 0.23296E+03	0.25753E+02
3'anch-1	' 0.16700E+00	0.00000E+00
4'pos-1	' 0.39975E+03	0.34887E-01
5'fondo-int	' -0.22604E-02	0.84478E-03
6'intens-2	' 0.70942E+00	0.00000E+00
7'anch-2	' 0.70000E+00	0.00000E+00
8'pos-2	' 0.27000E+01	0.00000E+00
9'intens-3	' 0.22087E+01	0.56956E+00
10'anch-3	' 0.22583E+01	0.57547E+00
11'pos-3	' 0.72000E+01	0.24088E+00
12'intens-4	' 0.00000E+00	0.00000E+00
13'anch-4	' 0.31571E+00	0.00000E+00
14'pos-4	' 0.12671E+02	0.00000E+00
15'intens-5	' 0.00000E+00	0.00000E+00
16'anch-5	' 0.87175E+00	0.00000E+00
17'pos-5	' 0.10054E+02	0.00000E+00
18'i-surf	' 0.38000E+00	0.00000E+00
19'a-surf	' 0.13645E+00	0.27041E+00
20'pos-6	' 0.15049E+01	0.00000E+00
21'Q-back-c	' 0.38966E+02	0.14202E+01
22'Q-back-A	' 0.78163E-02	0.12757E-03
23'Q-back-x0	' 0.48751E+03	0.95924E+00
24'intens-1-2'	0.20148E+07	0.11871E+08
25'intens-2-2'	0.22002E+01	0.46068E+08
26'intens-3-2'	0.28619E+01	0.46068E+08
27'intens-4-2'	0.71897E-01	0.46068E+08
28'intens-5-2'	0.64522E-01	0.46068E+08
29'intens-6-2'	0.00000E+00	0.00000E+00
30'fondo-int2'	0.39559E-01	0.00000E+00
31'Q-back-c-2'	0.78458E+06	0.00000E+00
32'Q-back-A-2'	0.86531E+03	0.00000E+00
33'Q-back-x02'	0.42970E+03	0.00000E+00
34'intens-1-3'	0.00000E+00	0.00000E+00
35'intens-2-3'	0.00000E+00	0.00000E+00
36'intens-3-3'	0.00000E+00	0.00000E+00
37'intens-4-3'	0.00000E+00	0.00000E+00
38'intens-5-3'	0.00000E+00	0.00000E+00
39'intens-6-3'	0.00000E+00	0.00000E+00
40'fondo-int3'	0.00000E+00	0.00000E+00
41'Q-back-c-3'	0.00000E+00	0.00000E+00
42'Q-back-A-3'	0.00000E+00	0.00000E+00
43'Q-back-x03'	0.00000E+00	0.00000E+00
44't	' -0.13221E+00	0.46068E+08

PES Ni 2p3/2 of bulk NiO (1KeV)

1'res ' 0.70000E+00 0.00000E+00
2'intens-1 ' 0.12935E+03 0.43635E+01
3'anch-1 ' 0.16700E+00 0.00000E+00
4'pos-1 ' 0.39899E+03 0.57441E-01
5'fondo-int ' 0.42301E-02 0.60920E-03
6'intens-2 ' 0.70942E+00 0.00000E+00
7'anch-2 ' 0.70000E+00 0.00000E+00
8'pos-2 ' 0.29500E+01 0.00000E+00
9'intens-3 ' 0.39317E+01 0.29190E+00
10'anch-3 ' 0.24000E+01 0.00000E+00
11'pos-3 ' 0.70470E+01 0.17238E+00
12'intens-4 ' 0.14403E+00 0.95710E-01
13'anch-4 ' 0.31571E+00 0.00000E+00
14'pos-4 ' 0.12671E+02 0.00000E+00
15'intens-5 ' 0.26658E+00 0.16227E+00
16'anch-5 ' 0.87175E+00 0.00000E+00
17'pos-5 ' 0.10054E+02 0.00000E+00
18'intens-6 ' 0.14800E+01 0.00000E+00
19'anch-6 ' 0.53000E+00 0.00000E+00
20'pos-6 ' 0.16200E+01 0.00000E+00
21'Q-back-c ' 0.87413E+02 0.21548E+01
22'Q-back-A ' 0.42821E-08 0.11022E-01
23'Q-back-x0 ' 0.45933E+03 0.59509E+02
24'intens-1-2' 0.20147E+07 0.69684E+05
25'intens-2-2' 0.22002E+01 0.13166E+07
26'intens-3-2' 0.28619E+01 0.13166E+07
27'intens-4-2' 0.71897E-01 0.13166E+07
28'intens-5-2' 0.64522E-01 0.13166E+07
29'intens-6-2' 0.00000E+00 0.00000E+00
30'fondo-int2' 0.39559E-01 0.00000E+00
31'Q-back-c-2' 0.78458E+06 0.00000E+00
32'Q-back-A-2' 0.86531E+03 0.00000E+00
33'Q-back-x02' 0.42970E+03 0.00000E+00
34'intens-1-3' 0.00000E+00 0.00000E+00
35'intens-2-3' 0.00000E+00 0.00000E+00
36'intens-3-3' 0.00000E+00 0.00000E+00
37'intens-4-3' 0.00000E+00 0.00000E+00
38'intens-5-3' 0.00000E+00 0.00000E+00
39'intens-6-3' 0.00000E+00 0.00000E+00
40'fondo-int3' 0.00000E+00 0.00000E+00
41'Q-back-c-3' 0.00000E+00 0.00000E+00
42'Q-back-A-3' 0.00000E+00 0.00000E+00
43'Q-back-x03' 0.00000E+00 0.00000E+00
44't ' -0.13221E+00 0.13166E+07

XPS Ni 2p3/2 of bulk NiO (1.486.6 KeV)

1'res ' 0.67000E+00 0.00000E+00
2'intens-1 ' 0.15401E+03 0.35777E+02
3'anch-1 ' 0.16700E+00 0.00000E+00
4'pos-1 ' 0.39731E+03 0.10412E+00
5'fondo-int ' 0.19475E-02 0.73089E-03
6'intens-2 ' 0.70942E+00 0.00000E+00
7'anch-2 ' 0.70000E+00 0.00000E+00
8'pos-2 ' 0.27000E+01 0.00000E+00
9'intens-3 ' 0.24702E+01 0.76590E+00
10'anch-3 ' 0.21776E+01 0.49755E+00
11'pos-3 ' 0.71104E+01 0.24854E+00
12'intens-4 ' 0.49852E-01 0.99086E-01
13'anch-4 ' 0.31571E+00 0.00000E+00
14'pos-4 ' 0.12671E+02 0.00000E+00
15'intens-5 ' 0.12663E+00 0.19129E+00
16'anch-5 ' 0.87175E+00 0.00000E+00
17'pos-5 ' 0.10054E+02 0.00000E+00
18'intens-6 ' 0.64330E+00 0.65391E+00
19'anch-6 ' 0.30409E+00 0.66212E+00
20'pos-6 ' 0.15163E+01 0.15608E+00
21'Q-back-c ' 0.81978E+02 0.21540E+01
22'Q-back-A ' 0.20842E-01 0.40288E-02
23'Q-back-x0 ' 0.42480E+03 0.99023E+00
24'intens-1-2' 0.20147E+07 0.39319E+07
25'intens-2-2' 0.22002E+01 0.39319E+07
26'intens-3-2' 0.28619E+01 0.39319E+07
27'intens-4-2' 0.71897E-01 0.39319E+07
28'intens-5-2' 0.64522E-01 0.39319E+07
29'intens-6-2' 0.00000E+00 0.00000E+00
30'fondo-int2' 0.39559E-01 0.00000E+00
31'Q-back-c-2' 0.78458E+06 0.00000E+00
32'Q-back-A-2' 0.86531E+03 0.00000E+00
33'Q-back-x02' 0.42970E+03 0.00000E+00
34'intens-1-3' 0.00000E+00 0.00000E+00
35'intens-2-3' 0.00000E+00 0.00000E+00
36'intens-3-3' 0.00000E+00 0.00000E+00
37'intens-4-3' 0.00000E+00 0.00000E+00
38'intens-5-3' 0.00000E+00 0.00000E+00
39'intens-6-3' 0.00000E+00 0.00000E+00
40'fondo-int3' 0.00000E+00 0.00000E+00
41'Q-back-c-3' 0.00000E+00 0.00000E+00
42'Q-back-A-3' 0.00000E+00 0.00000E+00
43'Q-back-x03' 0.00000E+00 0.00000E+00
44't ' -0.13221E+00 0.39319E+07

TABLE AND FIGURE INDEX

Table

Chapter II

Chapter III

Chapter IV

Chapter V

Figures

Chapter I

Chapter II

Chapter III

Chapter IV

Chapter V

Chapter VI

LIST of PUBLICATIONS

1. L. Soriano, A. Gutiérrez, **I. Preda**, S. Palacín, J.M. Sanz, M. Abbate, J.F. Trigo, A. Vollmer, P.R. Bressler, *"Splitting of the Ni 3d states at the surface of NiO nanostructures"*, **Physical Review B, v**ol. **74**, p. 193402-1-193402-4, 2006.

2. **I. Preda**, M. Abbate, A. Gutiérrez, S. Palacín, L. Soriano**,** *"Study of the Growth of NiO on Highly Oriented Pyrolitic Graphite by X-Ray Absorption Spectroscopy"*, **Journal of Electron Spectroscopy and Related Phenomena,** vol. **156–158**, p. 111–114, 2007.

3. S. Palacín, A. Gutiérrez**, I. Preda**, M. Hernández-Vélez, R. Sanz, J. A. Jiménez and L. Soriano, *"Core-level electronic properties of nanostructured NiO coatings"*, **Applied Surface Science,** vol. **254**, p. 278–280, 2007.

4. L. Soriano, A. Gutiérrez, **I. Preda**, S. Palacín, M. Abbate, and A. Vollmer, *"Surface effects in the Ni 2p photoelectron spectra of NiO"*, **Physical Review B,** vol. **75**, p. 233417, 2007.

5. **I. Preda**, A. Gutiérrez, M. Abbate, F. Yubero, J. Méndez, L. Alvarez and L. Soriano, *"Interface effects in the Ni 2p X-ray photoelectron spectra of NiO thin films grown on oxide substrates",* **Physical Review B,** vol. **77**, p. 075411-7 , 2008.